



FINAL REPORT:
Benchmark Experimental Measurements
of Turbulent Compressible Mixing Layers
for CFD Validation

Co-PIs: J. C. Dutton and G. S. Elliott

Department of Aerospace Engineering, University of Illinois at Urbana-Champaign

NASA Collaborative Agreement: NNX15AU94A

December 2020

This report is divided into two parts:

Section I discusses the unheated mixing layer studies.

Section II discusses the heated mixing layer studies.

PART I

UNHEATED MIXING LAYER STUDIES

(Based on the Ph.D. Dissertation of Kevin Kim)

ABSTRACT

In this work, experiments on planar free shear layers are conducted to obtain a set of benchmark computational fluid dynamics-validation data and to examine compressibility effects on shear layer turbulence. Five different dual-stream air mixing layers are studied, with levels of compressibility that range in convective Mach number from 0.19 to 0.88. The chief benchmark experimental data are high resolution, three-component velocity fields on the streamwise-transverse plane that are acquired via stereoscopic particle image velocimetry. Large ensembles (> 3000) of instantaneous measurements are obtained to confirm fully-developed, self-similar conditions of the mean velocity and each component of the Reynolds stress tensor. Transverse-spanwise plane velocity measurements are also acquired, and their mean velocity results confirm spanwise symmetry. Other flow conditions that are documented include the incoming boundary layer integral parameters on four different transverse location walls and sidewall static pressure distributions for the full streamwise extent of each mixing layer to verify that the test-section pressure is constant. A full uncertainty analysis is provided for each measured and calculated quantity, including the individual Reynolds stresses. Mean spanwise velocity magnitudes are shown to be below the maximum uncertainty values (for a 95% confidence interval). All experimental results for each case, as well as the wind tunnel geometries, are made available to the public on the project website: <https://wiki.illinois.edu/wiki/display/NCSLF/>.

Novel experimental fluid dynamic analyses that are performed regarding compressibility effects on mixing layer turbulence include trends of the full Reynolds stress tensor and its anisotropy, turbulence length scales, dominant dynamic eigenmodes, evolution of the large-scale turbulent structures, and differing entrainment mechanisms, among others. As compressibility is increased, the reduction of the transverse normal, spanwise normal, and primary shear stresses, in conjunction with the constant streamwise normal stress, causes the mixing layer turbulence to become more anisotropic and trend toward one-component, streamwise-dominated turbulence from more isotropic turbulence in the incompressible case. This result is likely related to the turbulence length scales increasing for the streamwise velocity fluctuations in the transverse and streamwise directions, and the flow becoming dominated by streamwise pulsing motions, as compressibility is increased. In contrast, the length scales of transverse velocity fluctuations decrease in the transverse direction with increasing compressibility, and the large vortical

structures that span the entire transverse height of the mixing layer, which are present in incompressible cases, become smaller in size and elongated in the streamwise direction. The evolution of the large structures in the mixing layer results in differing turbulent interface geometries for different levels of compressibility, ultimately reducing the length scales of entrainment in more compressible mixing layers. The compressibility effects listed here can also be linked to the unanimously agreed upon result in the literature (including here) of reduced normalized mixing layer growth rate for increased compressibility.

ACKNOWLEDGMENTS

All of the work presented in this dissertation was possible due to the funding from the D.3 Transformational Tools and Technologies (TTT) Revolutionary Computational Aerosciences (RCA) Project issued by NASA Headquarters, Award No. NNX15AU94A, with Dr. Mujeeb Malik as the project manager. This work would also not have been possible without the guidance of project technical managers at NASA Glenn Research Center: Jim DeBonis, Dave Davis, Nick Georgiadis, Dennis Yoder, and Manan Vyas.

TABLE OF CONTENTS

1. INTRODUCTION	1
1. 1. Background and Motivation	1
1. 2. Mixing Layer Literature Review	4
1. 2. 1. Analytical Approach	4
1. 2. 2. Experimental Investigations.....	8
1. 2. 3. Computational Investigations	13
1. 3. Present Investigation	16
2. EXPERIMENTAL METHODOLOGY	18
2. 1. Wind Tunnel Facility	18
2. 2. Flow Diagnostics	23
2. 2. 1. Pressure/Temperature Measurements	24
2. 2. 2. Incoming Boundary Layer PIV	25
2. 2. 3. Flow Visualization	26
2. 2. 4. Mixing Layer Stereoscopic Particle Image Velocimetry	29
3. EXPERIMENTAL RESULTS.....	38
3. 1. Operating Conditions	38
3. 2. Pressure Measurements.....	39
3. 3. Incoming Boundary Layer Measurements.....	40
3. 4. Mixing Layer Flow Visualization	43
3. 4. 1. Schlieren Photography	44
3. 4. 2. Mie Scattering Images	47
3. 5. Spanwise-Central SPIV Velocity Measurements	50
3. 5. 1. Instantaneous Velocity Fields	50
3. 5. 2. Mixing Layer Development.....	55
3. 5. 3. Growth Rate	60
3. 5. 4. Mixing Layer Self-Similarity.....	62
3. 6. End-View Plane SPIV Velocity Measurements	67
3. 6. 1. Instantaneous Velocity Fields	68
3. 6. 2. Mean Velocity Results.....	72

4. COMPRESSIBILITY EFFECTS ON MIXING LAYER TURBULENCE	77
4. 1. Mixing Layer Normalized Growth Rate	77
4. 2. Reynolds Stress and Anisotropy Trends	79
4. 3. Higher-Order Velocity Statistics.....	87
4. 4. Turbulence Production.....	91
4. 5. Turbulence Length Scales.....	93
4. 6. Relevant Mach Numbers.....	97
4. 6. 1. Revisiting the Convective Mach Number.....	97
4. 6. 2. Turbulence Mach Number	102
4. 6. 3. Gradient Mach Number	103
5. TWO-DIMENSIONAL FLOW ANALYSES	106
5. 1. Proper Orthogonal Decomposition	106
5. 1. 1. POD Background and Method Description	106
5. 1. 2. POD Results and Discussion	111
5. 2. Linear Stochastic Estimation	125
5. 2. 1. LSE Background and Method Description	125
5. 2. 2. Spatial Velocity Correlations	128
5. 2. 3. LSE Results and Discussion	134
5. 3. Entrainment Analysis.....	138
5. 3. 1. Detection of the Turbulent/Non-Turbulent Interface.....	140
5. 3. 2. TNTI Statistics	143
5. 3. 3. Conditional Statistics Across the TNTI	146
5. 3. 4. Entrainment Length Scales and Mechanisms	151
6. UNCERTAINTY OF EXPERIMENTAL RESULTS	160
6. 1. Operating Condition and Pressure Measurement Uncertainties	160
6. 2. SPIV Uncertainty	161
6. 2. 1. Instantaneous Uncertainty.....	161
6. 2. 2. Uncertainty of Mean Velocities	165
6. 2. 3. Uncertainty of Reynolds Stresses	167
7. CONCLUSIONS	169
7. 1. Summary of Present Work.....	169

7.2. Suggestions for Future Work	174
REFERENCES	177
APPENDIX A: Website Documentation	182
APPENDIX B: Uncertainty Parameters	184
APPENDIX C: Velocity Comparison Between Diagnostics.....	186
APPENDIX D: Expansion of Turbulence Production Terms.....	188

1. INTRODUCTION

1. 1. Background and Motivation

Turbulence in mixing layers is a subject of wide-spread interest, both due to its prevalence in numerous engineering applications, as well as its importance in furthering our fundamental knowledge of the fluid mechanics that govern such a canonical flowfield. This ubiquitous problem is a feature in many performance-critical applications, such as high-speed jets and ejectors, aircraft subject to separation (with a shear layer forming above the separated region), and most notably, scramjet engines. In regard to the last, gaseous fuel and oxidant streams must mix on the molecular level within the very short residence times available in the combustor, making the mixing process a critical design aspect. Moreover, specific to scramjet engines is the notion of compressing the flow through the inlet so that it remains supersonic in the combustor, as this condition is the only way to operate efficiently at hypersonic speeds. From a flow physics standpoint, this condition introduces the aspect of fluid compressibility (*i.e.*, changes in fluid density governed by thermodynamics), which affects the efficiency with which the fuel and oxidizer are able to mix. Herein, the problem of the two-stream mixing layer becomes of direct relevance, with specific importance placed on understanding the different mixing layer physical behaviors under varying levels of compressibility. As scramjet research in the U.S. was heavily funded during the 1980's and early 1990's,¹ compressible mixing layers became a prevalent subject of investigation. As such, there were numerous studies, many of which are now considered seminal, conducted on mixing layer turbulence during and near that time period.

Although simple in geometry, the planar free shear layer exhibits complicated turbulent behavior, especially at high Reynolds numbers and, in some instances, supersonic conditions. The effects of compressibility on the underlying physics make the flowfield difficult to accurately model and predict. And while incompressible mixing layers have been studied abundantly for many decades, their compressible counterparts have been relatively less examined, both due to the difficult nature of obtaining quality experimental data under compressible conditions, as well as the large amounts of computing power required for related numerical simulations. Since the early studies of incompressible mixing layers, however, there have been tremendous advances in different areas of science that have allowed for experiments and computational fluid dynamic

(CFD) studies alike, to investigate shear layers with high levels of compressibility. Some examples include the development of highly sensitive scientific cameras, laser technology, massive increases in computer data memory capacity, and intricate image-processing algorithms. Specifically, progress in CFD techniques has led to many recent computational investigations regarding the effects of compressibility on mixing layer turbulence.²⁻⁵

As for compressible mixing layer experiments, many were conducted in the 1990's using non-intrusive optical diagnostic techniques such as laser Doppler velocimetry (LDV), schlieren photography, and planar laser-induced fluorescence (PLIF). Unfortunately, for most experiments, the planar data obtained were largely qualitative flow visualizations, and quantitative diagnostics that measured velocity, pressure, etc. were done on a point-by-point basis. This made it especially difficult to study the important large-scale turbulent structures in the mixing layer in a quantitative manner. These structures play a central role in the entrainment of freestream fluid into the mixing region and affect the turbulence properties of the shear layer. At the time of this writing, quantitative analyses of large-scale structures in compressible mixing layers (*e.g.*, by linear stochastic estimation), based on large ensembles of experimental data, have not yet been performed. This is largely due to the lack of high-resolution, instantaneous velocity measurements available in the literature for higher levels of compressibility. In addition, no compressible shear layer experiment to date has fully documented the entire wind tunnel geometry with initial flow conditions, making direct comparisons between simulations and experiments all the more difficult. Thus, there is motivation for procuring a set of CFD validation-quality benchmark experimental data that characterizes the compressibility effects in mixing layers. A main objective of this dissertation is to address this current research need by using advanced flow diagnostic techniques (*i.e.*, stereoscopic particle image velocimetry) to obtain instantaneous, high-resolution, planar three-component velocity measurements. In addition to serving as a CFD validation tool, these data are used to analyze mixing layer turbulence statistics, as well as large-scale structures and entrainment.

In the context of experimental fluid mechanics, the problem of the spatially developing planar free shear layer is shown in Figure 1. The primary and secondary freestream flows are denoted by the subscripts 1 and 2, respectively, and may have different specific heat ratios (γ). u , ρ , P , and T are the local fluid velocity, density, static pressure, and static temperature, respectively. As indicated by the mean velocity profile in Figure 1, the primary stream is chosen to be the higher-

speed side. The origin of the Cartesian coordinate system is located at the splitter plate tip, with x aligned in the streamwise-direction, y aligned transverse to the splitter plate, and z aligned spanwise. In the spanwise direction, the origin is located at the splitter tip spanwise center (relative to the wind tunnel sidewalls). Flow diagnostics are generally performed on the mixing layer at various locations downstream of the splitter plate tip (*i.e.*, the splitter plate trailing edge, $x = 0$). Due to the planar nature of the problem, difficulties may arise as a result of sidewall effects. This issue can especially be true for facilities that are smaller in scale in order to achieve large Reynolds numbers, making compressible mixing layer experiments all the more challenging.

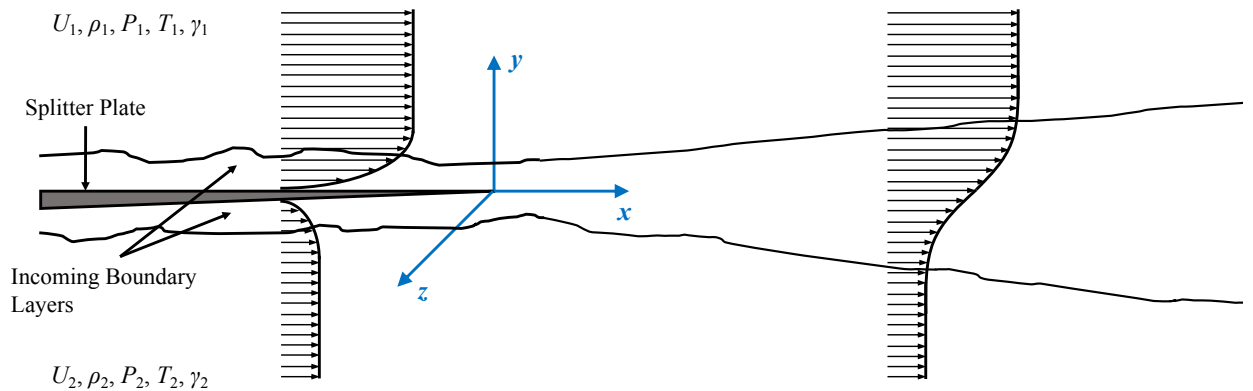


Figure 1. Spatially developing planar free shear layer in laboratory frame of reference.

Several considerations must be taken into account when acquiring the mixing layer turbulence data. These pertain specifically to ensuring that the measurements are of CFD validation-quality, and a few are introduced here with the intention of motivating the current work. One important aspect is allowing the turbulence to become fully developed, as incoming flow conditions (*e.g.*, the boundary layers shown in Figure 1) affect the flow physics near the origin and are different for each wind tunnel facility. Fully developed conditions can be confirmed by applying a transverse similarity transformation for each variable and demonstrating its self-similarity in the streamwise direction. Additionally, the previously mentioned sidewall effects must be far enough away from the measurement plane so as to not alter the mixing physics observed. This can be confirmed by measuring the cross-sectional y - z velocity field and inspecting the mean spanwise velocity. And although the geometry is planar, it has been shown that this canonical flow exhibits highly three-dimensional behavior under compressible conditions. A lack of spanwise turbulence statistics is apparent in the literature, with most experimental investigations obtaining two-component velocity

data. As the following subsections will show, currently available experimental mixing layer data are lacking in one or more aspects mentioned above, and hence, are unsuitable to serve as benchmark CFD validation measurements.

Having defined the problem of the turbulent free shear layer and motivated the current research gaps this dissertation aims to fill, the next section discusses seminal findings from the literature on mixing layer turbulence, with a focus on compressibility effects at high Mach numbers.

1. 2. Mixing Layer Literature Review

Due to its simple geometry and canonical nature, the two-stream planar mixing layer problem has been investigated thoroughly in the study of fluid mechanics. Here, the literature is reviewed to set an appropriate backdrop for the present investigation of compressible mixing layers. Incompressible mixing layers are included in the discussion, with the intention of providing a baseline condition to compare against the compressible cases. Characteristics of incompressible mixing layers are useful for determining the net effects of compressibility on mean flow and turbulence quantities, as well the flow structure in the shear layer. Included in many of these studies is the problem of quantitatively defining the level of compressibility in the mixing layer, as there are a number of parameters (*e.g.*, ρ_2/ρ_1 , U_2/U_1 , $(U_1 - U_2)/(U_1 + U_2)$, etc.) that may affect the turbulence to varying degrees. The broad range of mixing layer work performed to date can be generally categorized into analytical, experimental, and computational studies.

1. 2. 1. Analytical Approach

Various incompressible mixing layer analyses have been able to determine analytical solutions for the mean velocity. Schlichting (1979)⁶ presents a solution by H. Goertler that uses a kinematic eddy viscosity model. Since the problem is that of a free shear flow (*i.e.*, no walls present), this analytical approach makes use of the constant-pressure, incompressible turbulent boundary layer equations and neglects the viscous stress terms. These are given in Equations (1) and (2) as continuity and conservation of streamwise momentum in Cartesian coordinates, respectively, where u is the instantaneous streamwise velocity and v is the instantaneous transverse velocity. The overbar on flow quantities implies time-averaging using the standard Reynolds decomposition ($u = \bar{u} + u'$, with the prime denoting the instantaneous fluctuation). In order to determine the turbulent stresses, τ , a simple eddy viscosity model based on Prandtl's hypothesis for free shear

flows is used (Equation (3))⁶. For free shear layers, \bar{u}_{\max} is equal to the faster primary freestream velocity (U_1), \bar{u}_{\min} is equal to the slower secondary freestream velocity (U_2), b is the thickness of the mixing layer, and α is an empirically determined constant.

$$\frac{\partial \bar{u}}{\partial x} + \frac{\partial \bar{v}}{\partial y} = 0 \quad (1)$$

$$\rho \left(\bar{u} \frac{\partial \bar{u}}{\partial x} + \bar{v} \frac{\partial \bar{u}}{\partial y} \right) = \frac{\partial \tau_t}{\partial y} \quad (2)$$

$$\tau_t = \rho \alpha b (\bar{u}_{\max} - \bar{u}_{\min}) \frac{\partial \bar{u}}{\partial y} \quad (3)$$

Assuming a linear growth rate, $b = \beta x$ can be substituted into Equation (3), which yields the result $\tau_t = \rho \alpha \beta x (U_1 - U_2) (\partial \bar{u} / \partial y)$. The similarity variable $\eta = \sigma(y/x)$ can be used with a stream function (Ψ) to transform Equation (2) into an ordinary differential equation (ODE). The stream function is given in Equation (4), and the resulting ODE is given in Equation (5). All primes below denote differentiation with respect to η .

$$\Psi = x \bar{U} F(\eta), \quad \bar{U} = (U_1 + U_2) / 2 \quad (4)$$

$$F''' + 2\sigma^2 F'' F = 0 \quad (5)$$

$$\sigma = (\alpha \beta \lambda)^{-1/2} / 2, \quad \lambda = (U_1 - U_2) / (U_1 + U_2) \quad (6)$$

Using the definition of Ψ , the result $u = \bar{U} \sigma F'$ is obtained, which gives the freestream boundary conditions as: $F'(\eta \rightarrow \pm\infty) = 1 \pm \lambda$. Goertler then solves Equation (5) subject to these boundary conditions by assuming a power-series expansion and obtains the final analytical solution:

$$u = \frac{U_1 + U_2}{2} \left[1 + \frac{U_1 - U_2}{U_1 + U_2} \operatorname{erf}(\eta) \right], \quad \operatorname{erf}(\eta) = \frac{2}{\sqrt{\pi}} \int_0^\eta e^{-z^2} dz \quad (7)$$

In the case of compressible, turbulent planar free shear layers, the governing equations are given in Equations (8) – (11). These are the mean continuity, x -momentum, y -momentum, and energy conservation equations, in that order. Appropriate approximations are made for the flowfield illustrated in Figure 1: mean gradients in the streamwise and spanwise directions are

small compared to the transverse direction, root-mean-square values of the fluctuations u' , v' , and w' are of the same order, and the flow is statistically stationary.⁷ Note that the first three equations hold true in both compressible and incompressible, variable-density mixing layers.

$$\frac{\partial}{\partial x}(\bar{\rho}\bar{u}) + \frac{\partial}{\partial y}(\bar{\rho}\bar{v} + \bar{\rho}'\bar{v}') = 0 \quad (8)$$

$$\frac{\partial}{\partial x}(\bar{\rho}(\bar{u})^2) + \frac{\partial}{\partial y}(\bar{\rho}\bar{u}\bar{v} + (\bar{u})(\bar{\rho}'\bar{v}')) = -\frac{\partial}{\partial y}(\bar{\rho}u'\bar{v}') \quad (9)$$

$$\frac{\partial}{\partial y}(\bar{\rho}(v')^2) = -\frac{\partial \bar{p}}{\partial y} \quad (10)$$

$$\bar{p}\left(\frac{\partial \bar{u}}{\partial x} + \frac{\partial \bar{v}}{\partial y}\right) + \frac{\partial}{\partial y}(\bar{p}'\bar{v}') + \frac{1}{\gamma}\bar{v}\frac{\partial \bar{p}}{\partial y} = 0 \quad (11)$$

Due to the variable density in compressible shear layers, no closed form analytical solution of the given equations exists as for the incompressible case. In order to determine the effects of compressibility on the equations, Brown and Roshko (1974) examine the energy equation (Equation (11)).⁷ They note that if the last two terms are negligible, the relation identically satisfies the incompressible continuity equation. In the case of a near-constant pressure field, as is the case in many investigations, the last term is justifiably negligible; thus, at higher Mach numbers, the pressure-velocity correlation term ($\bar{p}'\bar{v}'$) must have a distinct effect on the underlying physics. This point is also affirmed by an analysis of variable composition incompressible mixing layers via the diffusion equation (which would replace the energy equation above). Brown and Roshko show that for uniform-temperature, subsonic flow, the diffusion equation for a mixture of gases (e.g., varying density mixing layer) results in reaffirmation of incompressible flow.⁷ Hence, compressibility effects are distinct from density ratio effects, a conclusion that is also supported by their experimental observations (Section 1. 2. 2).

Brown and Roshko also perform an order-of-magnitude analysis on the above relations. By combining Equations (8) and (9), the kinematic Reynolds shear stress, $\bar{u}'\bar{v}'$, is found to be on the order of $\sim(db/dx)U(\Delta U)$, where (db/dx) is the mixing layer growth rate, U is the mean velocity, and ΔU is the mean velocity difference across the mixing layer ($\Delta U = U_1 - U_2$). The shear layer thickness (b) can be defined in a variety of ways and is explained in detail in Section 1. 2. 2. Brown

and Roshko also reason that $\overline{u'v'}$ is on the order of $\sim \sigma_u \sigma_v$ and σ_u is on the order of $\sim \Delta U$, where σ denotes the root-mean-square of the fluctuating component. Both assumptions are supported by numerous experiments. This gives the result that $\sigma_v \sim (db/dx)U$. At this point, an order-of-magnitude estimate of the energy equation (Equation (11)) can be used to relate $(db/dx) \sim (1/M)(\Delta U/U)^{1/2}$. One assumption made to arrive at this relation is that the pressure-transverse velocity correlation satisfies $\overline{p'v'} \sim \sigma_p \sigma_v$, which may be inaccurate in high Mach number flows where pressure waves only affect a certain region of the mixing layer (since they are restricted by the local speed of sound), decreasing the pressure-transverse velocity correlation. Nevertheless, an important prediction from this analysis is that db/dx and σ_v both decrease with increasing Mach number, a result that is observed numerically and experimentally. From this analysis, it becomes clear that a representative Mach number is necessary to parameterize the effects of compressibility in shear layers.

Both Bogdanoff (1983) and Papamoschou and Roshko (1988) define the convective Mach number (M_c) by analyzing the mixing layer in the convective reference frame of the large-scale structures.^{8, 9} They argue that the two streams share a stagnation point between the large structures. Figure 2 depicts streamlines and the stagnation point (S) in the convective frame. If the two static pressures are equal ($P_1 = P_2$), then the isentropically determined relationship between the two streams in terms of the convective velocity (U_c) of the structures is as follows:

$$\left[1 + \frac{\gamma_1 - 1}{2} \left(\frac{U_1 - U_c}{a_1}\right)^2\right]^{\gamma_1 / (\gamma_1 - 1)} = \left[1 + \frac{\gamma_2 - 1}{2} \left(\frac{U_c - U_2}{a_2}\right)^2\right]^{\gamma_2 / (\gamma_2 - 1)} \quad (12)$$

where a is the speed of sound, and the subscripts 1 and 2 denote the faster primary and slower secondary streams, respectively. If the mixing layer is of uniform composition (*i.e.*, $\gamma_1 = \gamma_2$), then the convective velocity is of the form in Equation (13), and the convective Mach number can be defined as in Equation (14). M_c is commonly used to compare results of various experimental and

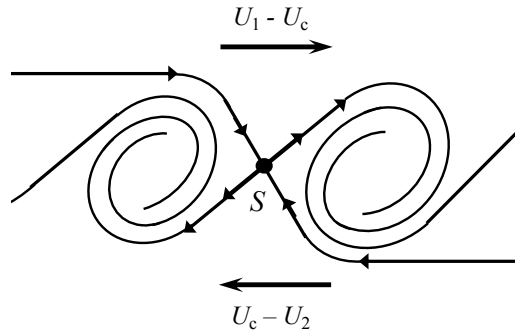


Figure 2. Mixing layer in convective frame of reference, adapted from Papamoschou and Roshko.⁹

numerical investigations and is theoretically the Mach number of the two freestreams relative to the large-scale structures in the shear layer.

$$U_c = \frac{U_1 a_2 + U_2 a_1}{a_1 + a_2} \quad (13)$$

$$M_{c_1} = \frac{U_1 - U_c}{a_1} = M_{c_2} = \frac{U_c - U_2}{a_2} = M_c = \frac{U_1 - U_2}{a_1 + a_2} \quad (14)$$

Although this model of convective Mach number is widely used to parametrize the level compressibility in the mixing layer, it should be noted that it may not be truly representative of the Mach number of the large-scale structures. This is especially true at higher levels of compressibility, where the isentropic stagnation pressure recovery may not be realistic, and various turbulent structures may convect at different speeds. A discussion on how to best empirically determine this quantity from the obtained measurements is given in Section 4. 6. 1. Nonetheless, this isentropic definition of M_c is easy to determine in investigations, and due to its universality in the literature, it is used in the current study.

1. 2. 2. Experimental Investigations

There have been numerous experimental investigations of mixing layers, both incompressible and compressible. A wide range of flow parameters have been examined across the studies, including velocity ratio ($r = U_2/U_1$), density ratio ($s = \rho_2/\rho_1$), and convective Mach number. The effects of velocity ratio, in particular, have been extensively documented in incompressible free shear layers. Several experiments, dating back to the 1940's, report constant-density ($s = 1$) mixing layer growth rates for different values of r .^{7, 10-14} A common parameter used to collapse the data is the velocity parameter, $\lambda = (1 - r)/(1 + r)$, first introduced by Abramovich (1963) and Sabin (1965).^{15, 16} Brown and Roshko, among others, show that the growth rate is well represented by a linear relationship with λ for incompressible, constant-density mixing layers.⁷ However, in the case of non-uniform density mixing layers, additional parameterization is necessary. Papamoschou and Roshko analyzed the effect of s in the convective reference frame of the large-scale structures and contend that the growth rate is directly proportional to $\sim \Delta U/U_c$, leading to the result in Equation (15).⁹ The subscript 0 denotes that the shear layer is incompressible, or $M_c \sim 0$, and c is a constant of proportionality.

$$\left(\frac{db}{dx}\right)_0 = c \frac{(1-r)(1+\sqrt{s})}{1+r\sqrt{s}} \quad (15)$$

Thus far, an explicit definition of the shear layer thickness, b , has not yet been presented here. Various experimentalists have used different definitions of b , including vorticity thickness (b_ω),⁷ visual thickness (b_{viz}),⁷ pitot thickness (b_{pit}),⁹ and the 10% ΔU thickness ($b_{10\%\Delta U}$).¹⁷ This last definition is the transverse length of the shear layer defined by the difference between the two points y_1 and y_2 , where $U(x, y_1) = (U_1 - 0.1\Delta U)$ and $U(x, y_2) = (U_2 + 0.1\Delta U)$. Depending on the diagnostic technique employed, the thickness definition used may be different among investigators; however, when direct velocity measurements of the mixing layer are available, $b_{10\%\Delta U}$ is used. The shear layer thickness can be calculated at x -positions where transverse velocity profiles are available. The thicknesses can then be used to determine the experimental growth rate using a linear curve fit of b vs. x . Using the 10% ΔU thickness definition, the constant in Equation (15) was found by Goebel and Dutton (1991) to be $c = 0.165/2$.¹⁷ This growth rate relation for $M_c \sim 0$ was shown to agree well with experimental results for incompressible shear layers,⁹ and is used herein to normalize the experimentally determined growth rate of compressible mixing layers. The incompressible mixing layer equation uses the same r and s values; thus, the normalization highlights the net effects of compressibility.

Following the advent of non-intrusive, optical flow diagnostic techniques, such as laser Doppler velocimetry (LDV), Schlieren photography, and planar laser-induced fluorescence (PLIF), experiments have shown that shear layers exhibit characteristic trends when subject to compressibility. Most notably, the reduction of the normalized shear layer growth rate with increasing M_c is widely agreed upon.¹⁷⁻²⁴ This result is shown clearly in Figure 3, where the normalized growth rate is plotted against M_c for

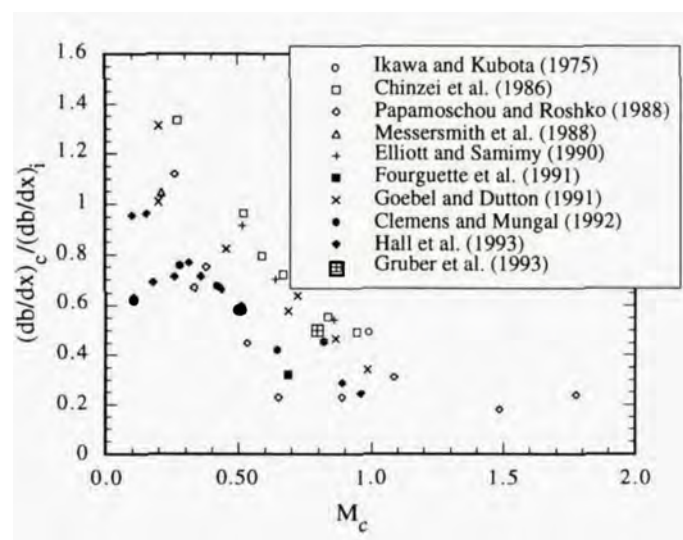


Figure 3. Normalized mixing layer growth rate vs. M_c for various experimental investigations.¹

various previous experiments. The substantial decrease of the normalized growth rate supports Brown and Roshko's conclusion that there are strong compressibility effects distinct from density ratio effects in supersonic mixing layers. The scatter in the data may be attributed to the use of various definitions of shear layer thickness among the investigators, requiring a conversion into the 10% ΔU thickness definition as outlined in Goebel (1990).²⁵ Additionally, the experiments were conducted in different wind tunnel facilities with different measurement techniques, and not all studies demonstrated that the mixing layer is in fact fully developed. Incoming boundary layers of either stream on the splitter plate have been shown to affect mixing layer properties in the initial developing region prior to self-similarity.²⁶ Therefore, in order to accurately compare results of the investigations, it is necessary to allow sufficient development of the shear layer.

Mehta and Westphal (1986) define fully developed conditions as follows: linear growth rate of the mixing layer, mean velocity profile self-similarity when y is scaled by the local shear layer thickness, and self-similar Reynolds stress profiles (with constant peaks) when y is scaled by the local thickness.²⁷ Since mean and turbulence quantities generally do not become fully developed at the same streamwise locations, these criteria are necessary to ensure full similarity of all statistics.

While there are numerous experiments that report mean compressible shear layer thickness and growth rate, studies that address turbulence statistics are fewer in number. Indeed, obtaining large ensembles ($\sim 1000 - 3000$) of instantaneous velocity measurements in supersonic flows presents difficult challenges. Figure 3 shows that there is reasonable agreement between many different researchers for mean growth rate results as a function of M_c . However, there is still a lack of complete unanimity on the trends of the Reynolds stress tensor with compressibility. Two seminal works that address this topic are that of Elliott and Samimy (1990),²⁰ and Goebel and Dutton (1991).¹⁷ The results of these two studies agree on the trend of reduction in peak transverse normal stress and primary shear stress with increasing M_c . However, for the peak streamwise normal stress, Goebel and Dutton report a relatively constant trend over a range of M_c , while Elliott and Samimy see the value decrease with increasing M_c , as with the other stresses. Following their work, Debisschop *et al.* (1994),²⁸ conducted experiments for various convective Mach numbers and saw a decrease in all three stresses, similar to Elliott and Samimy. However, the range of M_c for which they report turbulence quantities is small ($\sim 0.5 - 0.6$), and thus conclusive trends are difficult to establish from their results.

Even fewer studies obtain highly spatially resolved instantaneous velocity fields of compressible mixing layers via non-intrusive flow diagnostic techniques (*e.g.*, particle image velocimetry (PIV)). Urban and Mungal (2001) performed planar, two-component PIV on three different M_c mixing layers and show that the peak streamwise normal Reynolds stress is minimally affected by compressibility, while the peak transverse normal and primary shear Reynolds stresses were sharply reduced with increased convective Mach number, similar to Goebel and Dutton.²⁹

Regarding experimental results of spanwise turbulence statistics, only Gruber *et al.* (1993) and Barre and Bonnet (2015) address this subject.^{23, 30} Both investigations report the spanwise turbulence intensity to be lower with increased M_c . However, they only examined one M_c case each; thus, compressibility effects are again, difficult to characterize.

In addition to mean and statistical velocity data in compressible mixing layers, the study of large-scale turbulent structures is a topic of interest. It is generally understood that the existence of these structures, and their interaction with local freestream fluid (*e.g.*, entrainment), plays an integral role in the compressibility effects observed, such as reduced growth rate and shear stress with increasing M_c . Well documented on this subject is the transition of the large turbulent structure organization from spanwise-coherent, two-dimensional rollers, to three-dimensional in nature with no clear, consistent orientation as M_c increases.^{22, 31} This observation can be made through qualitative flow visualization techniques such as schlieren photography or Mie scattering images. Brown and Roshko were able to obtain shadowgraph images of incompressible mixing layers by using dissimilar gases, which causes a change in the index of refraction, making the optical technique possible. An example instantaneous image of a helium-nitrogen mixing layer at low Reynolds number is shown in Figure 4. Circular, spanwise-oriented vortices (termed ‘Brown-Roshko rollers’) are clearly apparent in this case, with thinner ‘braid’ regions connecting them together.

As compressibility increases in the shear layer, Clemens and Mungal (1995) showed that the large structures become less organized and highly three-dimensional.³¹ Figure 5 shows spanwise-resolved Mie scattering images of two different M_c shear layers. At the lower level of

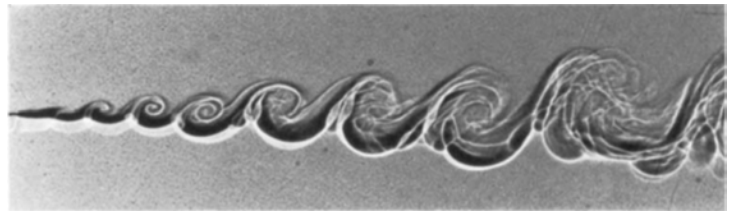


Figure 4. Schlieren photo of incompressible mixing layer, taken from Brown and Roshko, flow left to right.⁷

compressibility ($M_c = 0.28$), the images show quasi-two-dimensional rollers similar to the incompressible case. For the increased $M_c = 0.62$ case, however, the structures are less round and appear elongated or ‘stretched’ in the streamwise direction. The braid regions between the structures also exhibit a ‘kink’ unseen in the less compressible case (Figure 5b).

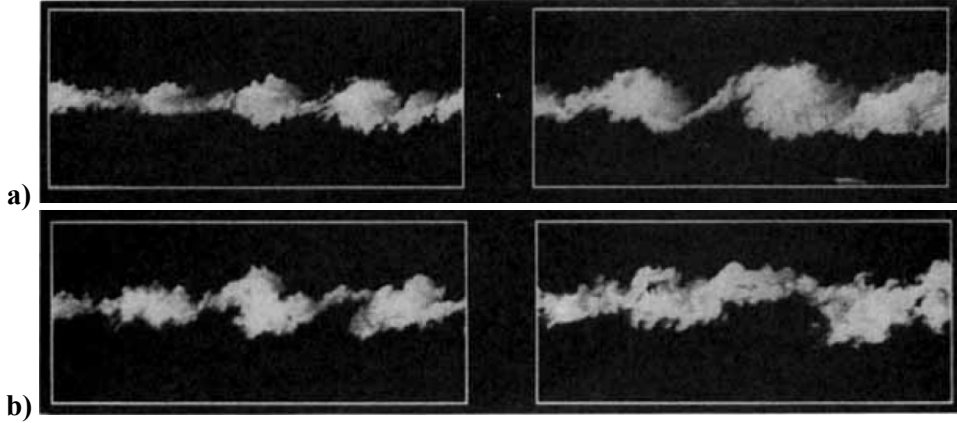


Figure 5. Side-view (x - y) planar product formation images for a) $M_c = 0.28$ and b) $M_c = 0.62$ mixing layers, taken from Clemens and Mungal (1995), flow left to right.³¹

The plan-view (x - z) product formation images shown in Figure 6 below further illustrate the lack of spanwise coherence in the large structures for higher M_c mixing layers. Vertical light and dark bands are present in the $M_c = 0.28$ case with regularity, indicating spanwise organization. These are not visible in the $M_c = 0.62$ case, and while some structures exhibit oblique orientation in the upstream (left) portion of the images, all spanwise coherence is lost by the downstream (right) end.

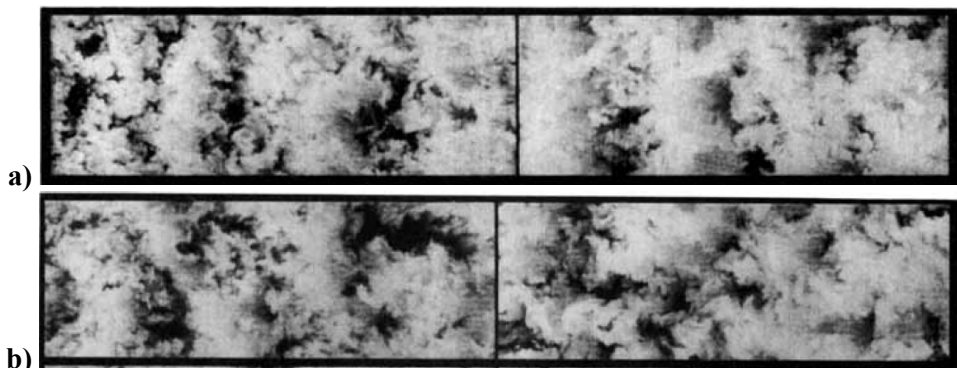


Figure 6. Plan-view (x - z) planar product formation images for a) $M_c = 0.28$ and b) $M_c = 0.62$ mixing layers, taken from Clemens and Mungal (1995), flow left to right.³¹

In addition to these qualitative observations from flow visualizations, quantitative results based on velocity field measurements are useful. One useful analysis technique that gives information about the characteristic eddy size/shape is linear stochastic estimation (LSE). It determines a conditionally averaged velocity field of a large structure based on some vortex identifying quantity. In what amounts to a two-point spatial correlation, the method calculates an average fluctuating velocity field surrounding a reference point. Further details on the LSE technique are discussed in Section 5. 2. Olsen and Dutton (2002) obtained 37 instantaneous PIV velocity fields and performed LSE on a mixing layer with $M_c = 0.38$.³² They found that by conditioning on the local deformation tensor, roller and braid structures could be identified, and when compared to the incompressible case, the rollers were flatter (*i.e.*, higher eccentricity), and the braids were vertically oriented rather than obliquely oriented, for this weakly compressible case.

Many of the various experimental findings discussed thus far have been reproduced by computational investigations, including the reduction of the normalized growth rate, transverse turbulence intensity, and primary shear Reynolds stress, with increasing M_c . A brief overview of seminal numerical work on compressible mixing layers is given in the next subsection. Relevant mixing layer simulations and their results are discussed.

1. 2. 3. Computational Investigations

Numerical solutions to the compressible mixing layer problem are often conducted as temporally evolving flowfields, due to the computational load required for the spatially developing case.³³ The former frequently make use of periodic boundary conditions in the homogeneous directions (streamwise and spanwise). Thus, due to the difference in nature of the shear layer development between computational and experimental studies (*i.e.*, temporally vs. spatially developing), it is important that investigators compare fully-developed, or statistically-stationary turbulence quantities. Many computational studies specifically stress temporally fully-developed conditions, since, as mentioned throughout this writing, the developing region of shear layers may be inconsistent for different studies depending on the inflow conditions.

In contrast to the sparsity of recent experimental work on turbulent compressible free shear layers, there have been several computational efforts as of late to model this canonical flowfield. Widely used in industry design, Reynolds-averaged Navier Stokes (RANS) models have difficulty simulating the large range of turbulence scales and compressibility effects in high-speed mixing

layers. Early work on Reynolds-averaged studies (*e.g.*, Zeman (1990),³⁴ Zeman (1991)³⁵) led to the belief that compressibility effects are manifested through the importance of dilatational dissipation at high convective Mach numbers, due to the formation of eddy shocklets. Continued efforts on dilatational dissipation models (*e.g.*, Sarkar *et al.* (1991)³⁶) were able to successfully exhibit the reduction in growth rate with increasing compressibility that is observed in experiments.

However, since then, various direct numerical simulation (DNS) studies have shown that it is instead the reduced pressure-strain rate correlation that is associated with compressibility effects. Vreman *et al.* (1996) showed that the dilatational dissipation is an insignificant contribution to the total dissipation.³⁷ Using an integrated statistical analysis, they conclude that decreased pressure fluctuations, which lead to a reduction in the pressure-strain term, is the cause for reduced growth rate. In addition, Sandham and Reynolds (1991) found, through their three-dimensional DNS study, that eddy shocklets are not present even in a high $M_c = 1.05$ case. The highly three-dimensional topology of the mixing layer removed the need for shock waves to be present around the turbulent eddies.³⁸

In their DNS studies, Freund *et al.* (2000) and Pantano and Sarkar (2002) also showed the reduced pressure-strain correlation with increasing compressibility; however, they both included Reynolds stress results.^{33, 39} Pantano and Sarkar report that all components of the Reynolds stress decrease with increasing M_c similar to the experimental results of Elliott and Samimy, while Freund *et al.* found all components to decrease with increasing M_c , except for the streamwise normal stress, as in the experiments of Goebel and Dutton. In addition, they both address the Reynolds stress anisotropy tensor in its full three-dimensional form (defined in Section 4.2). Freund *et al.* only report the shear stress anisotropy component and show that it decreases monotonically with increasing M_c (ranging from 0.21 to 1.80) in the middle of the shear layer.³³ Pantano and Sarkar also demonstrate this decrease in shear stress anisotropy with increasing M_c , although the reduction was far less than in Freund *et al.* Pantano and Sarkar also include streamwise normal stress anisotropy, which was found to be constant, and transverse normal stress anisotropy, which was found to decrease slightly with increasing M_c .³⁹ Overall, Pantano and Sarkar observed very little change, however, to the anisotropy tensor with convective Mach number. This may be due to the fact that their calculation of the anisotropy components involved integrating values along the shear layer, while Freund *et al.* present peak values in the shear layer.

One particularly interesting study that Freund *et al.* performed in their work is the determination of a transverse length scale in the mixing layer. Since they found that the transverse normal and shear Reynolds stresses do not scale with the velocity difference over the entire mixing layer thickness (in accordance with other experiments and computations), they argue that a different scale for the turbulence must be used in that direction. Thus, a typical eddy length scale, l was calculated via a two-point spatial correlation of the transverse velocity fluctuations. After rescaling the transverse normal and shear stresses with $(\Delta U l/b)^2$ (instead of $(\Delta U)^2$), they were found to be fairly constant with M_c .³³

Recent large-eddy simulation (LES) works have also been able to capture the physics of compressible shear layers. Foysi and Sarkar (2010) show the reduction of normalized growth rate and pressure-strain correlation with increasing compressibility.⁴⁰ They attribute the reduced pressure-strain term to the decreasing transverse velocity length scales (determined by a two-point correlation in a similar manner as Freund *et al.* discussed above) with increasing M_c . Fully-developed Reynolds stress profiles were also presented; and interestingly, they show that all three normal stresses decrease with increasing M_c . This result of the reduction of peak streamwise normal stress is in agreement with Pantano and Sarkar (DNS), and Elliott and Samimy (experiments). Streamwise normal and primary shear stress anisotropies were constant while the transverse normal anisotropy decreased with increasing compressibility.

Mankbadi *et al.* (2015) review high-order and low-order LES methods and compare their results for compressible mixing layer simulations based on Goebel and Dutton's experiments.⁴ The high-order method uses an eleven point, fourth-order accurate scheme in space, a fifth-order accurate, four-stage Runge-Kutta time-stepping method, and a subgrid-scale model by Vreman (2004).⁴¹ The low-order method, which does not utilize any subgrid modeling, uses a second-order accurate spatial scheme and a locally first-order accurate implicit Euler time-stepping scheme. They found that for a fine grid resolution, both techniques produced Reynolds stress results in agreement with the experiments (*i.e.*, constant streamwise normal Reynolds stress and decreasing other components with increasing M_c). The subgrid scale modeling was found to be negligible for the high-order method with the fine resolution. As the mesh coarsened, the high-order method showed grid independence, while the low-order method produced different results from the fine mesh. Interestingly, the subgrid modeling in the high-order method was found to be negligible for the coarse resolution as well and may possibly require even coarser meshes to have an effect.

As computational throughput continues to improve, LES investigations will be able to solve larger and higher-resolution spatial domains of high-speed flows. Thus, it becomes increasingly apparent that much of the point-by-point compressible mixing layer experimental data that is currently available, may no longer be sufficient as a CFD validation tool. The experimental work presented here aims to provide large ensembles (> 3000) of high-resolution, three-component velocity fields of compressible mixing layers that are sure to be useful to the fluid dynamics community.

1.3. Present Investigation

The first goal of this dissertation was to provide a full set of mixing layer experimental data that is suitable for CFD validation and covers a wide range of compressibility. Specifically for this purpose, five different convective Mach numbers were examined, ranging from 0.2 to 0.9, and the dataset for each mixing layer case includes incoming boundary layer measurements, the test-section static pressure distribution, three-component velocity measurements on both side-view (x - y) and end-view (y - z) planes, confirmation of flow self-similarity, flow visualizations using high-speed frame rates, and a full bottom-up uncertainty analysis for each measurement based on the diagnostic technique used. The chief three-component velocity measurements were made using the stereoscopic PIV (SPIV) diagnostic technique. This allowed for the study of spanwise turbulence statistics for various compressible mixing layers, a noted area that is severely lacking in experimental data.

In order to disseminate the findings, a project website was created that has the full dataset for each case available for download at: <https://wiki.illinois.edu/wiki/display/NCSLF/>. Results from all flow diagnostics were uploaded and are available there, including operating conditions, instantaneous velocity fields, and calculated mean/statistical quantities. Additionally, all wind tunnel facility dimensions are available in the form of engineering drawings and computer-aided design (CAD) files. A detailed outline of all data available on the website is given in Appendix A.

Once these data were collected, the thrust of the investigation shifted to turbulent flow analyses using the measurements obtained. The underlying motivation of each analysis is to best characterize the effects of compressibility on the turbulence in free shear layers. Quantities such as Reynolds stress anisotropy, velocity-fluctuation triple products, turbulence production, turbulence length scales (analogous to the Freund *et al.* analysis), turbulence Mach number, and

gradient Mach number are studied in a point-by-point manner, and compressibility trends are identified. Additionally, two-dimensional techniques that take advantage of the high spatial resolution velocity fields are applied, including proper orthogonal decomposition (POD), linear stochastic estimation (LSE), and an entrainment study based on instantaneous turbulent/non-turbulent interfaces (TNTIs). Overall, quantitative information about compressibility effects on the large-scale turbulent structures, dynamic turbulent motions, and entrainment mechanisms is obtained for these two-dimensional techniques. All analysis methods were applied for the fields of view that contain the fully-developed region of the mixing layer.

The overarching objective of the current investigation was to present the obtained experimental data and analyze them to construct a coherent argument regarding the effects of compressibility on mixing layer turbulence. Many of the analyses presented in this work have been performed in the literature on incompressible flows; however, due to the lack of previously available mixing layer data with high resolution and at high levels of compressibility, the results here are novel in the field experimental fluid dynamics. Moreover, the large ensembles of instantaneous 3-component velocity measurements are themselves a major contribution to the literature, especially considering that they were obtained for a wide range of compressibility. In addition to the analyses conducted herein with this data, other researchers will be able to download the same data and apply their own analyses to further the scientific community's understanding of compressible turbulence in mixing layers.

2. EXPERIMENTAL METHODOLOGY

This section describes the experimental approach for the initial data acquisition phase of this dissertation. Included here is a description of the wind tunnel facility as well as details of the various flow diagnostic techniques that were performed. All wind tunnel CAD files are available on the project website as Autodesk Inventor part/assembly files, .iges files, and engineering drawing pdfs.

2. 1. Wind Tunnel Facility

In order to study the effects of compressibility on mixing layers, five different convective Mach number cases were investigated in the same wind tunnel facility. It should be noted that this facility was specifically designed for these experiments by Gyu Sub Lee for his M.S. work at the University of Illinois at Urbana-Champaign. Thus, details on the design, fabrication, and assembly of the wind tunnel facility (beyond what is covered in this section) can be found in his M.S. thesis, including critical design aspects (*e.g.*, structural finite element analysis, safety factors, nozzle interchangeability, etc.) and justifications.⁴² An overall description of the facility is discussed here, with specificity given to aspects of the wind tunnel that pertain to its operation and the flow diagnostics performed.

Two individually supplied air streams are separated by a splitter plate that runs along the extent of the stagnation chambers and nozzles in the streamwise direction. The primary reservoir is an air tank farm kept at 1.03 MPa, and the secondary reservoir is the ambient room air. When the tunnel is under operation, ambient room air is entrained into the secondary settling chamber through a manual gate valve that can be throttled (since $P_{ts} < P_{atm}$). The entire wind tunnel assembly hangs from a structural I-beam support in the laboratory. The tunnel was operated in the Gas Dynamics Laboratory (Room 132 of the Aerodynamics Research Laboratory) for the extent of this investigation.

The entire facility including the piping assembly is shown in Figure 7. The top manual valve, highlighted in green, is opened to set a certain stagnation pressure in the primary plenum. Below that, the manual valve shown in red is opened just enough to supply dry air for the secondary stream to avoid condensation, when needed. Condensation is formed in the mixing layer when the air that is entrained from the room into the secondary stream has high enough humidity and the

mixing layer velocity is high enough (details on condensation are discussed in Section 3.4.2). While this phenomenon is desired for obtaining Mie scattering images, the condensation washes out particles in the mixing layer in SPIV images. Thus, the red valve is opened slightly to supply the secondary stream with dry air from the tank farm. Finally, the manual valve highlighted in yellow is throttled to control the secondary stagnation pressure, which is lower than atmospheric. In addition, a small gap exists between the yellow manual valve and the pipe cross upstream of it, keeping the pressure close to atmospheric there. Therefore, some room air in the laboratory could be entrained into the secondary flow (important for seeding), combined with the dry air supplied from the tank farm. The exact operating conditions for each case (see Section 3.1) were determined by matching the pressure at the two nozzle exits where the mixing begins.

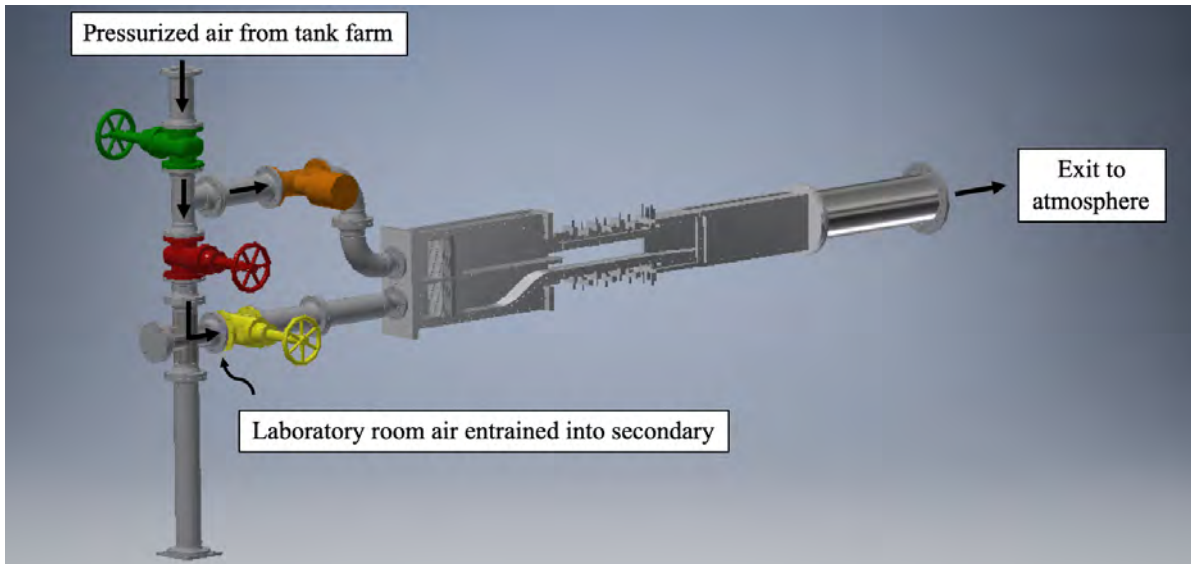


Figure 7. CAD mockup of wind tunnel facility (including upstream/downstream piping).

The operation of the wind tunnel was controlled via a LabVIEW program. To start the tunnel, the pneumatic control valve (orange valve in Figure 7) is opened 100% by sending it 20 mA of current through a National Instruments 9265 current output module. The primary manual valve (Figure 7, green) can then be opened by hand to set the appropriate stagnation pressures. Since the fine-tuning of the primary stagnation pressure is handled manually, the pneumatic valve acts as a safety measure (*i.e.*, quick shut-off) rather than as a controller. The LabVIEW front panel is shown in Figure 8 and was monitored during runs to ensure constant operating conditions. The specific conditions of each case were determined using schlieren photography in conjunction with the

nozzle-exit static pressure readings (see Section 3.4.1). Additional measurements made in LabVIEW (which can be seen in Figure 8) are discussed in Section 2.2.1.

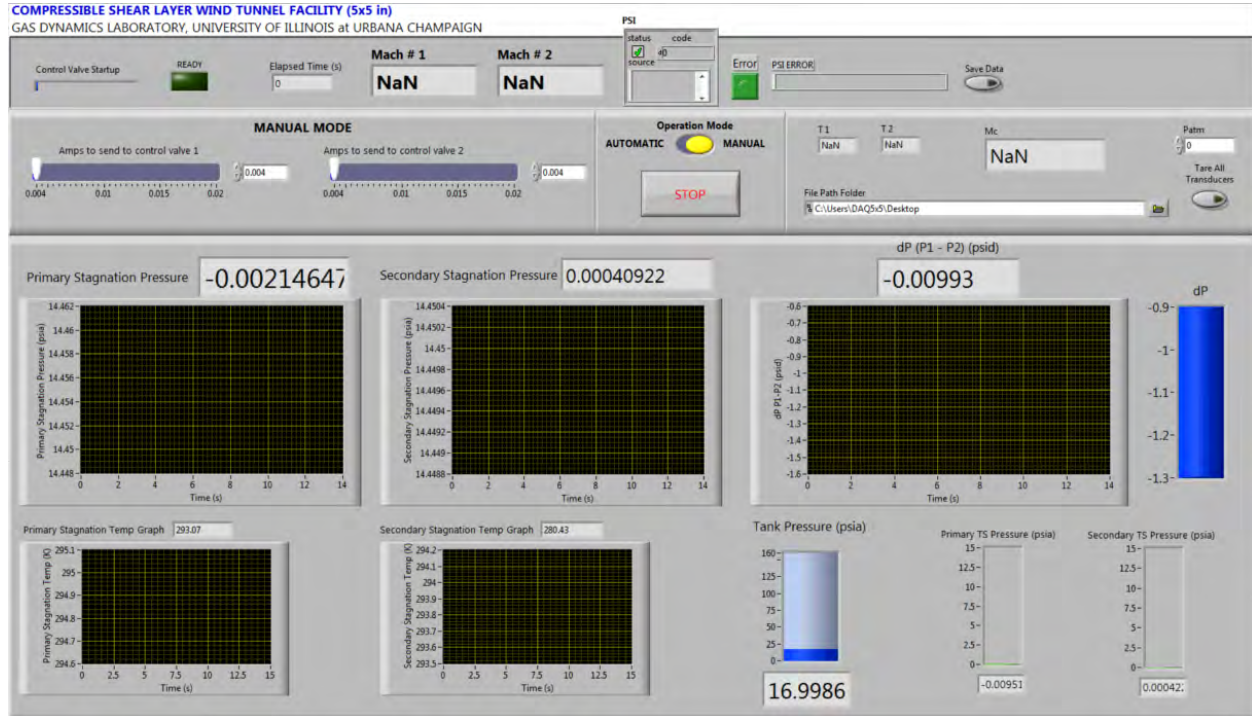


Figure 8. LabVIEW front panel for wind tunnel operation.

A more detailed cross-sectional view of the wind tunnel is shown in Figure 9. The two streams are separated by a splitter plate, until the test section region, where the two streams begin to mix and shear layers measurements are acquired. In each plenum there are a series of flow conditioners to reduce the turbulence and increase the uniformity of the flow upstream of the nozzle. The three flow conditioners in each stream, separated by the splitter plate, are shown in Figure 10. The initial perforated plate serves to make the incoming flow more uniform by spreading it across the entire area of the plate. Following each plate is honeycomb, which straightens out the flow and reduces perturbations in the transverse and spanwise directions. Lastly, a wire mesh screen is placed downstream of the honeycomb to reduce the turbulent length scales such that the small eddies dissipate quickly in the settling chamber upstream of the nozzles. Stagnation pressure and temperature measurements were made downstream of the wire mesh screens and upstream of the nozzle converging sections. In addition, much attention was given to sealing the tunnel via O-rings and sealants to mitigate leak paths as best as possible. O-rings that run along the length of the tunnel in the streamwise direction can be seen in Figure 10 above and below the flow domain. In

addition, room-temperature vulcanizing (RTV) sealant was applied between the sidewalls and splitter plate (along the streamwise direction) to seal between the top and bottom plenums/nozzle flows.

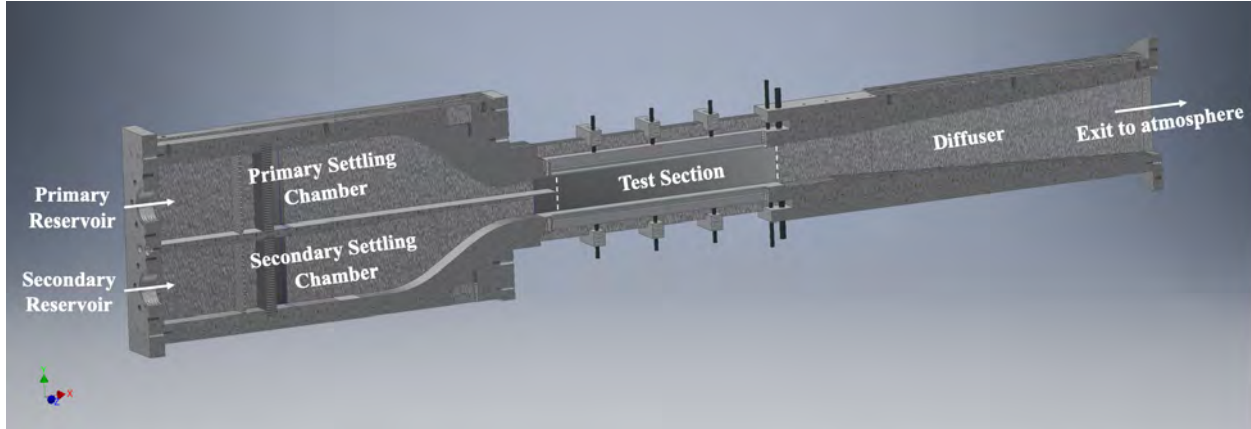


Figure 9. CAD mockup of wind tunnel facility cross-section.

In order to vary the primary freestream Mach numbers, different primary nozzles were interchanged for the five mixing layer cases. For the secondary stream, a single convergent nozzle was kept in place throughout, while four different nozzles were used for the primary stream. The primary Mach numbers vary from subsonic to supersonic, with nominal values of 0.5, 1.0, 1.5, 2.0, and 2.5. The convergent section of all primary convergent-divergent (CD) nozzles were modeled using seventh-order polynomials, while the two purely converging nozzles used a fifth-order polynomial spline. The divergent sections of the CD nozzles were designed using an in-house method of characteristics code ('NOZCS2').⁴³ All nozzle configurations were designed so that there was a 50.8 mm long constant-area section before the splitter tip in each stream. The five different nozzle configurations are shown in Figure 11 (nozzles shown as bronze to highlight differences between configurations).

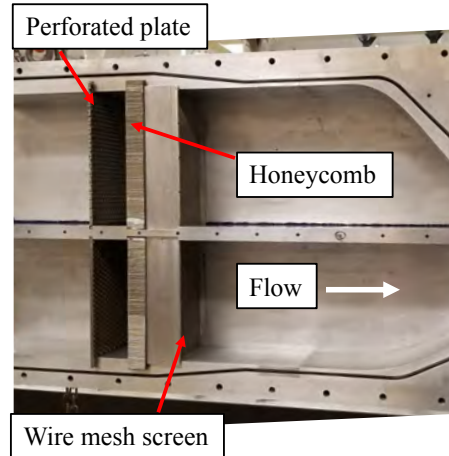


Figure 10. Flow conditioners in stagnation chamber.

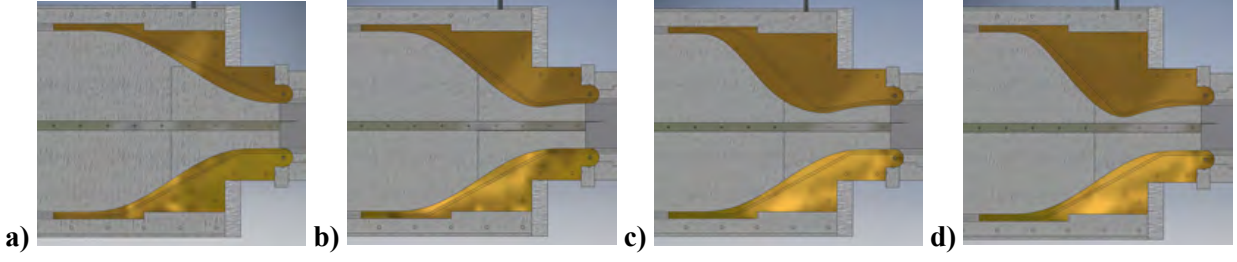


Figure 11. Nozzle configurations for all five mixing layer cases (flow left to right) with nominal Mach numbers a) $M_1 = 0.5/1.0$, $M_2 = 0.1/0.2$; b) $M_1 = 1.5$, $M_2 = 0.3$; c) $M_1 = 2.0$, $M_2 = 0.3$; and d) $M_1 = 2.5$, $M_2 = 0.2$.

During the wind tunnel design stage, an important consideration was ensuring that the nozzles could be interchanged (relatively) easily. The process begins by removing the muffler, the most downstream duct shown in Figure 7. The wind tunnel can then be detached from the upstream piping so that the upstream and downstream ends are free (as in Figure 9) as the tunnel hangs from the I-beam. Either one of the combination stagnation-test-section side walls can then be unbolted and separated from the assembly by jacking it apart (in the spanwise direction) from the inside of the tunnel, which is accessible via the upstream stagnation chamber end. At this point, the primary nozzle can be unbolted from the top wall and other side wall, and removed. Re-assembling the tunnel with a different nozzle follows the same directions in reverse, with the added step of applying RTV sealant along the splitter plate. As noted, this is necessary since there is no O-ring between the primary and secondary streams across the splitter plate.

The test-section begins immediately downstream of the splitter plate tip and is 127 x 127 x 762 mm in size, with full sidewall optical access along the entire length via fused silica windows. The sidewall windows are arranged so that the entire test-section length can be observed with three window positions, with 12.7 mm of overlap between each position. In addition, these windows start 19.05 mm upstream of the splitter tip for optical access to the boundary layers on either side of the splitter plate. In both the test-section top and bottom walls, one long window piece that is 38.1 mm wide allows for laser sheet access along the entire length of the test-section. These windows also start 19.05 mm upstream of splitter tip. The optical access described is necessary for the SPIV diagnostic, which is discussed in Section 2. 2. 4. With prior knowledge that the mixing layers tend to grow faster into the secondary (bottom) stream, the primary and secondary stream nozzle exit heights were designed to be 50.8 mm and 76.2 mm, respectively.

The flow exits from the test-section into the diffuser, where it decelerates, then exhausts through a muffler to the atmosphere. The top and bottom walls of the diffuser each have a constant

divergence angle of 3 degrees and feature a backward facing step at the test-section joint. While there are no measurements made in the diffuser itself, static pressure measurements are made on the side-wall at the diffuser entrance (*i.e.*, test-section exit), giving one set of boundary conditions (BCs). In addition, the muffler is not sealed to the diffuser exit and is fairly porous, thus the pressure there is likely close to atmospheric. These two sets of BCs and the exact known geometry of the diffuser should help with modeling the outflow conditions.

All tunnel walls and nozzles were machined from aerospace-grade aluminum 7075, with the exception of the splitter tip, which was machined from titanium. The decision to reinforce the splitter tip with titanium was made following the observation of large deflections in the cantilevered portion of the aluminium-machined tip. This was especially apparent when the primary stream was supersonic, which required a normal shock to pass through the test-section during tunnel start-up, thereby causing a large pressure difference across the splitter plate (top to bottom). In order to alleviate this issue, the primary stagnation pressure was increased to operating conditions as quickly as possible. Following structural analyses based on the expected stagnation and static pressures, it was determined that the optimal geometry of the splitter plate resulted in a tip thickness of 0.05 mm and a convergence angle of 2.38 degrees on the secondary side (primary side is flat everywhere). These dimensions, combined with the respective material properties, allowed for the thinnest possible splitter plate geometry that was able to withstand the maximum load conditions.

2. 2. Flow Diagnostics

A number of flow diagnostics were performed for each mixing layer case, with an emphasis placed on velocity measurements. Basic wind tunnel facility data used to operate the tunnel include stagnation temperature, stagnation pressure, and nozzle-exit static pressure measurements in each stream. In addition, the static pressure distribution on the test-section sidewall was measured via pressure taps. Planar PIV was used to measure the incoming boundary layers and their integral parameters. As for the mixing layer itself, flow visualization and SPIV were performed on two different planes: x - y (side-view) and y - z (end-view). Each diagnostic technique is discussed in detail next.

2.2.1. Pressure/Temperature Measurements

The most fundamental flow diagnostics for these experiments were pressure and temperature measurements in the facility. There are pitot probes and thermocouples in the center of each stagnation chamber to record total pressure and total temperature, respectively. Static pressures at the nozzle exits were also measured via pressure taps on the sidewall. Temperature and pressure measurements were recorded at 10 Hz using the LabVIEW program. Details on the operating conditions and how they were determined (including their uncertainties) are discussed in Section 3.1.

For each data collection run, the total pressures (P_{01} , P_{02}), total temperatures (T_{01} , T_{02}), and nozzle-exit static pressures of each stream (P_1 , P_2) were documented and used to determine the operating conditions of each mixing layer case. The stagnation chamber probes are shown, as installed in the wind tunnel, in Figure 12 (in blue). They are all placed halfway between the final flow conditioners (mesh screens) and the upstream end of the converging section of each nozzle. Due to the required optical access upstream of the splitter tip, the nozzle-exit static pressure taps are located at $x = -82.55$ mm, in the constant-area section downstream of the nozzle-exit and upstream of the splitter tip. These static pressure measurements were used to monitor the pressure difference across the splitter tip and operate the wind tunnel. The pitot probes and nozzle-exit static pressure taps were plumbed to a PSI Systems 9116 NetScanner pressure transducer module while the thermocouples (model no.: Omega TJ36-ICSS18E-6-SMPW-M) were read by Omega DP26-TC-A temperature meters.

A static pressure tap side-wall insert was also fabricated to measure the test-section side-wall pressure distribution. The insert piece features three streamwise-oriented rows of pressure taps at $y = 0$ and in the transverse center of each freestream ($y = 25.4$ mm and -38.1 mm). Along $y = 0$, the spacing between the taps is 25.4 mm, while in the primary and secondary streams the taps are 50.8 mm apart. All three rows of taps span the length of the test-section, from $x = 3.175$ mm to

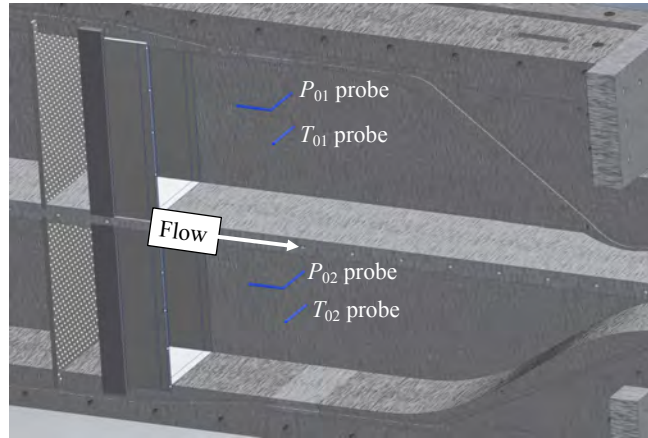


Figure 12. Location of stagnation chamber total pressure and total temperature probes.

739.775 mm. A CAD mockup and picture of the insert piece installed in the facility can be seen in Figure 13 below. These measurements were used to confirm that the test-section pressure was near constant throughout for each case. All taps from the sidewall are plumbed to a rack of PSI 9816 NetScanner modules.

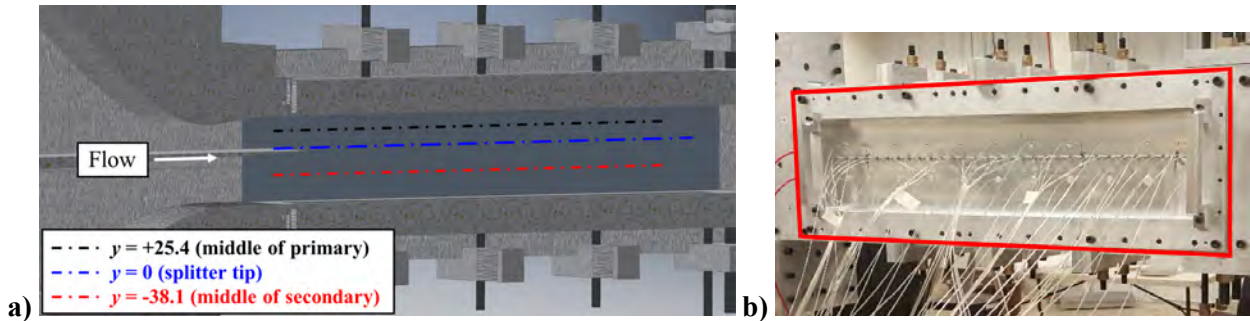


Figure 13. Sidewall static pressure tap insert a) CAD mockup showing y-locations and b) installed in wind tunnel.

2. 2. 2. Incoming Boundary Layer PIV

As part of obtaining CFD validation-quality data, incoming boundary layers (BLs) were measured via planar PIV on four walls: test-section top and bottom walls, and splitter plate top and bottom walls. These four walls are depicted in Figure 14. In order to determine integral parameters (*e.g.*, boundary layer thickness, displacement thickness, etc.) of the incoming boundary layers, two-component velocity measurements were made on the x - y plane at $z = 0$ near the splitter tip. As mentioned in the wind tunnel facility description, the splitter plate and adjacent sidewall were designed specifically to have optical access to the splitter tip (*i.e.*, trailing edge), as shown in Figure 14.

Near-wall PIV measurements are known to be particularly difficult, as laser reflections from the wall tend to limit how close the nearest velocity vector can be to the wall. For the present investigation, the closest vector to the wall ended up being $\sim 0.5 - 1.0$ mm away for all boundary layers. The sensitive laser reflections also affected the exact x -locations at which the final boundary layer profiles were obtained to determine the integral parameters. This issue was mitigated, however, by the fact that the boundary layers are shown to be fully developed (see Section 3. 3). All profiles were measured within $-20 < x < 6$ mm, with a few test-section top/bottom wall BLs being obtained slightly past $x = 0$.

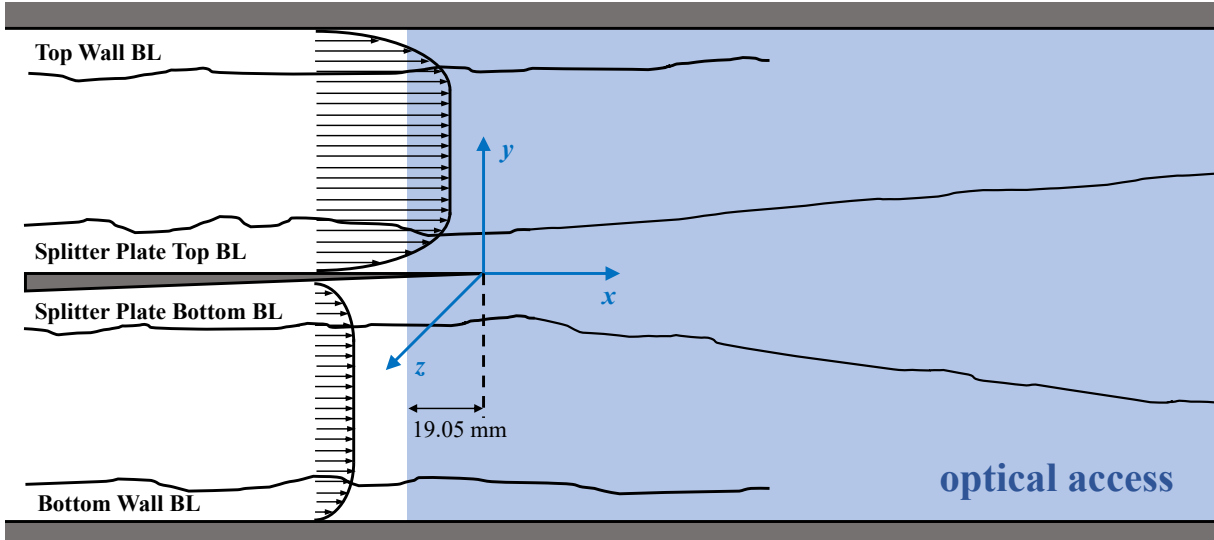


Figure 14. Four walls on which incoming boundary layers are measured (via PIV) with shaded blue region indicating optical window access to test-section.

The setup for these planar PIV measurements was a single PCO.2000 charge-coupled display (CCD) camera with a laser sheet parallel to its lens and image plane (*i.e.*, camera lens axis perpendicular to laser sheet). All components used here were the same as for the SPIV setup (with only one camera being used for this two-component PIV vs. two for the stereo set-up) and are discussed in detail in Section 2. 2. 4 (Table 3). The two-component PIV for these boundary layer measurements also used a smaller two-level calibration plate from LaVision (model: 058-5) instead of the Type 11 that was used for SPIV. Since out-of-plane measurements were not being made, the laser sheet thickness was reduced to < 1 mm to reduce the reflections. Processing parameters used were also identical to those in Section 2. 2. 4 (Table 2), with the exception of the vector calculation parameter being set to planar PIV.

2. 2. 3. Flow Visualization

In order to determine the operating conditions for a particular M_c case, the first flow diagnostic technique performed chronologically was schlieren photography. A Z-type setup was used for its simplicity. The schematic for this technique is given in Figure 15, with the light path highlighted in tan. Schlieren is based on the bending of light rays in a non-uniform refractive index medium and allows for the visualization of density gradients that are present in a flowfield. A point light source (LED used here) is placed a focal distance away from the first (left) parabolic mirror, which collimates the light rays reflected from that mirror. Those light rays then travel through the test-

section, are reflected off the second parabolic mirror (right), and then captured by the CCD camera. If density changes are present in the test-section (in the flowfield), then the rays become bent due to the change in refractive index of the medium. These bent rays then reflect off the second parabolic mirror at a different location and either are blocked-off or passed-through at the knife-edge, which is placed near the focal point of the second mirror (where all the rays pass through before the camera sensor). The red lines in Figure 15 represent light rays that travel through the system. If no density changes are present, the ray remains on the dotted red line, while the solid red line represents a bent ray that is cut-off at the knife-edge.

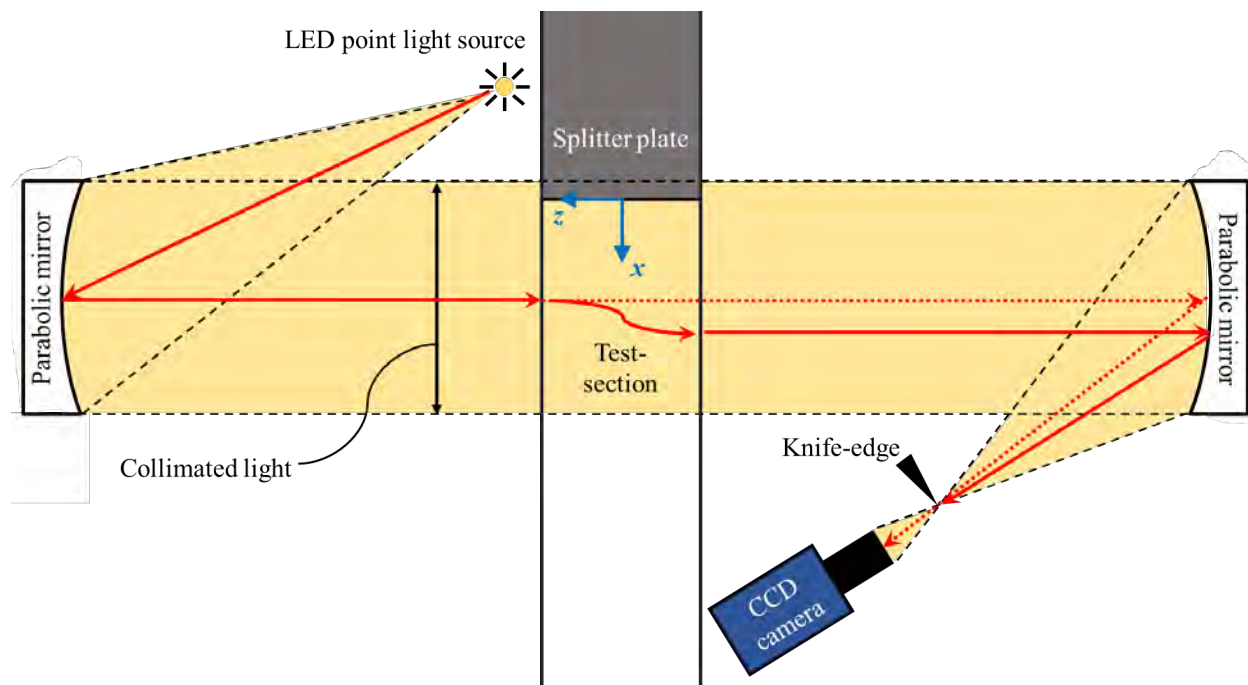


Figure 15. Schlieren Z-type setup schematic.

Two methods of schlieren were employed for each case, with the first being instantaneous snapshots of the entire test-section height, and the second being high frame rate movies that track the turbulent structures from image to image. The first full-test-section field of view (FOV) captures the entire window area per image at a lower frame rate (note that 19.05 mm of splitter plate is captured in the FOV, as shown in Figure 15). The high-speed movies have reduced FOVs that are zoomed-in on the shear layers and are especially useful for examining the entrainment of freestream fluid into the mixing layer via turbulent structure interactions. Furthermore, since the pressure taps for the test-section are not located exactly at the splitter tip, schlieren helps to determine the pressure-matched condition between the streams by visualizing the sensitive

compression/expansion waves at the tip. All components used in the schlieren setup are listed in Table 1 below.

Table 1. Components of schlieren system.

<u>Component</u>	<u>Description</u>	<u>Parameters Used</u>
Photron SA-5 camera	High-speed CCD camera, 1024 x 1024 pixels	1 μ s exposure time, Full T-S FOV @ 7,000 FPS, High-Speed @ [60,000 – 124,000] FPS
Nikon Nikkor zoom camera lens	70-210 mm focal length	Zoom: optimized for sensor size (~200 mm), Aperture: f/4
ThorLabs Mounted LED (MWWHLP1)	LED light source, Warm white color	Full brightness (700 mA current applied)
Parabolic mirror (x2)	30.48 cm diameter, 243.84 cm focal length	First mirror placed one focal length away from LED to collimate reflecting light
Knife-edge	Razor blade edge used to block bent light rays	Placed near second mirror focal point, Horizontal orientation

Schlieren, however, is a line-of-sight integrating technique that averages the density gradients in the spanwise direction; therefore, it is difficult to use to study the organization of large-scale turbulent structures that are three-dimensional in nature. Mie scattering images, on the other hand, are spatially resolved in the spanwise direction, as the particles are illuminated via a thin laser sheet (~1 mm). The Mie scattering technique used here indicates molecular mixing between the two streams, because it is based on the condensation of water vapor carried in the humid, low-speed stream when mixing with the cold, high-speed stream. The results of the technique are known as product formation images and were obtained for the more compressible mixing layer cases where the velocity was high enough to form condensation (*i.e.*, static temperature in flow was cold enough). No specific seed was used other than the humidity from the ambient laboratory air, and the experimental setup for Mie scattering was identical to that of the SPIV setup discussed in the next section (2. 2. 4). The only difference between the two diagnostics is shutting off the manual valve (red valve in Figure 7) that supplies dry air for the secondary stream when performing SPIV.

2.2.4. Mixing Layer Stereoscopic Particle Image Velocimetry

The chief flow diagnostic technique performed in these experiments was SPIV, which obtains three-component velocity data on a two-dimensional plane. SPIV requires (at least) two cameras to view a laser sheet at offset angles. Since the two (or more) cameras capture different perspectives of the same particles, the out-of-plane component of the particle displacement can be determined using the two projections. The two different cameras and their perceived particle displacements (d_1 and d_2) are shown in Figure 16. A multi-level calibration marker plate (with marker geometry/organization completely known) is used to create a three-dimensional mapping of the real-world space for each camera. Physical velocity vectors can then be calculated for all three components. The laser sheet must be thick enough such that the particles remain in the illuminated region, as indicated by Figure 16. The angle θ shown for each camera is the offset angle and its optimal setting is between 30-35 degrees.⁴⁴ An added benefit of this offset viewing is the removal of in-plane velocity (u, v) errors due to out-of-plane displacement of the particles in the laser sheet. In single-camera planar PIV viewing, the projection of the particle displacement on the image sensor has no way to account for the out-of-plane displacement. In addition, a stereo ‘self-calibration’ is performed in the processing software that is able to reduce errors from misalignment between the laser sheet and calibration plate. Further details on this process can be found in the LaVision FlowMaster 8.4 Manual.⁴⁴ A detailed review of the SPIV optical diagnostic technique can be found in Prasad (2000), including different stereoscopic camera arrangements (*e.g.*, translational vs. rotational) that may be useful depending on the optical access available in a facility.⁴⁵

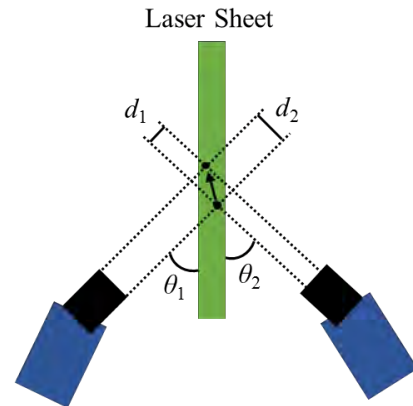


Figure 16. Stereoscopic camera viewing.

SPIV presents various optical challenges that are not faced in planar PIV. One key issue that arises is the loss of focus on the illumination plane when the viewing angle is offset. Without any correction for the difference in angle between the camera lens plane and laser sheet plane, only a vertical band within the image on the sensor will be in focus. This problem is common in the study of optics and can be corrected by tilting the angle of the camera image plane relative to the lens plane ahead of it, as shown in Figure 17. The entire image will be in focus when the illumination

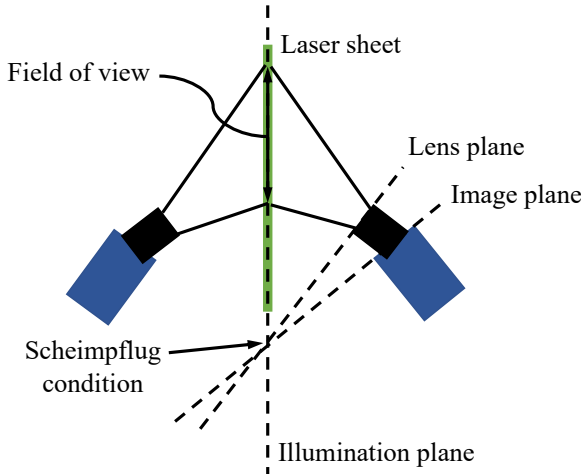


Figure 17. Scheimpflug condition for offset angle camera viewing.

plane, lens plane, and image plane all intersect at a point, known as the Scheimpflug condition.⁴⁴ There will still be, however, non-uniform magnification across the image, as the projections of the particles onto the tilted camera sensor will be uneven across it. Additionally, the lens aperture can be reduced (*i.e.*, higher f number) to increase the depth of field and improve the image focus quality; however, this comes at the cost of losing laser light intensity and reducing signal-to-noise ratio.

The SPIV system that was used in the current investigation is illustrated in Figure 18. Two particle generators produced seed (one for each stream) and were plumbed into the piping upstream of the stagnation chambers. A double-pulsed neodymium-doped yttrium aluminum garnet (Nd:YAG) laser (wavelength-halved to 532 nm) was used to illuminate the seed particles in the flow via a thin laser sheet, with the delay between pulses optimized for each M_c case and FOV (see Table 12). The illuminated sheet of particles was captured by two different CCD cameras viewing the same region in the test-section, at offset angles, as depicted in Figure 17. The cameras and laser were synced via a delay generator. Raw particle and calibration plate images were then downlinked from the camera memory to the data acquisition/tunnel operation computer and transferred to a SPIV processing computer equipped with 32 gigabytes of RAM. LaVision's DaVis 8.4 FlowMaster program was used to calculate instantaneous three-component velocity vector fields from the raw images.

The optical setup for the laser sheet consisted of multiple dichroic mirrors (with 532 nm coating), one diverging lens, and one converging lens. A double-pulsed collimated laser beam was generated by the Nd:YAG laser. In general, the laser beam was aligned using the dichroic mirrors' angles. A plano-concave diverging cylindrical lens and plano-convex converging spherical lens were placed in the beam path to create a laser sheet that was 1 – 2 mm thick and 85 – 90 mm wide. A few different cylindrical lenses were used that range in focal length from -50 to -75 mm. They were placed in the beam path at the location that produced the appropriate sheet width. The

spherical lens used has a focal length of 1000 mm and was placed to obtain the appropriate thickness that ensured the particles stayed in the illuminated region between laser pulses. Special attention was given to aligning the laser sheet relative to the wind tunnel test-section, confirming that it was parallel to the walls and placed at the correct location. Figure 19 shows the experimental setup of the laser sheet optics. The aperture was included to cut off any excess light straying from the collimated laser beam.

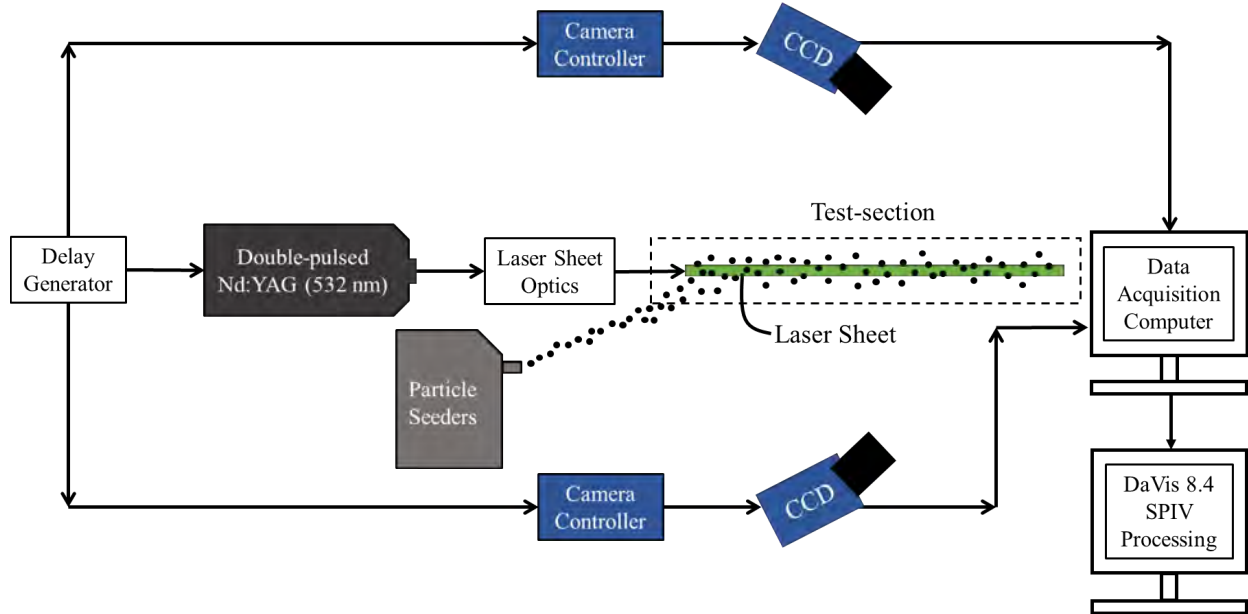


Figure 18. SPIV system schematic.

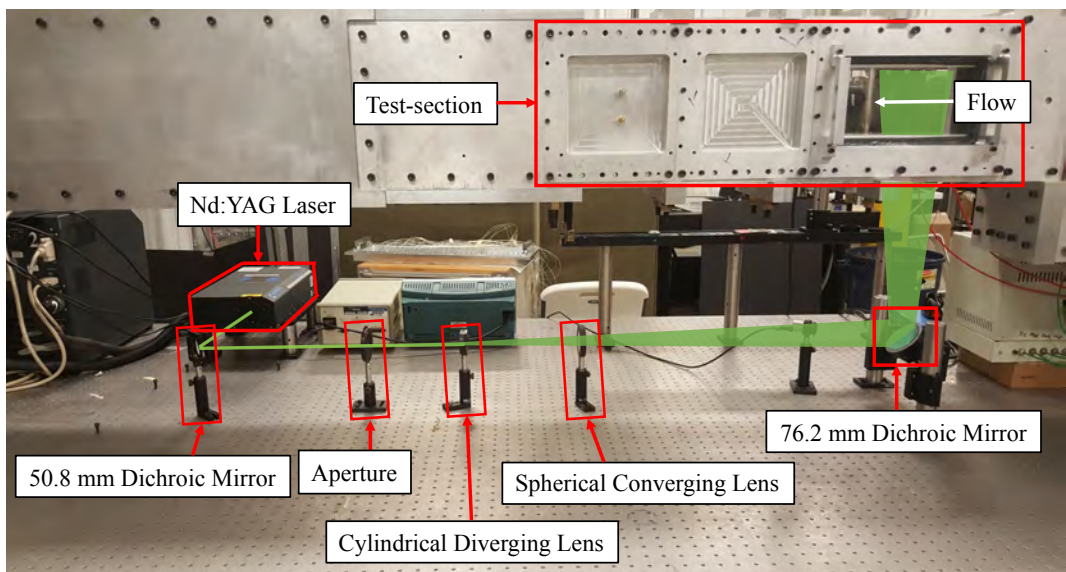


Figure 19. Laser sheet optics in experimental setup with green regions highlighting the laser path.

The laser power setting was controlled via the delay time between the flash lamp trigger and q-switch trigger. This delay time was set empirically for each FOV so as to be sufficiently high to illuminate the particles, but not high enough to create large reflections. In general, the laser power was \sim 65 – 85 mJ/pulse. All laser-related signal timing (between the flash lamp and q-switch, and between laser pulses) was controlled by the same delay generator (given in Table 3).

Two different types of seed particles were used in these experiments. The smaller of the two were \sim 0.2 μm in diameter and generated by Vicount 1300 Smoke Generators. These small particles have excellent response, even in supersonic flows, and were used for the determination of all turbulence statistics. A measure of a particle's ability to track with the flow is the Stokes number: the ratio of particle response time to flow time scale. For the two-stream mixing layer it can be defined as $St = (\rho_p d_p^2 \Delta U)/(18\mu_f b)$, where ρ_p and d_p are the particle density and diameter, respectively, and μ_f is the fluid viscosity. The maximum estimated Stokes number with the smoke particles for the mixing layer cases studied here is 0.02, which is below the desired value of 0.05 as discussed by Samimy and Lele (1991).⁴⁶ However, the use of these smoke machines incurred additional experimental difficulties; mainly, the smoke machine plumbed to the pressurized primary stream injected smoke fluid into the upstream piping of the facility. This excess oil substance streamed down the tunnel sidewalls/windows when running, sometimes obstructing the camera's view of the particles. In fact, this issue was a major time-consuming factor, since prior to each SPIV data collection run, two-to-three tunnel 'purge' runs were required, in addition to cleaning the windows from the inside of the tunnel.

The larger Laskin nozzle (TSI Model 9307) particle generators produced seed with \sim 1 μm diameter. The bigger particle size was necessary to achieve a high enough signal-to-noise ratio for cross-sectional y - z plane velocity measurements, which required large offset viewing angles. The experimental difficulties that were experienced with the smoke machines (*i.e.*, smoke oil obscuring particle images) were less significant with these seeders. However, due to the larger d_p , the highest Stokes number when using these seed is 0.62. Thus, the Laskin nozzles were only used for the cross-sectional end-view planes.

As mentioned, two SPIV FOV planes were captured for each case: side-views (x - y) and end-views (y - z). Side-view velocity measurements on the spanwise-central plane ($z = 0$) were used for determining all the quantitative mixing layer characteristics, since this view employed the ViCount smoke generators that have excellent particle response. Due to the emphasis placed on

demonstrating fully-developed flow conditions, the side-view measurement FOVs were marched downstream until these conditions were realized (as outlined in Section 3. 5. 4). Figure 20 below shows the two-camera setup for the side-view span-central measurements.

SPIV measurements were also made on various end-view (y - z) planes, as shown in Figure 21. However, since these views required the use of the larger particles (as just discussed), the measurements made on these planes were mainly used for qualitative purposes to study the spanwise flow structure, and to confirm that the mixing layer was symmetric and planar. Some of the optical limitations for these end views included: requiring the maximum offset angle setting allowable by the Scheimpflug adapter (45 degrees), highly non-uniform magnification across the CCD, uneven light distribution across the CCD, and the need for the cameras to be in forward scatter (*i.e.*, direction of laser light wave propagation toward the CCD sensor). This last limitation required both cameras to be on the same side of the wind tunnel due to the path of the laser sheet and optical access that was available (see Figure 21). Therefore, this constraint, in addition to the three fixed window positions, meant that the end-view data could only be obtained at limited number of streamwise locations. In general, three x positions were chosen for each mixing layer case that were evenly spaced apart and contained a view in the fully-developed region.

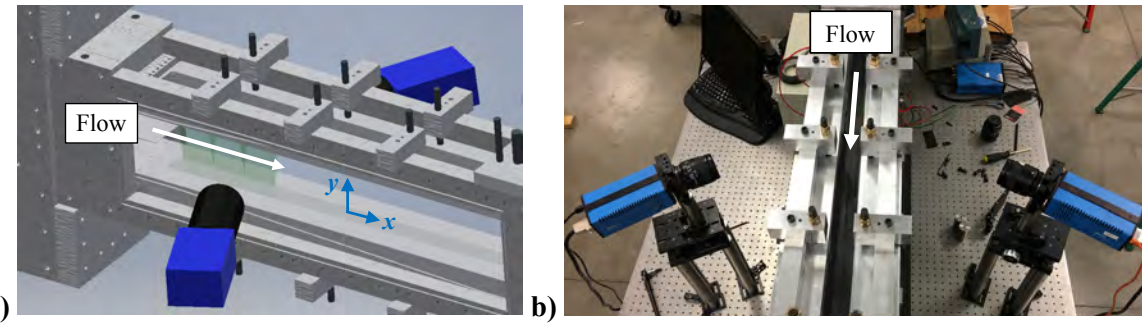


Figure 20. a) CAD mockup and b) in-laboratory picture of SPIV setup for side-view (x - y) planes.

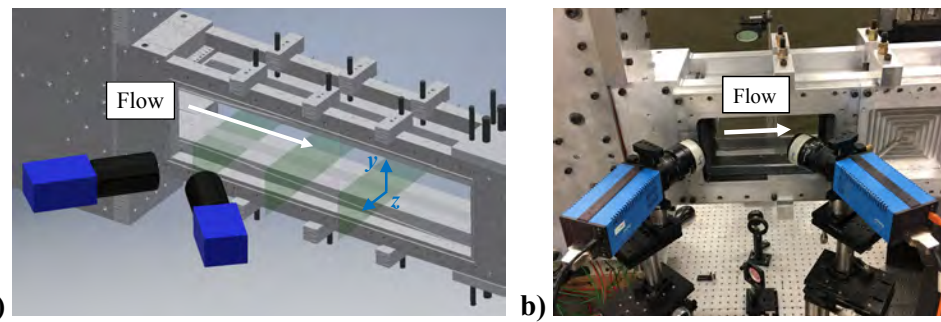


Figure 21. a) CAD mockup and b) in-laboratory picture of SPIV setup for end-view (y - z) planes.

Obtaining well-focused, high-quality raw particle images is imperative for any PIV technique; therefore, much time and effort was spent on optimizing the various aspects of the SPIV/PIV setups discussed thus far. In general, for each mixing layer case, the seeder settings (*i.e.*, pressure difference across them), laser power and sheet geometry, and camera focus had to be adjusted iteratively to produce the best images. In particular, the particle size on the sensor had to be > 2 pixels to avoid peak locking.⁴⁷ In addition, the seeding density was desired to be as uniform as possible between the two streams. This proved to be challenging, as the low-speed secondary stream was prone to over-seeding due to the difficulty of operating the smoke machines at low pressures. The target seed density was around 8 – 10 particles per SPIV interrogation window.⁴⁴ Example side-view raw particle images are shown in Figure 22 for both cameras at the same instant in time. The images presented here exhibit a clear large braid structure for the lowest convective Mach number case. The slanted orientation of the braid specifically makes it easy to see that the two cameras are mirror images of each other (a direct consequence of the setup shown in Figure 20).

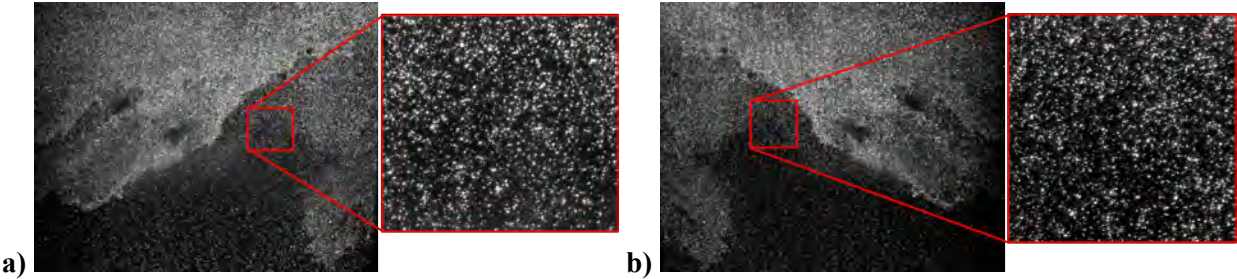


Figure 22. Instantaneous raw SPIV side-view particle image for a) camera 1 and b) camera 2.

The calculation of SPIV vectors included image pre-processing steps that were able to help improve the particle correlations, as well as vector postprocessing filters. These are all listed in Table 2 along with the vector calculation parameters used for the stereo cross-correlations. The overall process requires the two cameras to each record two sequential instantaneous frames obtained at a known Δt time apart. Images of a LaVision Type 11 two-level calibration plate (aligned with the laser sheet) are then used for each camera to determine real-world mappings. A picture of the calibration plate is shown in Figure 23. The known geometry of the calibration markers, including their layout, is used to initially correct the images to real space using a pinhole calibration model, since the windows do not have any curvature to them.⁴⁴ The third-order polynomial calibration model induced non-physical optical effects for some end-view planes, and

thus was not used. Following the initial calibration, a stereo ‘self-calibration’ method, offered in DaVis 8.4 FlowMaster, is used to iteratively improve the calibration based on matching particles between the two cameras for each image.⁴⁴ This allows slight misalignments between the calibration plate and laser sheet to be corrected.

For each mixing layer case, the interrogation window size was reduced to the smallest possible setting that still produced high-quality velocity vectors. Since there was sufficient time to let the computations run, the ‘adaptive PIV weighting’ and ‘high-accuracy mode for final passes’ settings were used to increase the robustness of the calculations, as recommended by the LaVision manual.⁴⁴ The high-accuracy mode uses a B-spline 6 reconstruction (Bicubic interpolation) instead of a bilinear interpolation for the image calibration. All of the processing parameters and algorithms given in Table 2 are standard for PIV applications in fluid dynamics and are similar to settings used in previous PIV experiments of high-speed, compressible flows.⁴⁸ In addition, the processing uncertainties of all three velocity components are calculated in LaVision’s DaVis 8.4 FlowMaster program and incorporated into a full system uncertainty analysis presented in Section 6.

All the components used in the SPIV measurements are listed in Table 3, along with the specific parameters/settings that were used. As mentioned previously, many of the same components were also used for the planar PIV and Mie scattering techniques. Other equipment that was used, but is not listed in Table 3, includes various optical posts and components to place the cameras and laser optics. Additional laser quantities that pertain to SPIV uncertainty (*i.e.*, Δt used for each case and laser jitter) can be found in Table 12 in Appendix B.



Figure 23. LaVision two-level calibration plate (Type 11).

Table 2. SPIV processing steps used in LaVision's DaVis 8.4 software.

<u>Processing Step Name</u>	<u>Description</u>	<u>Parameters Used</u>
<i>Image Pre-processing</i>		
Subtract sliding average (Gaussian profile)	High-pass filter that removes large patterns of intensity fluctuations (e.g., from laser reflections)	Scale length: 8 – 12 pixels
Subtract constant	Subtracts a constant intensity from entire image; used to reduce noise from non-zero background intensities	Constant 60 counts
Min-max filter for intensity normalization	Applies local particle intensity correction so all particles across image have a normalized intensity based on local min and max	Scale length: 4 – 6 pixels
<i>Vector Calculation</i>		
Stereo cross-correlation	Calculates three-component, two-dimensional velocity vector fields based on two frames from two cameras; the two frames are cross correlated for all interrogation windows for each camera, with the highest peak representing the resulting vector	<u>Side-views:</u> 2 passes 64x64 50% overlap, 4 passes 32x32 75% overlap; <u>End-views:</u> 2 passes 128x128 50% overlap, 4 passes 64x64 75% overlap; Adaptive PIV weighting; Use image correction; Calculate uncertainty; High-accuracy mode for final passes
<i>Vector Postprocessing</i>		
Allowable vector range	Removes vector if one of its components is outside of given range	$u: [0 - 1.3U_1] \text{ m/s}$, $v: [-0.5\Delta U - 0.5\Delta U] \text{ m/s}$, $w: [-0.7\Delta U - 0.7\Delta U] \text{ m/s}$
Peak ratio Q	Removes vector if peak ratio Q (ratio of strongest correlation peak to next highest peak) is below given threshold	Remove if $Q < 3$
Median filter (3x)	Strongly remove and iteratively replace vector based on the median and standard deviation of neighboring vectors	Remove if diff to avg $> 3 * \text{Stdev}$ of neighbors, Reinsert if diff to avg $< 4 * \text{Stdev}$ of neighbors
Remove groups	Remove vectors that use less than given number of vectors in its group for the median filter above	Remove group if < 10 vectors

Table 3. SPIV components and descriptions.

<u>Component</u>	<u>Description</u>	<u>Parameters Used</u>
PCO.2000 Camera (x2)	CCD camera, 2048x2048 pixels	1 μ s exposure time, double-shot mode
Nikon Micro Nikkor Camera Lens (x2)	60 mm focal length	Manual focus, Aperture: $f/5.8$
LaVision Scheimpflug Adapter (x2)	Camera mount that allows tilting of lens plane relative to CCD image plane	30 – 45 degree offset angle
LaVision Type 11 Calibration Plate	Two-level calibration plate from LaVision, 106 x 106 x 11.5 mm	-
New Wave Gemini Laser	Double-pulsed Nd:YAG laser, Frequency doubled to 532 nm	Laser power ~ 65 – 85 mJ/pulse
Laser Sheet Optics	Plano-convex spherical lens (1000 mm focal length), plano-concave cylindrical lens (-50 -- 75 mm focal length), dichroic mirrors (532 nm coating)	Laser sheet thickness: 1 – 3 mm, Laser sheet width: 85 – 90 mm
ViCount 1300 Smoke Generator (x2)	Smoke particle generator, uses smoke oil 180, particle diameter ~0.2 μ m, used for side-views	Empirically tuned for good seed density
TSI Model 9307 Oil Droplet Generator (x2)	Laskin nozzle particle seeder, uses Dioctyl sebacate, particle diameter ~1 μ m, used for end-views	Empirically tuned for good seed density
Quantum Composers 9518 Pulse Generator	Delay/pulse generator to sync cameras and laser	Laser $\Delta t = [1 - 2]$ μ s
LaVision DaVis 8.4 FlowMaster Program	Computer program to calculate stereo-PIV vectors from raw particle images	See Table 2

3. EXPERIMENTAL RESULTS

All experimental results from the diagnostics described in the previous section are presented in this section. These include the operating conditions of each case (*i.e.*, freestream and stagnation chamber conditions), side-wall pressure measurements, incoming boundary-layer integral parameters, flow visualizations, and the SPIV velocity measurements. Although uncertainty bars are not included for the pressure and velocity measurements in this section (for clarity of plots), a thorough uncertainty analysis is given for each result in Section 6.

3.1. Operating Conditions

The operating conditions of each mixing layer and their uncertainties are listed below in Table 4. The uncertainties listed are for a 95% confidence interval (see Section 6). As previously mentioned, the primary freestream Mach numbers were nominally targeted for values of 0.5, 1.0, 1.5, 2.0, and 2.5; and convergent/converging-diverging nozzles were designed and fabricated appropriately (see Section 2.1). The secondary freestream Mach numbers were then throttled to attain the proper convective Mach number such that a sufficiently wide range of compressibility could be examined, with consistent M_c spacing between the cases.

Table 4. Compressible mixing layer operating conditions and uncertainties.

<u>Input Parameters</u>	<u>Case 1</u>	<u>Case 2</u>	<u>Case 3</u>	<u>Case 4</u>	<u>Case 5</u>
M_1	0.463 ± 0.012	1.003 ± 0.021	1.571 ± 0.025	1.955 ± 0.021	2.463 ± 0.032
M_2	0.089 ± 0.009	0.189 ± 0.009	0.285 ± 0.014	0.269 ± 0.008	0.175 ± 0.009
P_{01} (kPa)	109.32 ± 0.05	151.84 ± 0.05	270.41 ± 0.05	445.50 ± 0.06	778.10 ± 0.09
P_{02} (kPa)	94.56 ± 0.05	82.47 ± 0.05	71.47 ± 0.05	63.83 ± 0.05	50.95 ± 0.05
P_1 (kPa)	93.94 ± 0.10	80.37 ± 0.11	62.02 ± 0.10	57.58 ± 0.10	50.84 ± 0.11
P_2 (kPa)	93.92 ± 0.10	80.59 ± 0.11	66.29 ± 0.10	61.51 ± 0.10	49.91 ± 0.11
T_{01} (K)	296.10 ± 0.50	294.60 ± 0.50	284.59 ± 0.50	298.02 ± 0.50	289.25 ± 0.51
T_{02} (K)	292.48 ± 0.50	293.58 ± 0.50	295.57 ± 0.50	298.22 ± 0.50	292.58 ± 0.50
T_1 (K)	283.95 ± 0.84	245.25 ± 2.04	190.50 ± 2.68	168.87 ± 2.26	130.70 ± 2.63
T_2 (K)	292.02 ± 0.51	291.49 ± 0.54	290.85 ± 0.69	293.96 ± 0.56	290.80 ± 0.54
U_1 (m/s)	156.25 ± 4.3	314.89 ± 6.32	434.76 ± 6.08	509.24 ± 4.35	564.16 ± 4.59
U_2 (m/s)	30.35 ± 3.0	64.75 ± 2.96	97.28 ± 4.87	92.57 ± 2.79	59.76 ± 3.19
$r = U_2/U_1$	0.194 ± 0.020	0.206 ± 0.010	0.224 ± 0.012	0.182 ± 0.006	0.106 ± 0.006
$s = \rho_2/\rho_1$	0.972 ± 0.004	0.844 ± 0.007	0.700 ± 0.010	0.614 ± 0.008	0.441 ± 0.010
M_c	0.185 ± 0.008	0.381 ± 0.011	0.546 ± 0.013	0.690 ± 0.009	0.883 ± 0.010

Directly measured quantities for each stream include total pressures (P_{01} , P_{02}), total temperatures (T_{01} , T_{02}), static pressures (P_1 , P_2), and freestream velocities (U_1 , U_2). Total pressures and temperatures were measured in the stagnation chamber, while static pressure and freestream velocity values were measured in the fully-developed region of each shear layer (see Section 3. 5. 4). U_1 and U_2 were taken close to the top and bottom edges of the shear layers from the SPIV measurements and were used to determine the static temperatures via the adiabatic relation: $T = T_0 - |V|^2/(2c_p)$, where $|V|$ is the local velocity magnitude and c_p is the specific heat at constant pressure for air (= 1004.7 J/(kg-K)). Using the static temperature, Mach numbers were then calculated as $M = |V|/a$, where a is the local speed of sound (= $\sqrt{\gamma RT}$, $R_{\text{air}} = 287.058 \text{ J/(kg-K)}$, $\gamma_{\text{air}} = 1.4$), and densities were calculated using the ideal gas law, $\rho = P/(RT)$. For uncertainties of individual velocity components, see Section 6.

3. 2. Pressure Measurements

For this particular planar mixing layer study, uniform freestream velocities were desired; thus, it was imperative that there be an essentially constant pressure field in the test-section. A sidewall pressure tap insert (described in Section 2. 2. 1) was fabricated to verify this condition. Mean static pressures along the length of the mixing layer were measured at three y locations: middle of the primary stream ($y = +25.4 \text{ mm}$), splitter plate tip location ($y = 0 \text{ mm}$), and middle of the secondary stream ($y = -38.1 \text{ mm}$). The results for each mixing layer case are presented below in Figure 24.

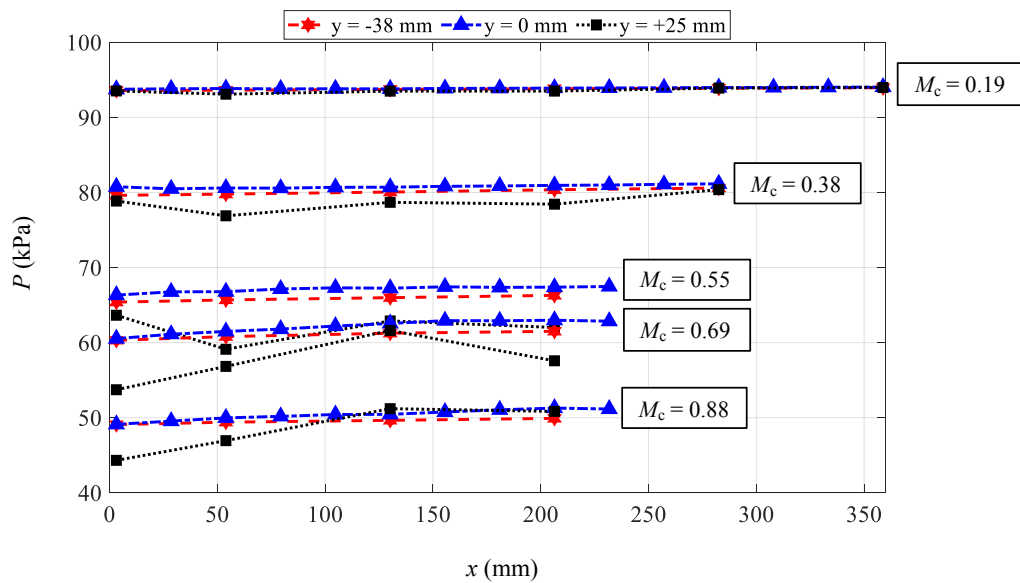


Figure 24. Side-wall pressure measurements of $M_c = 0.19, 0.38, 0.55, 0.69$, and 0.88 mixing layers.

The plot confirms near constant pressure conditions for each shear layer, although weak, unavoidable reflecting waves are present in the sonic/supersonic primary streams, as indicated by the fluctuations in the $y = +25$ mm profiles for $M_c = 0.38, 0.55, 0.69$, and 0.88 . These reflecting waves emanate from the joint between the nozzle and top wall, as well as the initial expansion fan/shock wave at the splitter-plate tip. To best mitigate this issue, the nozzle-wall joint was smoothed over with spot putty, and the pressure across the splitter tip was matched as well as possible using the highly sensitive schlieren photography technique (results given in Section 3.4.1). Pressures are reported up to the streamwise location at which each case becomes fully-developed/self-similar, and static pressures reported in Table 4 are taken from these side-wall measurements in the fully-developed region (described in Section 3.5.4).

The static pressure measurements reported in Figure 24, combined with the stagnation pressure measurements, can be used to approximate the velocity in the test section using isentropic relations. Their agreement with the freestream velocity results from SPIV (at the same y -locations) can be found in Appendix C. The differences between the two diagnostics are also a measure of how much total pressure is lost through the test section, since the isentropically determined velocities assume a constant P_0 throughout.

3.3. Incoming Boundary Layer Measurements

For each case, incoming flow conditions are documented in the form of boundary layer (BL) PIV measurements on four walls near $x = 0$. The four walls are: wind tunnel top wall, splitter plate top wall, splitter plate bottom wall, and wind tunnel bottom wall (see Section 2.2.2, Figure 14). The velocity measurements were all obtained within 20 mm of the splitter tip ($-20 \text{ mm} < x < 6 \text{ mm}$) along the spanwise-centerline ($z = 0$). Due to optical access difficulties, the exact streamwise location of

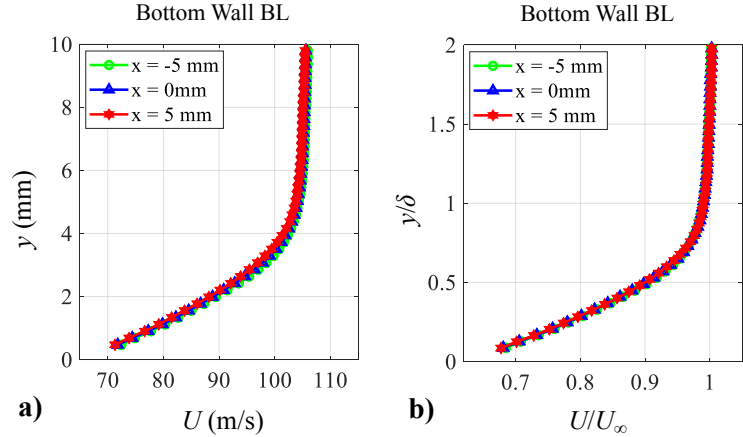


Figure 25. a) Dimensional and b) non-dimensionalized U profiles (wind tunnel bottom wall BL, $M_c = 0.55$).

each boundary layer profile varies slightly; however, this issue is mitigated since each boundary layer is fully developed by $x = 0$ and grows negligibly over this range. An example boundary layer U profile ($M_c = 0.55$, wind tunnel bottom wall) is shown in Figure 25 in both dimensional and non-dimensionalized forms. The former (Figure 25a) shows the negligible growth of the boundary layer over the range $-5 \text{ mm} < x < 5 \text{ mm}$, and the minute differences between the dimensional profiles disappear completely when normalized (Figure 25b), indicating self-similarity.

In order to determine the integral parameters of each boundary layer, experimental velocity results are curve fit using a modified wall-wake velocity profile for compressible, turbulent boundary layers following Sun and Childs (1973).⁴⁹ Their work focuses on eliminating the non-zero velocity gradient at the boundary-layer edge that results from the wall-wake velocity profile developed by Mathews *et al.* (1970) a few years prior.⁵⁰ The modified version was shown to better match experimental data for a range of freestream Mach numbers. In the modified wall-wake method, two parameters, skin friction coefficient (C_f) and boundary layer thickness (δ), are determined from the curve fit found by the method of least squares. For details on the procedure, including physical and mathematical bases upon which the profile equations are founded (as well as the profile equations themselves and relevant constants), the reader is referred to Sun and Childs.⁴⁹ It should be noted that the thickness determined via this method corresponds to the location where $U/U_\infty = 0.995$ (as opposed to the commonly used 99% definition). The best-fit curve can then be used to determine the incompressible displacement thickness (δ^*), incompressible momentum thickness (θ), shape factor (H), and the wake strength parameter (Π) using trapezoid-rule numerical integration.

As examples, the best-fit curves of the secondary stream boundary layers for the $M_c = 0.55$ case are shown in Figure 26 in both outer (left) and inner (right) wall normal coordinates. The inner coordinate transformation, denoted by the superscript +, requires normalization of U by the friction velocity $u_\tau (= (\tau_w/\rho_w)^{1/2})$ and y by $\mu_w/(\rho_w u_\tau)$, where the subscript w denotes properties at the wall. Since measurements cannot be made on the wall, the adiabatic wall temperature (T_{aw}) is calculated from the freestream velocity and stagnation temperature using the Crocco-Busemann relation: $T_{aw} = r(u_e^2)/(2c_p)$. For turbulent flow of gases, the recovery factor r is taken to be $Pr^{1/3}$, where Pr is the Prandtl number at the boundary layer edge ($= \mu_e c_p/k_e$), and the thermal conductivity, k is determined by Sutherland's law.⁵¹ u_e is the velocity at the BL edge (*i.e.*, freestream velocity) and μ_e is the fluid viscosity at the BL edge. The disparity in δ between the experimental data and

curve fit profile in Figure 26 can be attributed to the aforementioned $\delta^{99.5\%}$ definition for the curve fit, as opposed to $\delta^{99\%}$ being reported for the experimental value.

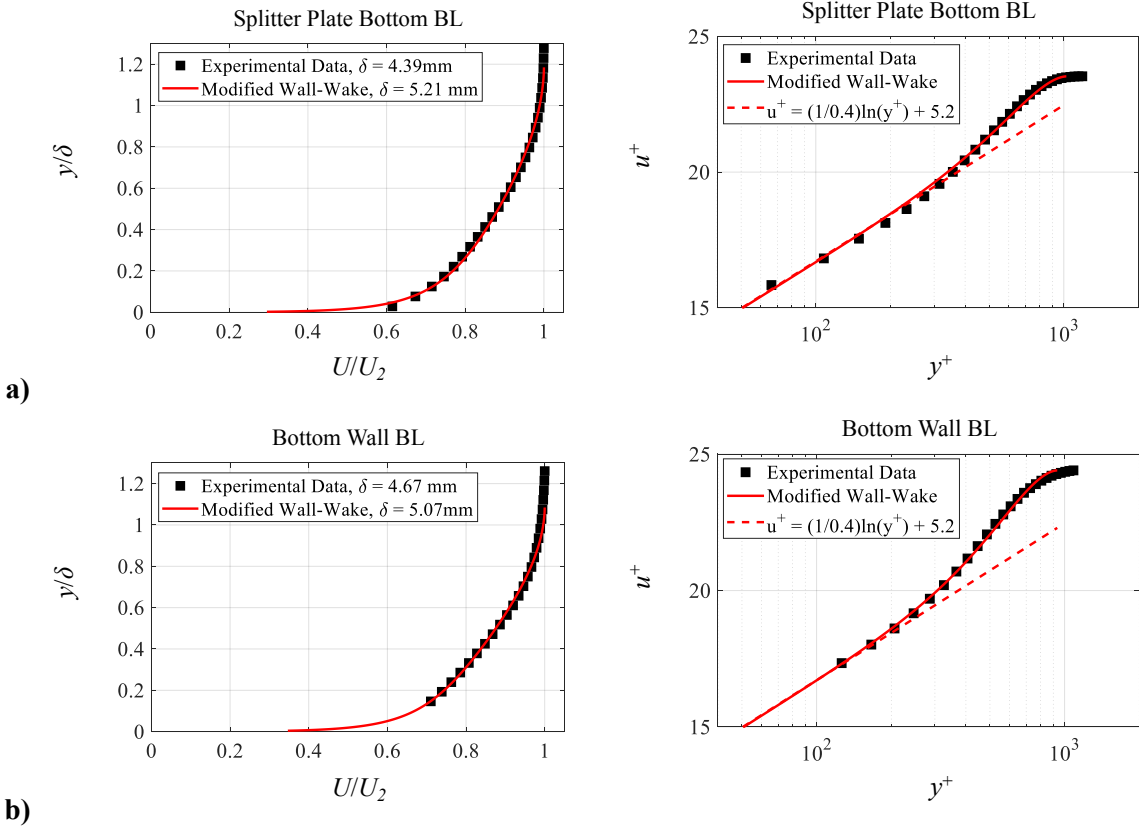


Figure 26. Curve fit and experimental BL data in outer (left) and inner (right) coordinates for a) splitter plate bottom wall and b) wind tunnel bottom wall ($M_c = 0.55$).

Integral parameters of all documented boundary layers are listed in Table 5 (with $\delta^{99\%}$ being reported). The two boundary layers in the secondary stream (bottom) are consistently thicker than those in the primary stream (top). All boundary layers for all cases are $\leq \sim 5$ mm thick ($\leq 7\%$ of channel height) and show good agreement for H with expected values for turbulent, compressible boundary layers ($\sim 1.3 - 1.4$).⁵² It should be noted that many experimental difficulties are involved with measuring these thin regions of flow close to the wall. Mainly, laser reflections limit how close the inner-most data point is to the wall. The dashed red line in Figure 26 represents the log-law region of the boundary layer, in which roughly one to ten experimental data points lie for each boundary layer. Outlier Π values for some of the cases may be attributed to the relative sparsity of data for $y^+ \leq 100$, made worse by the thinness of the boundary layer itself. Nonetheless, these

inflow velocity profiles are important boundary condition information for the development of the mixing layers. Ensemble sizes (N) for the boundary layer measurements were $\sim 900 \leq N \leq \sim 4000$.

Table 5. Incoming boundary layer integral parameters.

	δ (mm)	δ^* (mm)	θ (mm)	H	C_f	Π
<u>Case 1 ($M_c = 0.19$)</u>						
Top Wall BL	2.877	0.640	0.423	1.514	0.002201	1.7648
Splitter Plate Top BL	2.237	0.289	0.223	1.299	0.003716	0.3433
Splitter Plate Bottom BL	5.137	0.867	0.620	1.398	0.003635	0.7808
Bottom Wall BL	4.692	0.820	0.578	1.419	0.003594	0.8651
<u>Case 2 ($M_c = 0.38$)</u>						
Top Wall BL	2.278	0.436	0.307	1.419	0.002183	1.3415
Splitter Plate Top BL	1.397	0.131	0.106	1.240	0.003825	-0.1924
Splitter Plate Bottom BL	5.168	0.928	0.655	1.417	0.002953	1.0627
Bottom Wall BL	4.606	0.772	0.552	1.398	0.003222	0.8984
<u>Case 3 ($M_c = 0.55$)</u>						
Top Wall BL	3.054	0.567	0.405	1.401	0.001686	1.4711
Splitter Plate Top BL	2.250	0.357	0.269	1.325	0.002049	0.8887
Splitter Plate Bottom BL	4.394	0.645	0.486	1.326	0.003613	0.4960
Bottom Wall BL	4.673	0.721	0.529	1.363	0.003357	0.7184
<u>Case 4 ($M_c = 0.69$)</u>						
Top Wall BL	3.599	0.574	0.429	1.338	0.001561	1.1620
Splitter Plate Top BL	2.847	0.514	0.372	1.381	0.001526	1.3996
Splitter Plate Bottom BL	4.271	0.617	0.464	1.330	0.003711	0.4884
Bottom Wall BL	4.212	0.646	0.474	1.364	0.003547	0.6700
<u>Case 5 ($M_c = 0.88$)</u>						
Top Wall BL	4.605	0.808	0.587	1.377	0.001010	1.6497
Splitter Plate Top BL	3.108	0.582	0.419	1.390	0.000871	1.6398
Splitter Plate Bottom BL	4.007	0.510	0.390	1.308	0.004618	0.2008
Bottom Wall BL	3.060	0.435	0.322	1.349	0.004832	0.3353

3.4. Mixing Layer Flow Visualization

In general, for any experimental investigation of a flowfield, qualitative flow visualizations can be helpful for understanding the characteristics of large-scale turbulent structures that are present, in addition to the various compressible flow features (*e.g.*, shocks, expansion fans, etc.). The two methods used in the current study are schlieren photography and Mie scattering; results from the two are presented and discussed here.

3.4.1. Schlieren Photography

As described in the Section 2.2.3, schlieren photography highlights density gradients that are present in the flowfield. Figure 27 shows full test-section instantaneous schlieren images of all five M_c cases. The first two side window positions are shown for the $M_c = 0.19 - 0.69$ mixing layers, while only the first window position is shown for $M_c = 0.88$, as the shear layer was fully developed by the end of that position for that case. The two images shown for each of the first four cases are stitched together from different instants in time. It should be noted that the knife-edge was oriented horizontally for each configuration, thus highlighting gradients in the vertical direction.

Compressibility effects are clearly evident among the different shear layers. Most notably, the lowest $M_c = 0.19$ case exhibits the round spanwise-coherent Brown-Roshko rollers, with thin interconnecting braids, that have been extensively documented in incompressible mixing layers.⁷ The rollers maintain their spanwise coherence far downstream of the splitter tip, as shown by the large, round structure between $x = 300 - 400$ mm in the top image. In the image just below it, the $M_c = 0.38$ case still shows some spanwise organization with roller and braid regions; however, they become stretched-out, or elongated, in the streamwise direction and appear more elliptical in shape (*e.g.*, the roller structure near $x = 400$ mm for $M_c = 0.38$). In this image, the braids also appear thicker, as the pairing of structures occurs in a less organized manner. For the higher $M_c \geq 0.55$ cases, it appears that all spanwise coherence is lost, and the structures become highly three-dimensional and smaller in size relative to the local shear layer thickness. At these levels of compressibility, the line-of-sight integrating nature of schlieren does not allow for detailed observations of the large structures, due to their three-dimensionality.

In addition to large-scale structures, schlieren visualization highlights the reflecting wave system present in the supersonic primary stream of the $M_c = 0.55$, 0.69 , and 0.88 cases. The unavoidable initial compression/expansion wave (depending on whether P_2/P_1 is slightly greater than or less than unity) emanating from the splitter tip undergoes like reflections off the top wall and opposite-sense reflections off the shear layer. This initial wave from the splitter tip can be used to confirm the pressure match between the two streams, as it sensitively flips between being a compression or expansion wave. Thus, the schlieren technique was used at the outset of each case to finely tune the operating conditions, with the exception of $M_c = 0.19$, which does not feature an initial wave. Although emphasized in the schlieren photographs, the wave systems in the supersonic streams are weak, as will be indicated by velocity measurements in Section 3.5.

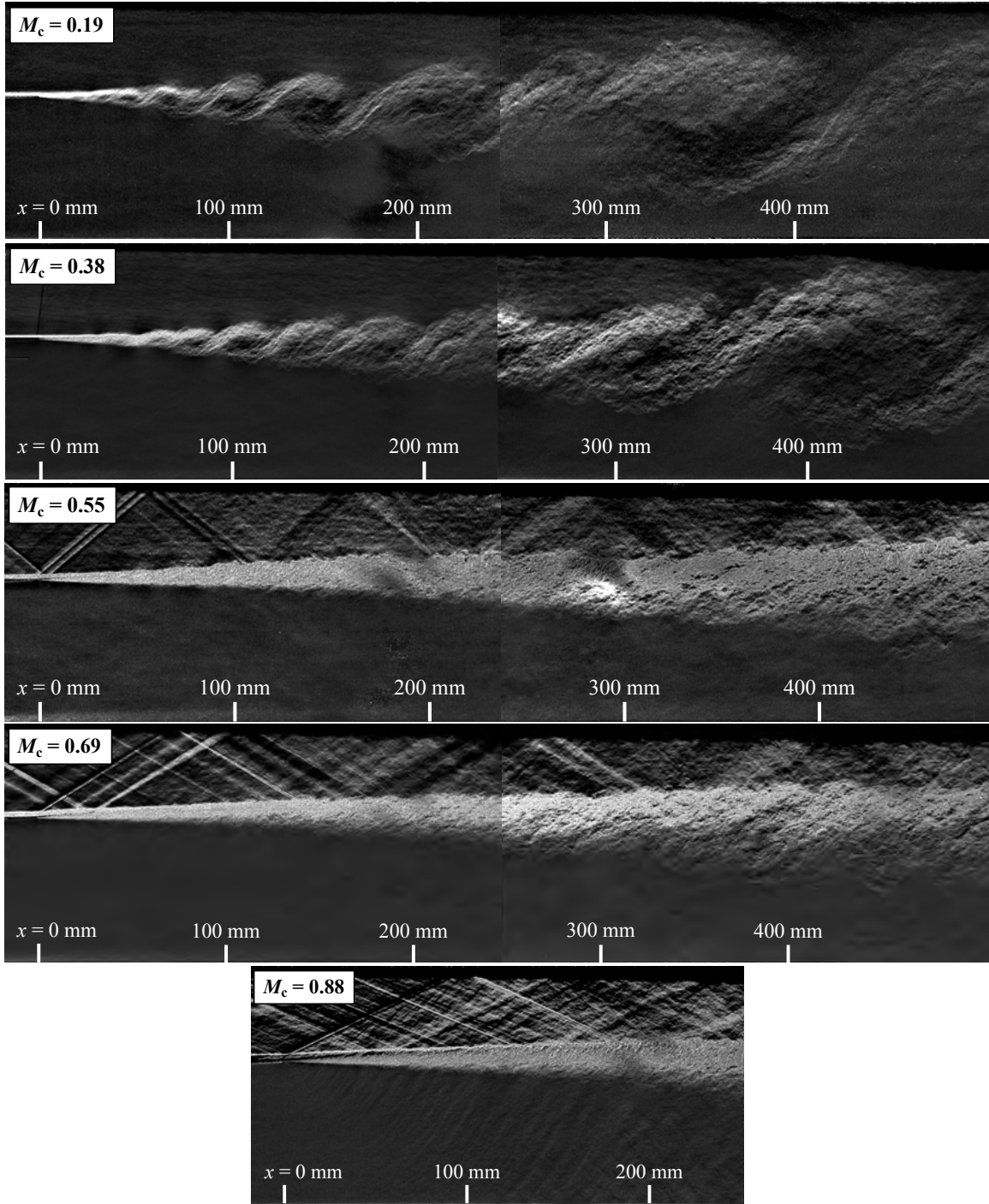


Figure 27. Full test-section FOV instantaneous schlieren images.

While, as expected, no sharp density gradients are present in the bottom subsonic streams, Mach waves can be seen in the secondary stream of the highest $M_c = 0.88$ case. This signifies that the turbulent structures in the mixing layer are moving supersonically relative to the secondary freestream, which is also supported by the fact that the convective velocity, U_c , for this case is

greater than a_2 . Using the isentropic definition of U_c given in Equation (13), the convective velocity for $M_c = 0.88$ is 361.7 m/s, while a_2 is 341.5 m/s (both calculated from U and M in Table 4).

Lastly, these full test-section FOV schlieren photographs show the growth of the boundary layers on the top wall. It is expected that the same is true on the bottom wall; however, density gradients are not strong enough in the secondary stream to highlight the boundary layers present there. The important conclusion from these observations is that the dark regions, which indicate the boundary layers, do not come into contact with the shear layer until far downstream ($x \geq 350$ mm) for $M_c = 0.19$ and 0.38 . By this point, the mixing layers are fully-developed, and the turbulence statistics have already been determined from the velocity measurements. For $M_c = 0.55$, 0.69 , and 0.88 , the boundary layers do not come close to the top side of the mixing layers, even at the downstream edge of the images. It can also be assumed that boundary layers on the bottom wall do not interfere with the mixing layer bottom sides (within the fully-developed region), since the secondary nozzle-exit height was made 25.4 mm taller than the primary, and the bottom wall boundary layers are only $\sim 2 - 3$ mm thicker than the top walls' (even with the faster mixing layer growth into the secondary).

Previously mentioned high-speed schlieren movies are also valuable data and are made available on the project website. The primary advantage of these movies is their time resolution, thus their ability to track turbulent structures from frame to frame. In the movies, the growth of the structures as they convect downstream is clearly evident, in addition to the pairing of large structures, especially at lower M_c . In order to increase the frame rates to sufficient speeds, the FOVs were reduced to maintain the same spatial resolution of the shear layers. The FOVs of each time-resolved movie stitched together in the streamwise direction are shown in Figure 28.

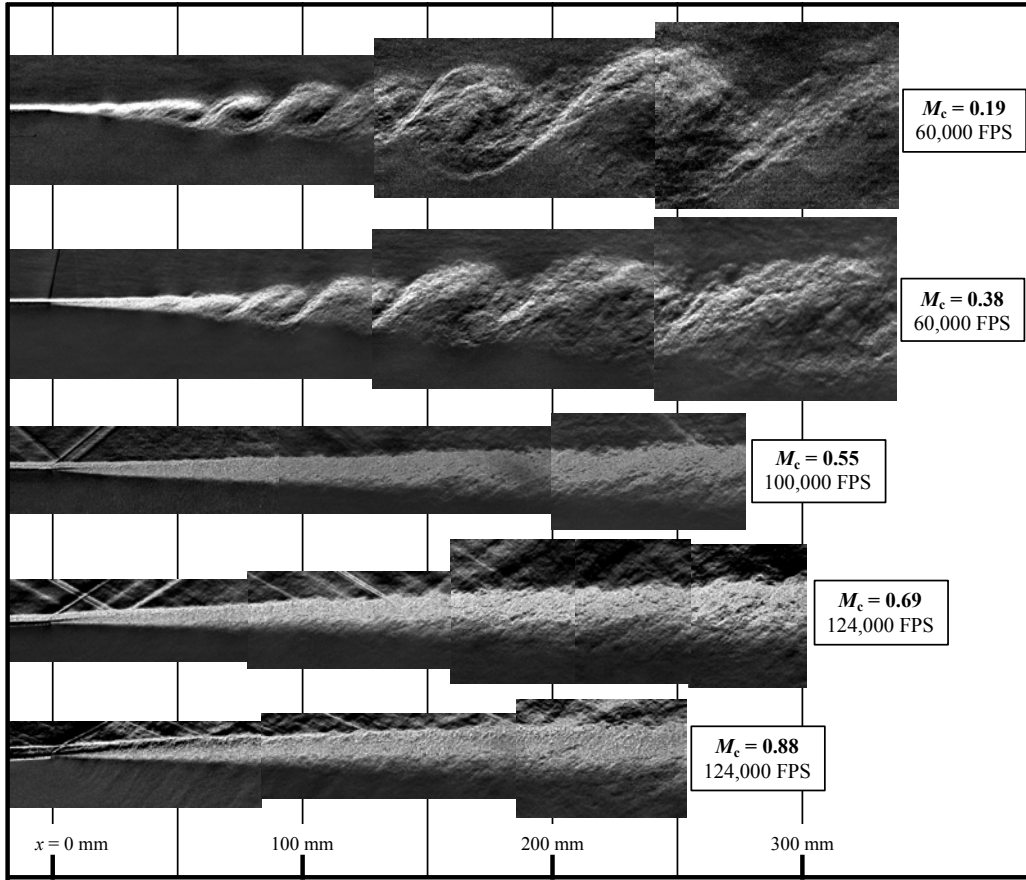


Figure 28. FOVs for high-speed, time-correlated schlieren movies.

3.4.2. Mie Scattering Images

As previously noted, detailed three-dimensional analysis of the structures is not possible with schlieren images, due to it being a line-of-sight integrating technique that averages density gradients in the spanwise direction. Therefore, Mie scattering visualization was also performed in order to obtain spatially-resolved flow visualization images. The technique performed here uses the condensation formed in the shear layer from the humidity in the secondary stream as seed; thus, the results are called product formation images and mark the molecularly mixed fluid. Since this method relies on the dew point temperature of the secondary reservoir (atmospheric room air) relative to the lower temperature in the mixing layer, it could not be performed for the two lowest M_c cases due to their low primary stream velocities (thus higher static temperatures).

Uncorrelated instantaneous product formation images of the $M_c = 0.55$, 0.69 , and 0.88 shear layers are shown in Figure 29 for the x - y plane at $z = 0$. Clearly absent in these higher M_c images are the round, roller structures seen in the top image of Figure 28 for $M_c = 0.19$. In contrast, the

structures become elongated, or ‘stretched’ in the streamwise direction (*i.e.*, flatten out longitudinally), with the braid regions developing a slight ‘kink’ deformation (note, the elongating trend of the rollers started with the $M_c = 0.38$ case, as observed in the schlieren images above). This ‘stretching’ of the turbulent structures for higher M_c is characterized by Clemens and Mungal as a ‘polygonal’ shape.²² As M_c is increased further (Figure 29b,c), the structures become even less two-dimensionally organized, and the obliquely oriented braided regions appear closer together in the streamwise direction. The higher level of structure detail seen in the $M_c = 0.88$ image also indicates that smaller-scale turbulence is present in addition to the large structures for the higher Reynolds number, more compressible shear layers. Small ‘finger-like’ structures can be seen attached to the large-scale structures in Figure 29c. These observations are all consistent with previous studies of large-scale flow structures in compressible mixing layers, including those of Clemens and Mungal (1992, 1995),^{22, 31} Elliott *et al.* (1995),⁵³ and Messersmith and Dutton (1996).⁵⁴

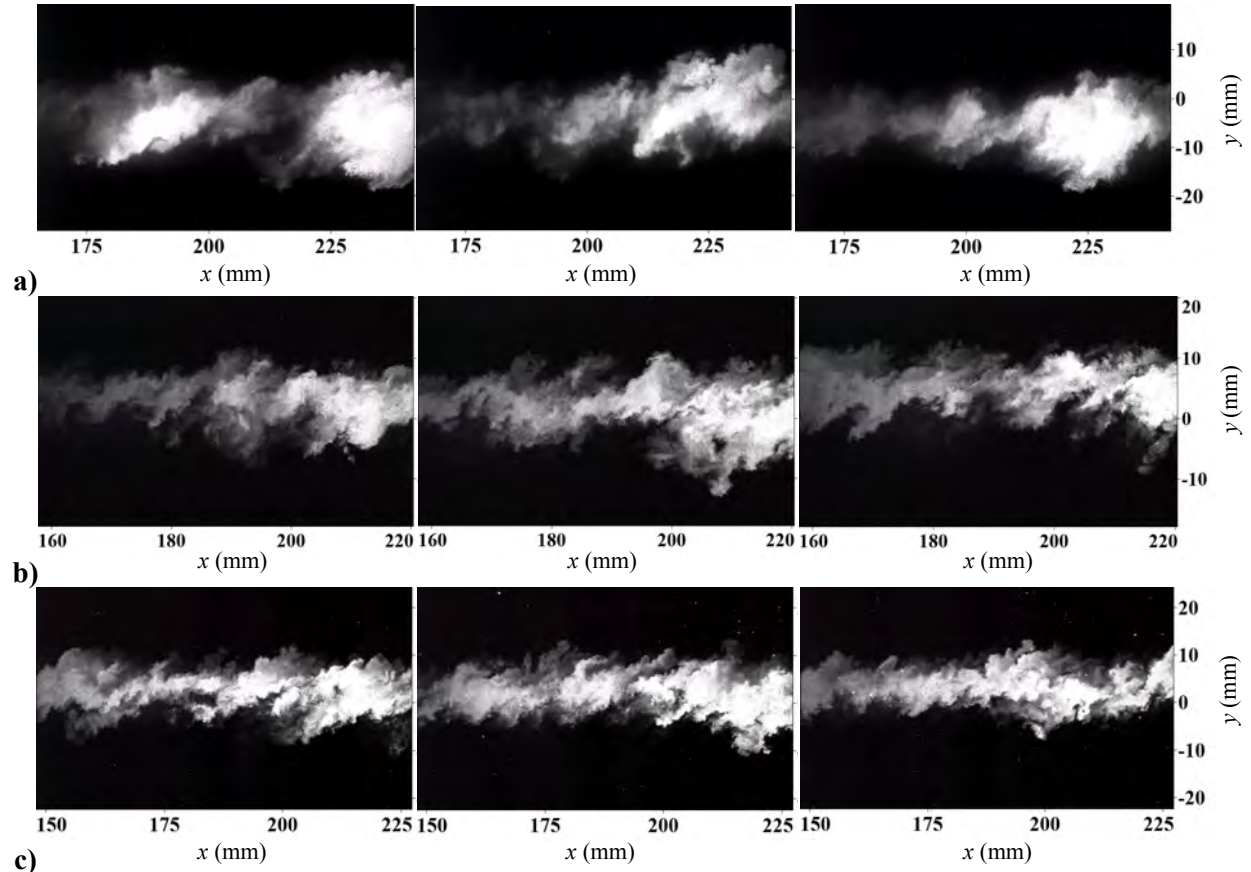


Figure 29. Side-view (x-y plane) product formation images of $M_c = \text{a)} 0.55$, b) 0.69, and c) 0.88 mixing layers.

Planar product formation images were also captured for the y - z cross-sectional, end-view planes. Since the experimental setup for Mie scattering is identical to SPIV, its fields of view overlap with those of the velocity measurements. The streamwise locations at which these images were obtained correspond to the most downstream x -locations of the SPIV end-view planes. These are $x = 160, 310$, and 310 mm for $M_c = 0.55, 0.69$, and 0.88 , respectively. The results are shown in Figure 30 and further reinforce the notion of highly three-dimensional structures in compressible mixing layers. All cases shown below feature tortuous instantaneous shear layer interfaces on both the top and bottom, with the turbulent structures in the shear layer apparently decreasing in size with increasing compressibility. Additionally, these results do not show any discernible qualitative differences across the span of the mixing layers, which is important, since confirming planar symmetry in the z -direction is an aspect of these data being CFD validation-quality. The uneven light intensity distribution for the two higher M_c cases (higher intensity on the left side, especially

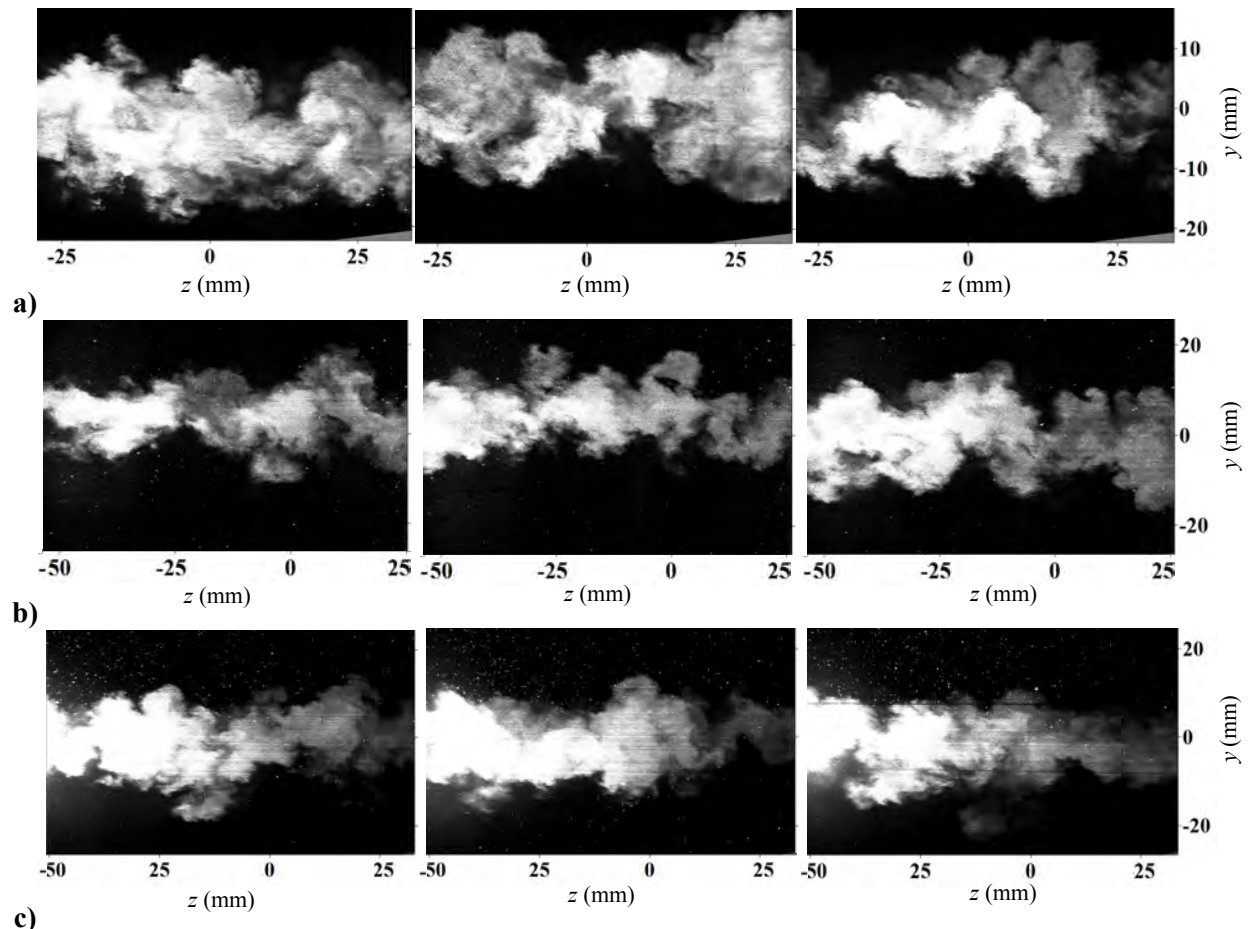


Figure 30. End- view (y - z plane) product formation images of $M_c =$ a) 0.55, b) 0.69, and c) 0.88 mixing layers.

noticeable in Figure 30c) is an artifact of the end-view diagnostic setup, which requires harsh viewing angles that result in uneven illumination across the CCD sensor.

3. 5. Spanwise-Central SPIV Velocity Measurements

In this section, the planar three-component velocity fields are presented and discussed for the x - y plane. End-view y - z velocity data are presented in the following Section 3. 6. The data obtained are presented here so as to best portray their substance and quality, with subsequent sections discussing the effects of compressibility on the turbulence and large-scale structures in the mixing layers (Sections 4 and 5).

3. 5. 1. Instantaneous Velocity Fields

For each mixing layer case, an ensemble of more than 3500 instantaneous velocity vector fields were obtained for each FOV. These are uncorrelated in time, with the time-spacing between the images being orders of magnitude longer than the typical flow-through time of the convecting turbulent structures. Thus, the vector fields are statistically independent from one another and ensemble averages can be used characterize the turbulence (*e.g.*, Reynolds stress tensor).

The side-view FOVs were required to be marched downstream until each mixing layer exhibited self-similarity for all turbulence quantities. The streamwise extent of each FOV was limited by the camera zoom, since dense vector fields were desired with a sufficient number of vectors across the transverse width of the mixing layer. On average, each FOV was \sim 80 mm in length in the x -direction and extended far enough above and below the shear layers to capture the freestreams. For each case, example instantaneous color contours of streamwise (u), transverse (v), and spanwise (w) velocity components are shown in Figure 31, Figure 32, and Figure 33, respectively (normalized by the mean velocity difference, $\Delta U = U_1 - U_2$). In the images, a reduced sample (1/4 in both x and y directions) of velocity vectors are overlaid, with U_c subtracted from the streamwise component. Here, the vectors are shown primarily to emphasize the resolution of the data, since the actual heads and directions of the vectors are difficult to visualize on the spatial scales given below. Only one color-bar is shown for each velocity component, since all cases are set to the same range specifically to examine how the velocities scale with the normalization factor ΔU . It should be noted that the different FOVs that are stitched together are not from the same instant in time.

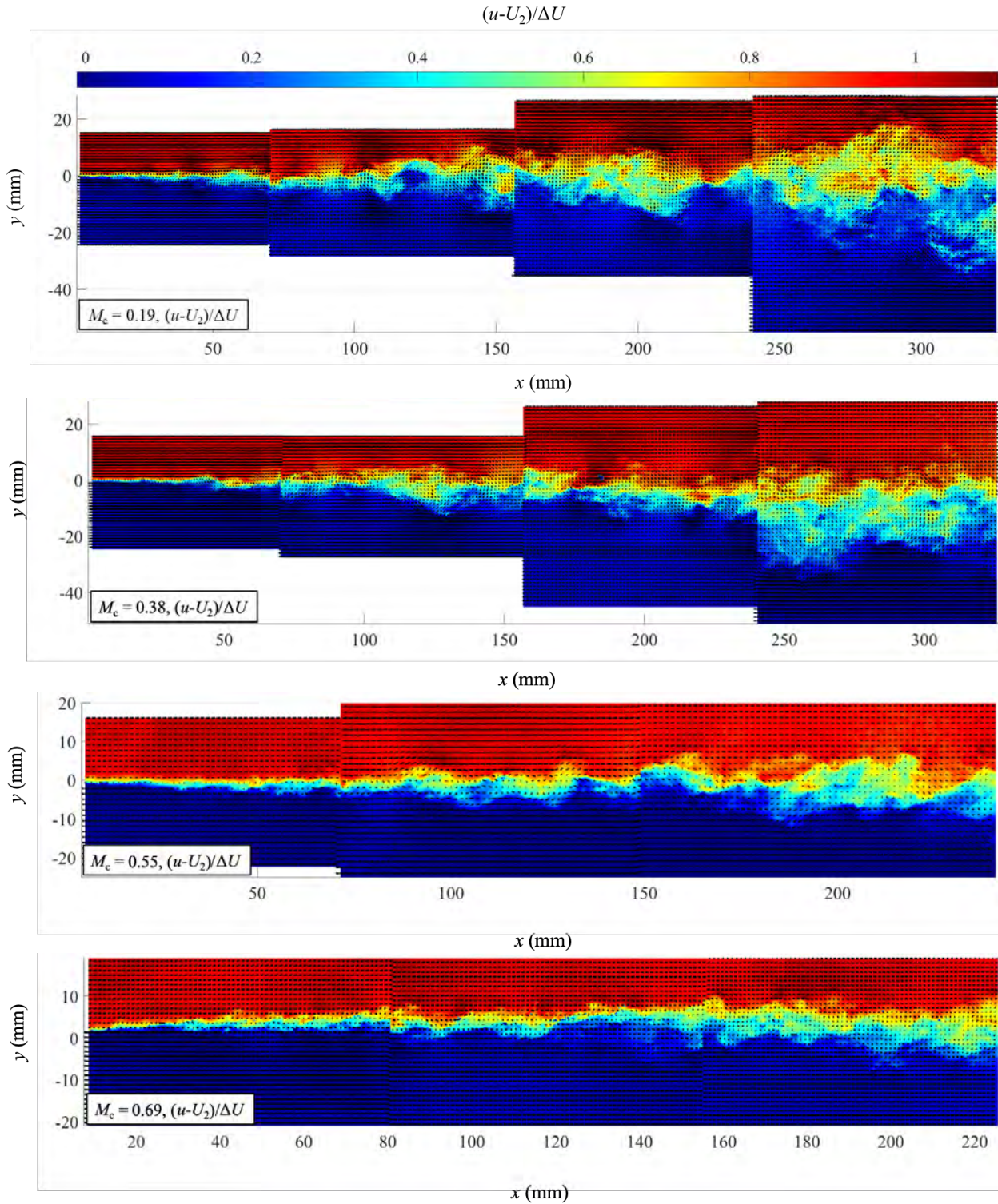


Figure 31. Color contours of instantaneous u -velocity fields of $M_c = 0.19, 0.38, 0.55, 0.69$, and 0.88 mixing layers.

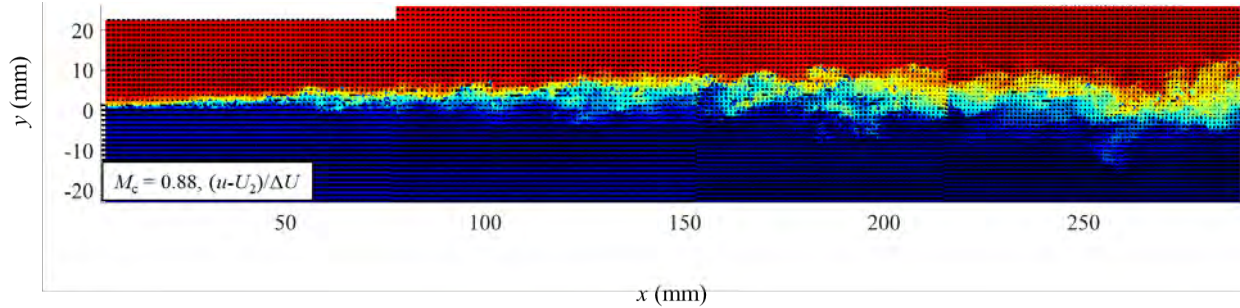


Figure 31. (cont.)

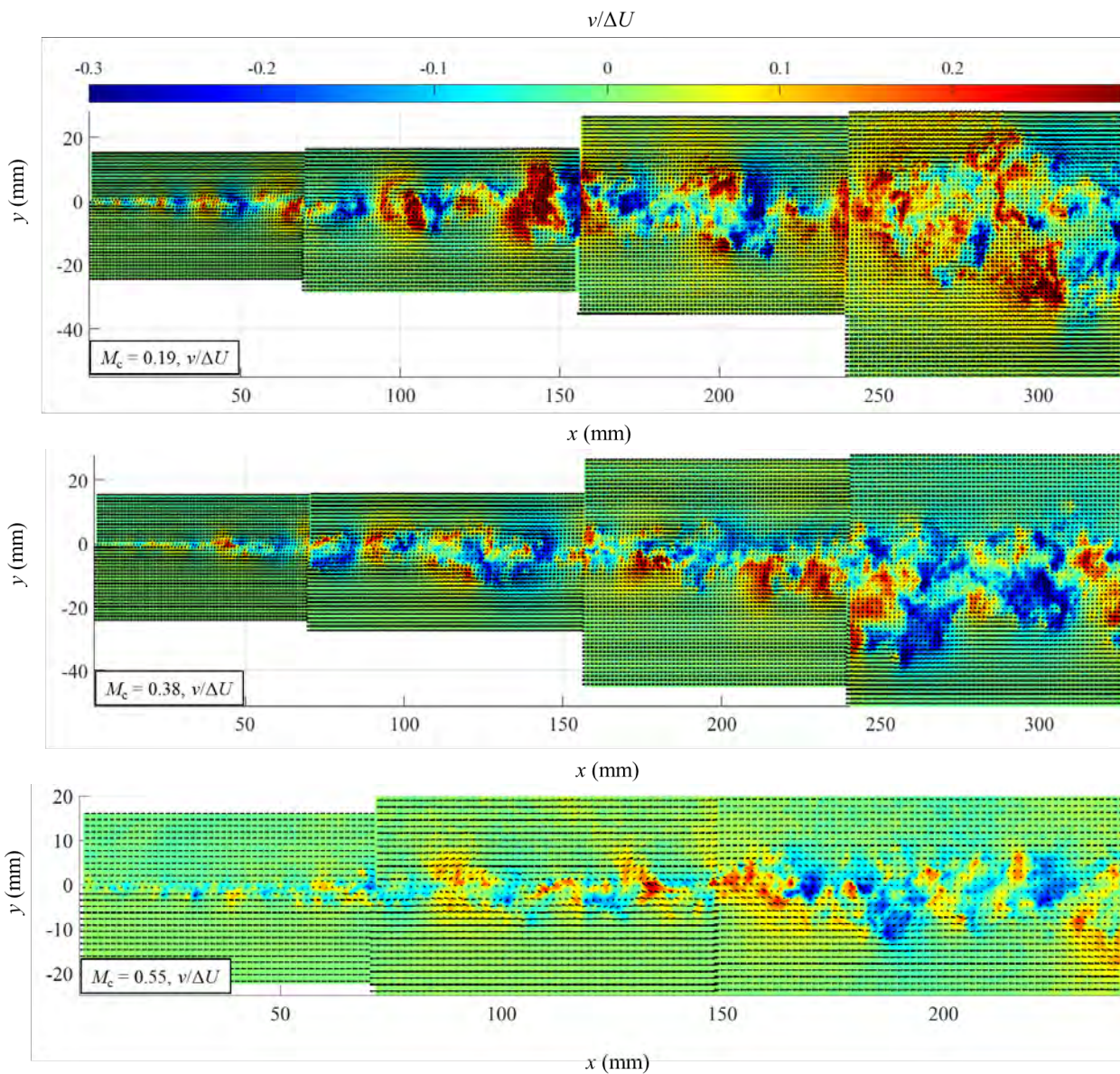


Figure 32. Color contours of instantaneous v -velocity fields of $M_c = 0.19, 0.38, 0.55, 0.69$, and 0.88 mixing layers.

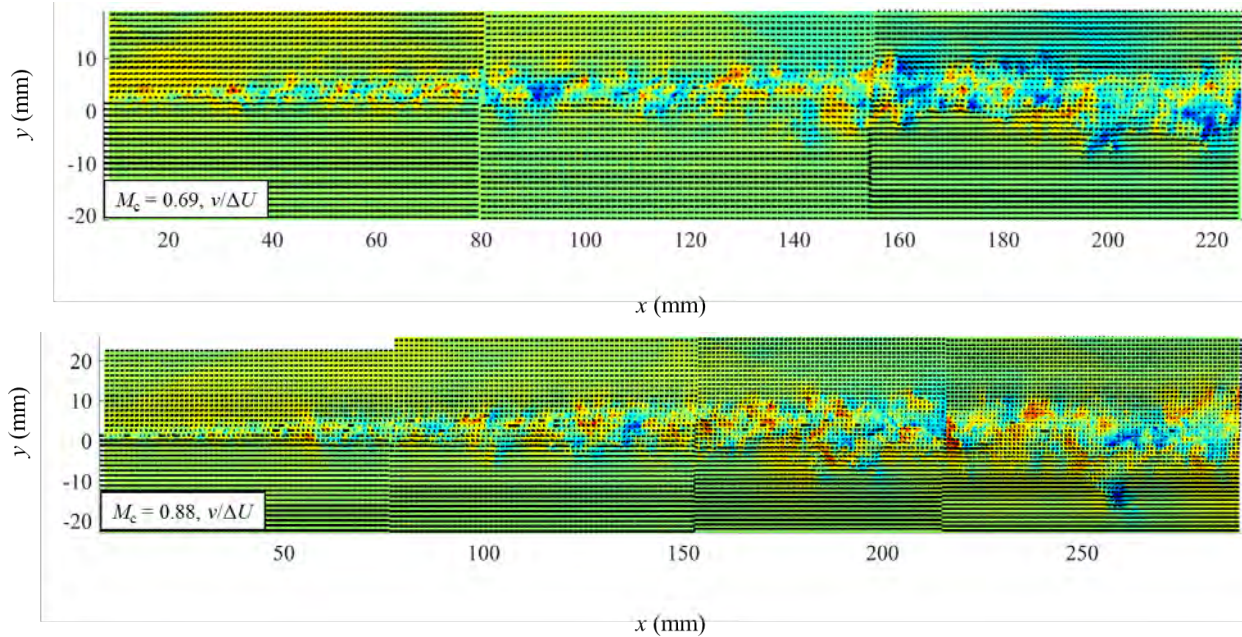


Figure 32. (cont.)

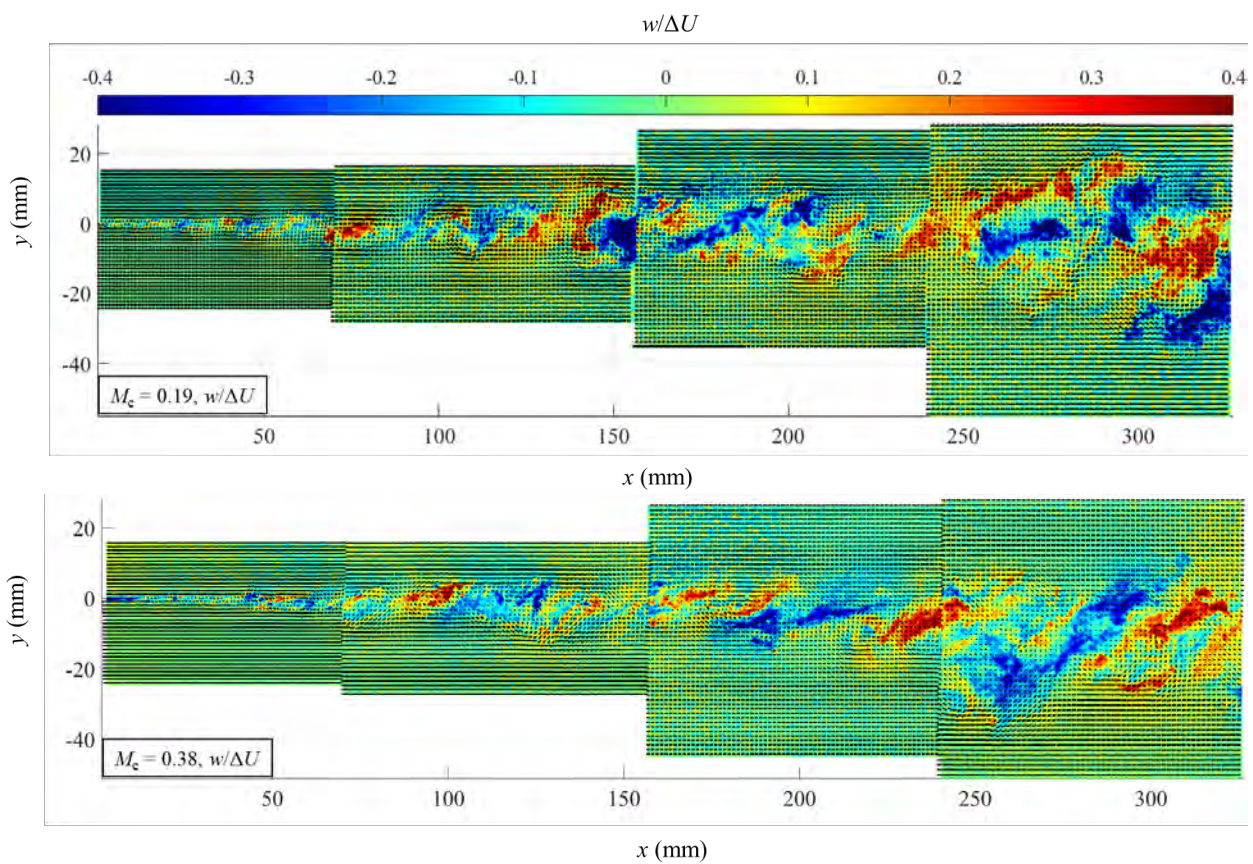


Figure 33. Color contours of instantaneous w -velocity fields of $M_c = 0.19, 0.38, 0.55, 0.69$, and 0.88 mixing layers.

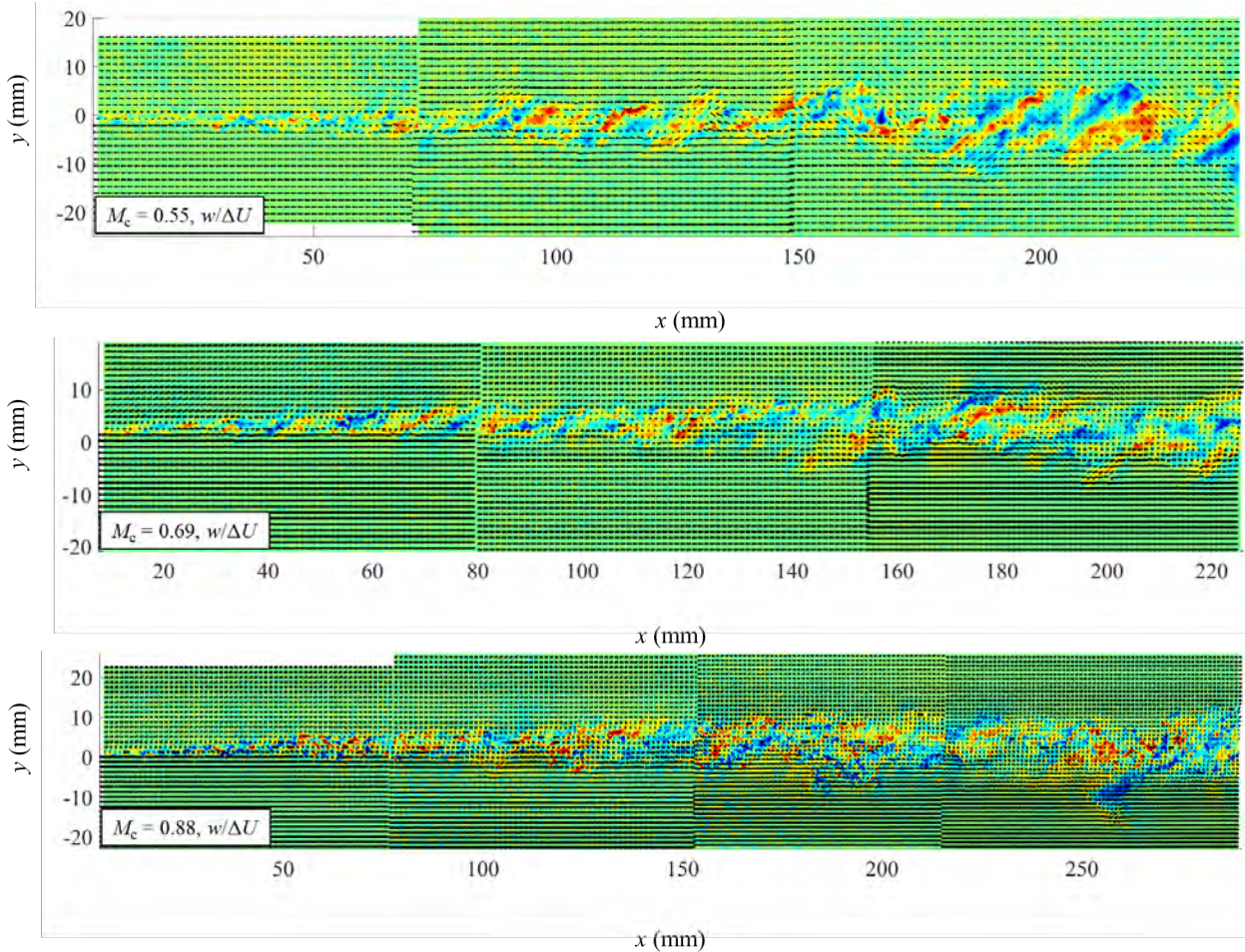


Figure 33. (cont.)

Qualitatively, it can be seen that as compressibility increases, the mixing layers contain eddies that are smaller in scale, and the mixing layers themselves are noticeably thinner. For all cases, both freestreams show near-zero v and w as expected, although some cases with supersonic primary freestreams show weak instantaneous transverse velocities from the unavoidable waves (Figure 32, $M_c = 0.69$ and 0.88). The $M_c = 0.19$ and 0.38 cases in Figure 33 show large regions of positive and negative w -braids in the mixing layers, indicating the presence of dominant large-scale structures, whereas the $M_c = 0.69$ and 0.88 cases show thinner, less-organized braided regions (same Figure 33). The intermediate $M_c = 0.55$ case seems to be a good representation of the transition between the low and high compressibility cases, with strands of +/- w -braids still spanning the transverse width of the shear layer but becoming very thin. Similar observations can be made of the decreasing size of turbulent eddies when examining the v -component of velocity in Figure 32. Here, it is clear that in the lowest compressibility case, the large rollers maintain their

shape from the onset of mixing at $x = 0$ through the most downstream FOV ($x > 300$ mm). In the $M_c = 0.38$ case, quasi-rollers that can be seen in the first two FOVs start to lose their coherence in the last two FOVs. Again, the three highest M_c cases feature highly disorganized structures and smaller-scale transverse turbulence. These qualitative observations of the instantaneous velocity fields are useful, as they serve as the heuristic backdrop upon which quantitative turbulence length-scale analyses are motivated. These analyses are discussed in Section 4. 5.

3. 5. 2. Mixing Layer Development

A key advantage of the PIV technique used here is the ability to obtain highly spatially-resolved velocity vector fields with rather large fields of view, as compared to the point-by-point measurement techniques (*e.g.*, LDV, hot-wire anemometry) used in many previous experiments. This allows for the close examination of the streamwise development of mean and higher-order statistical flow quantities. The standard Reynolds decomposition is used here, with ensemble averages denoted by an overbar, or capitalization: $\bar{u}_i = U_i = (1/N) \sum(u_{i,1} + u_{i,2} + \dots + u_{i,N})$. N is the ensemble size and is at least 3500 at each x - y grid point. Instantaneous fluctuations from the mean are denoted with primes ($u_i' = u_i - \bar{u}_i$), and by definition, their ensemble averages are zero. Note that the subscript i here does not refer to the freestream index, but rather the component of velocity.

Mean normalized streamwise velocity profiles at various x -locations (starting at $x = 10$ mm with 20 mm spacing for each case) are shown with a color contour background in Figure 34. The transverse growth of the shear layers can be seen clearly, as the y -locations required for freestream conditions ($((U - U_2)/\Delta U = 0, 1)$) become further apart as the velocity profiles are traversed downstream. When closely examined, the most upstream velocity profiles shown for the three supersonic M_1 cases exhibit only the slightest non-uniformities in their primary freestreams due to the initial splitter-tip shock/expansion. Furthermore, the profiles downstream of $x = 10$ mm for these cases show little-to-no effects from the wave system that was highlighted in the schlieren images.

Additionally worth noting are the slight velocity deficits in the secondary streams near the splitter tip for the upstream $x = 10$ mm profiles. These deficits are caused by the incoming boundary layers on the splitter plate and represent the momentum deficit near the wall. They completely disappear by the $x = 50$ mm profile for all cases and will be important in determining when the

shear layer growth rate becomes fully developed. These deficits are the key factor that affect the streamwise length required for mean velocity self-similarity.

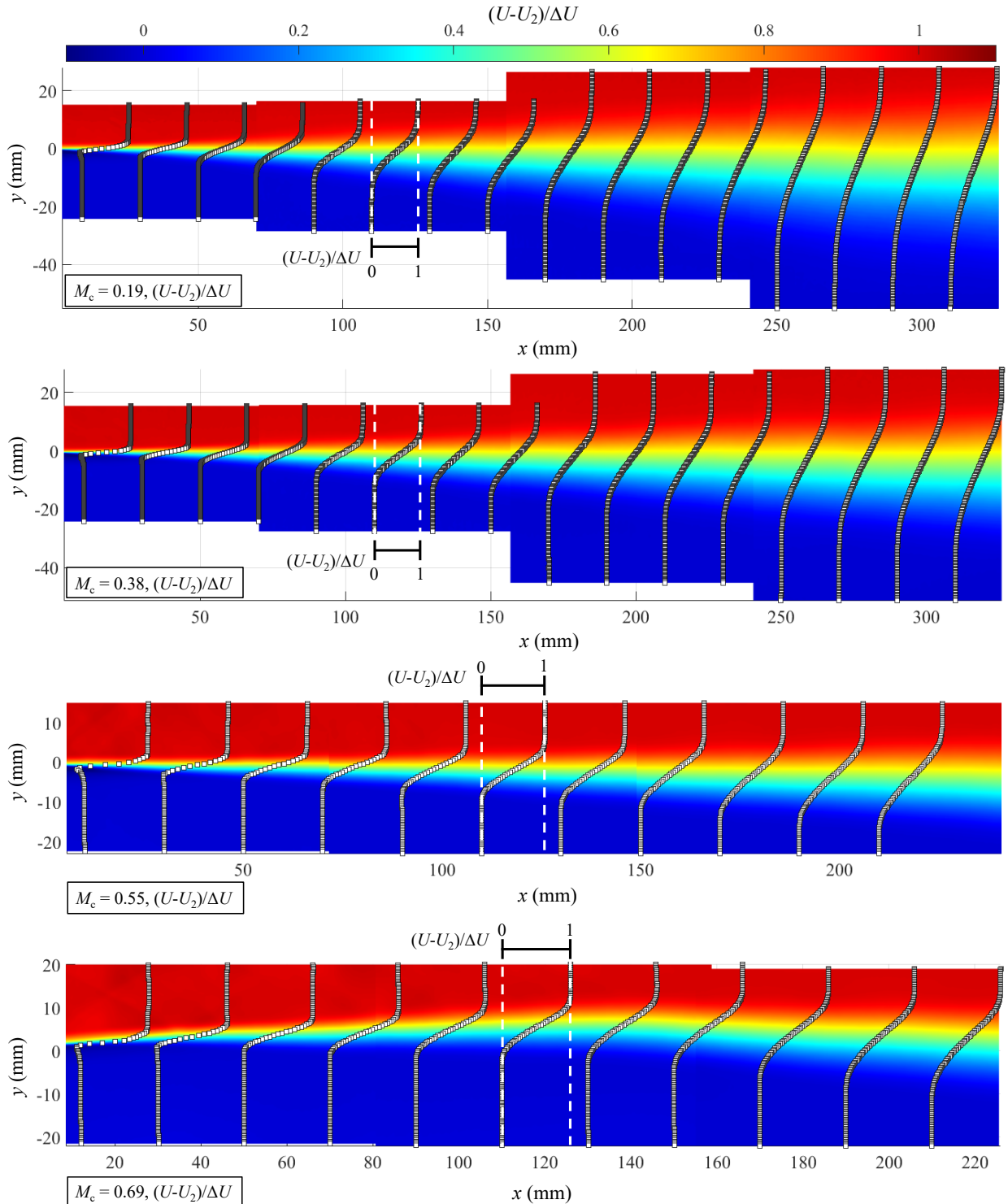


Figure 34. Streamwise development of normalized U shown as profiles overlaid on color contours for $M_c = 0.19, 0.38, 0.55, 0.69$, and 0.88 mixing layers.

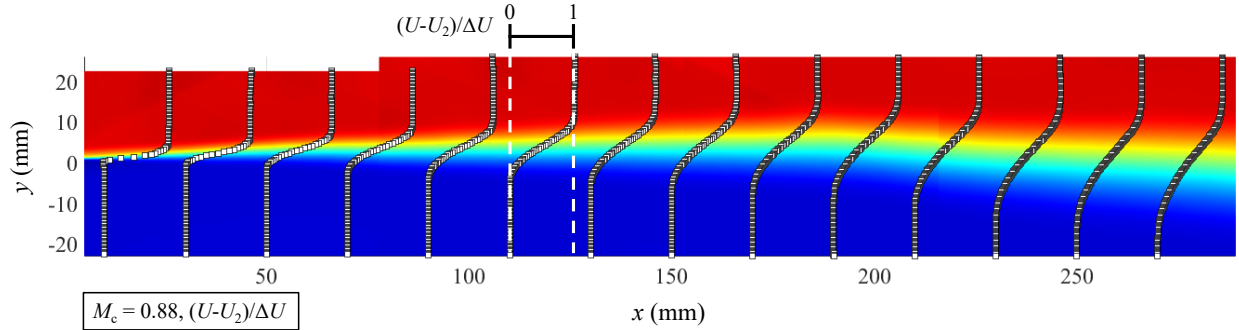


Figure 34. (cont.)

Although they are not shown here, the mean V and W fields are small everywhere for each mixing layer. In each case, the mean transverse velocity is slightly negative in the top half of the shear layer and slightly positive in the bottom half, agreeing with the understanding that there is a mean entrainment downward into the mixing layer on top, and vice-versa. The weak wave systems in the supersonic primary freestream cases can also be observed in the V fields, with the initial splitter-tip shock wave angles matching well with the corresponding primary freestream Mach angles. Mean spanwise velocity fields show no discernible flow patterns for any M_c case, as expected and desired for this planar geometry. To give a sense of the magnitudes of the V and W mean velocities, the maximum and minimum values (normalized by ΔU) for all FOVs are listed below in Table 6 for each mixing layer. The higher $V/\Delta U$ values for $M_c \geq 0.69$ are due to the supersonic wave systems, and non-zero $W/\Delta U$ can be attributed to measurement noise and uncertainty (see Section 6).

Table 6. Minimum-maximum range of $V/\Delta U$ and $W/\Delta U$ for entire dataset.

<u>$M_c = 0.19$</u>	<u>$M_c = 0.38$</u>	<u>$M_c = 0.55$</u>	<u>$M_c = 0.69$</u>	<u>$M_c = 0.88$</u>
$V/\Delta U:$ [-0.023, 0.023]	[-0.014, 0.017]	[-0.026, 0.020]	[-0.058, 0.087]	[-0.051, 0.065]
$W/\Delta U:$ [-0.066, 0.025]	[-0.042, 0.032]	[-0.015, 0.043]	[-0.025, 0.017]	[-0.037, 0.041]

Figure 35 presents profiles of turbulence kinetic energy (TKE), $k = \frac{1}{2}(\overline{u'u'} + \overline{v'v'} + \overline{w'w'})$, normalized by $(\Delta U)^2$ at the same x locations as in Figure 34. These also clearly show the growth of the mixing layer thickness, in addition to the streamwise evolution of the peak k value in the shear layer as it develops. The peak k values also show an interesting trend across the M_c range. Comprehensive Reynolds stress compressibility trends will be analyzed in a quantitative manner in Section 4. 2; however, a first-cut qualitative examination of Figure 35 reveals that the TKE

clearly decreases with increasing compressibility when scaled by $(\Delta U)^2$. This is evident both from the color contours as well as the profile heights according to the scales shown in dashed white lines. In addition, the streamwise development of the TKE for each case appears to increase at first, reach a peak, then decrease to a constant value. This result is especially evident in the $M_c = 0.69$ and 0.88 cases, where a sharp decrease in k can be seen in the mixing layer at the x -location where the initial shock reflects off the top wall and impinges back onto the shear layer, inhibiting self-similarity of the turbulence ($x \sim 140$ mm for $M_c = 0.69$ and $x \sim 175$ mm for $M_c = 0.88$). Both Figure 34 and Figure 35 confirm prior understanding that the shear layer grows faster into the secondary stream than the primary (save for the two highest M_c cases).

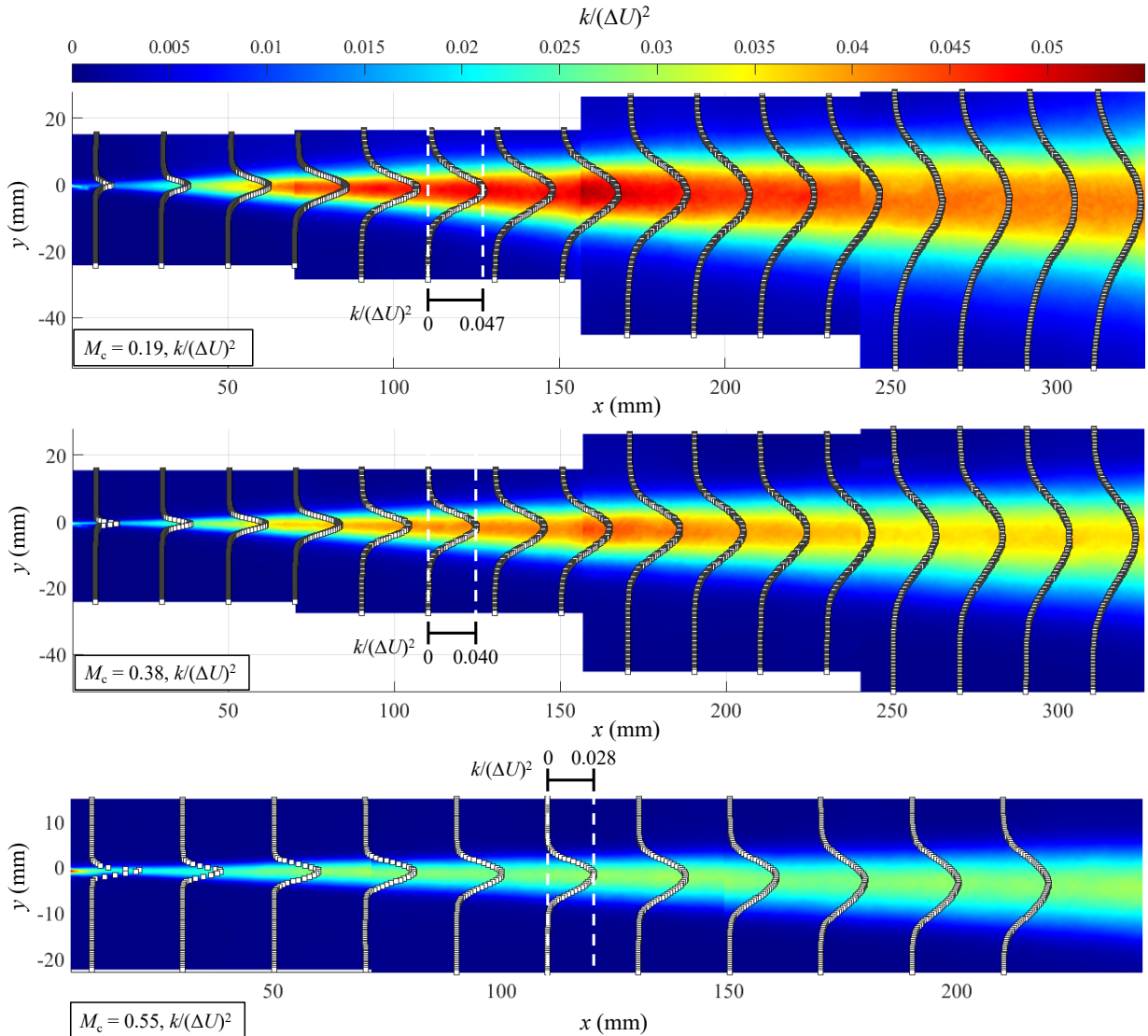


Figure 35. Streamwise development of normalized k shown as profiles overlaid on color contours for $M_c = 0.19, 0.38, 0.55, 0.69$, and 0.88 mixing layers.

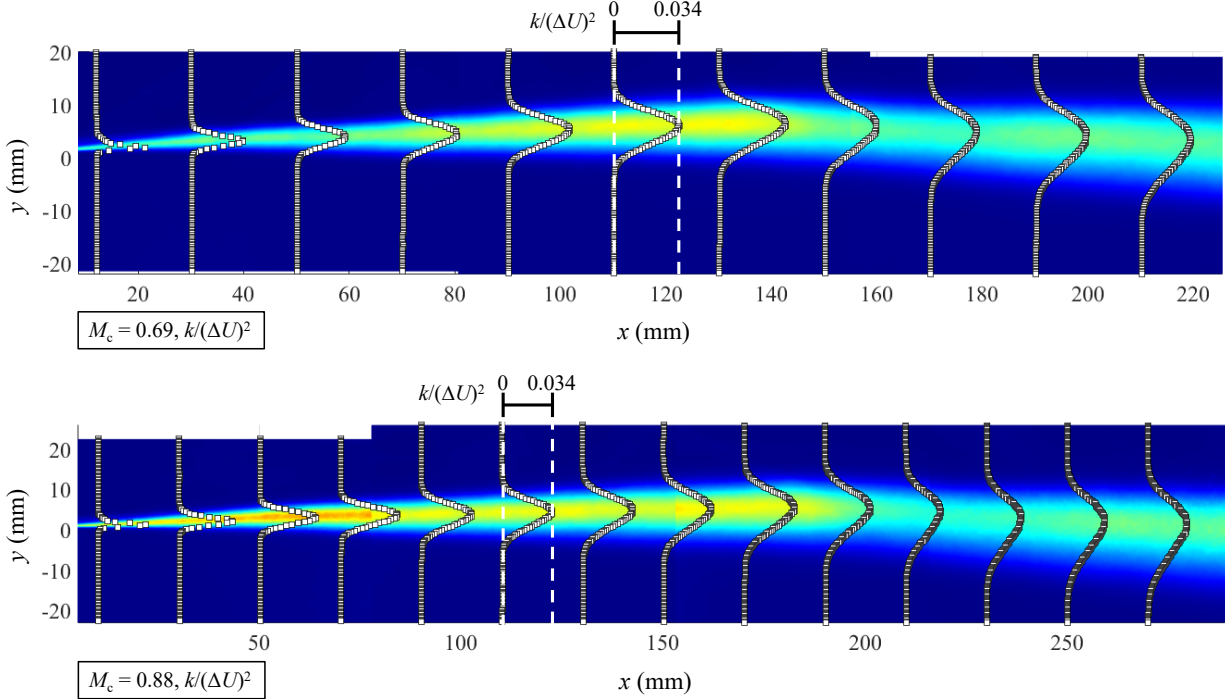


Figure 35. (cont.)

Finally, a presentation of the streamwise development of the freestream velocities is warranted to ensure that the mixing layer is subject to constant freestream conditions at its transverse edges. This is important since the mixing layer thickness, which will be presented in the next subsection, is directly determined from the local freestream velocities. Even though the static pressure was shown to be constant in the streamwise direction for each mixing layer, some total pressure losses are expected in the wind tunnel; an inspection of the freestream velocity in the streamwise direction is shown in Figure 36. For each FOV, a streamwise profile of U is acquired at the top and bottom edges of the shear layer at a constant y -location. The freestream velocities are determined by averaging U over 3 mm in the transverse direction just above and below the mixing layers where U is constant (the difference in velocity across these 3 mm is generally < 0.2 m/s). The mean velocities match up well at the right and left edges of each FOV for both U_1 and U_2 for each case. Slightly mismatched values on the edges of the FOVs are generally within the uncertainties of U_1 and U_2 , which are $\sim 4 - 6$ m/s for U_1 and $\sim 3 - 5$ m/s for U_2 for all mixing layers (see Table 4). The primary streams remain nearly constant for the streamwise extent of the shear layers, with minor non-uniformities near $x = 0$ due to the initial waves. However, the secondary velocity decreases slightly for each case from $x = 0$ to the downstream end (between 10 – 20 m/s). It appears, though,

that in the last FOV for each case, where the similarity values are reported, both streams maintain constant freestream velocities (although U_2 for $M_c = 0.19$ still drops about 10 m/s in its last FOV). The freestream velocity values in Figure 36 are used to normalize all mean and statistical velocity profiles locally (*i.e.*, at each x -location), including the profiles shown in Figure 34 and Figure 35.

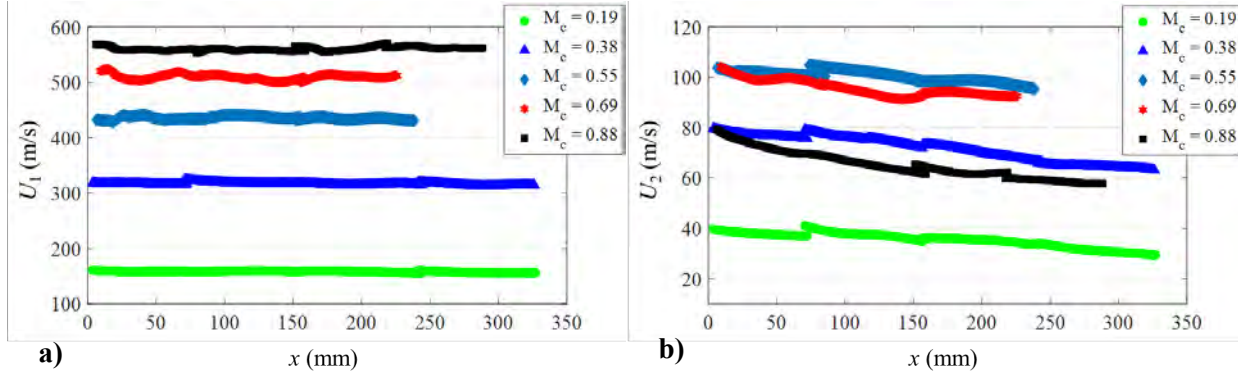


Figure 36. Streamwise development of a) primary and b) secondary freestream velocities for $M_c = 0.19, 0.38, 0.55, 0.69$, and 0.88 mixing layers.

3. 5. 3. Growth Rate

To demonstrate the linear growth of the shear layer, the $10\% \Delta U$ thickness (b) is plotted against streamwise location in Figure 37 for all five mixing layer cases. This definition was introduced in Section 1. 2. 2 and is defined again here as the transverse width of the shear layer, $b = y_1 - y_2$, where $U(x, y_1) = (U_1 - 0.1\Delta U)$ and $U(x, y_2) = (U_2 + 0.1\Delta U)$. The axes in all five plots are set to the same range of [0 – 45 mm] for b and [0 – 330 mm] for x . As expected, all cases grow linearly after the initial developing region ($x < \sim 50$ mm) where the velocity deficit from the incoming boundary layers affect the mixing.

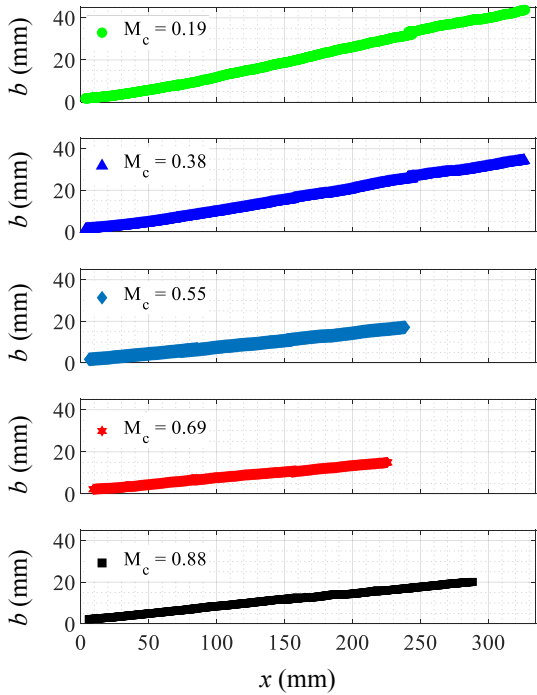


Figure 37. Shear layer 10% ΔU thickness development for all cases.

mixing layer in its respective downstream FOV can be confirmed, as the curve fit-line equation and the experimental data are directly on top of one another. The growth rate determined by the curve fits, as shown in the legends of Figure 38, are 0.117, 0.095, 0.070, 0.064, and 0.066, in order of increasing M_c . Interestingly, the last, most compressible $M_c = 0.88$ case has a slightly higher growth rate than the next-most compressible $M_c = 0.69$ case. While it is expected that the calculated compressible growth rate should decrease monotonically with M_c here, the more important parameter that is generally reported in mixing layer studies is the normalized growth rate, which will be presented in Section 4. 1. There, these compressible growth rates calculated from the experiments are normalized by the corresponding incompressible growth rate at the same density (s) and velocity ratios (r) (relation introduced in Section 1. 2. 2). Thus, one can expect that the raw compressible db/dx values may not trend exactly with M_c , since the effects of r and s have not been taken into account. In fact, r remains constant at ~ 0.2 for the first four M_c cases, while it is nearly reduced by a factor of two to 0.1 for the most compressible case — certainly a possible source of explanation for this discrepancy. Furthermore, s decreases monotonically from 1 to 0.4 from $M_c = 0.19$ to 0.88, which could also play a role.

61

The growth rate of the shear layer is simply the slope of the thickness curve, db/dx , determined from a linear least-squares curve fit of the experimental data. While, as demonstrated in Figure 37, the mixing layer grows linearly for most of its streamwise extent, db/dx is determined from the most downstream FOV where all Reynolds stresses are also fully developed for consistency. The curve fit for each case can be seen in Figure 38. The high spatial resolution of the SPIV data is especially apparent in the plots here, with the single data-point markers overlapping and giving the appearance of a continuous line plot. Of course, the linear curve fit is simply an analytic expression (equation given in each legend), and thus is a continuous line plot. The linear growth of each

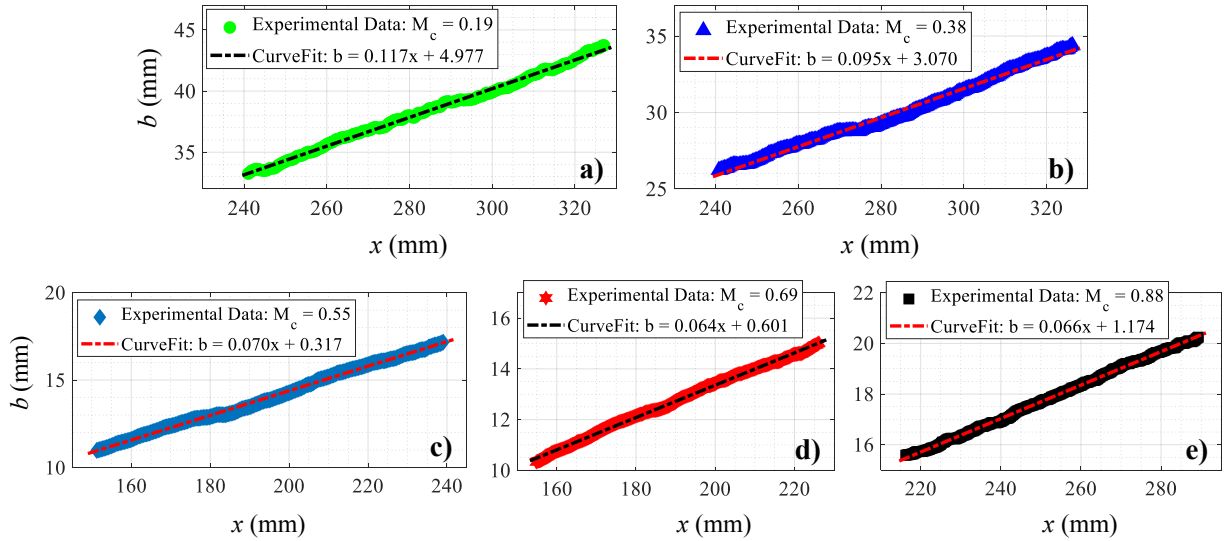


Figure 38. Growth rate curve fits for M_c = a) 0.19, b) 0.38, c) 0.55, d) 0.69, and e) 0.88 cases.

3. 5. 4. Mixing Layer Self-Similarity

The achievement of shear layer self-similarity, or fully-developed conditions, has been mentioned numerous times herein and is especially important when comparing results of different mixing layer cases across investigations. This point of discussion was prefaced in the literature review (Section 1. 2. 2) and is reinforced here, as it has been shown that the incoming flow conditions, which may vary vastly for different wind tunnels, affect the initial developing region. Therefore, in order to accurately compare shear-layer characteristics, it is necessary to realize a set of fully-developed, self-similar conditions, as outlined by Mehta and Westphal.²⁷ The three conditions are: (1) linear growth rate of the mixing layer thickness and (2) self-similar mean velocity and (3) Reynolds stress profiles (with constant peak values) when scaled by the local thickness. These criteria are necessary to ensure full self-similarity of the mixing layer, as the turbulence quantities generally require longer development lengths compared to the mean velocity.

Of the three criteria, the linear growth rates of the mixing layers were confirmed for the entirety of the most-downstream FOVs for each case in the previous section (Figure 38). In order to verify the second two criteria, a similarity coordinate transformation is applied. The variable η is introduced as the similarity coordinate and is defined as $\eta = (y - y_0)/b$, where y_0 is the mixing-layer

centerline — the midpoint between points y_1 and y_2 used to define the thickness. Clearly, η is a function of x and y since y_0 and b vary with x . However, when the mixing layer grows linearly, y_0 and b are linear functions of x ; thus, η can be used to collapse the data in the streamwise direction to verify self-similarity of a flow quantity. This is shown for U for the $M_c = 0.55$ mixing layer in Figure 39 on the right. The profiles

in dimensional form (Figure 39a) show the growth of the mixing layer thickness as it develops in the streamwise direction. When the similarity transformation is applied and U is non-dimensionalized by local ΔU (Figure 39b), the profiles downstream of $x = 80$ mm collapse identically. The aforementioned velocity deficit can be seen to affect the profiles at $x = 5$ and 20 mm; therefore, the momentum deficit caused by the incoming boundary layers is the primary inhibitor to the development of the mean velocity field. Clearly, the incoming boundary layers on the splitter plate affect the initial developing region via this deficit, and confirmation of mean velocity self-similarity is paramount when comparing different experimental works (which may vary vastly in their incoming flow conditions).

The same notion is true of the Reynolds stresses within the mixing layer; in fact, these higher-order statistical moments are far more sensitive to any disturbances that may be present in the flow (*i.e.*, waves) and require longer spatial development lengths for self-similarity than mean values. The relevant components of the Reynolds stress tensor for the planar free shear layer are the three normal stresses ($\overline{u'u'}$, $\overline{v'v'}$, and $\overline{w'w'}$) and the primary shear stress ($\overline{u'v'}$). These are given by the nomenclature Re_{ij} when normalized by $(\Delta U)^2$ throughout this dissertation (*e.g.*, $Re_{xx} = \overline{u'u'}/(\Delta U)^2$). The other two stress, $\overline{u'w'}$ and $\overline{v'w'}$ have no physical significance due to the lack of mean spanwise gradients for this geometry. As an example, the same similarity transformation (with $(\Delta U)^2$ scaling) is shown in Figure 40 for k ($M_c = 0.55$), which incorporates all three normal stress components. There, it can be seen that even at $x = 80$ mm, the peak k value is still slightly changing,

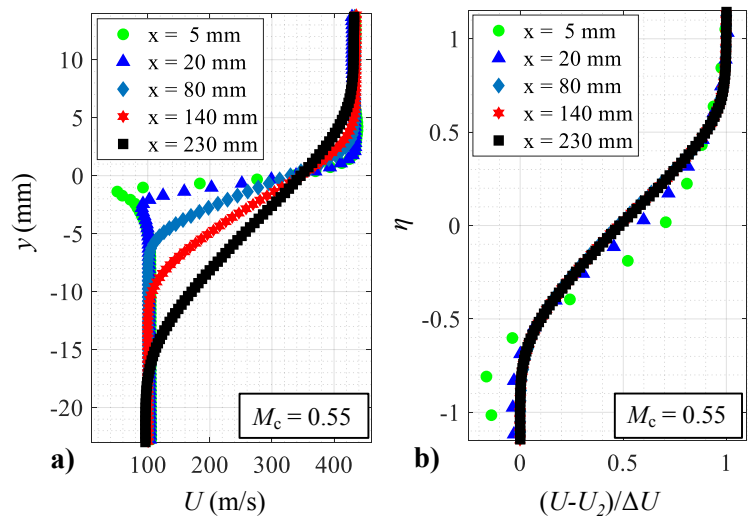


Figure 39. Similarity of U for $M_c = 0.55$ mixing layer.

and only the last two profiles are self-similar, as opposed to the last three profiles in Figure 39 for the U profiles. The profiles of each Reynolds stress component collapse identically only when their respective peak values remain constant, which warrants a close examination of the streamwise development of normalized peak stresses in the shear layer.

The evolution of Reynolds

stress tensor peak values is shown for each case in Figure 41. The angled brackets in the legend have identical meaning to the overbar and denote ensemble averaging of the quantity therein. The streamwise location at which all stress values begin to remain constant can be defined as the mixing layer development length (l_D), since by this location, the first two criteria (linear growth and self-similar mean velocity) have already been realized. l_D is indicated for each case in Figure 41 as ‘FD Region’. Mixing layer development lengths for the five cases in the present study were found to be: 290, 250, 210, 210, and 220 mm in order of increasing M_c . While, in general, l_D decreases for increasing M_c , the two highest M_c cases required additional length for development due to the impinging wave on the shear layer top-side delaying the development (with the location of impingement depending on the Mach angle of the primary freestream). This can be seen clearly in the drop-off of the blue Re_{xx} profiles for $M_c = 0.69$ and 0.88 at $x \sim 150$ and 200 mm, respectively. Normalizing l_D by the mixing layer thickness at that location can also be useful, as it gives a measure of the inverse growth rate assuming a purely linear slope with zero thickness at the splitter tip. ξ_D , defined as l_D/b_D (where b_D is $b(x = l_D)$), for the five cases in order of increasing M_c are: 7.4, 9.3, 13.8, 15.0, and 14.0. Goebel and Dutton use the Reynolds number defined by shear layer thickness, $Re_b = (\bar{\rho}(\Delta U)b_D)/\bar{\mu}$, to identify a Reynolds number-based fully-developed criterion. For their cases, they report that a value of $Re_b \sim 1 \times 10^5$ is required for self-similarity.¹⁷ Using the same definition, the values of Re_b required for fully-developed conditions of the current mixing layers, in order of increasing M_c , are: 3.1×10^5 , 4.3×10^5 , 3.2×10^5 , 3.8×10^5 , and 5.6×10^5 . This indicates that

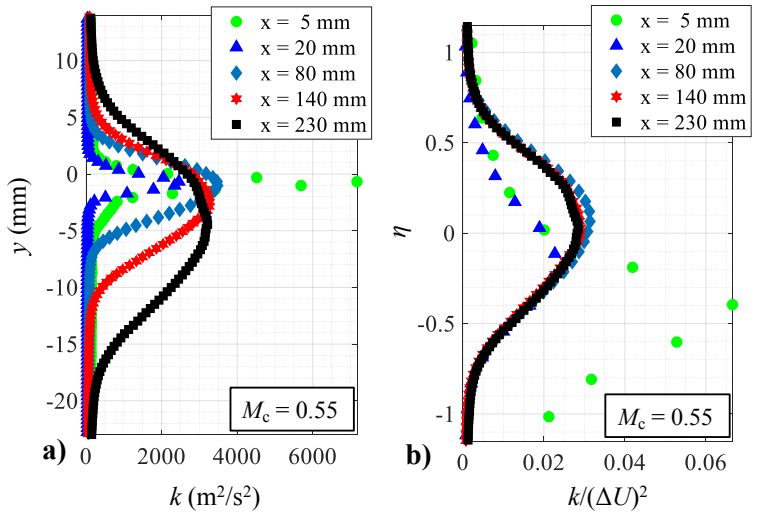


Figure 40. Similarity of k for $M_c = 0.55$ mixing layer.

a value of $Re_b \sim 3 \times 10^5$ is required for fully-developed, self-similar conditions of the present mixing layers, which is on the same order of magnitude as Goebel and Dutton's results. It is also possible that without the shock wave impinging on the two highest M_c cases here, the $Re_b = 3.8 \times 10^5$ and 5.6×10^5 values for those cases become closer to the 3×10^5 value for $M_c = 0.19$.

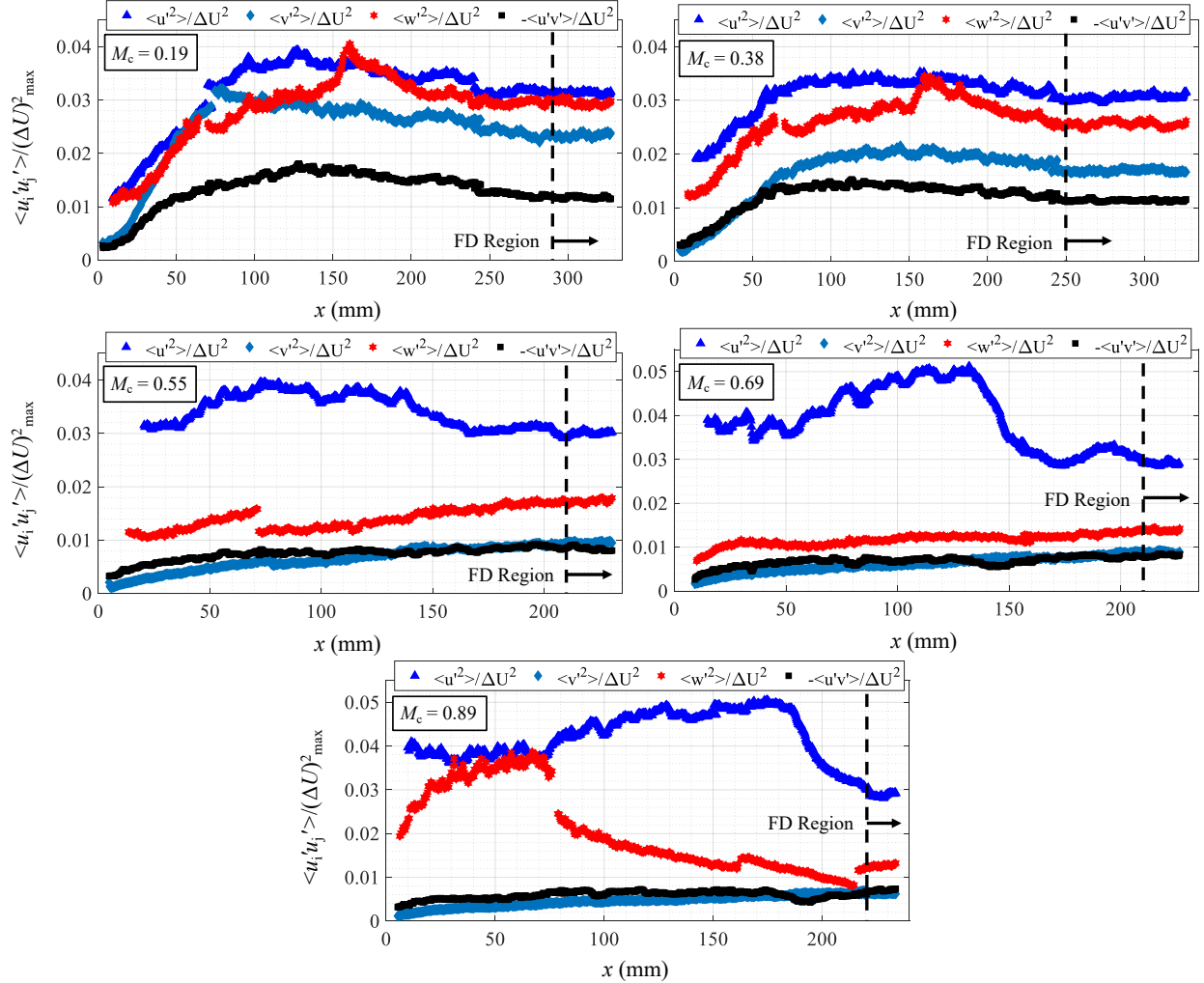


Figure 41. Peak Reynolds stress development in shear layer for $M_c = 0.19, 0.38, 0.55, 0.69$, and 0.88 cases.

While, in general, the peak values agree very well between the FOVs for each case, noticeable discontinuities of Re_{zz} peaks between the FOVs are present for $M_c = 0.55$ and $M_c = 0.88$. It is not surprising that the spanwise normal stress shows these inconsistencies, as the out-of-plane velocity component has much higher uncertainty than the in-plane components (Re_{zz} uncertainty is as high as 0.0142). The propagation of the out-of-plane errors into the fluctuating components exacerbates

the uncertainty of the spanwise normal stress and is outlined in Section 6. 2. 3. Nonetheless, a fully developed region exists for these cases where constant peaks can be seen.

Similarity profiles of each mixing layer case are shown in Figure 42 for mean streamwise velocity and in Figure 43 for the TKE. Since all three normal stresses are incorporated in the TKE, and each component's peak value was shown to be constant in the fully-developed region in Figure 41, only the TKE similarity profiles are shown for conciseness. Individual Reynolds stress profiles are shown in Section 4. 2 along with their anisotropies to examine the relative magnitudes of the three normal stresses. The primary shear stress similarity profiles are shown separately in Figure 44. As can be seen, all mean velocity and Reynolds stress similarity profiles are identical in the fully-developed region for each mixing layer case. In general, this region starts at $x = l_D$ and extends until the end of that field of view. Since each flow quantity independently satisfies self-similarity,

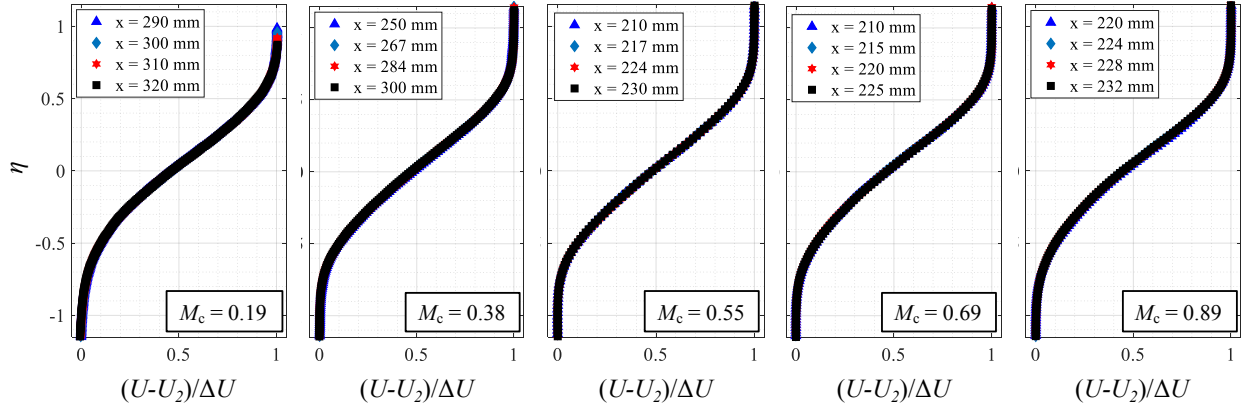


Figure 42. U velocity similarity profiles in the fully-developed region for $M_c = 0.19, 0.38, 0.55, 0.69$, and 0.88 cases.

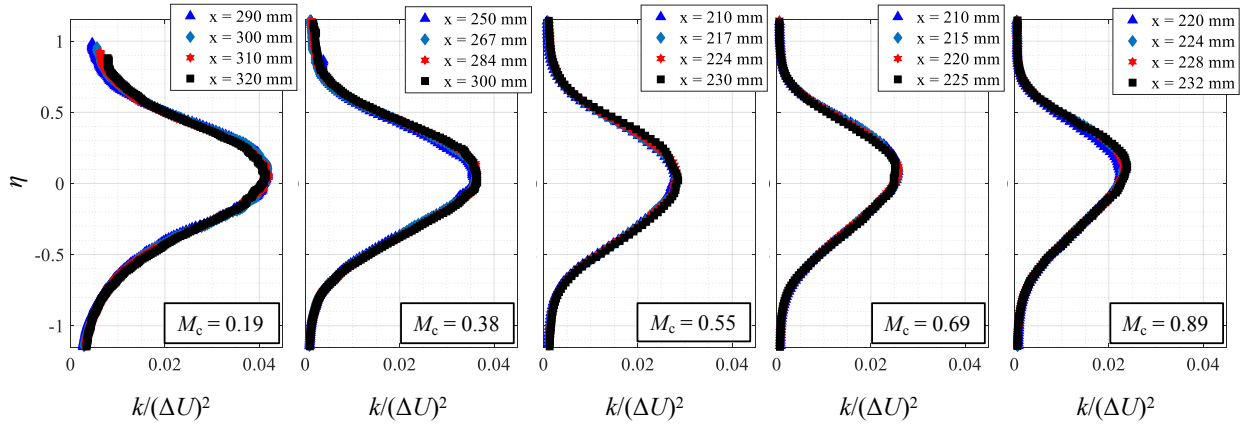


Figure 43. TKE similarity profiles in the fully-developed region for $M_c = 0.19, 0.38, 0.55, 0.69$, and 0.88 cases.

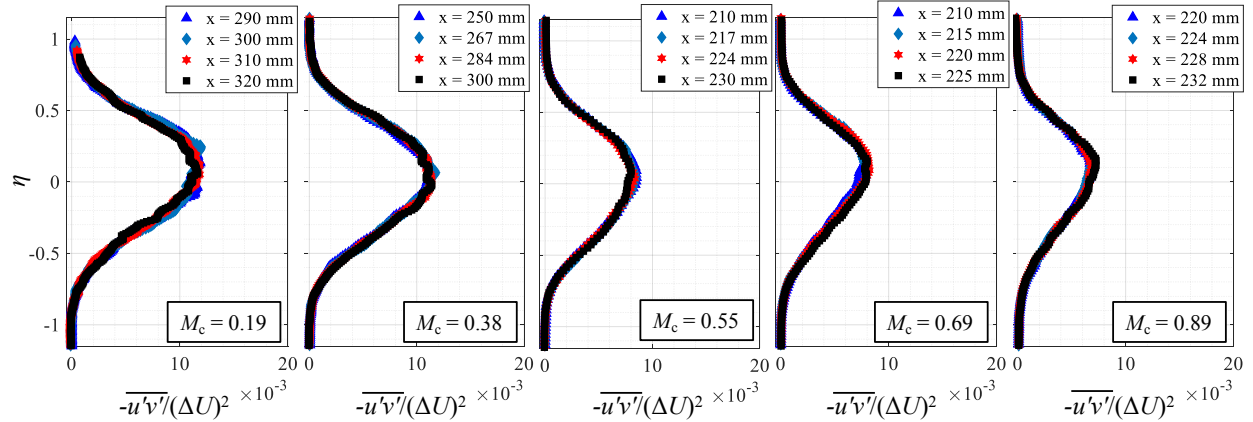


Figure 44. Reynolds shear stress similarity profiles in the fully-developed region for $M_c = 0.19$, 0.38 , 0.55 , 0.69 , and 0.88 cases.

data points downstream of $x = l_D$ can be averaged for the same η location to increase ensemble size. The first and last x -location profile plotted for each M_c case encapsulates the fully-developed region over which each similarity profile shown in future sections is averaged.

3. 6. End-View Plane SPIV Velocity Measurements

In addition to the primary side-view SPIV measurements, end-view measurements at three different x -locations were obtained for each case. The optical access for these cross-sectional views was limited by the fact that each camera had to be set up in a forward-scatter configuration, which required that they both be on the same side of the wind tunnel. Forward-scatter setups, in addition to larger-diameter seed particles (see Section 2. 2. 4), were required due to the large offset viewing angles, which in turn, required large Scheimpflug correction angles, severely impacting the signal-to-noise ratio on half of the CCD sensor. In addition, these larger-than-optimal offset viewing angles for the end-view SPIV system resulted in highly non-uniform magnification across the image sensors, which was certainly not ideal. Therefore, these y - z velocity measurements are used for qualitative purposes of investigating the flowfield rather than quantitative inspection of, say, statistical turbulence quantities. It is expected however, that these FOVs can be used to verify spanwise symmetry in the mean. Their absolute velocity values are compared to the results from the side-views to verify the measurement accuracy in the mean. Specific x -locations of these end-views are limited by the optical access granted by the window positioning and forward scatter configurations required. For $M_c = 0.19$ and 0.38 , the x -locations of the end-views are 70, 160, and 310 mm; for $M_c = 0.55$, x -locations are 70, 110, and 160 mm; and for $M_c = 0.69$ and 0.88 , x -

locations are 70, 160, and 300 mm. The reasoning behind these locations had specifically to do with how close to the upstream/downstream ends of each window position that could be successfully captured with the forward scatter configuration (*i.e.*, only the middle third of the window streamwise length could be examined).

3. 6. 1. Instantaneous Velocity Fields

Example instantaneous end-view velocity fields are shown as color contours for each component in the following figures. They are shown in Figure 45 – Figure 49 in order of increasing compressibility. First and foremost, importance is placed on the close-to-zero v and w velocity components in the freestreams for all M_c cases. This was expected from the w -velocity side-view measurements; however, verification via these independent cross-sectional FOVs further speaks to the flow symmetry. Absence of any strong waves in the supersonic primary streams in the spanwise direction is also confirmed.

For the $M_c = 0.55$, 0.69 , and 0.88 cases, inspection of the streamwise component of velocity for the most-downstream FOVs (bottom-left corner of each figure) shows that the tortuous interfaces of the mixing regions across the span closely resemble the end-view Mie scattering images in Figure 30 (Section 3. 4. 2). For the two lower M_c cases, the convoluted boundaries between the freestreams and mixing layers are also apparent, although the bulges and valleys in the most downstream FOV of the $M_c = 0.19$ and 0.38 cases are seemingly larger in spanwise width than for the downstream FOV of the higher M_c cases. This suggests that the spanwise width of the turbulent structures in the shear layer decreases with increasing M_c . Instantaneous v and w fields reveal that streamwise-oriented vortices may be present for all cases, and also support the notion that the eddies decrease in spanwise width relative to the mixing layer thickness as M_c increases (with smaller regions of positive and negative v and w for higher M_c). The streamwise length of the x -aligned vortices cannot be examined with these end views, as they are planar cross-sectional slices of the flow placed far apart. However, pressure iso-surfaces from a DNS compressible mixing layer study (Freund *et al.*) showed that thin, long streamwise vortices dominate at higher levels of compressibility.³³ The streamwise-aligned large-scale vortical structures are also studied via the proper orthogonal technique applied to these end-view velocity measurements in Section 5. 1. 2.

In addition to the turbulent structures, the growth of the mixing layer thickness for each case can be seen clearly from the velocity fields of the three x -locations presented. By the most downstream location ($x = 310$ mm) for the $M_c = 0.19$ case, the mixing layer grows to the extent that the FOV just barely captures the full thickness and both freestreams. The following section quantitatively compares mean velocity results from these end-views to the side-view data by comparing dimensional U profiles at the same x -locations. Mean shear layer thicknesses are also plotted across the span and compared to the values calculated from the side views.

Furthermore, lacking in these color contours are any apparent sidewall effects on the shear layer or either freestream in the given FOVs. While it is certainly expected that the boundary layers grow on both sidewalls and affect the mixing layer close to $z = \pm 63.5$ mm (wall locations), no obvious effects can be seen for the given FOV spanwise ranges. In general, the FOVs range a total width of at least $\sim 30 - 40$ mm (except for a few of the most-downstream locations) centered at $z = 0$, and it can therefore be said that no sidewall effects are present in the chief spanwise-central SPIV measurements shown in Section 3.5 or in any of the flow analyses that are to be presented in the following sections. One sidewall effect that would be a major issue for this investigation would be any strong shock waves induced by non-uniformities in the sidewalls for cases with a supersonic primary freestream. This, however, is shown to not be an issue with the uniformly near-zero w in the freestreams for all cases. While all the observations that can be made from the following figures are qualitative, the insights gained from these instantaneous velocity fields are still valuable.

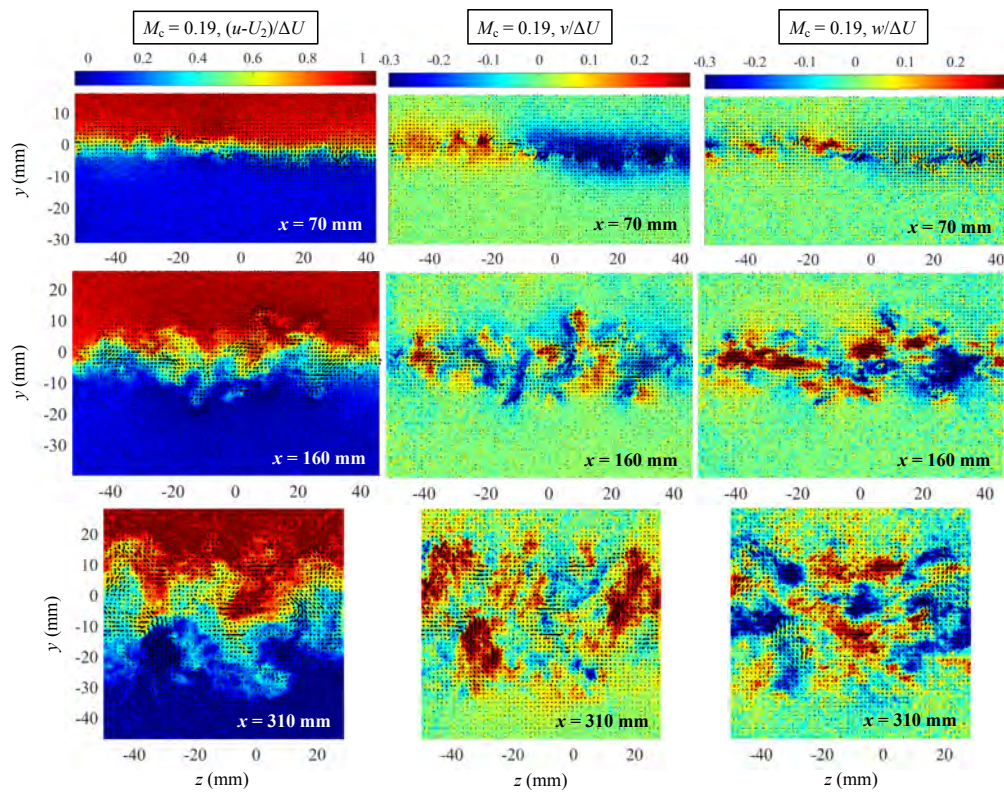


Figure 45. Instantaneous end-view velocity fields for $M_c = 0.19$.

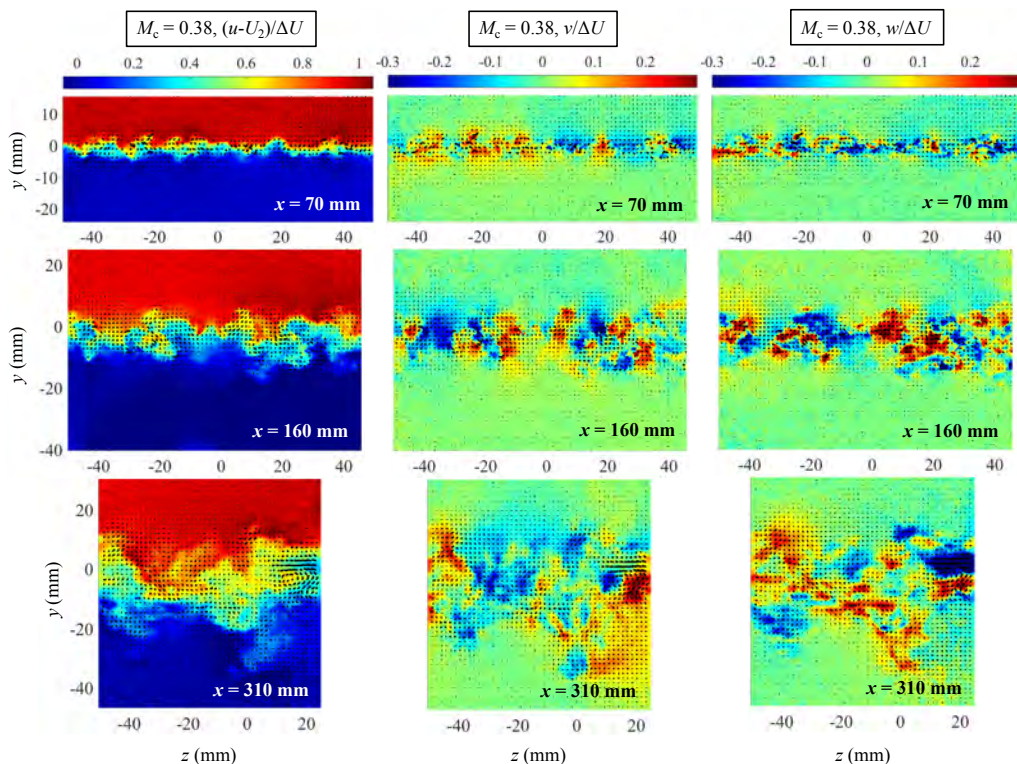


Figure 46. Instantaneous end-view velocity fields for $M_c = 0.38$.

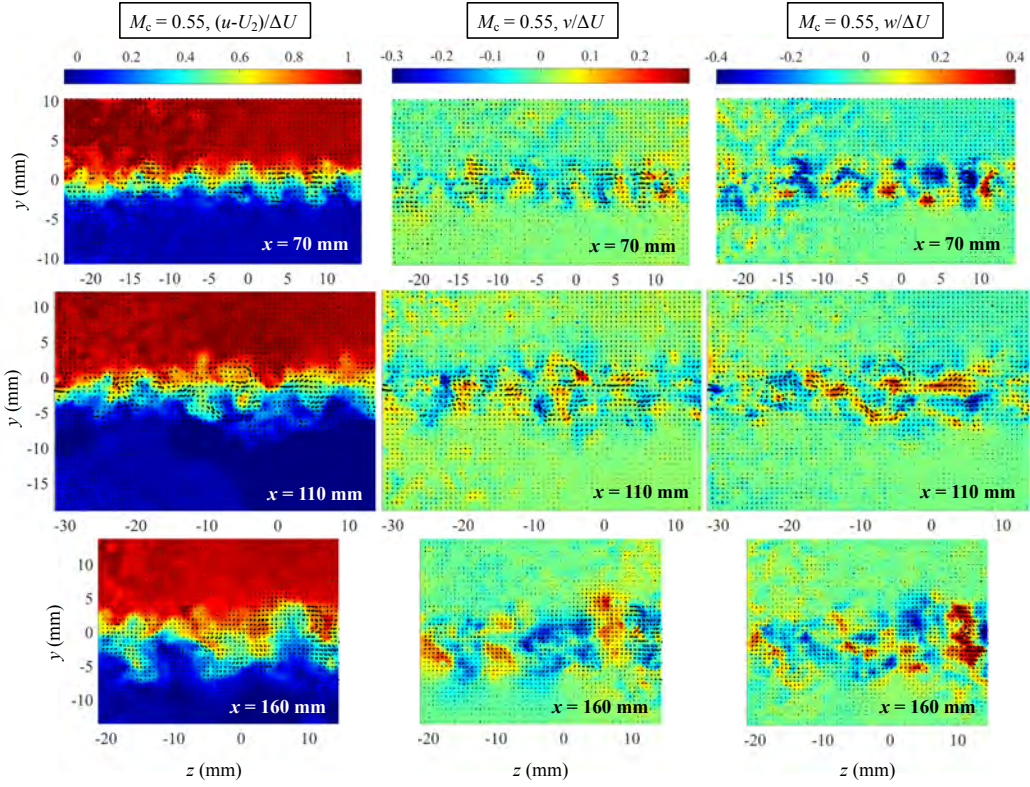


Figure 47. Instantaneous end-view velocity fields for $M_c = 0.55$.

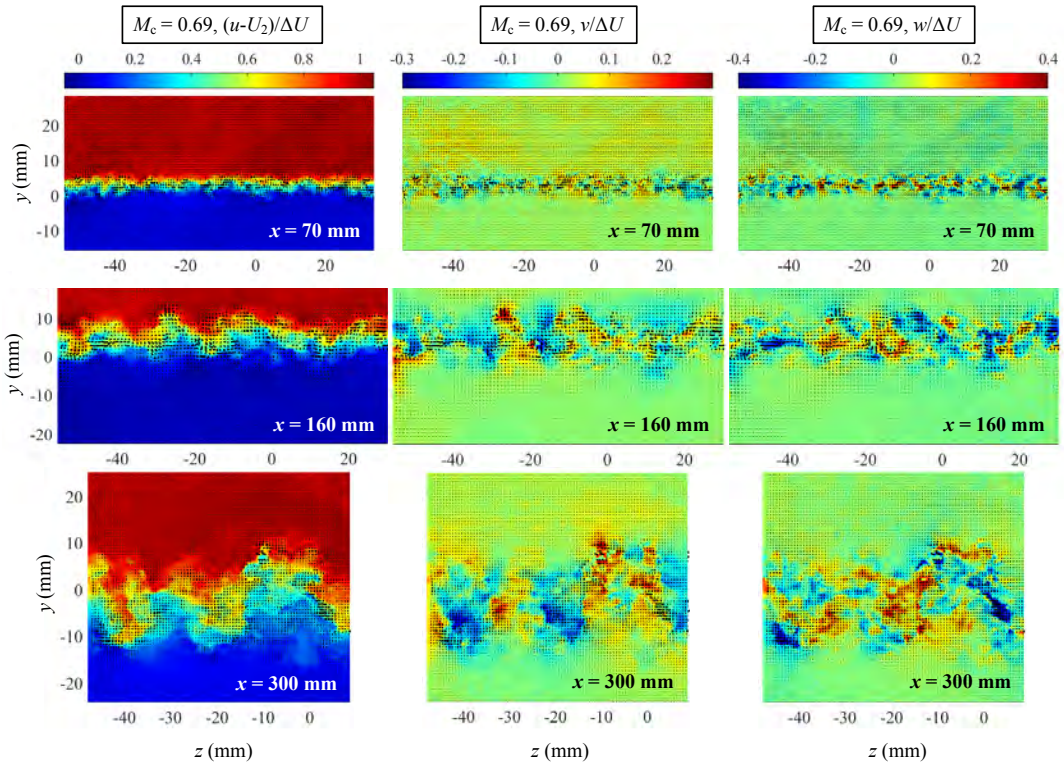


Figure 48. Instantaneous end-view velocity fields for $M_c = 0.69$.

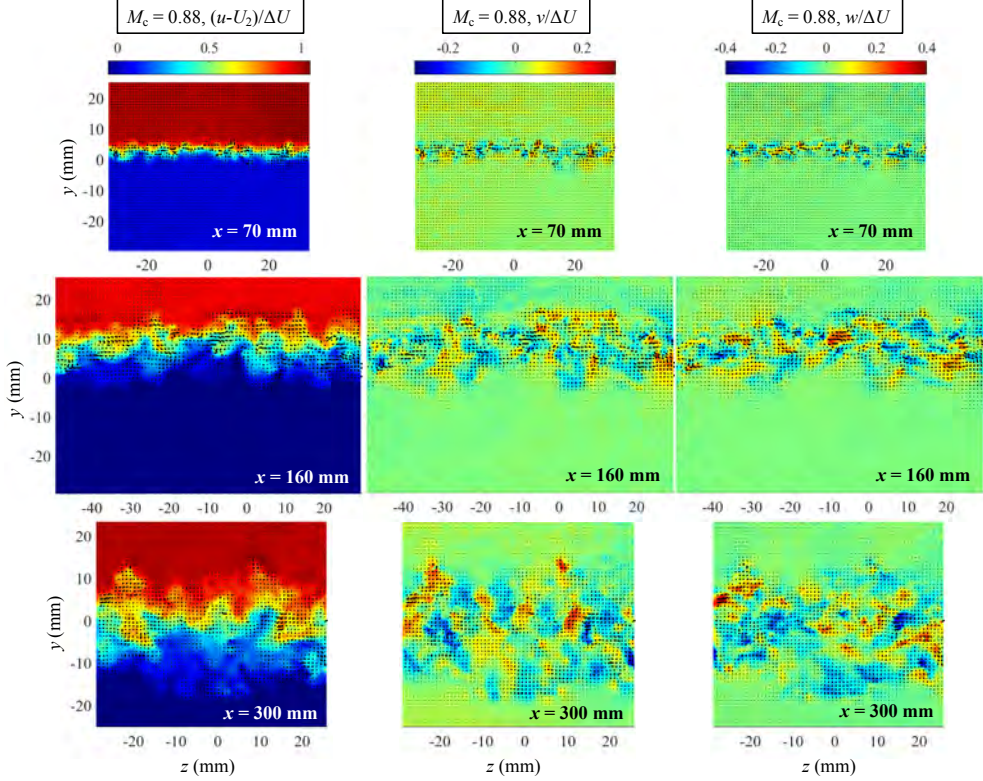


Figure 49. Instantaneous end-view velocity fields for $M_c = 0.88$.

3.6.2. Mean Velocity Results

Several mean velocity profiles are presented in this section for each mixing layer case, first to verify constant conditions across the spanwise-central plane (where the primary side-view SPIV measurements are made), then to compare the end-view results to the side-view measurements. In Figure 50 – Figure 54, the first three plots on the left show the dimensional U profiles for $z = -15$, 0, and +15 mm (with the exception of $M_c = 0.55$ at $x = 110$ mm and $M_c = 0.69$ at $x = 300$ mm, for which the FOVs did not extend to $z = +15$ mm). All profiles match well across the span when plotted as raw dimensional values, demonstrating that the shear layers are symmetric across $z = 0$ for all M_c at the given streamwise locations. As discussed, this would not be the case in the presence of any dominant spanwise waves, as the mixing layer would exhibit a kink at the location where the wave impinges on it, and profiles would not match in the transverse direction.

The plots on the right side of each figure show the dimensional U profiles from the end-views as dashed lines (at $z = 0$) and U from side-views as cross symbols, at the same x -locations. For the two highest M_c cases, the $x = 300$ mm end-view positions were unable to be compared, since the

side-view FOVs did not extend that far downstream. For all profiles shown, the secondary freestream velocities match extremely well for the two different SPIV views. The two views also match well in the primary streams for the three highest M_c cases; however, for $M_c = 0.19$ and 0.38, the end-view velocity values are consistently slightly lower than for the side views. This result is most likely due to the higher uncertainty involved with the larger particles in the end-view measurements, in addition to the lower primary freestream velocities for these cases (while the particle shift in pixels remains constant). Overall, the transverse locations of the mean velocity profiles are also in good agreement between the two different SPIV setups, indicating good repeatability of the experiments.

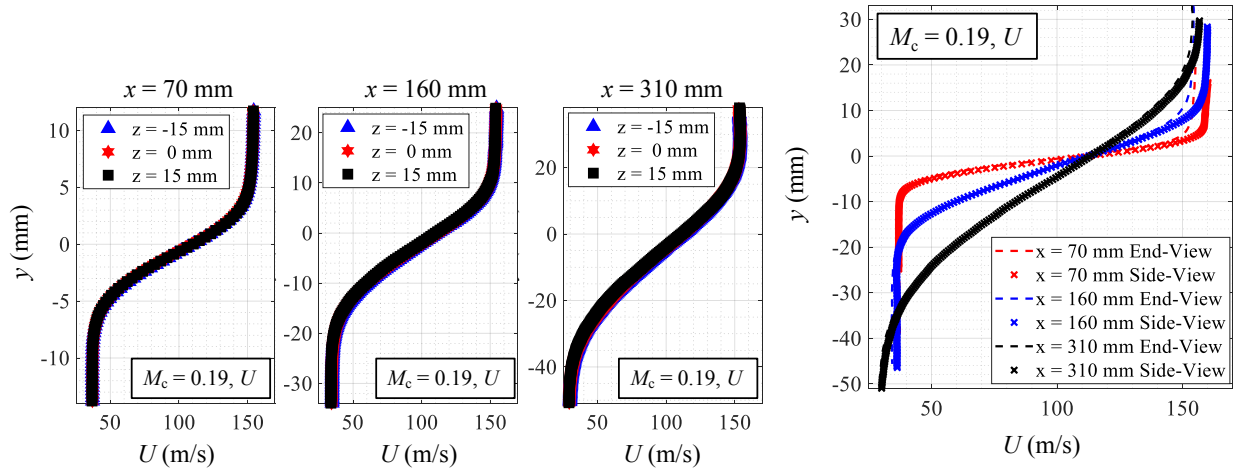


Figure 50. Dimensional U profiles at three different x -locations from end-view and side-view SPIV measurements for $M_c = 0.19$.

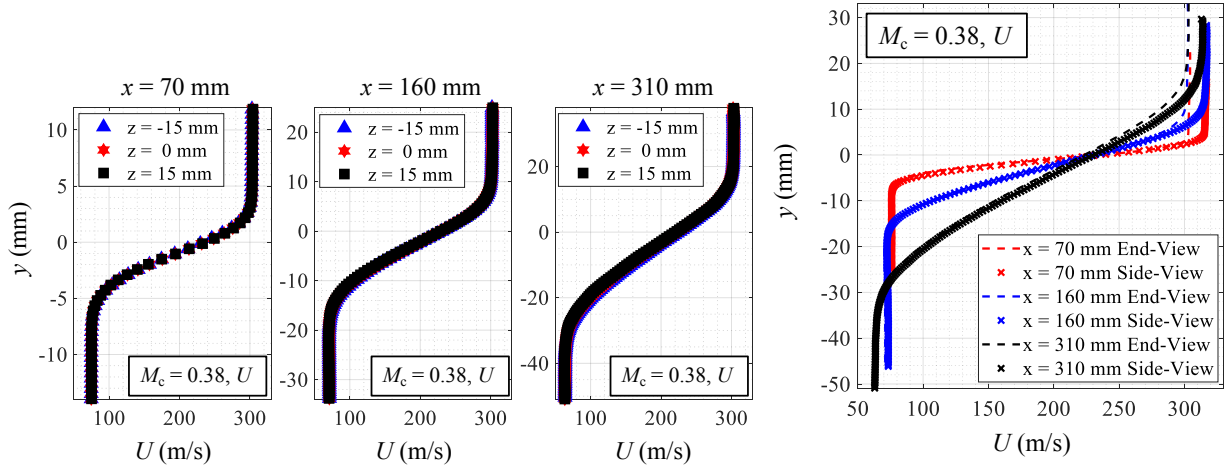


Figure 51. Dimensional U profiles at three different x -locations from end-view and side-view SPIV measurements for $M_c = 0.38$.

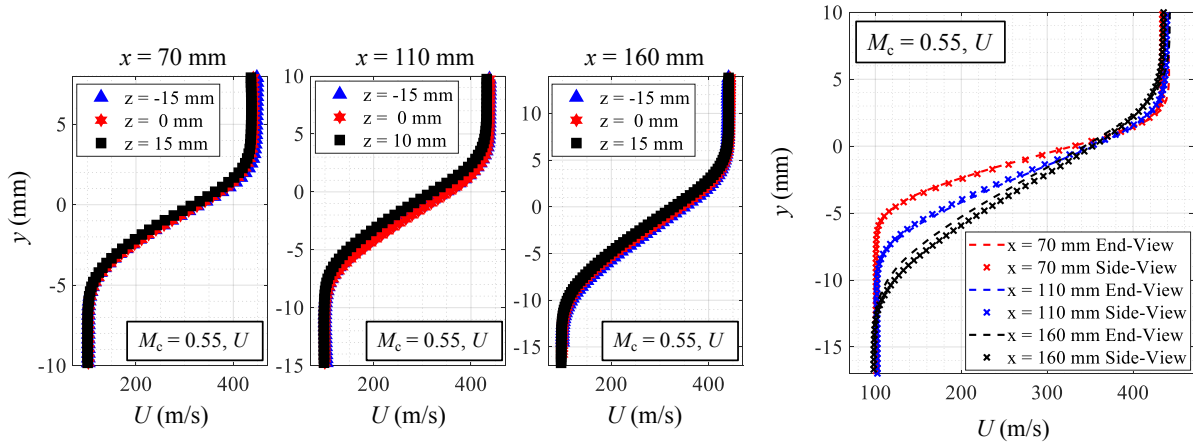


Figure 52. Dimensional U profiles at three different x -locations from end-view and side-view SPIV measurements for $M_c = 0.55$.

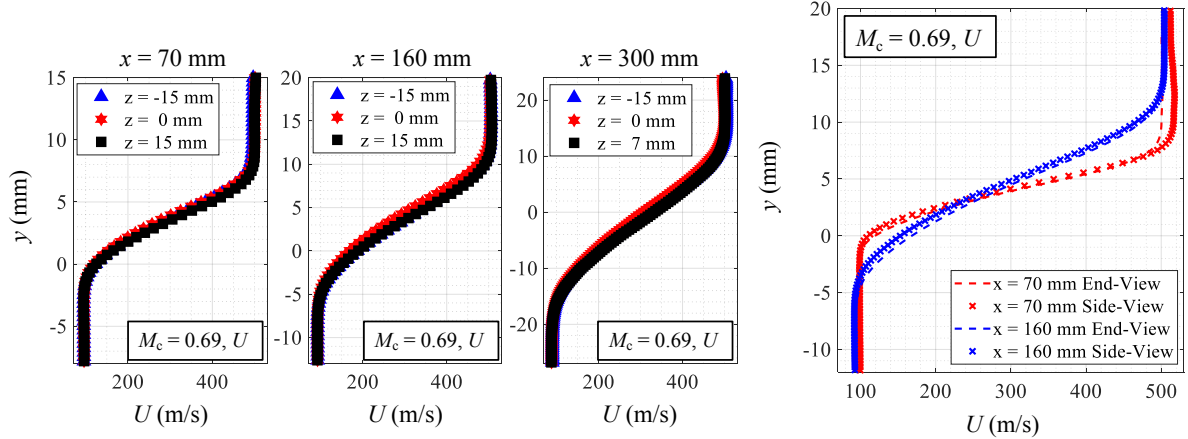


Figure 53. Dimensional U profiles at three different x -locations from end-view and side-view SPIV measurements for $M_c = 0.69$.

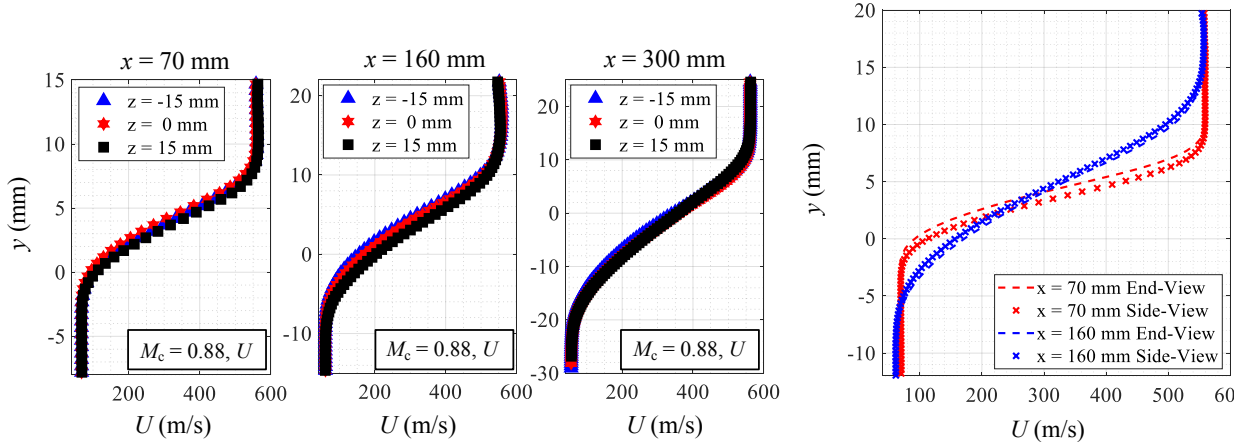


Figure 54. Dimensional U profiles at three different x -locations from end-view and side-view SPIV measurements for $M_c = 0.88$.

The spanwise variation of the mixing layer thickness is presented in Figure 55 for all five cases. Differences in the z -range plotted for each position has to do with the optical access issues that were expounded on in the previous section (*i.e.*, forward scatter requirement and window arrangements). For the ranges plotted, constant shear layer thickness across the span at each x -location is confirmed. The thicknesses calculated from the side views are plotted with green circle markers and agree very well with the end-view results. Again, the most-downstream end-view x -locations for $M_c = 0.69$ and 0.88 were not available for comparison in the side-views.

Overall, the mean results from these y - z cross-sectional planes are in good agreement with those of the side-view x - y planes and serve as redundant measurements that only add to the overall consistency of the results from these experiments. It should be noted that, given the experimental difficulties involved with these cross-sectional measurements (especially made difficult by supersonic conditions), even the agreement of mean results was considered a success. Higher-order statistical moments of the velocity fluctuations (*e.g.*, Reynolds stresses) are not presented, or expected to be correct, as the particle lag due to the significant increase in seed diameter by a factor of five (which increases the Stokes number by a factor of 25) leads to questionable particle tracking for statistical analysis of the instantaneous fluctuations.

The entire dataset for each mixing layer case has now been presented as thoroughly as possible. The subsequent sections will expand on the compressibility effects on mixing layer turbulence and the results of various flow analyses applicable to two-dimensional planar mixing layer velocity fields. In the following Section 4, various quantities are examined as a function of M_c , and an attempt to empirically determine the convective Mach number is made, since the isentropic model (Section 1.2.1, Figure 2) likely does not apply as the compressibility increases and turbulent structures become highly disorganized. In Section 5, two-dimensional proper orthogonal decomposition, linear stochastic estimation, and entrainment analyses are presented with a focus on understanding compressibility effects on the large-scale structures, and how their shapes and organization are related to the entrainment mechanisms present in the different M_c mixing layers. Comparisons to experimental and computational compressible shear layer study results are made where appropriate. Finally, Section 6 lays out a detailed uncertainty analysis of the experimental results reported in this section, including a robust SPIV uncertainty calculation based on four different error sources.

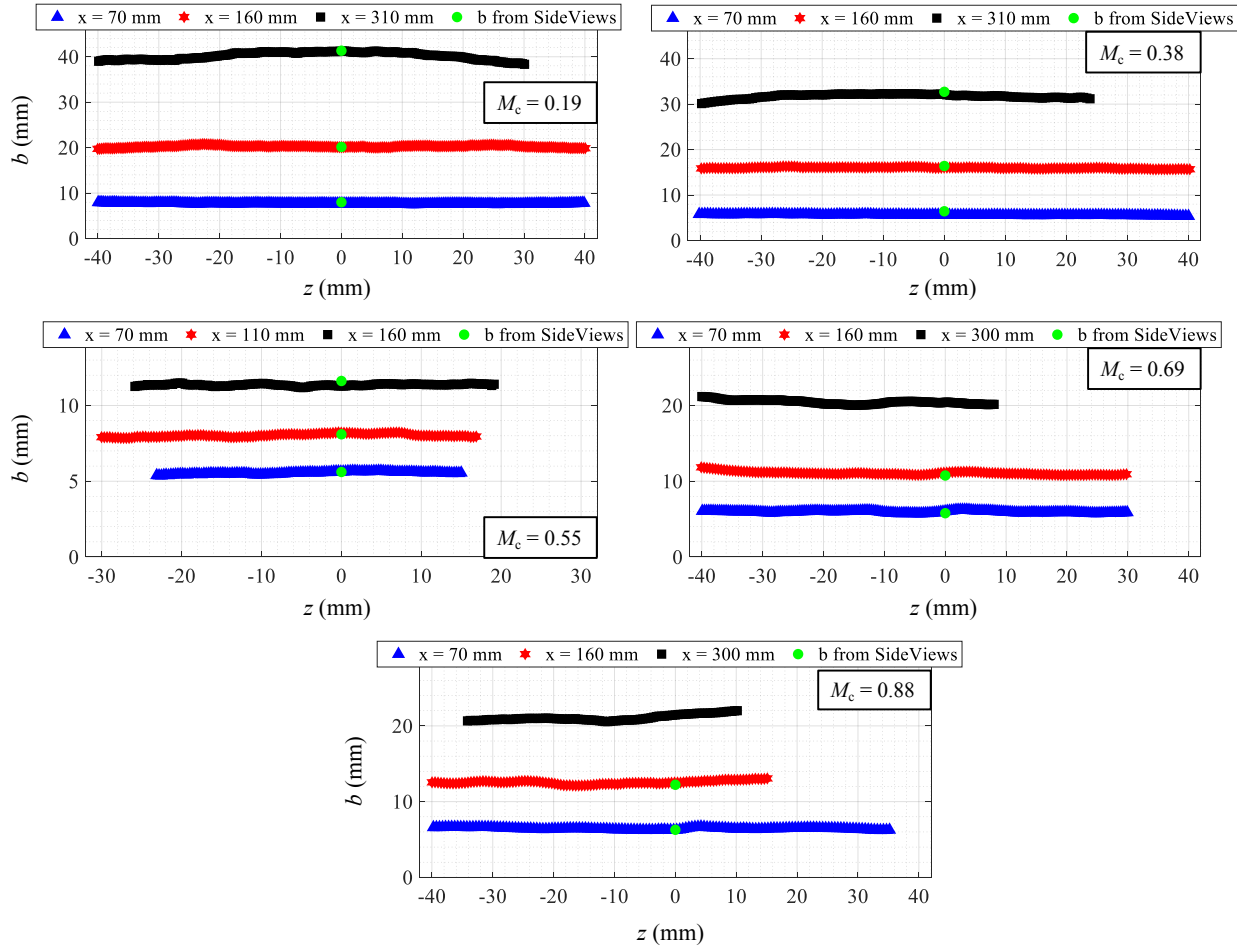


Figure 55. Mixing layer thickness spanwise variation for $M_c = 0.19, 0.38, 0.55, 0.69$, and 0.88 .

4. COMPRESSIBILITY EFFECTS ON MIXING LAYER TURBULENCE

The significance of three-component velocity measurements in compressible turbulent mixing layers was motivated at the outset of this dissertation, and further throughout. Flow visualizations show that the turbulence becomes highly three-dimensional under compressible conditions; therefore, it is imperative that all three components of velocity be analyzed when characterizing the effects of compressibility on the mixing layer turbulence. In this section, trends of mixing layer quantities such as the growth rate and peak Reynolds stresses with M_c are discussed. Other quantities relevant to compressible turbulence, such as production, turbulence length scales, and turbulence Mach numbers, are also investigated. Unless stated otherwise, all profiles of the quantities presented in this section are ensemble averaged over the fully developed region of each mixing layer, as discussed in Section 3. 5. 4.

4. 1. Mixing Layer Normalized Growth Rate

In the compressible mixing layer literature, the most commonly reported quantity, with the most widely accepted compressibility trend, is the normalized growth rate. As stated in Section 3. 5. 3, the experimentally determined growth rate of a compressible mixing layer can be normalized by the analytical expression derived by Papamoschou and Roshko,⁹ given in Equation (15), with the constant for the 10% ΔU thickness definition determined by Goebel and Dutton to be 0.165/2.¹⁷ This normalization emphasizes the net effects of compressibility, as the analytical expression in Equation (15) represents the growth rate of an incompressible mixing layer at the same velocity and density ratios. Thus, the effects of compressibility are highlighted, with variability from r and s taken into account. Values far from unity indicate that there are physical mechanisms other than differences in the velocity and density across two streams that are inhibiting the growth of the shear layer. The normalized growth rates (plotted on the y -axis and denoted by an asterisk) are plotted in Figure 56 for the current experiments along with results of other experiments from the literature.

Clearly, there is a reduction of the normalized growth rate with increasing M_c . This trend is observed by all experimentalists, and although not shown here, is agreed upon by several direct numerical simulation (DNS) results as well.^{33, 37, 39} Findings from the computations have been

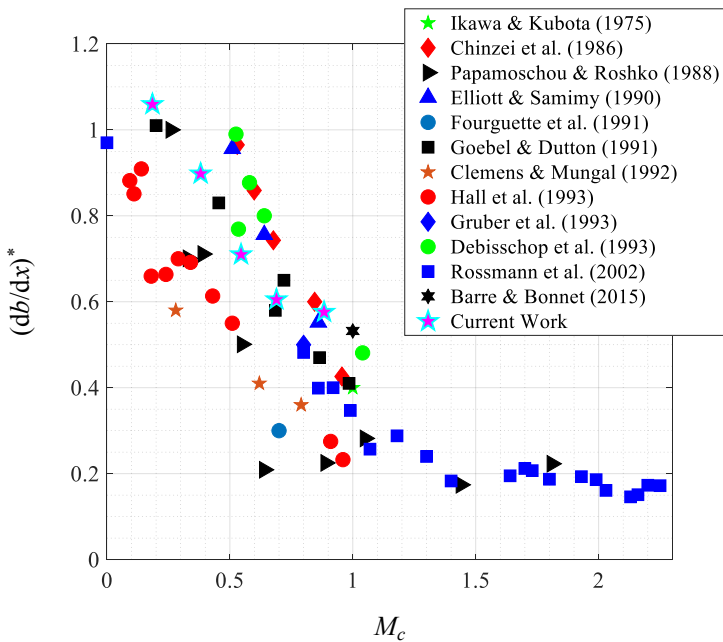


Figure 56. Normalized mixing layer growth rate vs. M_c .^{9, 17-24, 28, 30, 55}

be examined in Section 4.4. In addition, the qualitative observation that the large-scale turbulent structures become stretched in the streamwise direction with increased compressibility likely contributes to the inhibited mixing in the transverse direction, which would also reduce the growth rate. As for the current experimental results, they are in good agreement with the previous works and are generally in the middle of the data for $0.2 \leq M_c \leq 0.9$.

The decrease in growth rate is associated with the entrainment of freestream fluid into the mixing layer, as that is the physical mechanism by which the mixing layer is able to grow in the transverse direction as the turbulent region thickens. The different mechanisms for entrainment (*i.e.*, small-scale ‘nibbling’ vs. large-scale ‘engulfment’) are expected to play roles with varying importance, depending on the level of compressibility in the shear layer. A detailed investigation of entrainment mechanisms and their trends with compressibility is presented in Section 5.3.

The scatter in the data shown in Figure 56 is not surprising when considering that various definitions of thickness and different measurement methods were used among the experimentalists. Depending on the diagnostic techniques that were performed in each experiment, growth rates were calculated from visual, vorticity, and $10\%\Delta U$ shear layer thickness definitions. When taking into account the variability of definitions, the unanimous agreement of growth rate

particularly revealing in regard to a physical explanation for this reduction in growth rate. Vreman *et al.* show that the long thought-to-be important dilatational dissipation and pressure-dilatation terms are not significant to the reduced growth rate; rather, the cause is related to the reduction of the pressure-strain correlation with increasing M_c .³⁷ This result is determined through an integrated budget analysis of the Reynolds stress transport equations and is coupled to the reduction of turbulence production, which will

reduction with increasing M_c is significant and further establishes the result as a fundamental characteristic of compressible mixing layers.

4. 2. Reynolds Stress and Anisotropy Trends

In order to understand how compressibility affects the turbulence in mixing layers, investigation of the Reynolds stress tensor is paramount, as its place in the Reynolds-averaged Navier-Stokes equations as an unclosed term remains an important thrust of predictive modeling in turbulent flows. Effects of turbulence on the mean flowfield can be traced to the Reynolds stresses;⁵⁶ thus, their compressibility trends are of interest. Since simultaneous density-velocity measurements are not available in the current study, the kinematic Reynolds stress tensor is presented herein (as was done in Section 3. 5).

As discussed in detail in Section 3. 5. 4, each component of the Reynolds stress tensor is confirmed to independently satisfy self-similarity and can therefore be ensemble averaged over its respective fully-developed location. For each Re_{ij} component, similarity profiles of all five mixing layer cases are plotted together in Figure 57. As expected, the stresses all peak near the shear layer center and drop off to near-zero values at either freestream. The peak Re_{xx} values show little change with M_c , while peak values of the Re_{yy} , Re_{zz} , and $-Re_{xy}$ profiles clearly decrease with increasing M_c . The slightly non-zero freestream Re_{xx} and Re_{zz} values shown for $M_c = 0.19$ can be attributed to measurement uncertainty and noise (see Section 6. 2. 3). All stress profiles shown in Figure 57 are statistically well-converged as indicated by their smoothness. For all mixing layer cases, ordering

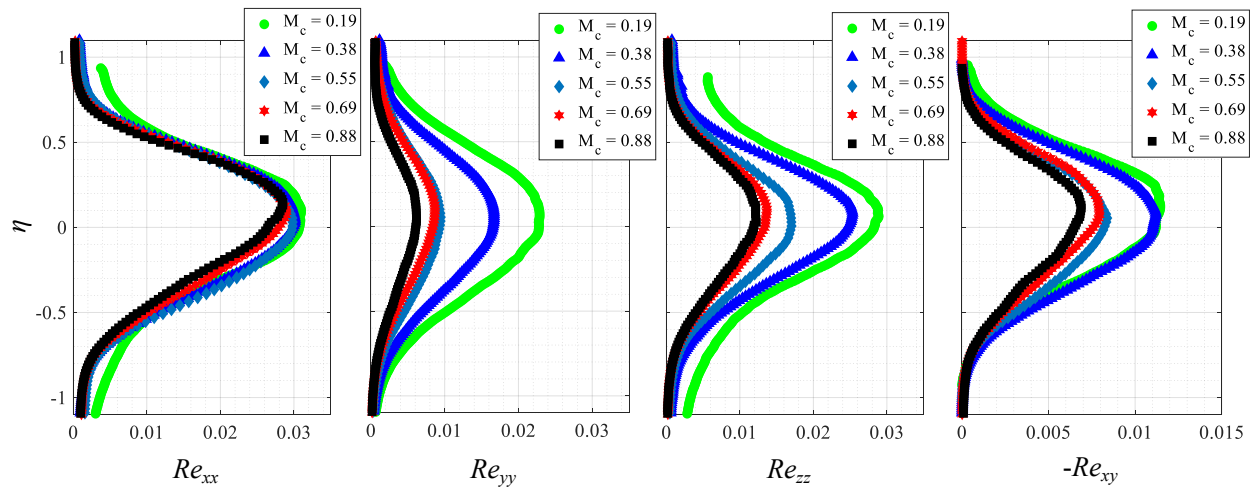


Figure 57. Re_{ij} similarity profiles for $M_c = 0.19, 0.38, 0.55, 0.69$, and 0.88 mixing layers.

of the stresses from largest in magnitude to smallest is: streamwise normal, spanwise normal, transverse normal, and primary shear stress. This ordering agrees with the two other experiments that report spanwise stress, Gruber *et al.* and Barre and Bonnet, both of whom also found Re_{zz} to be the second largest stress in magnitude after Re_{xx} .^{23, 30}

Using a similar approach to the normalized growth rate, it is common to normalize the turbulence quantities with the corresponding values for an incompressible mixing layer. Peak Reynolds stresses in incompressible mixing layers have been shown to be relatively constant over wide ranges of r and s ,¹⁷ thus, they are taken as 0.031, 0.018, 0.022, and 0.011 for Re_{xx} , Re_{yy} , Re_{zz} , and $-Re_{xy}$, respectively, from Bell and Mehta (using the same $(\Delta U)^2$ scaling).²⁶ The normalized peak stresses (compressible divided by incompressible, denoted by an asterisk) for the current cases are plotted with various experimental results from the literature in Figure 58. Due to the difficult nature of obtaining accurate, instantaneous velocity measurements in high-speed flows, the number of studies that report turbulence statistics are far fewer than that for the normalized growth rate. Results from the present study agree overall with previous works where they are available. Re_{yy} and Re_{zz} have the largest reduction with increased compressibility, while Re_{xy} has a less steep decline, and although the peak values for these three stresses decrease monotonically with increasing M_c , the trends are not linear. Conversely, peak Re_{xx} is close to constant for all levels of compressibility.

As mentioned in the Introduction, and as evidenced by Figure 58, the decreasing trends for Re_{yy} and Re_{xy} with increasing M_c have been generally agreed upon by researchers. The Re_{xx} trend, however, has not been unanimous, and results from the current experiments agree with the conclusion of Goebel and Dutton that the peak streamwise normal stress value in the mixing layer remains largely unaffected by M_c . A possible reason for the discrepancy of the Re_{xx} trend among different investigators is that the streamwise normal stress component is highly sensitive to the impinging shock wave present for the two highest M_c cases (more so than the other components, see Figure 41). While the value of peak Re_{xx} is shown to drop significantly after the impingement location for this study (and thus if values were reported prior to full development the Re_{xx} trend would increase with M_c , while other experiments report a drop in Re_{xx}), if the mixing layers in other experiments were subject to any disturbances from the supersonic primary freestreams, Re_{xx} would likely be affected the most. Thus, the importance of confirming self-similarity for each of the Reynolds stresses is once again emphasized.

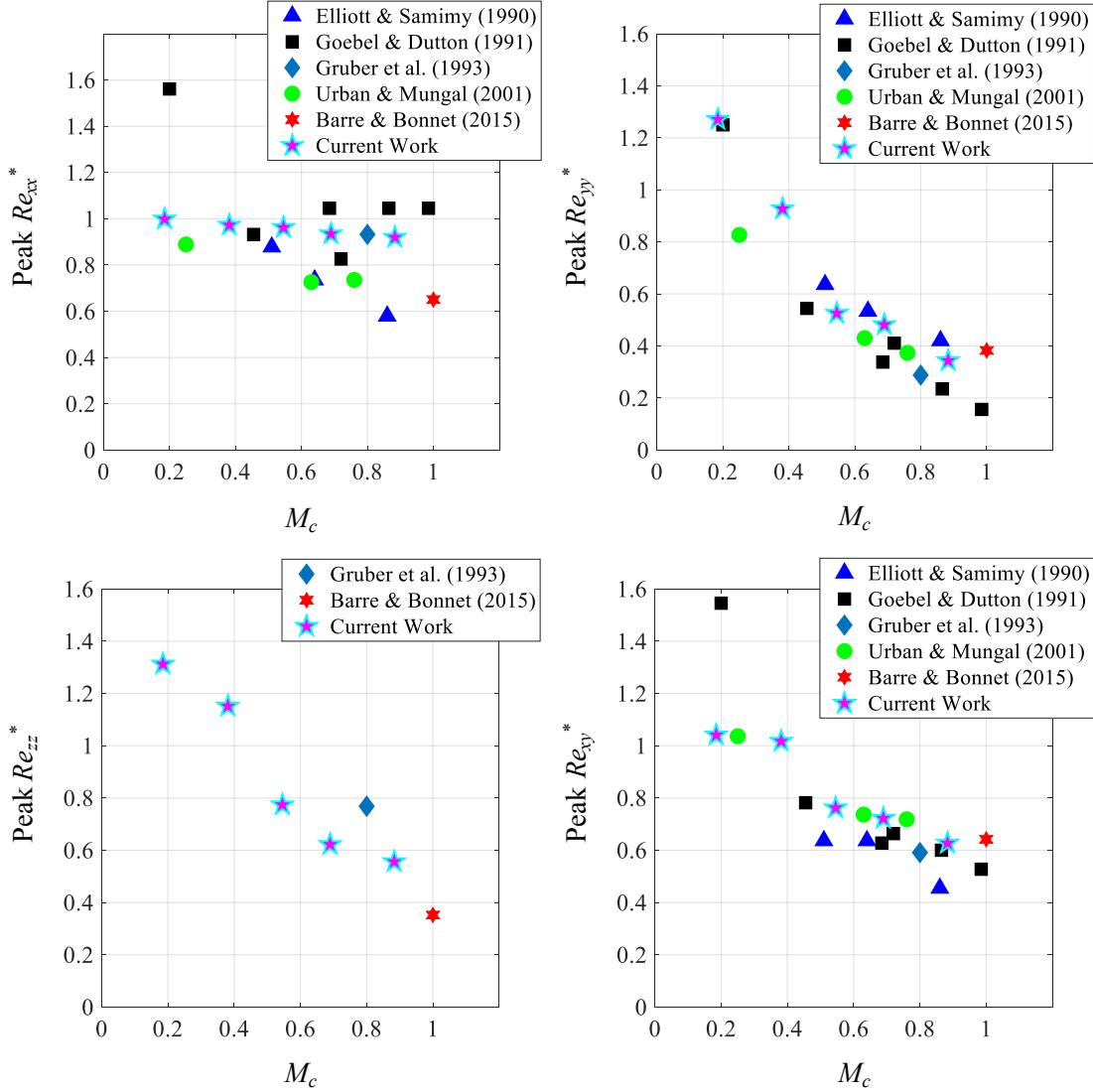


Figure 58. Normalized peak Reynolds stress values vs. M_c for current and previous experiments.^{17, 20, 23, 29, 30}

The disparity in the compressibility effects on Re_{xx} compared to the other stresses seen in this study is an important result and will have implications on many other turbulence analyses to be presented herein. A physical explanation for this finding, in line with the reduced growth rate and flow visualizations, is that as compressibility is increased and the large-scale turbulent structures become elongated in the x -direction relative to y and z (*i.e.*, flatten out longitudinally), the streamwise velocity fluctuations are preserved and remain on the same scale as in the incompressible case. In contrast, fluctuations in the transverse and spanwise directions both decrease relative to the incompressible case for increasing M_c , when scaled by $(\Delta U)^2$. This result

indicates that the streamwise velocity fluctuations in the mixing layer scale with ΔU even under compressible conditions, while fluctuations in the other directions do not.

Information about the spanwise normal stress is novel, since no previous experiment directly measures w' over a range of compressibility in the same wind tunnel facility. Though reduction of the spanwise normal stress with increasing M_c was expected from the two previous experiments that report the component, the present results give insight into the extent of reduction at various levels of compressibility over a fairly wide M_c range.

An advantage of acquiring all three normal stress components is the ability to calculate the full Reynolds stress anisotropy tensor. The three-dimensional anisotropy tensor, defined in Equation (16), differs from the two-dimensional definition reported in previous experimental studies ($= (Re_{xx}/Re_{yy})^{1/2}$) and includes the spanwise normal stress in its calculation. Clearly, from the results presented thus far, spanwise fluctuations contribute a significant amount to the turbulence energy in mixing layers and are affected by compressibility. Thus, an investigation of the full three-dimensional definition is desired. In addition, further motivation for understanding how compressibility affects mixing layer turbulence anisotropy stems from the fact that some computational models use the anisotropy tensor to close the averaged equations. Vreman *et al.* were able to predict the reduced growth rate with increasing M_c using a model based on reduced pressure fluctuations, which they closed using the anisotropy of velocity fluctuations they observed.³⁷ In the equation below, c_{ij} is the Reynolds stress anisotropy tensor, k is the turbulent kinetic energy and δ_{ij} is the Kronecker delta.

$$c_{ij} = \frac{\overline{u_i' u_j'}}{2k} - \frac{\delta_{ij}}{3} \quad (16)$$

Profiles of the anisotropy tensor components are plotted across the mixing layer for each M_c case in Figure 59. c_{ij} values across the shear layer, away from the edges, remain relatively constant for all cases. This result, that there exists a region in the mixing layer across which c_{ij} remains constant, agrees with the analytical prediction of Eisfeld (2019) in incompressible mixing layers.⁵⁷ Following Hinze (1975), he uses the argument that in high Reynolds number, self-similar flows, for which the boundary layer assumptions hold (*i.e.*, flows with a thin region of velocity gradient normal to the predominant mean flow direction, such as in the planar mixing layer), there exists a layer where the turbulence production, dissipation, and pressure-strain correlation tensors in the

Reynolds stress transport equations are in equilibrium.⁵⁸ This turbulence equilibrium, in conjunction with the self-similarity condition, results in a solution form for the three budget terms that contain the same similarity profile function, $h(\eta)$, that is simply scaled by a constant factor. Since the pressure-strain correlation is a function of c_{ij} and the dissipation, which also has the same profile function, $h(\eta)$, c_{ij} must be a constant scaling factor in the region of turbulence equilibrium. The same outcome can be understood heuristically from Equation (16) as all Reynolds stress components having the same profile shape near the midpoint ($-0.25 < \eta < 0.25$), with different peak values. Interestingly, in his analysis, Eisfeld uses the condition of incompressibility to enforce an isotropic dissipation tensor, which allows for explicit formulation of the pressure-strain correlation.⁵⁷ While his analysis was performed for the incompressible limit, the profiles in Figure 59 indicate that the constant anisotropy region is present even as compressibility is increased to a fairly high level of $M_c = 0.88$.

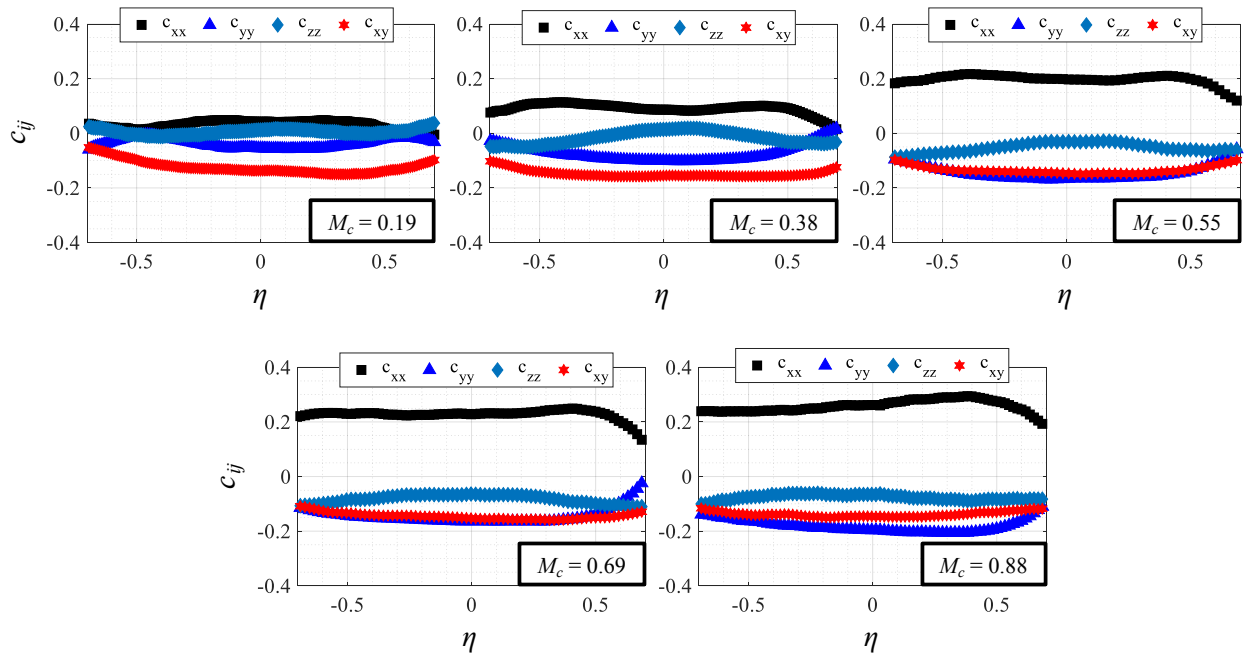


Figure 59. Anisotropy similarity profiles across shear layer.

For the lowest $M_c = 0.19$ mixing layer, the c_{ij} bands in Figure 59 are close together, indicating that all components of stress have similar levels of contribution to the overall turbulence (*i.e.*, close to isotropic). As M_c increases, however, the streamwise normal stress dominates the other components, and the c_{xx} profile increases above the other three. Thus, at higher levels of compressibility, the turbulence is clearly more anisotropic in mixing layers, and models using

isotropic assumptions will likely be increasingly inaccurate. The increase in anisotropy can be easily understood from the stress profiles in Figure 57, since the peak for Re_{xx} remains constant, while peaks for Re_{yy} , Re_{zz} , and $-Re_{xy}$ all decrease with increasing M_c . To the author's knowledge, the current experimental measurements are the first to conclusively show the increase in mixing layer turbulence anisotropy with increasing compressibility over a range of M_c cases, due to the lack of previous three-dimensional velocity measurements.

The average values of anisotropy across the shear layer center ($-0.25 < \eta < 0.25$) for the various cases are plotted against convective Mach number in Figure 60. As M_c increases, the streamwise normal anisotropy increases, transverse normal and spanwise normal anisotropies decrease, and the primary shear stress anisotropy remains constant, as expected from Figure 59. From the definition of c_{ij} in Equation (16), these trends indicate that as compressibility is increased, Re_{xx} begins to dominate compared to the average of the three normal stresses ($= (2/3)k$), while Re_{yy} and Re_{zz} become smaller than the average normal stress. The fairly constant c_{xy} trend shows that, when normalized by k , Re_{xy} remains constant for varying M_c . A lack of spanwise turbulence statistics (for multiple M_c) in the literature makes it difficult to compare the obtained anisotropy results to previous experimental work.

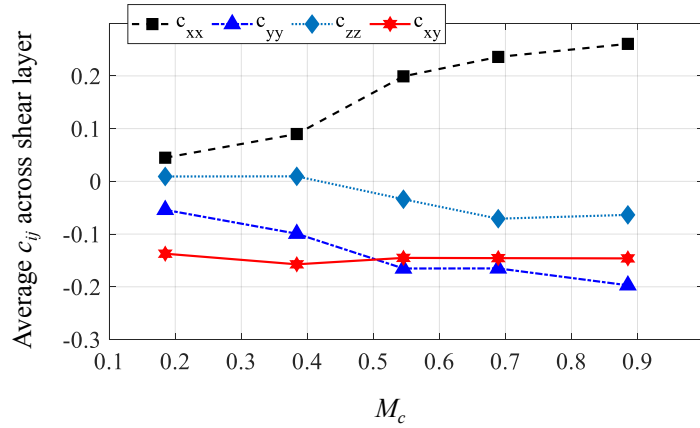


Figure 60. Average anisotropy value across shear layer center ($-0.25 < \eta < 0.25$) vs. M_c .

The DNS investigations of Vreman *et al.*, Freund *et al.*, and Pantano and Sarkar, however, do report the anisotropy tensor in its full three-dimensional form. The peak Reynolds stress trends of Vreman *et al.* agree with the present study for Re_{yy} , Re_{zz} , and $-Re_{xy}$, which all decrease with increasing M_c . For Re_{xx} , they report a slight decrease in peak value with increasing M_c , which is not consistent with the present results. However, the decrease of Re_{xx} is far less than the other two

normal stresses, and they still report an increase in c_{xx} , which is in agreement with Figure 60. While not explicitly reported in their paper, their c_{yy} and c_{zz} trends would decrease according to their Reynolds stress trends, both of which also agree with the present data.³⁷ Freund *et al.* agree wholly on the compressibility effects on the entire Reynolds stress tensor, both in terms of the ordering of magnitude among components for a single case, as well as the trends of the components' peak values for varying M_c .³³ However, their shear stress anisotropy decreases with increasing M_c , which is in disagreement with the results here. This is a result of the relative magnitude of Re_{xy} decreasing compared to the sum of the normal stresses, which would be the case if the ratio was off even by a small amount. Pantano and Sarkar report constant streamwise normal anisotropy, while their transverse normal and shear stress anisotropies decrease.³⁹ Disagreement between their anisotropy trends and the current results is expected, since their Reynolds stress trends were also in disagreement. They report a decrease for all three peak normal stresses as well as the shear stress with increasing M_c . While the trends of anisotropy of the latter two DNS studies are not in exact agreement with the results here, the magnitude of all anisotropies are similar, at around $\pm 0.1 - 0.2$ (for all three DNS studies). It should be noted that these computational investigations report temporally developing mixing layer quantities, thus, required fully developed Reynolds stress and anisotropy quantities in the temporal sense (compared to the spatially fully-developed conditions here). This difference, as well as additional inconsistencies such as Freund *et al.* reporting values at a constant spatial location (as opposed to peak values) or Pantano and Sarkar reporting integrated quantities, could all certainly play a role in the discrepancies described above.

Having the full anisotropy tensor at each location allows for the analysis of its invariants in regard to the realizability constraints given by the Lumley triangle.⁵⁹ The second and third invariants of the anisotropy tensor are given as $II = -c_{ij}c_{ji}/2$ and $III = \det(c_{ij})$, respectively, with the first invariant ($I = \text{trace}(c_{ij})$) zero by definition.⁶⁰ These relations are derived from the Cayley-Hamilton theorem and are kinematically founded. From the definitions of II and III, limiting values can be found corresponding to a certain state of turbulence. The isotropic condition ($c_{ij} = 0$) is located at the origin ($II = III$), with the two equations, $III = \pm 2(-II/3)^{3/2}$, forming the axisymmetric bounds of turbulence (e.g., $c_{xy} = 0$, $c_{xx} \neq 0$, and $c_{yy} = c_{zz} \neq 0$). The two limits of these equations occur when the two equal components of normal stress dominate, leading to two-component, isotropic turbulence ($c_{xx} = 0$, $c_{yy} = c_{zz} \neq 0$), or tend toward zero leading to one-component turbulence ($c_{xx} \neq 0$, $c_{yy} = c_{zz} = 0$). The two-dimensional bound is determined as the line connecting these two

limits, $\text{III} = (-\text{II}/3 - 1/27)$, and represents the other possible turbulence states where two normal stresses are non-zero.⁵⁹ The resulting invariant mappings of all current mixing layer cases are shown in Figure 61, with the Lumley triangle boundaries labeled. For each case, the average anisotropy mapping across the shear layer ($-0.25 < \eta < 0.25$) is plotted, as in Figure 60.

The invariant mappings of the mixing layers tend toward the one-component limit of the Lumley triangle as M_c is increased. As expected, the lowest compressibility case is closest to the isotropic point (origin), and as M_c increases, the invariant mappings move toward the one-component limit along the axisymmetric bound to the right. This result is in agreement with Figure 60, as the streamwise normal stress dominates the other terms as M_c is increased. In addition, since c_{xy} is non-zero, none of the mixing layers' data points are directly on the $\text{III} = 2(-\text{II}/3)^{3/2}$ axisymmetric curve to the right. It should be noted that the Reynolds-averaged anisotropy tensor presented here does not include density in its calculations (*i.e.*, kinematic Reynolds stress is used); however, simulation data have shown that Favre-averaged and Reynolds-averaged invariant mappings in a supersonic shock/boundary layer interaction show minimal differences.⁶¹

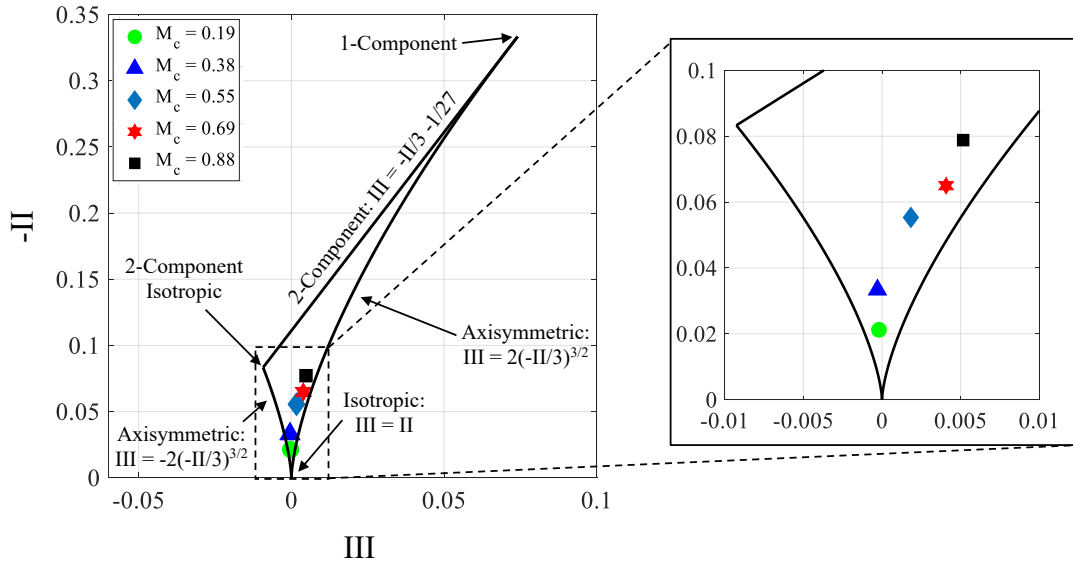


Figure 61. Reynolds stress anisotropy invariant mapping for $M_c = 0.19, 0.38, 0.55, 0.69$, and 0.88 mixing layers.

In addition to c_{ij} , the Reynolds stress correlation coefficient, defined as $-Re_{xy}/(Re_{xx} \times Re_{yy})^{1/2}$ is calculated and plotted in Figure 62. Interestingly, its average value within the shear layer (~ 0.47) is nearly constant across all M_c cases, signifying that the shear stress magnitude compared to the product of streamwise normal and transverse normal stresses remains relatively constant with M_c .

Since both Re_{xx} and the stress correlation coefficient remain constant, this indicates that Re_{xy} magnitude decreases on the order of $Re_{yy}^{1/2}$, which is also apparent in Figure 58. The values observed here for the correlation coefficient are in good agreement with previous experimental results which quote a value between 0.4 and 0.5 for all convective Mach numbers.^{17, 20}

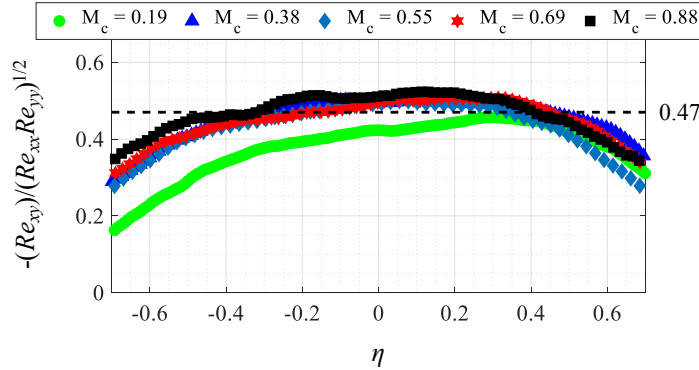


Figure 62. Reynolds stress correlation coefficient across shear layer.

4. 3. Higher-Order Velocity Statistics

In addition to the Reynolds stresses, which are second-order moments, large ensembles of instantaneous velocity measurements also allow for the calculation of third and fourth-order statistical moments of the velocity fluctuations, such as triple products, skewness, and kurtosis. An examination of these statistics can give further insight into the turbulence of mixing layers and how it is affected by compressibility. Triple products/correlations of the velocity fluctuations, defined as $\overline{u_i' u_j' u_k'}$, are important terms that appear in the Reynolds stress transport equations, and are used in numerous computational techniques that seek to model them in their solutions.⁶²⁻⁶³

Normalized triple product similarity profiles are shown for the u' and v' components in Figure 63. They all have a similar shape, with three zero crossings at the shear layer midpoint ($\eta = 0$) and the two freestreams ($\eta \sim \pm 1$). These triple product terms represent transport of the normal stresses,²⁵ and are organized into streamwise transport terms in the top row and transverse transport terms in the bottom row (each with the first fluctuation term indicating direction of transport and second squared fluctuation term indicating the normal stress component). For both the top and bottom rows in Figure 63, the triple products involving turbulent transport of streamwise normal Reynolds stress (left column), show the least amount of change with compressibility, while the transverse and spanwise normal stress transport terms (middle and right columns, respectively) show a larger

amount of reduction with increasing M_c . This is in agreement with Figure 57, where Re_{yy} decreases the most, followed by Re_{zz} for increasing M_c . The $\overline{u'^3}/(\Delta U)^3$ term remains constant on the primary side, but slightly decreases in the secondary with increasing M_c , similar to the slightly lower Re_{xx} profiles on the secondary side for higher M_c shown in Figure 57. It is difficult to say whether this decrease on the lower-speed side shown here is due to a reduction of Re_{xx} transport in the streamwise direction, or due to the reduction of Re_{xx} itself there, with increasing M_c . The $\overline{v'u'^2}/(\Delta U)^3$ term on the other hand, decreases across the entire shear layer, indicating that there is indeed decreased transport of Re_{xx} in the transverse direction for increased compressibility (since the Re_{xx} profiles in Figure 57 show no change for $\eta > 0$).

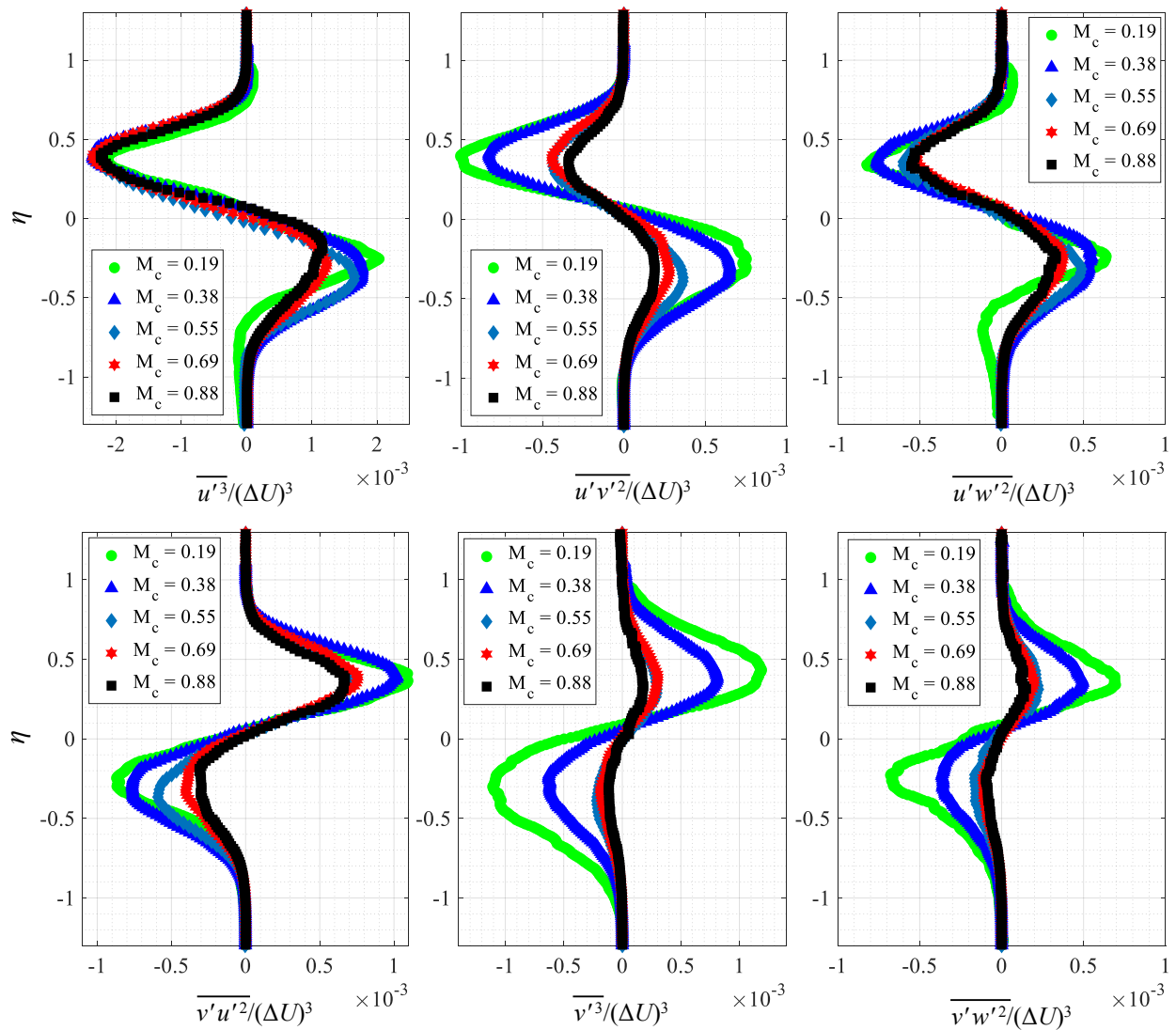


Figure 63. Normalized triple products for $M_c = 0.19, 0.38, 0.55, 0.69$, and 0.88 mixing layers.

For the terms involving the transverse and spanwise normal stresses, reduction of transport in the transverse direction ($\overline{v'^3}$ and $\overline{v'w'^2}$) is again larger than in the streamwise direction ($\overline{u'v'^2}$ and $\overline{u'w'^2}$) for the same normal stresses (for increased compressibility). Like before, in the streamwise direction, it cannot be said with certainty whether the decreasing trends observed for $\overline{u'v'^2}$ and $\overline{u'w'^2}$ are due strictly to the decrease in stress magnitudes, or if compressibility affects the streamwise transport. However, when compared to $\overline{v'^3}$ and $\overline{v'w'^2}$, it is clear that increased compressibility reduces the transport of Re_{yy} and Re_{zz} more in the transverse direction than in the streamwise. This recurring result of reduced turbulent transport of normal stresses in the transverse direction gives further insight into the reduced entrainment and growth rate in the shear layer for higher levels of compressibility.

Not shown here are the triple products involving odd powers of w' . Since these triple correlations are representative of spanwise transport of the normal stresses, they are all close to zero, as expected for this planar geometry. As with the Reynolds stresses, it should be kept in mind that the trends seen in Figure 63 are due to the $(\Delta U)^3$ normalization. Nevertheless, since only the velocity fluctuations are considered in the moments, the scaling is an appropriate one here.

In addition to triple products, skewness and kurtosis are useful quantities for statistical analysis of the velocity fluctuations. Skewness is a measure of symmetry for a given probability density function (PDF) and is defined as $\overline{u_i'^3}/(\sigma_{ui})^3$, where σ_{ui} denotes the root-mean-square of u_i' . Similarity profiles of skewness for u' , v' , and w' can be seen in Figure 64. Black dashed lines indicate the Gaussian skewness value of zero. The profiles are similar in shape to those of the third moments shown above; however, the peaks in the shear layer are at locations further away from the centerline ($|\eta| > 0.5$). The streamwise skewness is negative when $\eta > 0$ and positive when $\eta < 0$, which indicates that the tail of the u' PDF is toward the negative (left) end for $\eta > 0$ ($u' \ll 0$ more likely than $u' \gg 0$) and towards the positive end (right) for $\eta < 0$ ($u' \gg 0$ more likely than $u' \ll 0$). The signs are flipped for the transverse skewness, meaning large positive v' is more likely than large negative v' on the high-speed side and vice-versa. In contrast to the triple products, compressibility effects are more pronounced for the skewness of the streamwise velocity than for the transverse velocity. In the primary stream, peak streamwise skewness values increase in magnitude with increasing M_c , and in the secondary stream, the lowest M_c case has a much smaller peak than the others. In contrast, the transverse velocity skewness shows little change with M_c .

Spanwise velocity skewness, although fairly noisy due to its uncertainty being the highest, is essentially zero across the entire shear layer region. This shows that the direction of fluctuations is not skewed in the spanwise direction, and once again, confirms planar symmetry for z . The signs, peak locations, and magnitudes of the streamwise and transverse skewness components shown here are in good agreement with the LDV measurements of Elliott and Samimy.²⁰

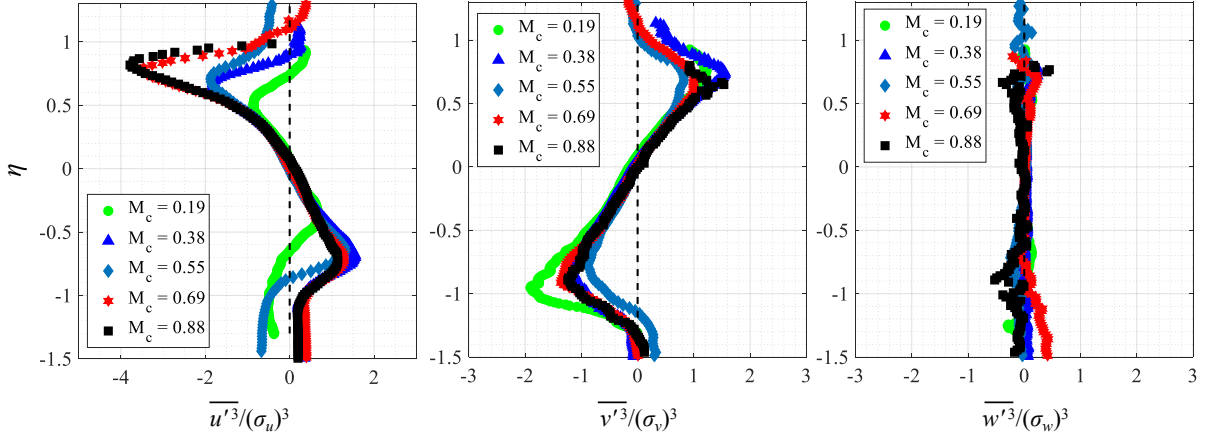


Figure 64. Skewness similarity profiles of streamwise (left), transverse (middle), and spanwise (right) velocity fluctuations in the mixing layer fully-developed regions.

Kurtosis profiles are also presented for u' , v' , and w' in Figure 65. Again, black dashed lines are drawn for all components at the Gaussian kurtosis value of three. It can be seen that near the mixing layer center and in the freestreams, the kurtosis of all three velocity components is close to the Gaussian value. Peaks of kurtosis are observed near the shear layer edges at η locations close to where the skewness also peaks. The transverse kurtosis shows wider regions of non-Gaussian values near each shear layer edge than the other two components. Since kurtosis is a measure of the probability of a fluctuation being far from the mean, the profiles are intuitively reasonable, as u' , v' , and w' are expected to deviate most from the mean near the turbulent interface between the mixing layer and freestreams.

Both skewness and kurtosis are measures of intermittency caused by the interaction of freestream fluid and turbulent structures entering and exiting the shear layer. Thus, it is expected that there are peaks near the edges of the mixing layer for both at similar η locations. As M_c increases, the peak magnitudes of both u' skewness and kurtosis show a clear increase in the primary stream, indicating higher levels of intermittency for u' for increasing M_c . While this result may be due to physical compressibility effects, it should also be noted that unavoidable waves in

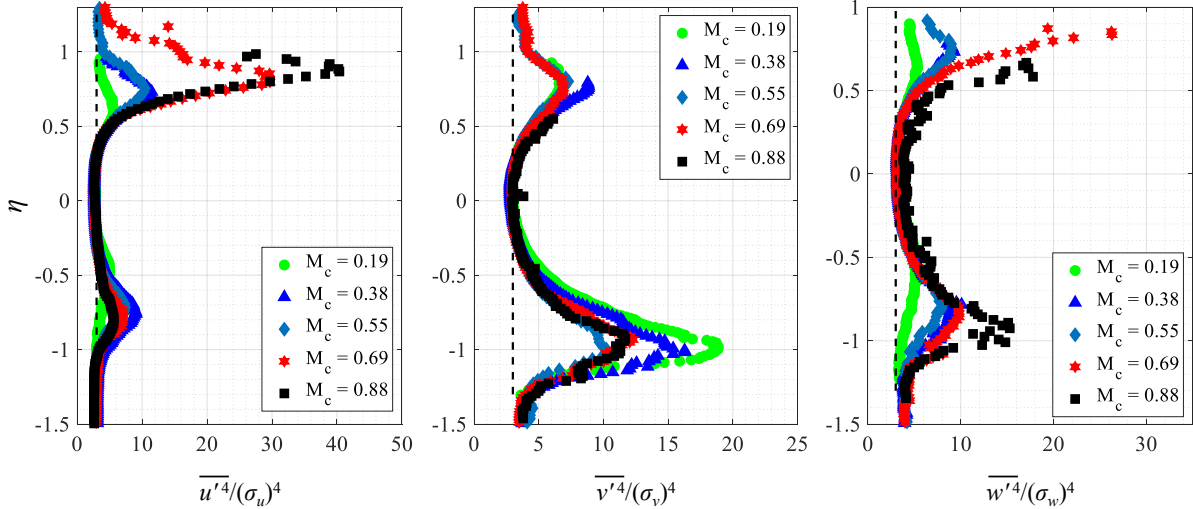


Figure 65. Kurtosis similarity profiles of streamwise (left), transverse (middle), and spanwise (right) velocity fluctuations in the mixing layer fully-developed regions.

the primary stream for the two highest M_c cases may have played a role. This is mentioned because the peaks for those two cases show a large jump from $M_c = 0.55$ to 0.69 for both u' skewness and kurtosis. v' kurtosis has higher peaks in the secondary stream for all cases, while v' skewness has approximately equal peak magnitudes in both streams and shows little change with M_c . Interestingly, the peaks of v' kurtosis in the mixing layer decreases slightly with increasing M_c , a sign that large transverse fluctuations are somewhat diminished in the secondary stream for higher levels of compressibility. In contrast, kurtosis of w' seems to increase with increasing M_c , indicating that larger spanwise fluctuations are present at higher levels of compressibility. However, these profiles are noticeably noisier (similar to w' skewness) for these higher-order statistical moments.

4. 4. Turbulence Production

An analysis of the compressibility effects on the turbulence production terms is of interest, since these are relevant to the turbulence budget analyses given in many computational studies. With knowledge of the full Reynolds stress tensor, the production P_{ij} , given in Equation (17),³³ can be calculated with minimal assumptions. The production tensor consists of the Reynolds stress and mean velocity gradient tensors, and since all Reynolds stress components are known, only the spanwise derivative components of the velocity gradient tensor are unknown. From the end-view FOV analysis given in Section 3. 6. 2, as well as the mean transverse and spanwise velocity values

given in Table 6, these can be safely assumed to be near-zero for this spanwise-symmetric geometry. Additionally, of all the terms in P_{ij} that contain a spanwise derivative, only $\overline{w'^2}(\partial\bar{w}/\partial z)$ contains a Reynolds stress component that is non-zero, further reducing the contribution from these terms. As for $\overline{w'^2}(\partial\bar{w}/\partial z)$, the mean spanwise velocity across the mixing layer is confirmed to be constant in the z -direction (and near-zero in magnitude) from transverse profiles plotted across the span-central plane with data from the end-views. Thus, all terms with non-negligible contribution to the production can be calculated here.

$$P_{ij} = -\overline{u'_i u'_k}' \frac{\partial \bar{u}_j}{\partial x_k} - \overline{u'_j u'_k}' \frac{\partial \bar{u}_i}{\partial x_k} \quad (17)$$

A close examination of Equation (17) reveals that the P_{yy} and P_{zz} components are close to zero, as the mean transverse and spanwise velocity gradients are very small for all shear layers. Therefore, the P_{xx} and P_{xy} components are the main contributors to the production, and are shown in Figure 66 for each M_c . The profiles are normalized by $(\Delta U)^3/b$ and have similar unimodal shapes to that of the Reynolds stresses, but are slightly narrower in the transverse direction due to the velocity gradient terms. Both production terms are zero by $\eta \sim \pm 0.75$. The peak magnitude of P_{xx} and P_{xy} are virtually identical for $M_c = 0.19$, a result that follows from the relation that $-2Re_{xy,peak} \sim Re_{yy,peak}$ for that case. This becomes evident when Equation (17) is expanded for each component and only the terms with $(\partial\bar{u}/\partial y)$ are considered. The expansion of P_{ij} in Cartesian coordinates and the neglected terms are shown in Appendix D.

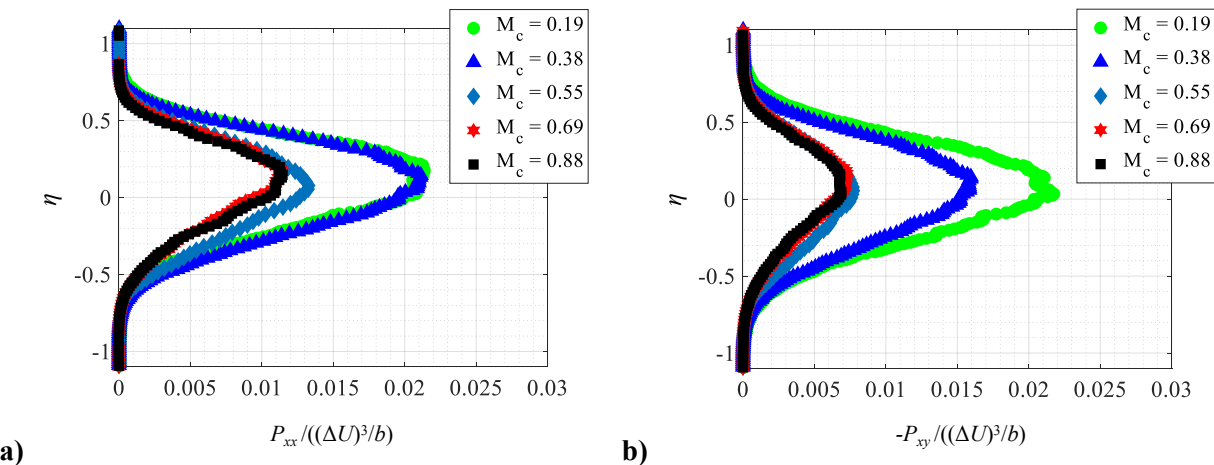


Figure 66. a) Streamwise normal and b) shear stress production for $M_c = 0.19, 0.38, 0.55, 0.69$, and 0.88 mixing layers.

Peak production magnitudes are plotted against M_c in Figure 67. Both P_{xx} and P_{xy} decrease until $M_c = 0.69$ and remain fairly constant from there, while P_{yy} is, as expected, near-zero for all M_c . Additionally, the peak production of turbulent kinetic energy is also plotted, and is given by the relation $P_k = \frac{1}{2}(P_{xx} + P_{yy} + P_{zz})$. Due to the second two terms being negligible, it is essentially $\sim P_{xx}/2$, which can be seen in the plot. Overall, the decrease of production with increasing M_c is agreed upon by DNS studies. Vreman *et al.*, Freund *et al.*, and Pantano and Sarkar all observed decreasing production terms (for streamwise normal and shear stresses), and in particular, Vreman *et al.* show very good agreement with the trend in Figure 67, as they found integrated P_{xx} and P_{xy} values to decrease until $M_c \sim 0.6$, then level off for higher M_c . P_{yy} remained at zero for all cases. Vreman *et al.* also give a relation between the production and growth rate of the mixing layer, where db/dx is proportional to the integrated P_{xx} term. Considering this relation, and examining the results for P_{xx} here, the almost identical values of P_{xx} for the last two M_c cases may be a source of explanation for the very close growth rate values calculated for these cases (Figure 56).

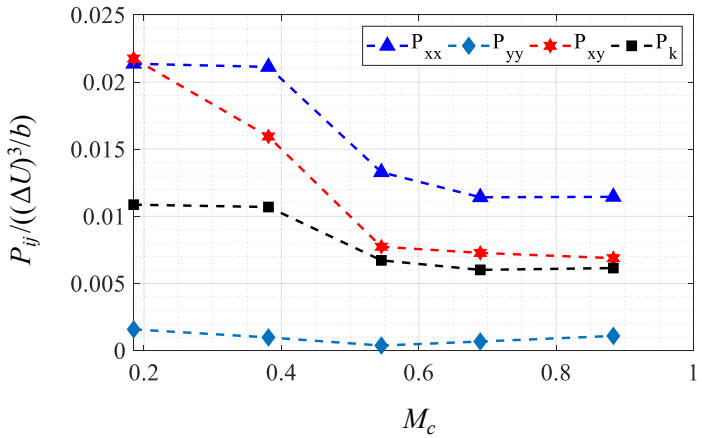


Figure 67. Peak production in the shear layer vs. M_c .

4. 5. Turbulence Length Scales

As alluded to in the discussion of instantaneous velocity fields in Section 3. 5. 1, the length scales of turbulence in the mixing layer are likely to show distinct trends with compressibility. This can also be perceived from the schlieren and Mie scattering images, as the large-scale turbulent structures clearly change shape, size, and orientation depending on the convective Mach number. Here, a quantitative evaluation of the length scales present in the x and y -directions is given for each velocity component. These analyses are performed via two-point velocity correlations and were motivated by the analogous work done by Freund *et al.*, who were able to distinctly show that the length scale of transverse velocity fluctuations decreased in the transverse direction with increasing M_c . In addition, they were able to use the newly found transverse length

scales to normalize the transverse normal and Reynolds shear stresses such that they remained constant for a wide range of compressibility.³³

The definition of the two-point velocity correlation in the transverse direction is given by Equation (18) for a velocity fluctuation component u_i' and length scale $l_{u_i'}$, with the reference point chosen denoted by the subscript ref . The same equation can be used for correlations in the streamwise direction by applying $\pm l_{u_i'}/2$ to x_{ref} instead of y_{ref} . If $l_{u_i'}$ is thought of as a typical length scale of an eddy in the x or y -direction, then the correlation value should remain above zero, or a certain threshold that may be determined empirically, for that length scale.

$$C_{u_i'} = \frac{\overline{u_i'(x_{ref}, y_{ref} + \frac{l_{u_i'}}{2}) u_i'(x_{ref}, y_{ref} - \frac{l_{u_i'}}{2})}}{\overline{u_i'(x_{ref}, y_{ref}) u_i'(x_{ref}, y_{ref})}} \quad (18)$$

The need to test various values of $l_{u_i'}$, in order to understand how the correlation decays as the points are moved away from the reference point, is apparent. In addition, the decision of where to probe in the shear layer needs to be made (*i.e.*, reference point location). For y_{ref} , the shear layer midpoint is a logical location, since, in the case that an eddy spans the entire thickness of the layer, this point will allow the correlation to capture the full extent of the eddy (based on the fixed $l_{u_i'}/2$ spacing). As for x_{ref} , the optimal location varies depending on whether $l_{u_i'}$ is being determined for the streamwise ($x_{ref} \pm l_{u_i'}/2$) or transverse ($y_{ref} \pm l_{u_i'}/2$) direction. For the former, a location near the center of each FOV is desired, as this allows for maximum $l_{u_i'}$ to be tested within the measurement domain. Thus, a range of 10 mm centered around the midpoint of each FOV was chosen and ensemble averaged. In the transverse direction, no such constraints are present. Therefore, for consistency with other analyses presented in this section, the x -location ranges the fully developed section and is ensemble averaged (resulting in the average reference location being the midpoint of the fully-developed region). Example results of correlation value versus length scale are given for the streamwise correlation of u' and transverse correlation of v' in Figure 68. Note that the length scales are normalized by the local mixing layer thickness b at the reference point for each case. For the streamwise direction, it is not surprising to see the correlation value remain above zero for large values of $l_{u_i'}$. The two points being correlated are always within the shear layer region even when they are a distance apart greater than twice the local thickness. On

the other hand, correlations in the transverse direction will go to zero within the bounds of the FOVs, since within each FOV, at least some freestream is captured on both sides. Once the points being correlated are in the freestreams, $C_{u_i'}$ goes to zero since the fluctuations are zero there.

Compressibility trends of the length scales can be deduced from Figure 68. In the streamwise direction, the u' correlations decrease at a slower rate for higher M_c , and vice-versa for v' in the transverse direction. In order to determine a length scale from Figure 68 without having to set an arbitrary fixed correlation threshold, the area under each curve is calculated by numerical integration (*i.e.*, trapezoid method) to determine an integral length scale for each velocity fluctuation in either direction.⁵⁶ Integral length scales of each velocity component are shown for the streamwise and transverse directions in Figure 69 below.

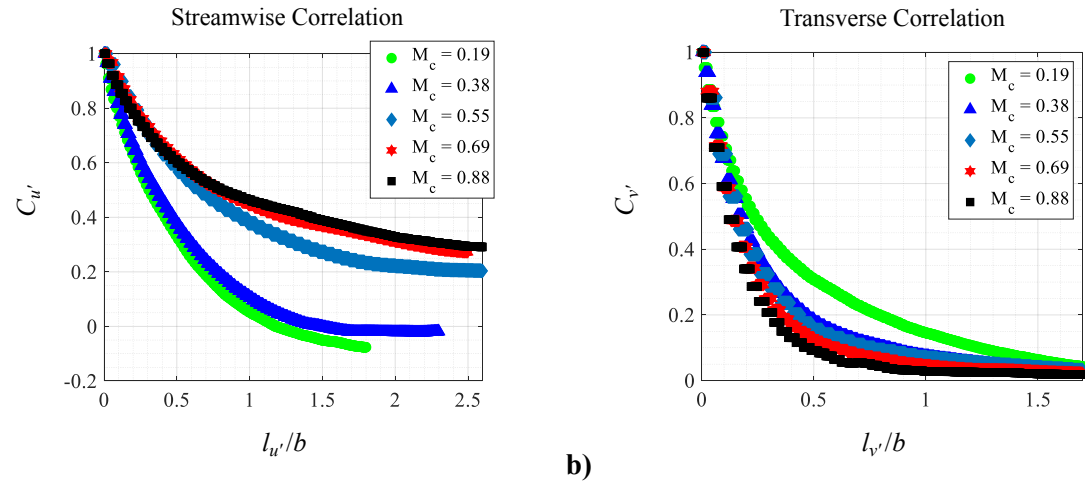


Figure 68. Two-point a) streamwise correlation of u' and b) transverse correlation of v' for $M_c = 0.19, 0.38, 0.55, 0.69$, and 0.88 mixing layers.

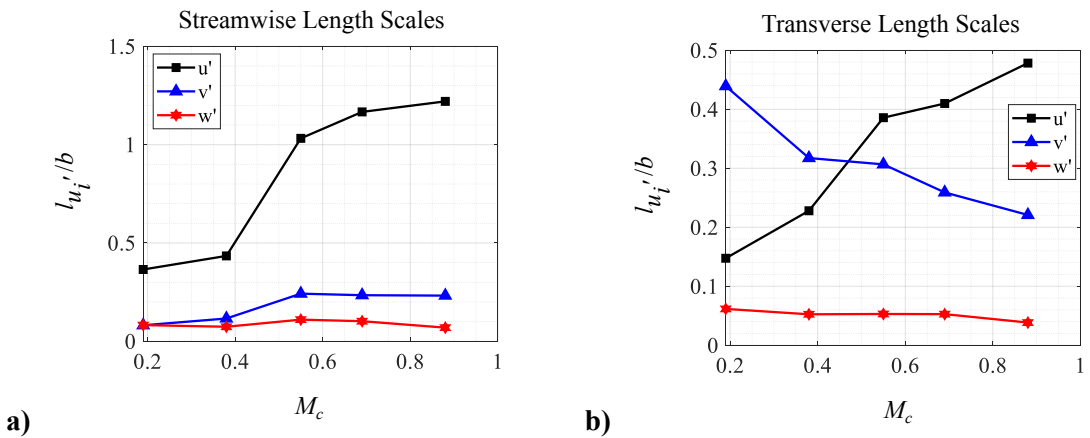


Figure 69. Turbulence length scales for u'_i in a) streamwise and b) transverse directions.

The two trends that most clearly illustrate the evolution of the structure shapes as discussed thus far in this dissertation, are the increasing l_u/b correlation in the streamwise direction (black curve on the left) and the decreasing l_v/b correlation in the transverse direction (blue curve on the right) with increasing M_c . These results agree with the description of the large-scale structures becoming elongated and flattened-out longitudinally with increasing compressibility. Freund *et al.* show a similar decrease in v' transverse length scale for increasing M_c ; however, they do not normalize the length scales by the local mixing layer thickness. Rather they normalize by the shear layer radius at the midpoint, a constant value for their annular mixing layer investigation. Thus, the decrease in size of the turbulent structures relative to the shear layer thickness is more clearly demonstrated here. While Freund *et al.* were able to conclusively show that their transverse eddy length scale could be used to normalize the peak transverse normal and shear stress values such that they remained constant with M_c , the same could not be achieved in the present study. Freund *et al.* use the velocity scaling, $\Delta U(l_v/b)$, to represent the velocity difference across a large eddy and scale their transverse normal and Reynolds shear stresses by $(\Delta U(l_v/b))^2$. Doing the same in the present study results in an increase of peak Re_{yy} and Re_{xy} with M_c , rather than constant peaks.

The trend of increasing $l_{u'}$ in the transverse direction (black curve on the right) with increasing M_c is an interesting finding. While it may not necessarily relate directly to the physical shape of the turbulent eddies in the mixing layer, it may be representative of a pulsing dynamic that begins to dominate at higher M_c . Examination of instantaneous u' fields for the highest M_c case (example shown in Figure 70) shows that large positive and negative regions of u' are present that span the transverse thickness of the mixing layer. This form of instantaneous motion suggests that, as compressibility is increased, the structures are subject to a dynamic mode that is characterized by large regions of correlated streamwise fluctuations, both in the streamwise and transverse directions (both black curves in Figure 69). This strong streamwise pulsing motion, combined with the reduced transverse and spanwise fluctuations (shown from c_{yy} and c_{zz} vs. M_c in Figure 60), likely cause the elongation and stretching of the structures as described

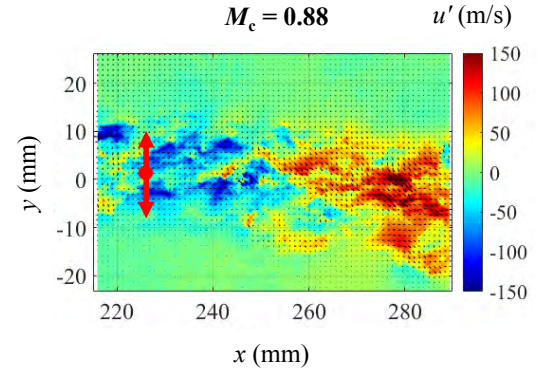


Figure 70. Example u' field for $M_c = 0.88$ case with red arrows indicating two-point transverse correlation.

previously. This dynamic mode is further discussed in detail in Section 5. 1. 2, where proper orthogonal decomposition is applied to the present data.

Lastly, while in the discussion of the instantaneous spanwise velocity fields, the lowest M_c case exhibited some large-scale organization of what were termed ‘w-braids’, it is not surprising that these were not captured with this technique. In Figure 33, the braids were all oriented at an oblique angle, and thus simply moving up-and-down or side-to-side would not capture these correlations. Rather, these are captured in full two-dimensional spatial velocity correlations, which will be discussed in Section 5. 2. 2.

4. 6. Relevant Mach Numbers

To round out the analysis of compressibility effects on the turbulence of mixing layers, the relevant Mach numbers in this flowfield are investigated. Mach number, by definition, is a useful quantity to examine when studying compressibility effects, as it gives the relative measure of a specified velocity compared to the speed of sound at which information is able to travel in that medium. The convective, turbulence, and gradient Mach numbers are discussed below.

4. 6. 1. Revisiting the Convective Mach Number

The first term to be examined is the convective Mach number, which has been used extensively thus far. Physically, this value should represent the relative Mach number of the convecting large-scale structures in the mixing layer compared to the two freestreams. The analytical form, $M_c = \Delta U/(a_1 + a_2)$, that has been used broadly in the compressible mixing layer literature (and throughout this work thus far), is founded on the physical basis that there exists a saddle point between the large structures where the stagnation pressures of the two streams match. While this notion may hold true for lower levels of compressibility, where Brown-Roshko rollers dominate, it likely breaks down for mixing layers with higher levels of compressibility, where the structures are highly disorganized. Isentropic relations are expected to become increasingly inaccurate for these cases; therefore, empirical quantification of convective velocity and Mach number are desired, at least in part to validate the expression used thus far.

One method of determining an empirical U_c of the structures in the mixing layer, is to first determine the structures in the mixing layer with some defining parameter, then conditionally average the streamwise velocity (in the laboratory reference frame) based on a certain threshold of

the parameter. In flows where coherent structures are expected to exist, the swirling strength (λ_{ci}) can be used identify local vortex structures. λ_{ci} is the imaginary component of the complex eigenvalue of the local velocity gradient tensor and identifies vortex cores without being affected by regions of high local shear (unlike vorticity).⁶⁴ Here, since only the two-dimensional velocity gradient tensor is available, a two-dimensional version of swirling strength is used. An example swirling strength field with velocity vectors overlaid is shown in Figure 71 (with U_c isentropic subtracted from u).

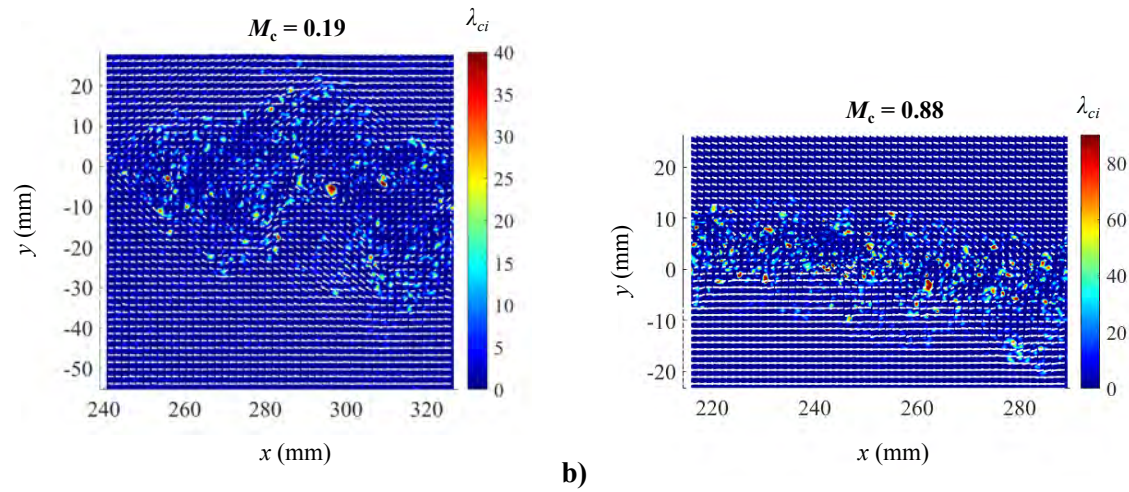


Figure 71. Swirling strength field for a) $M_c = 0.19$ and b) $M_c = 0.88$ mixing layers with velocity vectors overlaid (1/5 sub-sampled in each direction).

Once the swirling strength is calculated for each instantaneous velocity field, a conditional average of u can be determined based on locations where λ_{ci} is above a certain threshold in the ensemble: $U_{c, \text{empirical}} = \overline{u(x,y) | \lambda_{ci}(x,y) > \text{threshold}}$. To ensure that the result is independent of the threshold value, threshold convergence needs to be confirmed. For each case, the ensemble average of all images' maximum swirling strength value is used to define a range of thresholds that are considered. Threshold convergence is achieved for every case past the threshold value of $0.3(\lambda_{ci, \text{max}})$, as shown in Figure 72. This relatively low threshold is not too surprising, since the swirling strength should theoretically only be non-zero when a vortex structure is present. The isentropic U_c is also plotted for each case in the same color as a solid line. It can be seen that the difference between the isentropic value, $U_{c, \text{isentropic}} = (U_1 a_2 + U_2 a_1) / (a_1 + a_2)$ and $U_{c, \text{empirical}}$ increases with M_c , agreeing with the assumption that deviations from the idealized $U_{c, \text{isentropic}}$ value increase with increased compressibility (with $U_{c, \text{empirical}}$ always lower than $U_{c, \text{isentropic}}$).

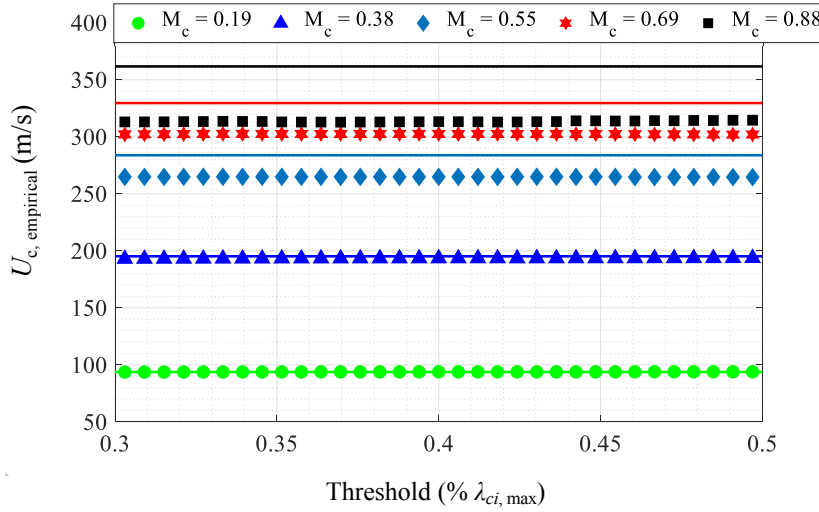


Figure 72. Threshold convergence for $U_{c,\text{empirical}}$ for $M_c = 0.19, 0.38, 0.55, 0.69$, and 0.88 mixing layers (solid lines represent $U_{c,\text{isentropic}}$).

Since the isentropic definition of M_c is such that it is equal for the primary and secondary streams (for $\gamma_1 = \gamma_2$), any deviation of the empirical convective velocity from $U_{c,\text{isentropic}}$ means that $M_{c1} \neq M_{c2}$. Thus, differences between the two in Figure 72 will result in different convective Mach numbers for each stream with the following definitions: $[M_{c1} = (U_1 - U_c)/a_1] \neq [M_{c2} = (U_c - U_2)/a_2]$. This was, in fact, found to be the case in highly compressible shear layers, where a stream-selection rule was observed by various previous researchers, including Papamoschou (1989) and Poggie and Smits (1996).⁶⁵⁻⁶⁶ They observed that for $\Delta U/(a_1 + a_2) > \sim 0.6$, their measured U_c approached U_2 when both streams were supersonic, and approached U_1 when one stream was subsonic and the other supersonic. The M_{c1} vs. M_{c2} curve is plotted for the results of the current study, along with those of Papamoschou and Poggie and Smits in Figure 73.

The empirical results of the present work show little agreement with the described stream-selection rule. The trend of $U_c \rightarrow U_2$ ($M_{c2} < M_{c1}$) is very gradual, and is in fact, the opposite trend for the subsonic-supersonic combination that the stream-selection rule would predict, $U_c \rightarrow U_1$. The difference in results, however, is not all too surprising, as the nominal convective Mach numbers here are, in general, much lower than the ones Papamoschou and Poggie and Smits examined, and the techniques by which U_c is determined are very different. The system used by

Papamoschou is based on a double-pulsed instantaneous schlieren system, where the velocity of large structures is determined from a calculated displacement from the visualizations and a Δt between images known a priori. Poggie and Smits used a similar concept, but with Rayleigh scattering instead of schlieren.

A few notes regarding the level of accuracy (in a heuristic sense) are made for the differing methods in their attempts to extract a convection velocity. In Papamoschou's method, the detection of structures, as they evolve in a three-dimensional manner (especially at high levels of compressibility), via a line-of-sight integrating technique such as schlieren, leads to questions regarding the capability to accurately determine the structures. Perhaps it is due to this factor that the ensemble size for all cases in his experiments is between only 2 – 16 realizations, which also would play a role in the level of uncertainty of an ensemble-averaged result. In Poggie and Smits' investigation, the issue of line-of-sight integration is not present with their spatially resolved planar Rayleigh scattering images. However, their experimental set-up required a large non-dimensional time between images ($U_1\Delta t/b \sim 2$). While this may be interpreted as only allowing the largest-scale and longest-lived structures to be correlated (as they argue in their paper), it certainly introduces additional uncertainty, since the highly disorganized structures at high levels of compressibility likely undergo rapid distortion as they develop spatially. This was the case for the $M_c = 0.88$ high-speed schlieren movies observed in the present study, as the structures were not found to coherently convect over a streamwise length on the order of twice the local shear layer thickness. And while larger than Papamoschou's, Poggie and Smits' ensemble size was also fairly small at 50 image pairs per correlation. Additionally, the technique of obtaining a convective velocity from flow visualizations introduces the challenge of discerning between structure types, and if rollers and braids convect at different speeds and on a different scale from the pairing process altogether, it would be difficult to accurately determine the convection velocity of a nominal structure. Of course, this last point is one that applies to the concept of obtaining a

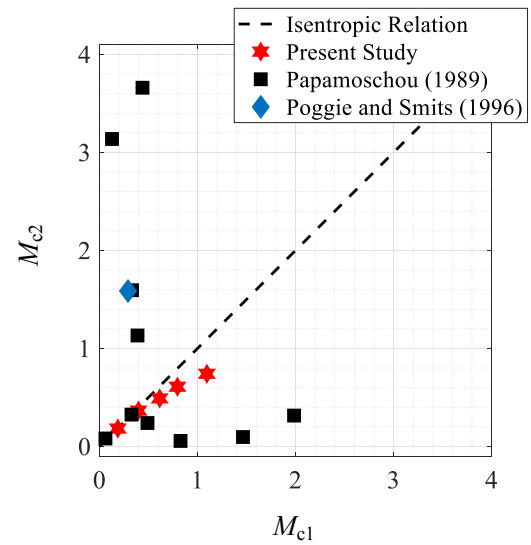


Figure 73. M_{c1} vs. M_{c2} using empirically determined convective velocities.

singular convective velocity of large-scale structures in turbulent mixing layers in general. Nevertheless, the fact that multiple different experiments (including a few others that also observed it but are not reviewed here) were able to arrive at the stream-selection rule gives a certain level of authority to the result.

The empirical technique applied via the quantitative swirling strength criterion given here is not without its own uncertainties. To start, the two-dimensional definition of swirling strength is unable to capture any three-dimensional information about the structures, similar to the planar Rayleigh scattering images and the line-integrated schlieren images. And the aforementioned point regarding structures that may convect at different speeds in the shear layer is not addressed in this analysis. One beneficial aspect of this technique, however, is the fact that U_c is determined directly from the measured velocity field (from SPIV), and is not determined through correlations of qualitative flow visualizations (SPIV is also an image correlation technique; however, it is particle based with algorithms specifically optimized to calculate flow velocities at discrete locations). Thus, if the location of a structure can be determined, then the local convective velocity (in the lab frame) of that structure can be given with high confidence. It is the former structure identification step that incurs the most uncertainty and interpretation in the present method. This shortcoming is dealt with as well as possible by confirming good threshold convergence as shown in Figure 72. Ensemble sizes in the current empirical U_c method are also much larger, at $\geq 2.9 \times 10^6$ data points per calculated $U_{c, \text{empirical}}$ (on average one out of every 50 grid points meeting the $\geq 0.3\lambda_{ci, \text{max}}$ condition in each image).

It should be stressed once again that the heuristic nature of obtaining an empirical convective velocity in mixing layers makes it difficult to report this quantity with high certainty, at least without some interpretation. This is due largely the definition of U_c itself, as a nominal convection velocity of structures that become difficult to even identify at high levels of compressibility. Therefore, the stream-selection rule not being followed for the present analysis (in Figure 73) was somewhat expected. It could also be the case that the nominal M_c values considered here simply are not high enough to exhibit the stream-selection rule. Elliott *et al.* also performed a correlation technique similar to Poggie and Smits on product formation images and found that their empirical U_c was close to the isentropic definition near the shear layer center. The M_c cases that they investigated were 0.51 and 0.88, much closer to the values in the current study.⁵³

Lastly, while the analysis discussed here gives new empirically determined convective Mach numbers, work presented in subsequent sections will still be referred to by the nominal $\Delta U/(a_1+a_2)$ definition, for consistency throughout the writing, and to avoid confusion with the operating conditions defined in Table 4. The empirically determined convective velocities, however, will be utilized in the linear stochastic estimation technique that is laid out in Section 5. 2.

4. 6. 2. Turbulence Mach Number

In addition to the convective Mach number, an important measure of compressibility of the turbulent fluctuations is the turbulence Mach number. The definition of turbulence Mach number, M_t , and transverse turbulence Mach number, M_{tr} , are given in Equation (19), wherein it becomes clear that the speed of sound, a , must be determined. Some of the various compressible mixing layer works that report M_t use the average a between the two streams $(a_1 + a_2)/2$. However, in examining the numerator of the turbulence Mach numbers, it can be seen that the fluctuations are calculated at each transverse location in the shear layer; thus, the local a at each η location can be used rather than a single average value. a is determined from the local static temperature ($a = (\gamma RT)^{1/2}$), which is calculated via the adiabatic relationship used to determine the operating conditions given in Table 4.

$$M_t = \left(\overline{u'^2} + \overline{v'^2} + \overline{w'^2} \right)^{1/2} / a, \quad M_{tr} = \left(\overline{v'^2} \right)^{1/2} / a \quad (19)$$

The similarity profiles of M_t and M_{tr} from the fully-developed region are plotted for each case in Figure 74 and Figure 75, respectively. By definition, their shapes are determined from the TKE, Re_{yy} , and a profiles. The increasing asymmetry of the M_t and M_{tr} profiles about $\eta = 0$ (biased towards the primary side) with increasing M_c , is due to the lower speed of sound on the primary side for higher M_c . As a consequence, the peaks of the turbulent and transverse turbulence Mach number profiles are slightly toward the primary side. The peak M_t increases with convective Mach number and reaches a maximum of ~ 0.36 for the highest $M_c = 0.88$ case, while the M_{tr} peak values increase at first, then level off at ~ 0.13 at the higher end of compressibility examined here. The peak values of both M_t and M_{tr} are all close to those reported by Freund *et al.* in their DNS study, as shown in Figure 76.

Of particular interest, is the trend of M_{tr} with M_c , as the results from the present study, in addition to Freund *et al.*, show that the transverse turbulence Mach number begins to level off near

$M_c = 1$. On the other hand, M_t continues to increase with M_c . This result agrees with the decreased transverse normal stress anisotropy and indicates that the transverse fluctuations that are important for mixing between the two streams, become less prominent compared to the other directions as

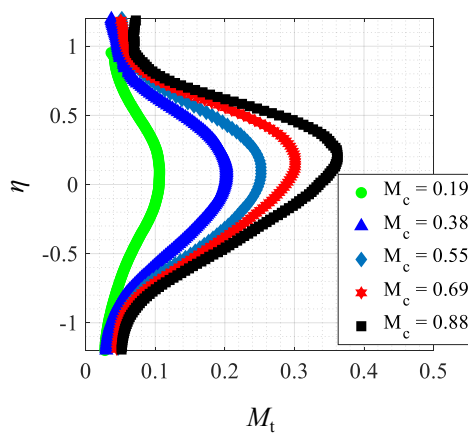


Figure 74. Similarity profiles of M_t .

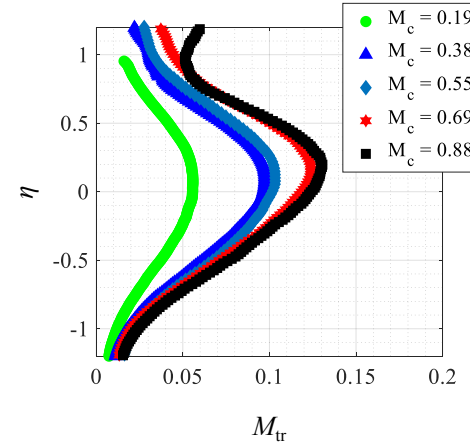


Figure 75. Similarity profiles of M_{tr} .

compressibility is increased. The RMS of v' does not increase past a certain fraction of the local speed of sound ($\sim 15 - 20\%$), while the total RMS of all three components continues to increase relative to the speed of sound with increasing M_c . This result agrees with the compressibility effects on the anisotropy tensor (c_{yy} decreasing with M_c) and confirms that the portion of TKE in the transverse direction decreases as the convective Mach number increases.

4. 6. 3. Gradient Mach Number

Lastly, the gradient Mach number, M_g , is an important term in compressible mixing layer studies and is defined in Equation (20). It can physically be interpreted as the Mach number across a typical eddy of length l in the shear layer. As with the turbulence Mach number, the local speed of sound, a , in the transverse direction is used to determine M_g . For the mean streamwise velocity gradient term, a second-order central finite differencing scheme is used.

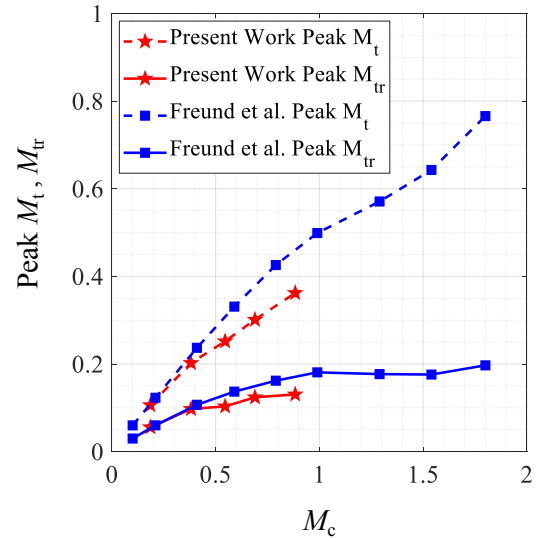


Figure 76. Peak M_t and M_{tr} vs. M_c .

$$M_g = \frac{\frac{\partial \bar{u}}{\partial y} l}{a} \quad (20)$$

The transverse similarity profiles of M_g using $l = b$ are plotted in Figure 77 for the present mixing layer cases. Once again, the peaks of each profile are slightly shifted to the primary side due to the lower speed of sound in that region. While it is true that the typical eddy length in the transverse direction was found to decrease compared to b (Section 4.5), the mean gradient term is representative of the velocity difference across the entire shear layer, thus the local thickness is used in the calculation of M_g here. In addition, this scaling allows for the comparison of results to the analytical finding of Sarkar (1995), who obtained the relation $M_g \sim 2.2M_c$ on the basis of using the local shear layer thickness for l .⁶⁷ In his work, he compares the compressibility effects in boundary layers and shear layers using the gradient Mach number. He obtains an analytical relation for M_g in terms of M_c for compressible mixing layers and the freestream Mach number in boundary layers. The results are vastly different, as the linear relationship given above is obtained for the former, while for the latter, M_g is less than 0.2 for freestream Mach numbers as high as three.

The peak M_g in the shear layer is plotted against M_c in Figure 78 for the present work, along with the work of Freund *et al.* and Sarkar's relation. It can be seen that all three trends agree well until $M_c \sim 1$, where Freund *et al.* see a leveling-off of M_g . They argue that this saturation of M_g is due to the limiting acoustic time scale (based on a) compared to the flow distortion time scale (based on $\partial \bar{u} / \partial y$). If $M_g > 1$, the turbulent eddies are being distorted faster than information can travel across them ($M_g = \text{distortion time scale}/\text{acoustic time scale}$); thus, there must be some limiting time scale at which the eddies become distorted.³³

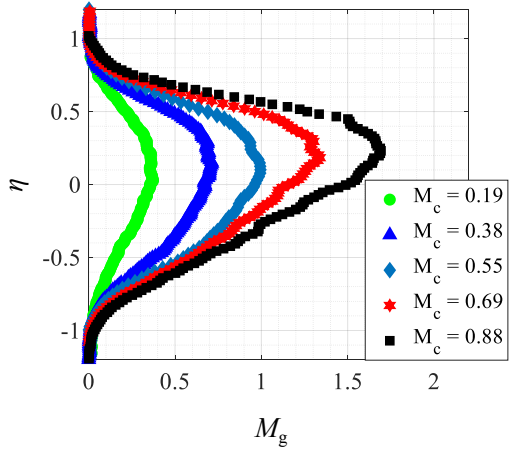


Figure 77. Similarity profiles of M_g .

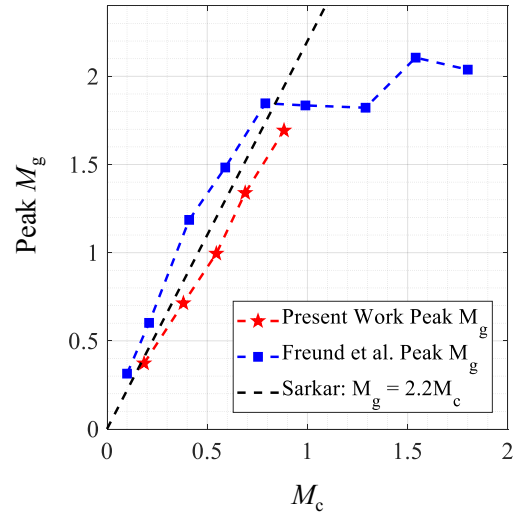


Figure 78. Peak M_g vs. M_c .

Furthermore, by analyzing the wave equation, Pantano and Sarkar show that the gradient and turbulence Mach numbers can be used to explain the pressure-strain correlation reduction with increasing compressibility.³⁹ They argue that, as compressibility is increased, the time delay of pressure signals across the mixing layer causes decorrelation across an eddy and reduction of the pressure-strain term. While pressure fluctuation measurements are not available in the current experiments, the results for M_g here are nonetheless valuable for validating computational models that are based on physical arguments regarding the gradient Mach number.

5. TWO-DIMENSIONAL FLOW ANALYSES

Most of the turbulence analyses presented in the previous section have been one-dimensional (*i.e.*, results plotted against η for a single profile) and have yet to take full advantage of the instantaneous two-dimensional velocity fields that have been measured. In this section, analyses that make use of the spatial resolution of the planar data are presented. The three specific techniques discussed here are proper orthogonal decomposition, linear stochastic estimation, and an entrainment analysis based on turbulent-non turbulent interfaces. These techniques provide information regarding the spatial energetic modes, conditional large-scale turbulent structures, and entrainment mechanisms present in the flow, respectively. For each analysis, the method is described, with appropriate seminal references given. The goal for each analysis is to identify the effects of compressibility on the results and to make physical connections back to the findings obtained thus far whenever possible.

5. 1. Proper Orthogonal Decomposition

5. 1. 1. POD Background and Method Description

Proper orthogonal decomposition (POD), also known as the Karhunen-Loève (K-L) expansion, is a statistical pattern recognition, or ‘feature extraction’, technique that is used in numerous science and engineering disciplines. It lends itself well to the study of large-scale structures in turbulent flows and has been used for this purpose extensively. From a qualitative standpoint, the concept of POD is to capture a set of features that is able to accurately describe sample signals. It then follows that if the signals can be described accurately with a small number of features, the features can be considered as dominant in the signal. In the context of fluid mechanics, it becomes clear that this method can be useful for the extraction of repetitive large-scale structures that characterize the flow. It was Lumley (1967) who first applied this concept to fluid mechanics, where he argued that orthogonally decomposing spatial velocity fluctuation correlations is a reasonable quantitative method for identifying coherent structures.⁶⁸ Due to the technique’s high level of generality, as well as the wide variety of forms applied in the literature, the method itself is discussed in detail starting with the statistical theory, then focusing on the exact computational methods used to analyze the present data.

An outline of the discrete K-L expansion is given here that follows Fukunaga (1990).⁶⁹ It lays the appropriate mathematical groundwork and aims to be a quick primer for the general application of POD in stochastic processes. Quantitatively, the K-L expansion determines an optimal set of linearly independent orthonormal basis vectors (features) that best describe a random variable (signal). This can be represented mathematically as: $\mathbf{g} = \Phi \mathbf{q}$, where Φ contains the n basis vectors $[\varphi_1, \varphi_2, \dots, \varphi_n]$, each having length n ; \mathbf{g} is the n -dimensional random variable equal to $[g_1, g_2, \dots, g_n]^T$; and \mathbf{q} is the vector of n linear coefficients, q_1, q_2, \dots, q_n . Vectors are bold-faced and lower-case, matrices are bold-faced and capitalized, and scalars are non-bold and lower-case. The optimization process is based on the goal described above of finding a small number of dominant features that accurately describe the random variable. It involves minimizing the mean square error (MSE) between the random variable (\mathbf{g}), and an approximate reconstruction, $\hat{\mathbf{g}}$, that uses a subset of m ($< n$) coefficients/bases from \mathbf{q} and Φ . Since the approximation $\hat{\mathbf{g}}$ does not utilize all n components of \mathbf{q} , a placeholder variable, s_k , is inserted for the $k = m + 1, \dots, n$ basis vectors (*i.e.*, $\hat{\mathbf{g}} = \sum_j (q_j)(\varphi_j) + \sum_k (s_k)(\varphi_k)$ for $j = 1, \dots, m$; $k = m + 1, \dots, n$). The MSE between \mathbf{g} and $\hat{\mathbf{g}}$ is then equal to $\sum_k E[(q_k - s_k)^2]$, where $E[]$ is the expected value operator. Minimizing the MSE with respect to s_k gives the result that s_k be equal to the expected value of q_k ($= E[q_k]$), and since the columns of Φ form an orthonormal set (*i.e.*, $\varphi_i^T \varphi_j = \delta_{ij}$), the expressions $q_k = \varphi_k^T \mathbf{g}$ and $s_k = E[q_k] = \varphi_k^T E[\mathbf{g}]$ can be derived. Substituting this expression for s_k back into the MSE gives the result: $MSE = \sum_k (\varphi_k^T E[(\mathbf{g} - E[\mathbf{g}])(\mathbf{g} - E[\mathbf{g}])^T] \varphi_k) = \sum_k (\varphi_k^T (\text{Cov}(\mathbf{g})) \varphi_k)$, where $\text{Cov}(\mathbf{g})$ is the autocovariance of random variable \mathbf{g} . From here, Fukunaga gives a proof showing that $\sum_k (\varphi_k^T (\text{Cov}(\mathbf{g})) \varphi_k)$ is minimized when $\text{Cov}(\mathbf{g}) \varphi_k = \lambda_k \varphi_k$, which gives the result that φ_k are the eigenvectors of $\text{Cov}(\mathbf{g})$. The proof is not included here, but relies on the orthonormality among the φ_k 's.⁶⁹ While the framing of the mathematical derivation for POD varies slightly by author/subject (*e.g.*, Lumley describes the problem as finding Φ that maximizes the normalized mean square magnitude of the projection $\Phi^T \mathbf{g}$),⁶⁸ the key result is that an optimal set of orthogonally independent basis vectors (eigenvectors) can be calculated for a stochastic process. Moreover, the eigenvalue associated with each eigenvector gives the relative importance (or dominance) of that mode, and orthogonality ensures that the eigenvalues converge optimally fast.

The use of POD to capture coherent structures in turbulence requires a proper representation of the flow through the random variable kernel. In his pioneering work, Lumley uses the cross-spectral density tensor, a term containing information both in space and time. It is defined as the

Fourier transform of the two-point space-time velocity correlation tensor (time being referred to as a single time delay variable).⁶⁸ This method is certainly preferred if temporally resolved velocity fields are available, as they are in computational investigations and a few previous experiments (Delville *et al.*, 1990, Citriniti and George, 2000).^{70, 71} However, this task becomes increasingly difficult in high-speed/supersonic flows due to the very fast temporal resolutions required, even with today's advanced flow diagnostic methods.

A variation of POD for instantaneous velocity fields that are uncorrelated in time, called the ‘method of snapshots’, was developed by Sirovich (1987).⁷² He uses the velocity autocovariance matrix as the kernel, in which each element represents the total correlated energy between two instantaneous images (*i.e.*, inner product of velocity fluctuations between two snapshots). An added benefit of this method, beyond not requiring time-correlated data, is that the computational time depends mostly on the number of snapshots in the ensemble, and not on the spatial resolution of the velocity fields. For each instant in time, the $N_x \times N_y$ fields are reduced to one dimension through an inner product, and only N_t number of eigenvalues are required to be calculated (multiplication and addition operations required in the inner products are much faster than the solution of a system of equations required in the eigenvalue problem). This is important since the SPIV grids in the current experiments are as large as $N_x \sim N_y \sim 250$ resulting in over 62,000 grid points per image, while N_t is $\sim 3000 - 4000$ (with N_x and N_y being number of grid points in the x and y directions, respectively, and N_t being the ensemble size). The computational algorithm for the current method is given in Figure 79 and follows Meyer *et al.* (2007) very closely.⁷³ The eigenvectors of the autocovariance matrix make up a basis for the POD modes, and each spatial velocity mode can be calculated as the projection of each eigenvector onto the instantaneous velocity fields (Figure 79, step 4). The temporal coefficients for each snapshot are calculated as the inner product between the velocity field of that snapshot and the POD modes, as shown in Figure 79, step 5. With this formulation, a reconstruction of an instantaneous velocity field can be defined as in step 6, where the reconstruction approaches the exact original field as the number of modes used (N_m) increases. The subscript k denotes velocity component, t denotes the snapshot number, and i denotes the mode number.

$$C_{ij} = \sum_{x=1}^{N_x} \sum_{y=1}^{N_y} \left[(u'_x, y)^{(i)} (u'_x, y)^{(j)} + (v'_x, y)^{(i)} (v'_x, y)^{(j)} + (w'_x, y)^{(i)} (w'_x, y)^{(j)} \right] \quad \text{Step (1)}$$

$$i = 1, 2, \dots, N_t \quad j = 1, 2, \dots, N_t$$

$$\begin{aligned} & \text{Eigenvalue Problem} \\ & \mathbf{CA} = \lambda \mathbf{A} \end{aligned} \quad \text{Step (2)}$$

$$\begin{aligned} & \text{Energy in each Mode} \\ & \text{Energy}(\text{Mode } i) = \lambda_i, \quad |\lambda_1| > |\lambda_2| > \dots > |\lambda_{N_t}| \end{aligned} \quad \text{Step (3)}$$

$$\Phi_{\mathbf{u}_k}^i = \frac{\sum_{t=1}^{N_t} [A_t^i \mathbf{u}'_t]}{\left\| \left[\sum_{t=1}^{N_t} [A_t^i \mathbf{u}'_t], \sum_{t=1}^{N_t} [A_t^i \mathbf{v}'_t], \sum_{t=1}^{N_t} [A_t^i \mathbf{w}'_t] \right] \right\|} \quad \text{Step (4)}$$

$$\text{Coeff}_{it} = \left[(\mathbf{u}'_t) \cdot (\Phi_{\mathbf{u}})^i + (\mathbf{v}'_t) \cdot (\Phi_{\mathbf{v}})^i + (\mathbf{w}'_t) \cdot (\Phi_{\mathbf{w}})^i \right] \quad \text{Step (5)}$$

$$\begin{aligned} & \text{Reconstruction of Snapshots} \\ & \mathbf{u}'_{t, \text{reconstructed}} = \sum_{i=1}^{N_m} \left[\text{Coeff}_{it} \Phi_{\mathbf{u}_k}^i \right] \end{aligned} \quad \text{Step (6)}$$

t = Instantaneous field chosen to reconstruct

N_m = Number of modes chosen for reconstruction

Figure 79. Snapshot POD method algorithm (with steps numbered) used in the present study.

While the snapshot POD method described above is widely used in the literature as a flow analysis technique, caution must be taken when interpreting the results. As one would expect, the idea that it is possible to extract coherent physical structures from a set of uncorrelated, unconditioned velocity fields may be too optimistic. Towne *et al.* (2018) point out the faults of what they term ‘space-only POD’ (referring to the present method).⁷⁴ Due to the lack of any time dependence in the autocovariance matrix used above, all information concerning the temporal evolution and correlation of the structures, a key characteristic for coherent turbulent structures, is lost. The lack of a known time delay in the autocovariance tensor used above means that the

temporal coefficients, and therefore the spatial POD modes, are neither necessarily correlated nor uncorrelated with each other. This result is simply because temporal information is not known *a priori*, and POD cannot give any new information regarding the temporal correlation. Hence, the ‘structures’ appear somewhat smeared due to the broadband range of frequencies included in each mode; thus, calling the space-only POD modes coherent physical structures would be inaccurate. Instead, the results can be interpreted as global energetic modes that represent the spatial dynamic effects the structures have on the mean flow organization. The relative energy contained in each mode is directly proportional to the mode’s eigenvalue, with the spatial size of the extracted features being directly related to their energy contribution.

As for applications of POD to experimental turbulent flow data, there have been both space-only and space-time variants performed in the literature. Delville *et al.* (1999) performed POD for experimental incompressible mixing layer data that were obtained with two cross hot-wire rakes.⁷⁰ The experiments were of a planar two-stream mixing layer with convective velocity of ~ 34 m/s ($= (U_1+U_2)/2$ for $M_c \sim 0$) and velocity ratio of 0.59. With this low velocity, they were able to obtain time-resolved data, which allowed them to perform the full space-time POD method using the cross-spectral tensor. Their analysis revealed that the most dominant mode contained 47% of the TKE and was represented by two-dimensional vortices aligned in the spanwise direction, with slight spanwise distortion from streamwise-oriented, counter-rotating vortices. This result was in agreement with previously documented lambda-shaped organization for incompressible mixing layers.⁷⁵ Conversely, space-only POD applied to the shear layer region of a compressible, turbulent, base flow showed that only $\sim 8 - 12\%$ of the TKE resided in the first mode.^{76,77} The poor energy convergence in the compressible base flow was attributed to the wide range of turbulent length scales that are typically present in high Reynolds number, compressible flows.

POD has yet to be performed on compressible turbulent planar mixing layer experimental data; therefore, its application to the data presented in Section 3 is an original contribution to turbulence research. The following subsection applies the space-only POD method to all five convective Mach number mixing layers in their fully-developed fields of view. Energy convergence and spatial mode organizations are discussed for the side-views primarily, with a few relevant end-view modes included. The higher particle-lag (and thus uncertainty of instantaneous fluctuations) have been discussed for the latter; however, global dynamics of the mixing in the spanwise direction are still likely to be captured by POD.

5.1.2. POD Results and Discussion

For the current experiments, spatial POD modes were calculated for all three velocity components using the three-component definition of TKE (*i.e.*, $TKE = \frac{1}{2}(\overline{u'^2} + \overline{v'^2} + \overline{w'^2})$). As discussed above, the energy that each mode contributes to the overall TKE is directly proportional to the eigenvalue of that mode relative to the sum of all modes' eigenvalues. The cumulative energy for each mode (*i.e.*, total energy contained up to that mode) is plotted in Figure 80 on a log-log scale for the present mixing layers, up to mode 50. The total number of modes for each case is equal to the ensemble size, which were $N_t = 4000, 4500, 3500, 3500$, and 3000 for the cases in order of increasing M_c . The energy distribution as well as mode shapes were confirmed to show ensemble convergence, with $N_t \sim 1000$ being sufficient. The relative energies contained in the first ten modes are listed in Table 7, where it can be seen that the relative energy is $\leq 1.3\%$ by mode ten for all mixing layers, indicating that those modes contribute a small amount to the overall turbulence energy.

Table 7. Energy contained in first ten POD modes.

Mode	$M_c = 0.19$	$M_c = 0.38$	$M_c = 0.55$	$M_c = 0.69$	$M_c = 0.88$
1	8.69%	7.76%	15.98%	23.74%	24.04%
2	8.03%	6.08%	4.67%	4.80%	4.85%
3	3.75%	3.71%	3.32%	2.81%	2.29%
4	3.40%	2.76%	2.63%	1.91%	1.68%
5	2.67%	2.72%	1.80%	1.64%	1.58%
6	2.51%	2.60%	1.53%	1.39%	1.42%
7	2.35%	2.26%	1.44%	1.31%	1.18%
8	2.17%	1.77%	1.38%	1.18%	1.04%
9	1.49%	1.68%	1.30%	1.12%	0.98%
10	1.32%	1.29%	1.20%	0.98%	0.87%

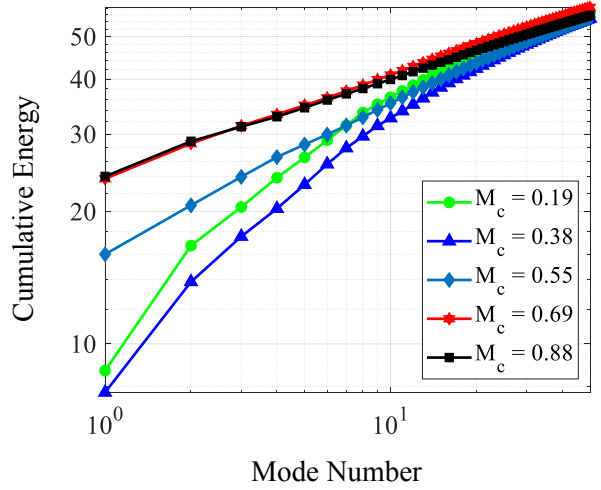


Figure 80. Cumulative energy in first 50 POD modes plotted on log-log scale (side-views).

The energy distribution as well as mode shapes were confirmed to show ensemble convergence, with $N_t \sim 1000$ being sufficient. The relative energies contained in the first ten modes are listed in Table 7, where it can be seen that the relative energy is $\leq 1.3\%$ by mode ten for all mixing layers, indicating that those modes contribute a small amount to the overall turbulence energy.

While, for all five mixing layers, $\sim 55\%$ of the total energy is recovered in the first 50 modes (as shown in the cumulative energy plot, Figure 80), Table 7 shows that the energy contained in the lowest-order first POD mode generally increases with increasing M_c . This result is quite surprising, as it was expected that the less compressible mixing layers would exhibit higher-energy lower-order modes, due to the larger and seemingly more coherent structures that are present for those cases. The result also disagrees with Delville *et al.*, who, as mentioned above, found 47% of the energy to be contained in their lowest-order mode. The stark difference between their results and the present $M_c = 0.19$ mixing layer, however, is most likely due to their ability to include temporal information, and the lack thereof herein. For the nearly incompressible $M_c = 0.19$ case in the present study, the high-speed schlieren movies showed that the structures were able to maintain their coherence for long periods of time. The absence of that information in the uncorrelated SPIV snapshots would then certainly decrease the ability to extract high-energy low-order modes. It should be noted that the inclusion of temporal information would elicit the use of spectral POD (as described in Lumley)⁶⁸ using the cross-spectral density tensor instead of simply applying the space-only POD (*i.e.*, snapshot method) to the time-correlated velocity fields (as was done here for the uncorrelated snapshots). The additional temporal information would likely not be taken advantage of with snapshot POD, since the structures convect downstream and would be positioned at different locations for each image.

Another possible reasoning behind the low relative energy for the $M_c = 0.19$ first mode, is that the first two modes are actually paired, and the dynamics that describe a single mode are actually split between two modes. Mode pairing has been reported in previous works (VerHulst and Meneveau, 2014, and Yang *et al.*, 2017), and is characterized by two modes having approximately equal relative energies (such as for modes 1 and 2 for $M_c = 0.19$ in Table 7) and similar spatial frequencies that are shifted.^{78, 79} This is described in further detail for $M_c = 0.19$ later in this section. However, even the sum of the energies in these two modes is still less than the first mode for the higher M_c cases, and this still does not explain why the first mode energy is also low for $M_c = 0.38$, where pairing with the second mode does not seem likely. Thus, there must be some underlying physical principle for this consistent trend where there is more energy in the first mode for mixing layers of higher compressibility. The three velocity components of the first POD mode are plotted as color contours with $u-v$ vectors overlaid in Figure 81. Mean boundary locations of the shear layers are also plotted in dashed lines, as defined by y_1 and y_2 .

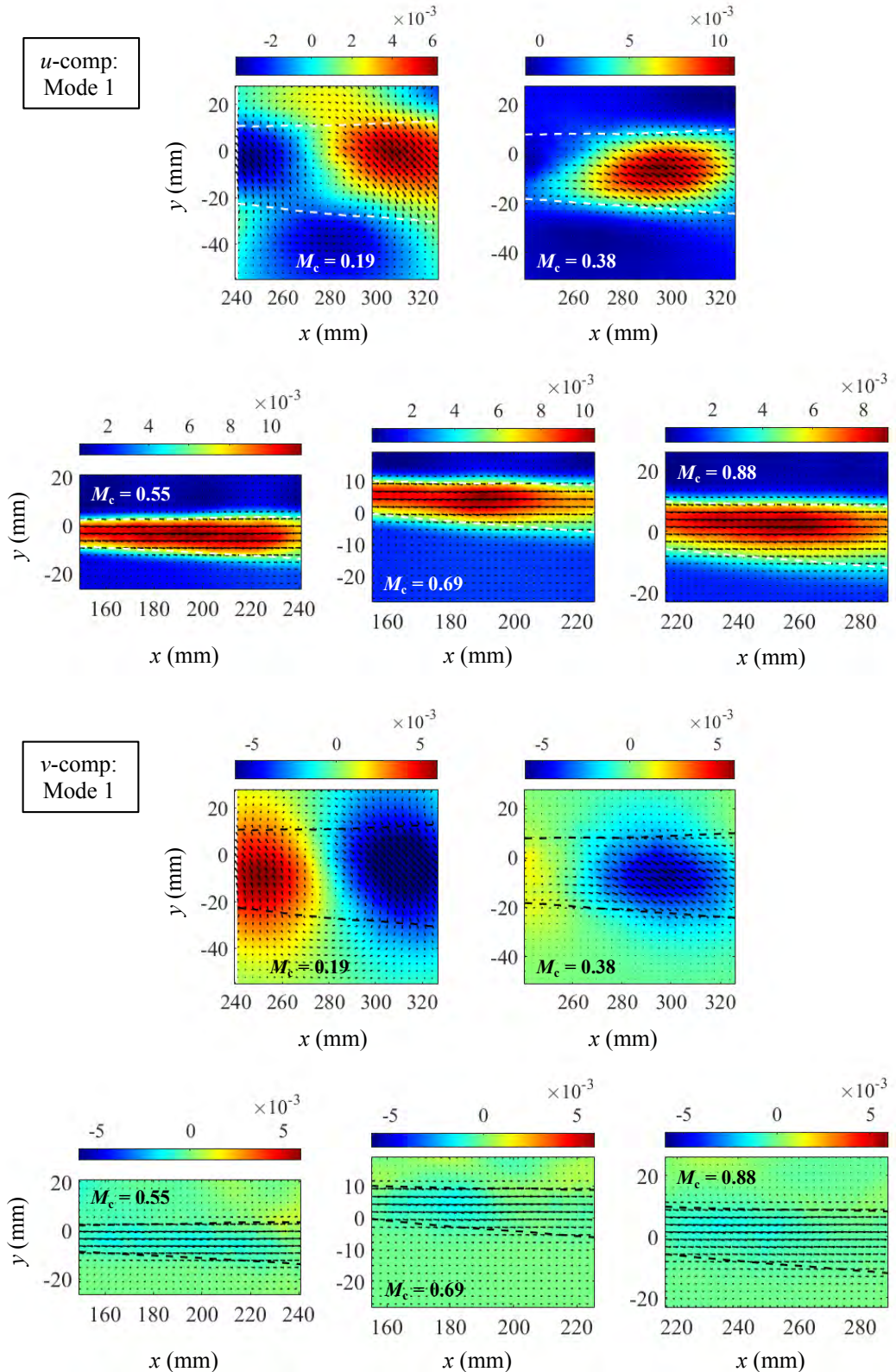


Figure 81. Color contours of POD mode one velocity components with vectors overlaid and mean shear layer transverse locations shown in dashed lines.

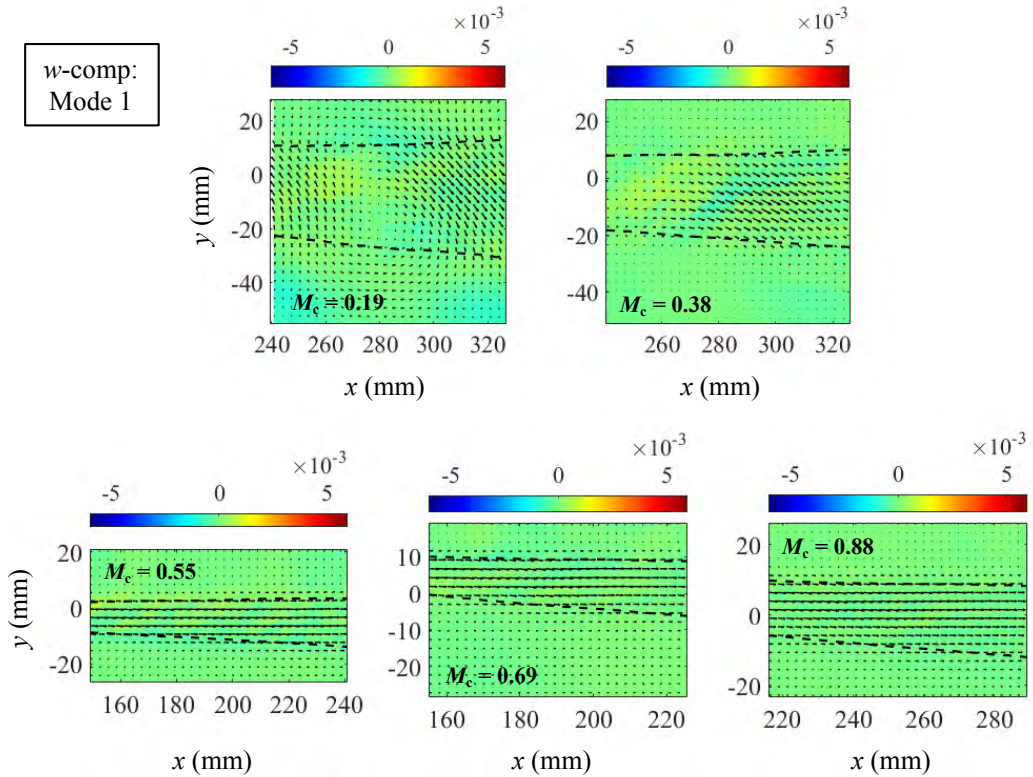


Figure 81. (cont.)

In order to elucidate the unexpected result of increasing first-mode energy with increasing M_c , an argument can be made based on the distinct Reynolds stress tensor trend that was observed. In Section 4.2, it was shown that Re_{xx} remains constant with M_c while the other two normal stress components decrease. It is clear that for the three highest compressibility cases, the first POD mode is dominated by the u -component. This can be observed in Figure 81, where the v and w POD mode magnitudes are an order of magnitude lower, at 10^{-4} for these three cases. Thus, the fact that more energy is contained in the mode that is dominated by u' for higher M_c , is actually in agreement with the sustained u' fluctuations compared to the decreasing relative v' and w' fluctuations for increasing M_c . The u -component for modes 2 – 4 (with vectors overlaid) are plotted in Figure 82. When examining these for the same three highest M_c mixing layers, it can be seen that the u and v components are much closer in magnitude than in mode one, as indicated by the vectors that are no longer parallel to the x direction. Starting with mode two, transverse velocity fluctuations are included in the POD results (w modes are still smaller than v) for these three cases; however, the energy drop-off is large between the first two modes, as the higher modes contribute less to the overall energy of the turbulence. It should be emphasized that the energy in each mode is relative

to the overall turbulent kinetic energy within a mixing layer case. This means that the higher first mode energies for the $M_c = 0.55$, 0.69 , and 0.88 cases do not necessarily mean those POD modes are more energetic as compared between cases, but that the instantaneous spatial organization of the fluctuations is more likely to resemble that mode for a certain case, with likelihood proportional to the energy. With this argument in mind, it is then not surprising that the first mode of the three highest M_c cases look very similar in Figure 81. A close inspection of Figure 57 and Figure 58 (Re_{ij} vs. M_c) reveals that the transverse and spanwise normal stresses do in fact drop off significantly from $M_c = 0.38$ to 0.55 , and then decrease at a much weaker rate with increasing M_c , while Re_{xx} remains constant. Thus, the three highest M_c cases being dominated by u' fluctuations and having similar-looking first POD modes is consistent with the Reynolds stress tensor results presented earlier in Section 4. 2.

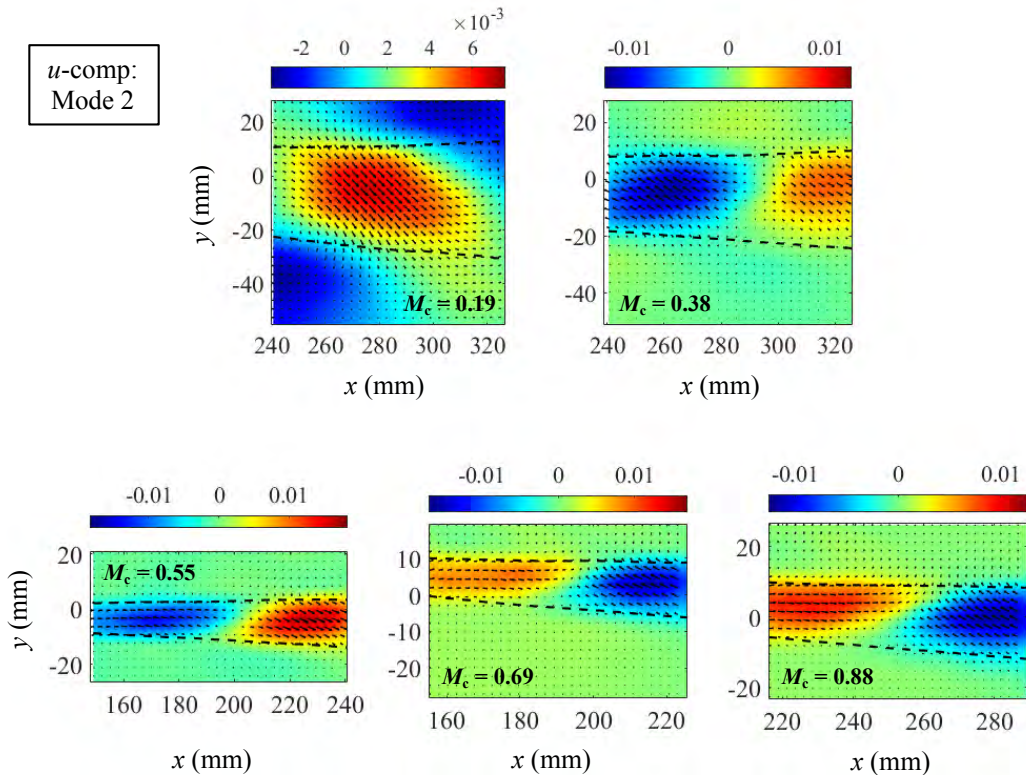


Figure 82. Color contours of u -component POD modes 2 – 4 with vectors overlaid and mean shear layer transverse locations shown in dashed lines.

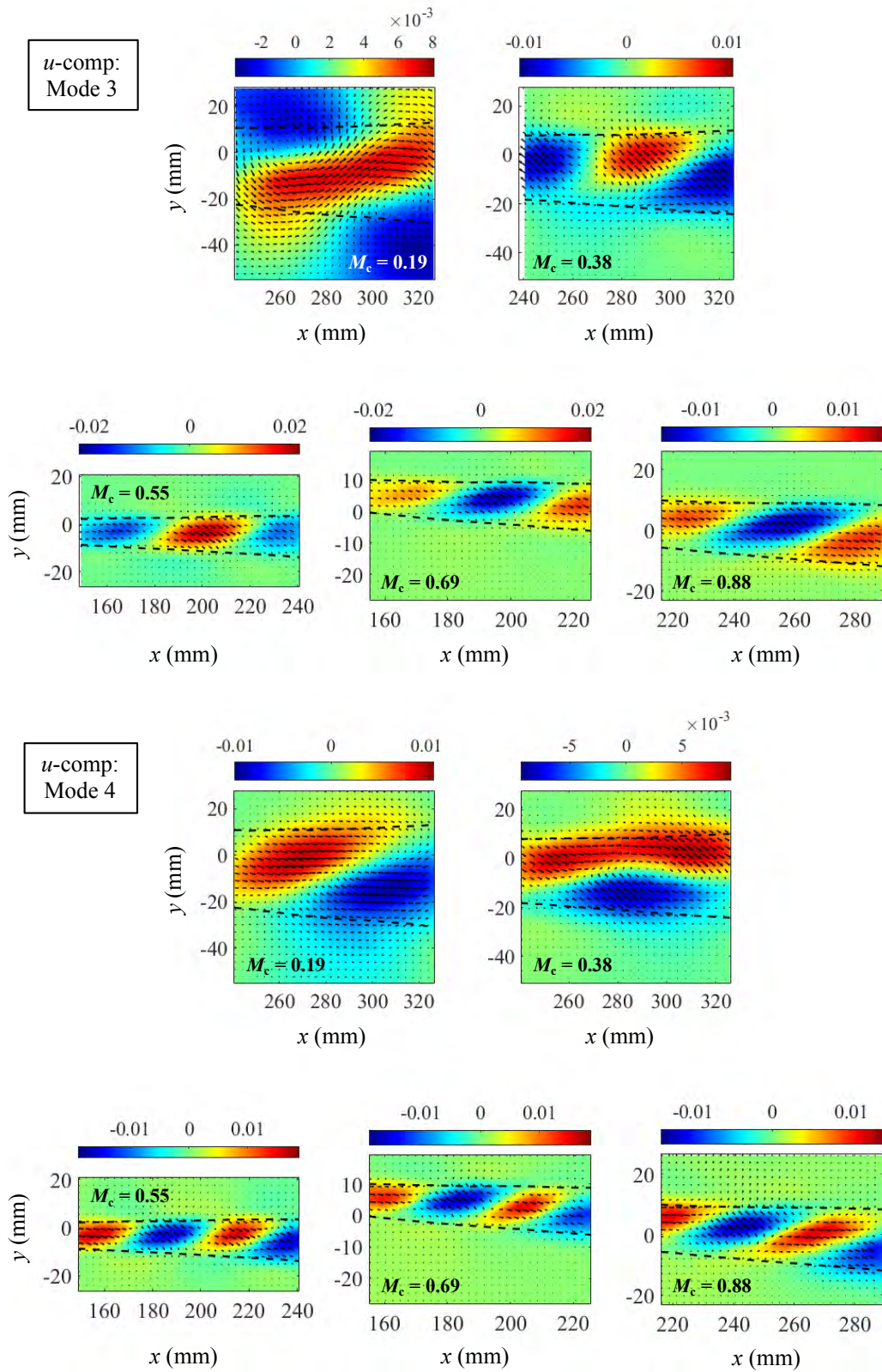


Figure 82. (cont.)

Physically understanding the results of the modes can be aided through an examination of the POD coefficients that correspond to each mode. In the velocity field reconstruction step of the snapshot POD algorithm (step 6, Figure 79), it can be seen that each instantaneous velocity snapshot can be written as a linear combination of the POD coefficients for that snapshot and the POD modes (as this was the goal of POD in the first place). Thus, each mode is manifested in the different snapshots with varying levels of importance, represented by the coefficient corresponding to that snapshot and mode. If the coefficients for all realizations are examined for a single mode, the product of that POD mode and the coefficients can then be interpreted as the dynamic effect that that mode has on the flow field, as the coefficients are temporal in nature (*i.e.*, $\mathbf{u}(x, y, t) = \sum[\text{POD}_{\text{coeffs}}(t)*\text{POD}_{\text{modes}}(x, y)]$, bold indicating three vector components). Note that throughout this section, the term ‘POD mode’ has been used to refer to the actual basis functions themselves (Φ), when in reality, a mode consists of Φ , the energy associated (λ), and a vector of temporal coefficients corresponding to the snapshots. The term ‘POD mode’ will continue to be used to refer to Φ , as the distinction between the three are fairly obvious (only Φ are vector fields). A histogram of the coefficients for modes 1 and 50 of the $M_c = 0.19$ and 0.88 mixing layers are shown as examples in Figure 83 below.

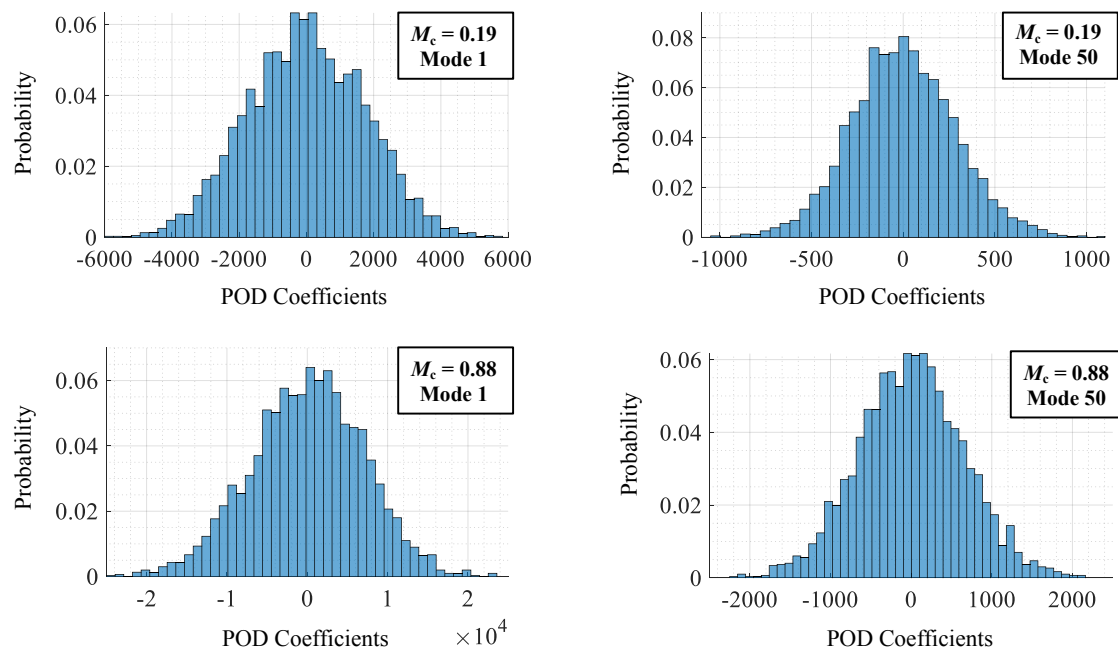


Figure 83. Temporal POD coefficients for modes 1 and 50 of $M_c = 0.19$ and 0.88 mixing layers.

Here, a discussion of the magnitudes of a POD mode, POD coefficient, and energy contained in a mode is appropriate. The three are all related and give relevant information regarding the mixing layer flow dynamics. The magnitude of a POD mode is entirely determined by the normalization factor in the calculation of the mode itself (step 4, Figure 79). Each mode is self-normalized, thus comparing magnitudes across modes is irrelevant. However, as was done in the preceding paragraphs, comparing magnitudes between the velocity components within a single mode gives information about the relative contributions of each fluctuating component to the overall energy of that mode (since each mode is normalized by the Euclidean norm of all three velocity components). The POD coefficient magnitudes are reliant on the magnitude of the POD modes and the actual velocity fluctuations. They give the appropriate scale to translate the POD mode magnitudes to real-space. Finally, the energy of a mode is the relative eigenvalue magnitude that represents the percent of total TKE contained in a mode's certain spatial frequency. A larger eigenvalue magnitude means that the structural patterns associated with that mode appear more frequently and contain large amounts of energy (*i.e.*, large-scale structures that appear commonly will be manifested as larger-eigenvalued modes). As the energy in a mode decreases, the POD coefficient magnitudes also decrease, as shown in Figure 83. This is because the coefficients are the only scaling information the POD modes have available to them to translate back to real-space (*i.e.*, a POD mode multiplied by its coefficient has dimensions of velocity). And since lower energy in a mode means that that mode contributes less to the overall turbulent fluctuations, this also results in smaller POD coefficient magnitudes. While this may all seem apparent from the snapshot algorithm, it is useful to clarify, as it explains why the magnitudes across POD modes are fairly constant even though the energies contained in the modes are clearly different.

Having established that the dynamics of a mode can be represented by the product of its temporal coefficients and the POD mode, the results in Figure 81 and Figure 82 can be analyzed in terms of their turbulent effects on the mean flow field. The first detail to note, is that the POD coefficients are centered about zero, with positive and negative values that are similar in magnitude. Therefore, a POD mode and its negative counterpart will have the same physical effect. In Figure 81, the highest-energy first mode for $M_c = 0.55$, 0.69 , and 0.88 resembles an axial ‘pulsing’ motion. The dominating streamwise fluctuations in the mixing layer for those cases results in most of the energy being related to this pulsing dynamic, as first introduced in Section 4. 5. In addition, there is no positive-negative pairing of the structures in the shear layer itself (such

as in modes 2 – 4 for those same cases in Figure 82), which indicates that the streamwise fluctuations for those modes are positively correlated throughout the shear layer (*i.e.*, either all negative or all positive). It is reasonable that the energy contained in this mode shape is highest, as the inner product of two snapshots that have a large region of positively correlated u' will have higher magnitude. In contrast, the lowest $M_c = 0.19$ case exhibits a round first mode that also has considerable contribution from the transverse velocity component in Figure 81. The non-zero transverse component of this POD mode causes the shear layer to bend up and down, and thus, is termed an ‘oscillatory’ mode. Mode one for the $M_c = 0.38$ case appears to be a transitional stage from the oscillatory mode for the lowest $M_c = 0.19$ case to the pulsing modes for $M_c = 0.55, 0.69,$ and 0.88 . It can be seen to have both pulsing and oscillating features in its u and v component color contours. Oscillatory modes are also apparent for the three highest M_c cases in their modes 2 – 4, which contain far less energy than their first modes (Figure 82). For the most part, these modes appear to have the same pattern for $M_c \geq 0.38$, except for mode four, which shows a larger structure for $M_c = 0.38$. The shapes and organization of the modes in Figure 82 agree with the result that the large-scale structures in the shear layer become elongated in the streamwise direction and flatten out in the transverse direction. This is especially apparent in modes three and four, where, with increasing M_c , the modes become stretched in the streamwise direction and even start to resemble the polygonal shape that was reported by Clemens and Mungal.³¹

While the POD modes are not to be strictly interpreted as coherent physical structures (for reasons discussed in the POD background), the dynamic effects that the coherent structures have on the flow can be thought of as being captured in these POD modes. It then follows that the spatial frequency of the oscillating modes are related to the size of the structures captured for that mode. While it is expected that the energies converge less quickly for more compressible shear layers (since there is a wider range of turbulent length scales, as verified by Mie scattering), this is not the case, and it is possible that the small-scale eddies contribute a negligible amount of energy to the turbulence.

An effective way to visualize the dynamics of the POD modes is to add the product of the coefficients and mode back to the mean velocity field, as this is the actual motion that the modes induce in the lab frame. From Figure 83, the maximum and minimum coefficients can be taken and multiplied to the POD mode to analyze the limiting dynamics of each mode. Coefficients that are near zero will simply eliminate the effects of the mode altogether, and the mean field will be

the result. Therefore, only the maximum and minimum coefficients are chosen for the plots in Figure 84, where color contours of u -component are plotted with vectors overlaid. A few examples are chosen across modes and cases to demonstrate the pulsing and oscillating dynamics described above. Since the results are plotted for the same velocity scale for each case, the effects of the pulsing motion are illustrated as higher velocity contours being present in the mixing layer for the maximum coefficient (towards red), and vice-versa for the minimum coefficient (towards blue). Mode one for $M_c = 0.55$ in the middle shows the pulsing, and mode one for $M_c = 0.19$ and mode four for $M_c = 0.69$ on the left and right, respectively, show the oscillating motions. The more compressible mixing layer appears to shear diagonally, while the near-incompressible case shows rounder oscillations, with both having a varying number of waveform nodes depending on the POD mode number. Note that the first modes for $M_c = 0.19$ and 0.55 (the left and middle plots) are the most dominant modes for those cases, while the fourth mode for $M_c = 0.55$ (the right plots) contains far less energy and is simply shown as an example of the oscillating mode being captured for the higher compressibility cases.

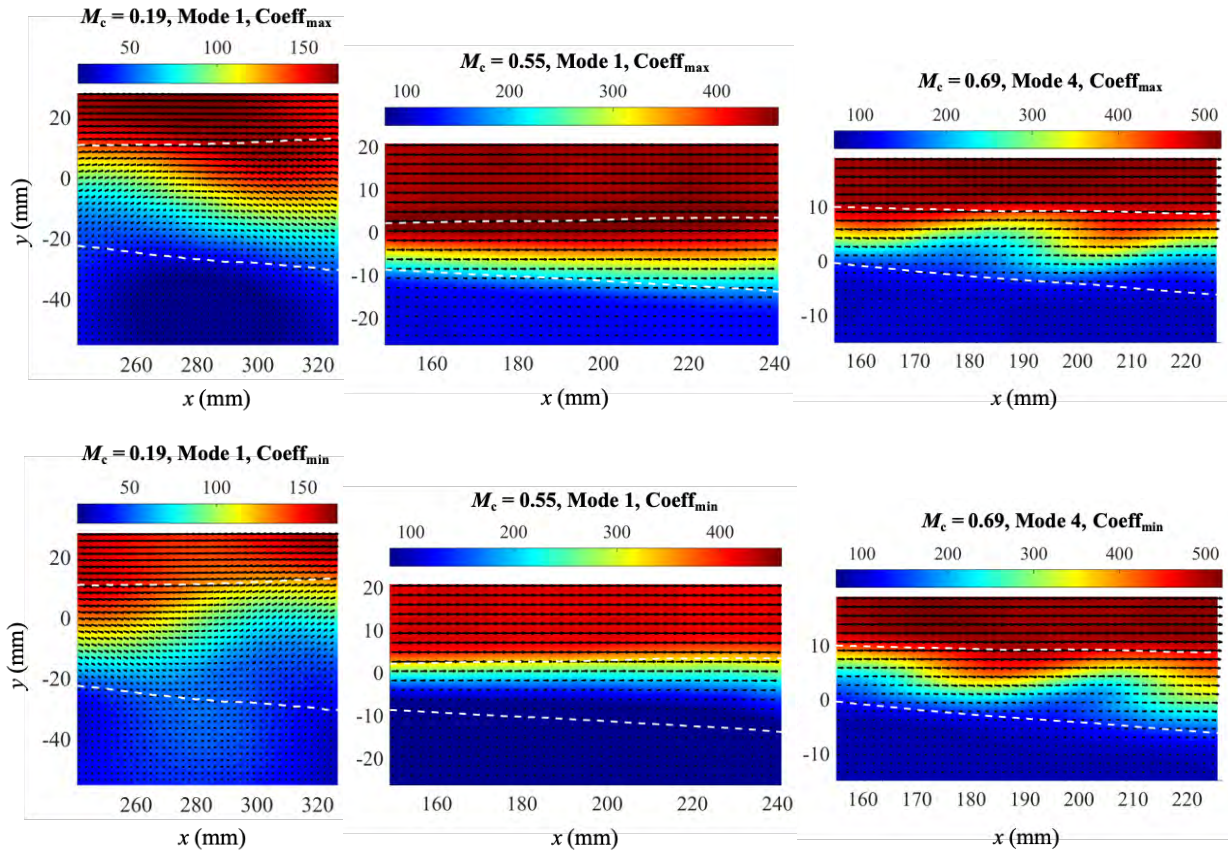


Figure 84. POD mode dynamics for $M_c = 0.19, 0.55$ and 0.69 mixing layers.

For $M_c > 0.19$, the dynamics of the POD are generally well-contained within the shear layer region (*i.e.*, zero in the freestreams); however, for the least compressible $M_c = 0.19$ case, the first three modes extend well beyond the mean shear layer location. For these, plotting streamlines of the POD modes can be a useful visualization of the vortical structures. Doing the same for modes that are near-zero in the freestreams is less useful, since the streamlines are sensitive to vectors with negligible velocity magnitudes. Thus, streamlines are only plotted for $M_c = 0.19$ modes one–three in Figure 85.

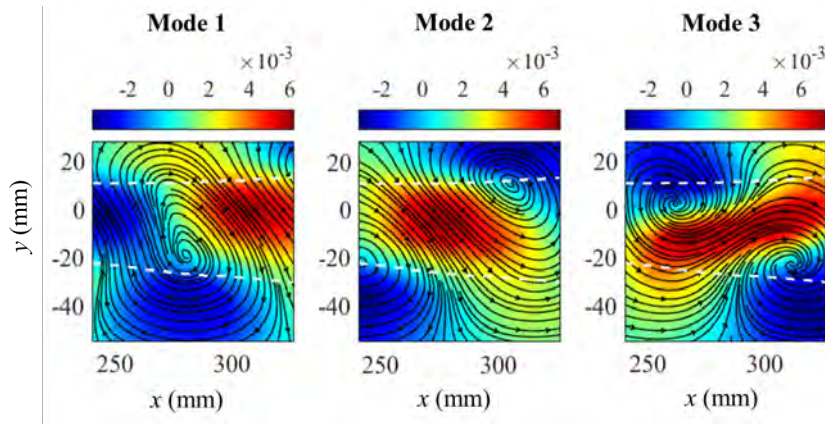


Figure 85. Streamlines drawn for $M_c = 0.19$, POD modes 1 – 3 (with u -component color contours).

It appears that very large structures, which essentially fill the entire FOV, are present for this case. The concept of mode pairing is revisited here, as the first two modes appear as though they are streamwise-shifted versions of each other with the same spatial frequency. It is likely that they both represent the same type of swirling dynamic that causes the shear layer to oscillate, just at different spatial phases. This result is not surprising when considering the fact that the space-only POD method has no access to time information; therefore, spatial frequencies that are phase-shifted may result in different modes. The third mode appears to contain two counter-rotating vortices in opposite corners, where in between them, a braid-like structure is present. The roller-type structure in modes one and two, and the braid-type structure in mode three, were observed and discussed in the schlieren images for this case in Section 3. 4. 1. From the streamlines in Figure 85, it appears that both types are able to be identified via space-only POD, signifying that these large-scale structures are present and dominate the turbulence for this near-incompressible mixing layer case.

The size of these energetic structures is also much larger than the mean shear layer thickness, which has implications on the entrainment mechanisms that are involved. The dynamic motions of the mixing layer extending beyond its mean location into the freestreams, imply that large-scale engulfment is a likely source for the faster growth in incompressible mixing layers. In contrast, the more compressible cases show no mode for which the shear layer dynamics extend far beyond their mean boundaries. This would adversely affect their ability to engulf large amounts of freestream fluid into the mixing region and grow as quickly. A detailed instantaneous entrainment analysis is given in Section 5.3.

To this point, the spanwise component of the POD modes has largely been left out of the discussion of the results. Since the spanwise velocity fluctuations clearly contribute to the turbulence, a discussion of their POD modes is warranted. Space-time POD of an incompressible planar mixing layer has shown that there are large, counter-rotating vortices oriented in the streamwise direction, which induce slight distortion of the Brown-Roshko rollers in the span (*i.e.*, lambda-shaped organization).^{70, 75} This result was obtained from a three-dimensional reconstruction of the first mode via a cross-rake of hotwires that was traversed in both the streamwise and spanwise directions. While such level of detail cannot be extracted from these space-only, planar POD modes, information can still be obtained about the spatial distribution of the spanwise velocity fluctuations. First, it should be reiterated that the highest-energy mode shown in Figure 81 had very little contribution from the w -component for any of the cases. Therefore, it can be said that the large-scale, dominant energetic eddies do not have well-correlated, repetitive spanwise motions for any level of compressibility. In fact, the w -component of the POD modes does not have significant contribution for any M_c until mode six for $M_c = 0.19$ and 0.38 , by which point the energy is decreased to $\leq 2.6\%$. This result is expected for a planar investigation, where symmetry should eliminate consistency of signed w' .

While spanwise fluctuations are not relevant in the lower-order POD modes, there are higher-order modes that show organization and high relative w -component magnitude compared to u and v . The highest-energy modes for which w has clear organization are 6, 6, 9, 10, and 12, in order of increasing M_c . These are plotted in Figure 86. The fact that the mode number at which the w -POD magnitude is on the scale of u and v POD magnitudes, increases with M_c , agrees with the relative decrease of Re_{zz} with increasing M_c . Additionally, it appears that the w -braids that were observed in the instantaneous velocity fields (Figure 33) are captured in these modes. The results shown

here follow the qualitative observation that the w -braids become thinner and are oriented at a more oblique angle (*i.e.*, closer to horizontal) with increasing compressibility. The stretching and orientation of these structures are also in agreement with the observations from qualitative flow visualizations.

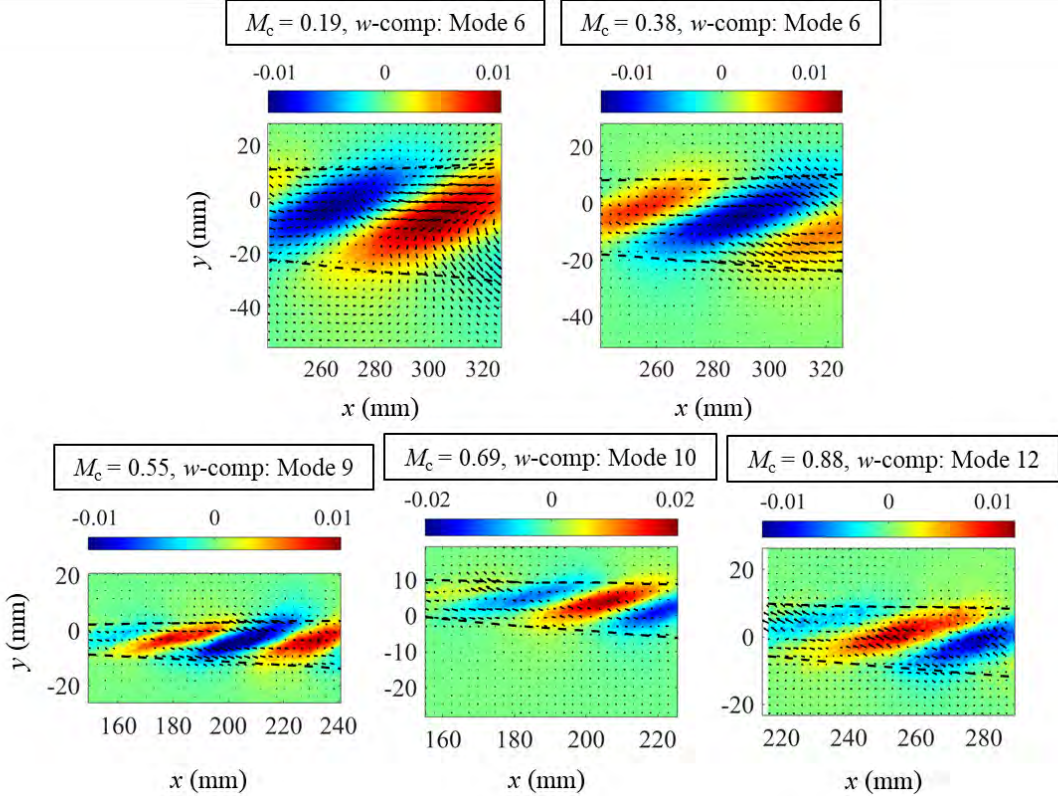


Figure 86. Color contours of side-view w -component POD modes.

The w -braids that are shown in Figure 86 imply that there are streamwise-oriented vortices present in the current mixing layers, as was shown in the purely incompressible case, albeit in lower-energy modes here. In order to investigate this notion further, POD was performed for the end-view (y - z) planes. For all M_c cases, the u and v components for mode one agreed with the first mode shown for the side-views, with oscillatory motions dominating at lower compressibility and pulsing being dominant for higher compressibility. In addition, the trend of more energy being contained in the first mode for higher M_c was also found to be the case. For these views, however, the primary objective was to detect the streamwise-oriented vortices, which are most apparent when plotted as w -component color contours, with v - w streamlines overlaid. These are plotted in Figure 87 for specific modes which highlight the desired structures (with relative energies given).

Streamwise vortices are present in mode three for $M_c \leq 0.55$, mode five for $M_c = 0.69$, and do not exist for any mode for the most compressible case. Their decrease in relative size to the shear layer with increasing M_c is apparent, where they are present. While the spanwise width of these energetic structures cannot be determined from the x - y planes (Figure 86), the reduction in size with increasing M_c found in Figure 87 is seemingly in agreement with the stretching and more oblique w -braids found in the side-views. More generally, the end-view results also agree with the higher level of three-dimensionality of the large-scale structures with increasing compressibility, as the streamwise vortices become smaller and less coherent. By $M_c = 0.88$, no mode is able to capture coherent organization of w' in the y - z plane, as evidenced by the streamlines.

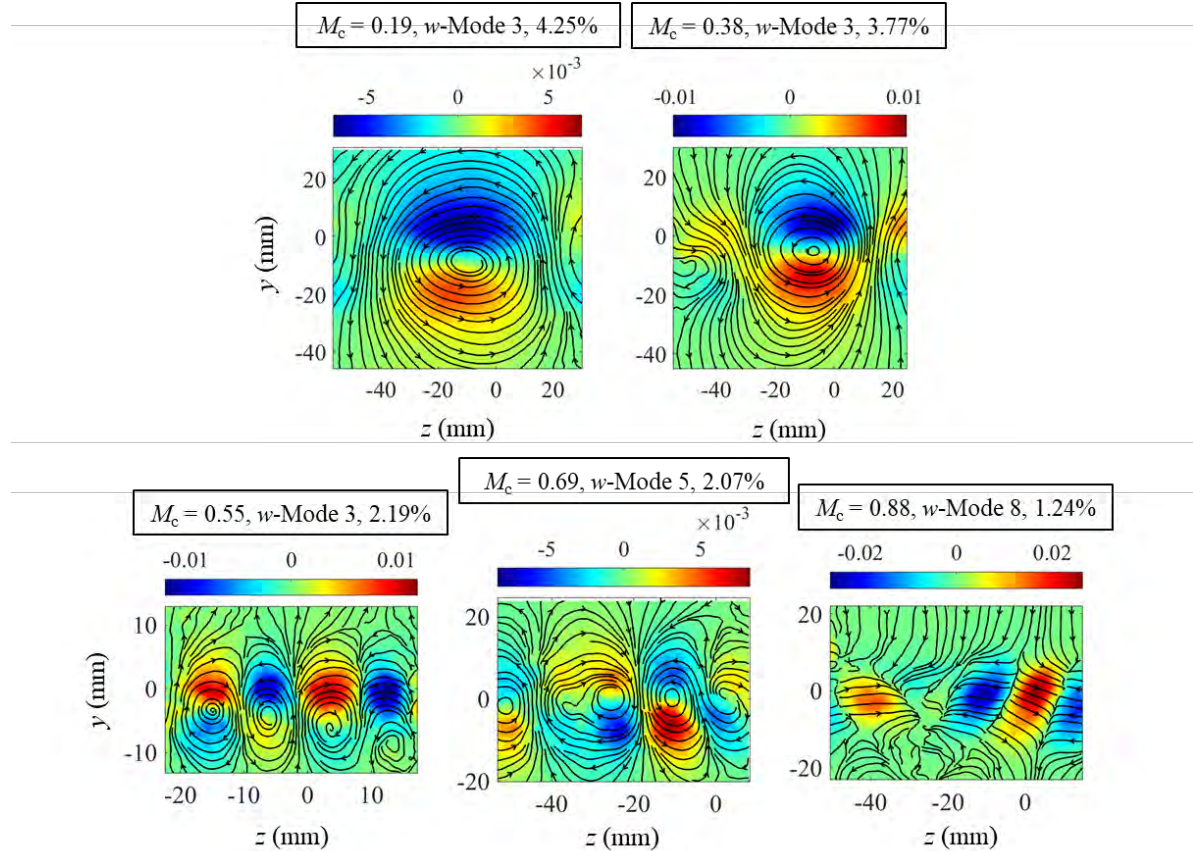


Figure 87. Color contours of end-view w -component POD modes.

The global dynamics present in turbulent mixing layers have been shown in this section, where planar velocity fields were used to obtain POD modes of all three velocity components. As discussed, while the spatial eigenmodes are based on large-scale structures, they are not quite representative of the structures themselves. Moreover, the modes are dimensionless and represent

the distribution of turbulent energy. A flow analysis technique that does result in turbulent structures via conditional averaging is discussed next.

5. 2. Linear Stochastic Estimation

5. 2. 1. LSE Background and Method Description

Unlike space-only POD, linear stochastic estimation (LSE) can be used to extract coherent physical structures that are present in the flow. While snapshot POD unconditionally incorporates the velocity fields to produce spatial energetic modes, the results of LSE are conditionally averaged flowfields of a specific large-scale structure. The condition is based on a particular event that can detect the existence of said structure. Instead of filtering the ensemble based on an occurrence of the event (*i.e.*, true conditional averaging), which drastically reduces the ensemble size, the conditional average can be calculated as a linear estimate. It should be noted that the concept of conditional sampling in turbulence has been abundantly investigated and comes in many different analysis forms (*e.g.*, turbulent zone averaging based on the intermittency function, conditional sampling based on quadrant analysis, periodic sampling, coherent structure extraction, etc.).⁸⁰ The method used here follows the linear mean-square stochastic estimation technique laid out by Adrian and Moin (1988),⁸¹ and its chief purpose is to obtain an average flowfield that describes a structure at a specified reference location, with the structure being characterized by a conditional event at that reference point (*i.e.*, last example given in list of conditional sampling techniques).

Much like in the Karhunen-Loève expansion, the mathematics behind LSE is based on mean-square error minimization between the desired conditional average and an estimation of it. In LSE, the estimate is calculated as a linear function of the conditional events that are chosen. In general, the events can be tensors, and there can be multiple events that are chosen to specify a coherent structure. The coefficients of the linear estimate are determined by minimizing the mean-square error, which results in two-point correlations between the event(s) and velocity data.⁸¹ Therefore, with LSE, a conditional flowfield can be determined using an unconditional correlation function. Not having to directly compute the conditional structures based strictly on an occurrence of the event is a powerful outcome. As was briefly mentioned, with the direct approach, the ensemble size used to determine the resulting mean field becomes drastically reduced, especially if the dimension or number of events is high. The probability of an event occurrence exponentially decreases with the dimension and/or number of events, since there are more conditions that must

be met to include an occurrence in the ensemble. Additionally, the event can be set to a highly specific condition, since, in essence, the result is a weighted average of the entire ensemble based on the event. The relationship between the linear estimate and conditional average is given in Equations (21) – (22), where u_i' represents the fluctuating velocity component, α is the physical event indicator (note this is a scalar value here), L_i is the linear estimation kernel, $(x_{\text{ref}}, y_{\text{ref}})$ is the location of the reference point, and (X, Y) are the streamwise and transverse range, respectively, of the reconstructed domain.⁸²

$$\overline{u_i'(x_{\text{ref}} \pm X, y_{\text{ref}} \pm Y) | \alpha(x_{\text{ref}}, y_{\text{ref}})} \approx L_i \alpha(x_{\text{ref}}, y_{\text{ref}}) \quad (21)$$

$$\overline{u_i'(x_{\text{ref}} \pm X, y_{\text{ref}} \pm Y) | \alpha(x_{\text{ref}}, y_{\text{ref}})} \approx \frac{\overline{\alpha(x_{\text{ref}}, y_{\text{ref}}) u_i'(x_{\text{ref}} \pm X, y_{\text{ref}} \pm Y)}}{\overline{\alpha(x_{\text{ref}}, y_{\text{ref}}) \alpha(x_{\text{ref}}, y_{\text{ref}})}} \alpha(x_{\text{ref}}, y_{\text{ref}}) \quad (22)$$

In the equations above, there are two variables involved in estimating a conditionally averaged flowfield with LSE: the instantaneous velocity fields (u_i') and the event to condition upon (α). Definition of the first term is fairly straightforward, with choices limited to the different types of decomposition that are generally used on velocity-field data (e.g., Reynolds, Galilean, LES decompositions).⁶⁴ For the present LSE analysis, as in the other analyses performed in this dissertation, the Reynolds decomposition is chosen where the mean velocity field is subtracted from the instantaneous flow. While many other LSE studies use the Galilean decomposition, where a constant nominal convective velocity is subtracted from the streamwise component of the flow, the definition of U_c in the present flowfield is not as well-defined at higher levels of compressibility. In addition, as mentioned in Section 4.6.1, it is not clear if the structures all convect at a constant velocity. Thus, removing the local mean velocity is a reasonable method and should highlight the conditional large-scale structures clearly in the mixing layer while eliminating the freestreams. Furthermore, subtracting the mean transverse velocity from the flow eliminates the slightly non-zero V from the unavoidable waves (in super/sonic primary streams). This helps to remove the effects of the waves in the sonic/supersonic primary streams on the resulting structure shapes.

The question of which condition to use as a structure identifier is one that is integral to the LSE analysis, with the event condition, α , having been examined in numerous different flows in various investigations. This topic of study is inevitable with the concept of identifying a conditional-eddy

structure, as there are different kinematic flow conditions that best identify certain types of structures. Adrian and Moin showed in a DNS of homogeneous turbulent shear flow, that upright and inverted hairpin vortices could be highlighted with second-quadrant and fourth-quadrant Reynolds shear stress events, respectively.⁸¹ Similarly, Christensen and Adrian (2001), using the previously introduced swirling strength quantity (Section 4.6.1), were able to detect packets of these hairpin vortex structures in a turbulent channel flow experiment.⁸² In what are the most relevant LSE studies to the present flowfield, Olsen and Dutton (2002 and 2003), investigated planar mixing layers that were incompressible ($M_c \sim 0$) and weakly compressible ($M_c = 0.38$).^{83,32} They used specific deformation tensor values to identify roller and braid structures and found that rollers corresponded to peaks in vorticity magnitude, while braids corresponded to peaks in shear strain rate magnitude. As for compressibility effects between the two mixing layer cases, the weakly compressible mixing layer exhibited roller structures that were higher in eccentricity (with a horizontal major axis) and braid structures that were vertically oriented as opposed to oblique in the incompressible case. They attribute the shift in braid orientation to the ‘kinked’ braid positioning in compressible mixing layers observed by Clemens and Mungal.³¹ Vorticity and strain rate magnitudes are chosen as conditional events for the present study to see if similar results for rollers and braids are attained for the current $M_c = 0.19$ and 0.38 cases and to see how they evolve as M_c is further increased.

The last point of discussion before the results are presented is where in the shear layer the reference location should be positioned. Unlike the previous POD analysis, LSE is a localized examination of the flow, and the results will differ depending on where in the shear layer (especially in the transverse direction) the reference position is located. Kirchner *et al.* (2018) found that for a supersonic base flow experiment, probing near the freestream side in the turbulent shear layer resulted in conventional hairpin vortices, while probing near the recirculating region resulted in counter-rotating hairpins (both with a three-dimensional swirling strength criterion).⁸⁴ In the present study, a reasonable transverse location can be determined from the empirical U_c that was determined in Section 4.6.1. The large structures convect near that U_c ; thus, the location where the mean streamwise velocity is equal to U_c should theoretically be where vortex quantities are most prominent, and about which the structures are centered. While the possible inaccuracies involved with using a single, constant convective velocity have been mentioned, the location where $\bar{u} = U_c, \text{empirical}$ is generally very close to y_0 and should suffice for the purposes of identifying a

reference location. As for the streamwise location, the center of each FOV is chosen to maximize the size of the reconstruction FOVs.

5. 2. 2. Spatial Velocity Correlations

The two-point velocity spatial correlation tensor can be thought of as a precursor to LSE (since it is essentially LSE with the condition set to the velocity vector itself) and can be useful in its own right to examine the typical spatial organization of the velocity fluctuations. Unlike LSE, these correlations are not necessarily meant to be interpreted as coherent physical structures themselves. Instead, they can give insight into the different shapes and orientations associated with the turbulent fluctuations and can be used to characterize the turbulent eddies in a qualitative sense.

The definition of the two-point velocity spatial correlation tensor is given in Equation (23), and color contour maps of the results are shown in Figure 88 – Figure 91. One correlation value is chosen in the contour maps and drawn in a black line to illustrate the evolution of the correlation shape and orientation with increasing compressibility. While the contour value chosen is somewhat arbitrary, as long as it is a fairly small number above zero ($\sim 0.2 - 0.3$), the same qualitative trends hold true. The reference point chosen for these are the same as for the turbulence length-scale correlations that are performed in Section 4. 5 (middle of FOV for x_{ref} and y_0 for y_{ref}), and the results are ensemble averaged over a streamwise length of $x_{\text{ref}} \pm 0.5$ mm. Note that each direction is normalized by the local shear layer thickness. The difference between these correlations and the ones performed in the turbulence length-scale analysis is the two points being correlated. The latter are at two different locations separated by l in either the streamwise or transverse direction, while in Equation (23), a correlation map is created surrounding the reference point (with range $(\pm X, \pm Y)$).

$$C_{ij} = \frac{\overline{u_i'(x_{\text{ref}}, y_{\text{ref}}) u_i'(x_{\text{ref}} \pm X, y_{\text{ref}} \pm Y)}}{\sqrt{\overline{u_i'^2(x_{\text{ref}}, y_{\text{ref}})}} \sqrt{\overline{u_i'^2(x_{\text{ref}}, y_{\text{ref}})}}} \quad (23)$$

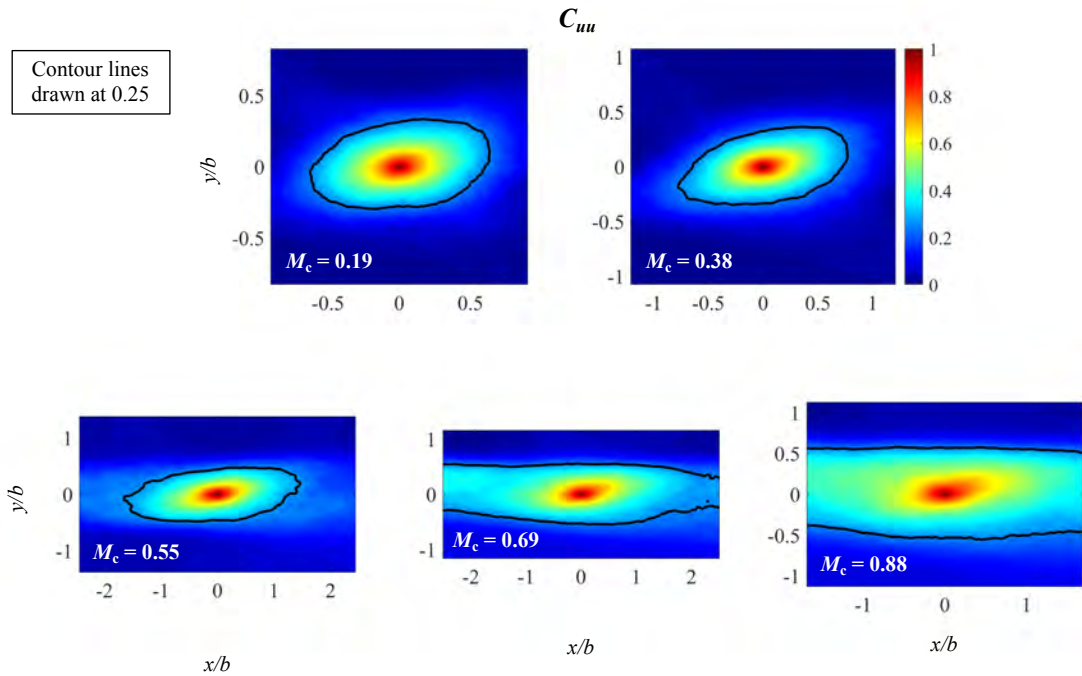


Figure 88. Color contours of C_{uu} .

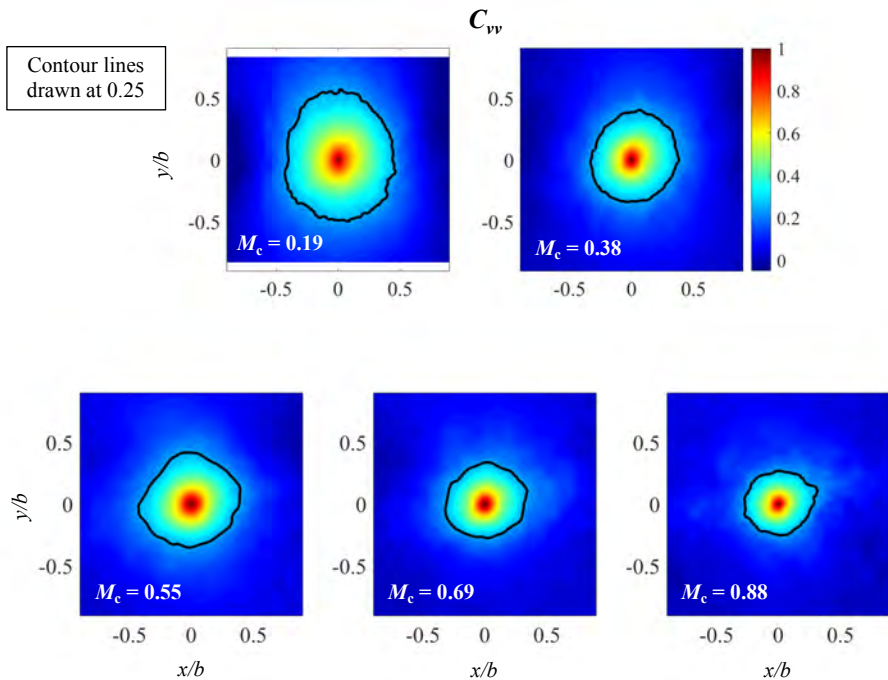


Figure 89. Color contours of C_{vv} .

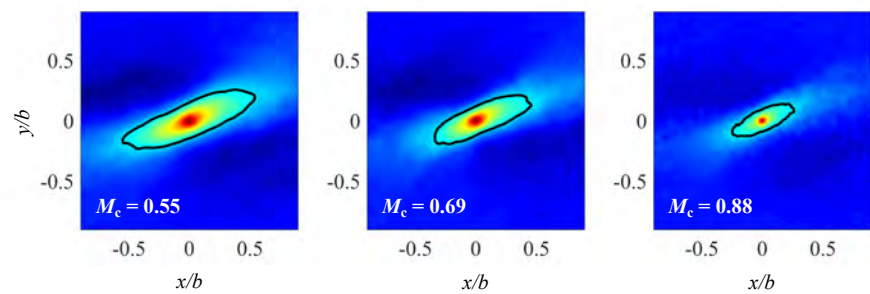
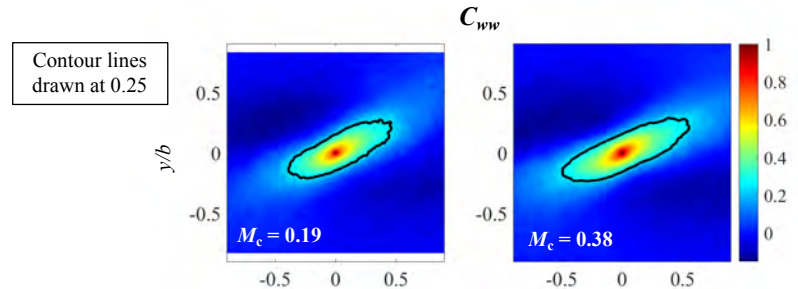


Figure 90. Color contours of C_{ww} .

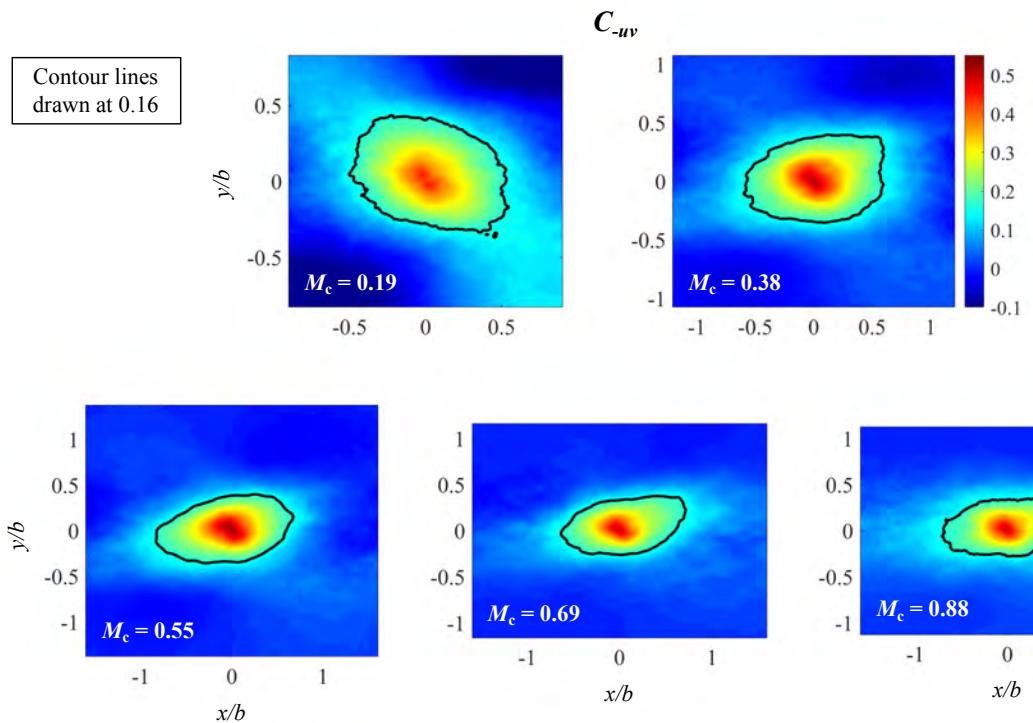


Figure 91. Color contours of C_{uv} .

Correlations of the lowest $M_c = 0.19$ mixing layer are examined first. The transverse extent of C_{uu} (as drawn for the value of 0.25 in Figure 88) is slightly taller than half the shear layer thickness, and in the streamwise direction, it extends slightly more than one shear layer thickness. This indicates that the typical size of a u' cluster (defined as a coherent region of positively correlated u') is $\sim b/2$ tall and $\sim b$ long. C_{vv} for $M_c = 0.19$ on the other hand (Figure 89), stretches the entire transverse extent of the mixing layer and is taller than it is wide. If an instantaneous large-scale structure is thought of as having both positive and negative components of u' and v' , the combination of these two correlation maps would indicate the existence of roller-type structures that are slightly larger than the local shear layer thickness in diameter (since for a single roller, one positive and one negative u' cluster would be stacked on top of one another, and one positive and one negative v' cluster would be adjacent, side-by-side; see Figure 92). A similar result can be seen for the $M_c = 0.38$ case, but with a more elongated C_{uu} and shorter, more circular C_{vv} , which is now less than b tall. The trends of these two correlations combined for this case results in stretched-out roller structures that are shorter than b in the transverse direction, but longer than b in the streamwise direction. This is in direct agreement with the schlieren photographs, which show that the rollers become elongated for this case (Figure 27).

As compressibility is further increased to $M_c = 0.55$, C_{uu} undergoes a transformation such that it is now b tall in the transverse direction (*i.e.*, extending the entire shear layer height) and non-zero for the entire streamwise extent of the FOV. While the 0.25 contour drawn is entirely contained in the FOV for this M_c , the color contour map shows the above-zero C_{uu} region that extends to the left and right edges of the FOV. This is an important shift from the previous $M_c = 0.38$ case and is coupled to the shift seen in the dominant, low-order first POD modes that were shown in Figure 81 ('pulsing' modes). Clearly, the u' clusters being b tall does not mean that roller structures that are $2b$ tall exist on average in the mixing layer (since a roller requires a positive and negative u' cluster stacked on top of one another). This can be verified qualitatively in the schlieren, as well as from the fact that C_{vv} is not $2b$ tall. Thus, the concept of a pulsing dynamic is once again shown to be significant for these high M_c cases, as it is likely that the domination of the streamwise

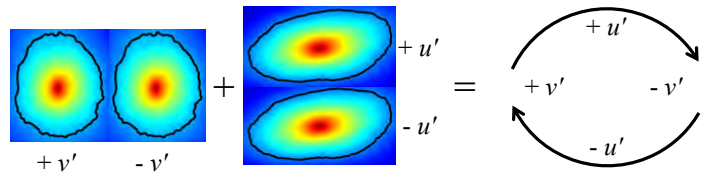


Figure 92. Combination of C_{uu} and C_{vv} in a nominal roller structure for $M_c = 0.19$.

fluctuations over the other components causes the large-scale structures to elongate and eventually lose their round shapes.

From $M_c = 0.55$ to 0.88 , C_{uu} increases in magnitude in the streamwise direction, and C_{vv} decreases in size overall with increasing M_c . As the pulsing mode becomes more dominant for higher M_c , streamwise fluctuation correlations increase for the entire transverse height of the shear layer, and the u' clusters are also longer in the x direction. C_{vv} decreasing in size indicates that the turbulent eddies decrease in size as they become less organized. While this was previously visualized with the Mie scattering images, these correlations show the result in a quantitative manner. The difference between the decrease in C_{vv} and increase in C_{uu} , especially in the transverse direction, is also consistent with the reduction of the normalized growth rate. As the v' clusters decrease in size relative to the shear layer and u' clusters increase in size, the ability of the turbulent fluctuations to transport fluid in the transverse direction from the freestream into the mixing layer decreases. Also, while it was clearly understood prior to this that the intensity of the transverse fluctuations decreased (via Re_{yy} reduction), these correlation maps conclusively show that they are also less spatially organized for higher M_c .

All contours of C_{uu} in Figure 88 are also in very good agreement with the results of the turbulence length scale analysis presented in Section 4.5. Overall, $l_{u'}$ increases in both the streamwise and transverse directions with increasing M_c , and when closely examined, it can be seen that there is a significant jump from $M_c = 0.38$ to 0.55 for streamwise $l_{u'}$ in Figure 69 (left, black curve). This result is consistent with C_{uu} above, and when considering that the first POD mode also shows a major change between these two M_c cases, it is likely that there is a distinct physical transition between the two levels of compressibility. The transition is characterized by the disappearance of large, quasi-spanwise coherent rollers, and the onset of major axial pulsing with correlated regions of u' that extend the entire shear layer thickness in the y direction and multiple thicknesses in the x direction. The schlieren images also indicate this, as the complete loss of large-scale spanwise organization occurs between $M_c = 0.38$ and 0.55 . Further support for this claim is the difference between the empirically determined convective velocity and the isentropic definition (Figure 72). The two are equal for $M_c = 0.19$ and 0.38 but start to deviate at $M_c = 0.55$, at which point their differences increase with M_c . Physically, this result agrees with the concept of the isentropic definition requiring a stagnation point (in the convective frame) in the thin braid region between roller structures. If the higher M_c mixing layers no longer contain these well-

defined, thin braid regions (and thus, do not contain well-defined saddle points), isentropic relations will overestimate the actual convective velocity. Clemens and Mungal also report complete loss of Brown-Roshko-like roller structures between their $M_c = 0.42$ and 0.62 cases, which is consistent with the transition between $M_c = 0.38$ and 0.58 for the present results.³¹

As for C_{ww} , Figure 90 confirms that the w -braids (in the same sense as the term ‘clusters’ has been used in the preceding paragraphs) decrease in size and become more aligned with the horizontal with increasing M_c , as will be shown quantitatively below. The decrease in size of C_{ww} relative to the local thickness is similar to the C_{vv} trends and agrees with the existence of smaller-scale turbulence for higher levels of compressibility. Additionally, the decreased organization of the structures in the span can likely be attributed to these smaller regions of correlated w' , which would reduce the ability of large structures to maintain organization in the spanwise direction. The closer-to-horizontal tilt angle of each correlation map qualitatively supports the stretching and elongation of the structures, as the stretching results in a more oblique orientation of the structures with respect to the transverse direction (in terms of their major axis). In an attempt to quantify the orientation of each C_{ww} map, a method to estimate their tilt angles is performed based on eigendecomposition of the covariance matrix of the correlation map. Second central moments in the x and y directions comprise the covariance matrix, and the eigenvectors correspond to the principal axes of the correlation map. To reduce the effects of noise in the C_{ww} maps, a threshold is set, and once the tilt angle calculated remains constant with respect to the threshold, the angle is determined. The resulting angle (with respect to the horizontal) is plotted against M_c in Figure 93, where the monotonic decrease of the angle with M_c can be seen. This quantitative confirmation of decreased w -braid orientation angle is a novel finding in mixing layer turbulence. It further explains the reduced ability of higher compressibility mixing layers to grow in the transverse direction, as the streamwise vortices become thinner in the transverse direction and elongated in the streamwise direction.

Finally, C_{uv} (Figure 91) shows the least amount of change with compressibility in the transverse direction, with it remaining slightly less than b tall for all cases. In the streamwise

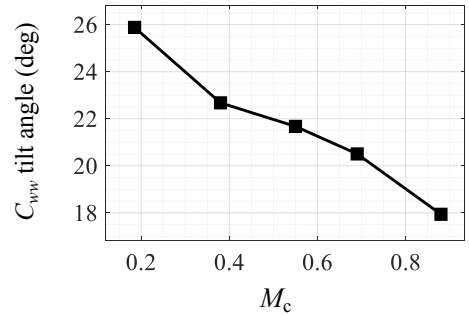


Figure 93. C_{ww} tilt angle (with respect to the horizontal) vs. M_c .

direction, the correlation map increases in size with increasing M_c , which is likely due to the streamwise component correlations increasing in the streamwise direction. The maximum correlation magnitude is ~ 0.5 for all M_c , which is in agreement with Olsen and Dutton, who report a value of 0.46 and 0.47 for their incompressible and mildly compressible cases, respectively.^{32, 83} The least compressible $M_c = 0.19$ case shows a slight negative-slope tilt in the contour map which becomes horizontal for the other more compressible cases. The contour map shapes of the two lowest M_c cases are in agreement with Olsen and Dutton's two cases. Overall, the C_{uv} shapes are less symmetric than the other correlations.

It should be emphasized that the trends of estimated correlation map heights and widths are given for the contour value plotted (0.25 or 0.16, in black lines), and while the value chosen will affect the exact size relative to b , the general trends hold true across M_c (since the same contour value is plotted across all cases). As mentioned in the beginning of this section, the correlation maps presented in Figure 88 – Figure 91 are representative of a typical cluster of correlated fluctuations. They can be useful for identifying the rough size and orientation of general turbulent structures, as was done above; however, for more detailed shapes of the turbulent eddies, LSE fields should be examined. The results of the LSE analysis that was described in the previous section are discussed next.

5. 2. 3. LSE Results and Discussion

Results of two distinct structures, rollers and braids, are presented here from the LSE technique described by Equation (22) in Section 5. 2. 1. Spanwise vorticity and shear strain rate are used to identify these structures following the work of Olsen and Dutton, who also investigated planar mixing layers and found the magnitudes of these two quantities to peak at the center of rollers and braids, respectively.³² For roller structures, α is set to a negative vorticity condition, with the reference vorticity magnitude set to a typical value found at the center of roller structures in the instantaneous images. For braids, the same procedure is performed with α set to strain rate. Note that the reference value (α outside the ensemble average operators on the right-hand-side of Equation (22)) is a scalar; thus, its magnitude simply scales the resulting flow field by a constant. Therefore, when analyzing the estimated conditional velocity fields, the total velocity magnitudes are less important than the magnitudes of the velocity components relative to each other, as both components are scaled identically by the magnitude of the reference condition chosen (which is

subject to hand-picking). The roller structures identified via negative vorticity are shown in Figure 94 as u' color contours with streamlines overlaid for the five M_c mixing layers. The reference vorticities for the five cases were -30 , -60 , -130 , -150 , and -150 (s^{-1}) in order of increasing compressibility. In Figure 95, the braids were obtained with reference strain rates of 30 , 60 , 130 , 150 , and 250 (s^{-1}) in order of increasing M_c . For both figures, the streamwise and transverse coordinates are normalized by the local shear layer thickness at the reference location for each case.

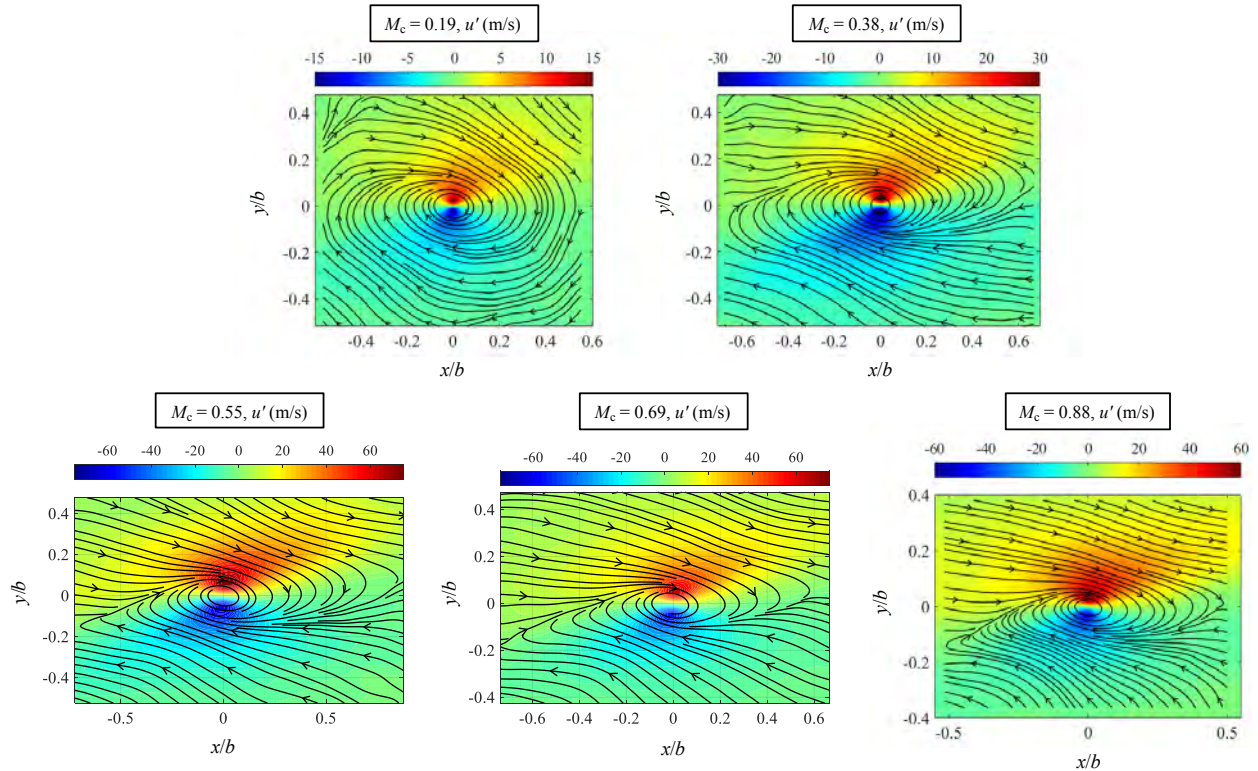


Figure 94. LSE roller structures for $M_c = 0.19, 0.38, 0.55, 0.69$ and 0.88 mixing layers with streamlines plotted on top of u -component color contours.

At the lowest level of compressibility, the $M_c = 0.19$ case exhibits a round roller structure, and as M_c increases, the rollers become flattened out in the transverse direction and appear stretched in the streamwise direction. The streamlines are overall more horizontal everywhere in the FOV as compressibility increases. These results are overall in agreement with the schlieren and spatial correlation results. While these structures were expected to be resolved for the two lower M_c cases, coherent rollers being shown for the three highest M_c cases is a novel finding that was absent in analyses prior to the conditional averaging technique. Due to the dominating pulsing dynamic for

those cases, the coherent eddies become difficult to detect when only velocity fluctuations are considered, and the vorticity conditioning is required to extract these structures. Thus, while roller-type eddies are present for $M_c = 0.55 - 0.88$ in Figure 94, they are likely less prominent in those cases than the two lower M_c cases, for which the spatial correlations also indicate rollers. In addition, as noted in the previous subsection, the shape transformation of the rollers for increased compressibility is likely a result of the pulsing dynamic. The magnitude of the u' velocity color scale represents the conditional fluctuating velocity magnitude given the chosen reference vorticity; however, as was discussed, the scalar nature of α means that the entire result is simply scaled by whatever the reference is chosen to be. Since the reference values of vorticity were chosen in a heuristic manner (*i.e.*, manually checked values for a few instantaneous fields), not much emphasis is placed on the magnitudes of the color bar scales other than that the absolute velocity increases with M_c .

The results for the braid structures using strain rate as the conditional event are plotted in Figure 95. The distinct trend of the braid orientation aligning more with the horizontal can be seen for increasing compressibility, as the stagnation streamlines become closer to horizontal for increasing M_c . In addition, it can be seen that portions of the roller structures are captured upstream and downstream of the braids on the left and right ends of the FOVs in Figure 95. This confirms the qualitative observations from flow visualizations that these braids exist between the rollers and serve as a connection mechanism between contiguous rollers. The flatter orientation of these braid structures, then, is an outcome that should be expected with the flattening of the roller structures observed in Figure 94. The outcome is also in agreement with the result of the spanwise fluctuations becoming flatter that was shown in Figure 93. While the spanwise velocity is not used in the LSE analysis (due to the symmetry that should remove correlation of signed w'), the overall streamwise stretching of roller and braid structures is in agreement with the flatter orientation of the spanwise mixing indicated in Figure 93.

Compared to the results of Olsen and Dutton, the results for the roller structures here are in agreement (higher eccentricity for higher M_c); however, the braid structures are slightly different. While for their incompressible mixing layer Olsen and Dutton report a braid that resembles the $M_c = 0.19$ case here, for their weakly compressible mixing layer (with the same M_c of 0.38) they report stagnation occurring along a vertically oriented line. In contrast, the results in Figure 95 all show stagnation occurring at a point. One possible reason for this difference could be that Olsen and

Dutton use the full deformation tensor for their condition, with tensor components that correspond to peak vorticity and strain rate magnitudes for the rollers and braids, respectively (rather than using the two scalar quantities directly as the conditions, as was done here in α). Their method requires a more robust definition of the reference condition, as it no longer is a scalar, and the tensor components would not simply scale the entire result by a constant. For their small ensemble size (37 instantaneous images) and relatively low levels of compressibility, hand-picking representative deformation tensor component values is certainly possible to do. However, for the current mixing layers, where M_c reaches as high as 0.88, hand-picking reference tensor components, for structures that are difficult to even identify via qualitative observation, is less effective than using a scalar value.

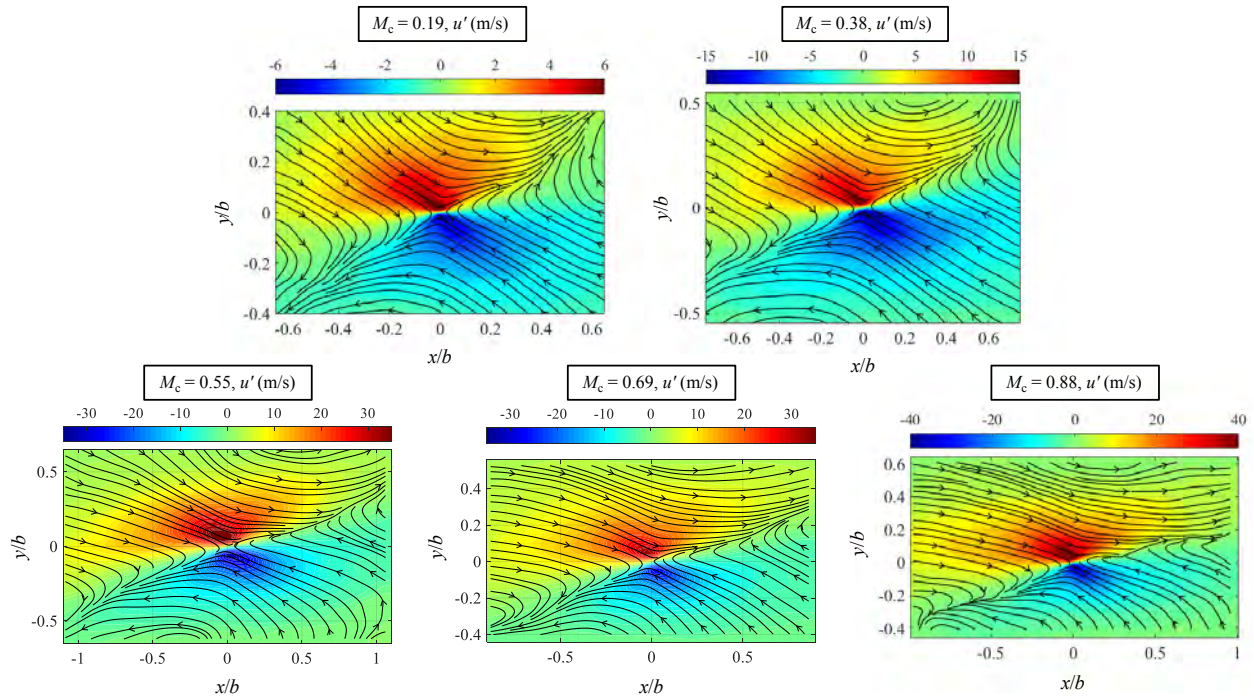


Figure 95. LSE braid structures for $M_c = 0.19, 0.38, 0.55, 0.69$ and 0.88 mixing layers with streamlines plotted on top of u -component color contours.

In addition, Olsen and Dutton use a Galilean decomposition ($u' = \bar{u} - U_c$) as opposed to the Reynolds decomposition chosen here. In the current mixing layers, where the freestream velocity magnitudes are much higher than the transverse fluctuations, the Reynolds decomposition better shows the detail of the structures by removing the freestream velocities. The fluctuations can be conditionally averaged without the fields being dominated by large streamwise velocity magnitudes above and below the structures (even with U_c subtracted). The qualitative information

contained within the LSE of the two decompositions should be similar (since they are both of the same flowfield and use the same conditional events); however, the Reynolds decomposition shown here gives the structures improved visibility and better highlights the compressibility effects. On the other hand, a disadvantage of the Reynolds decomposition is the removal of the mean streamwise velocity gradient in the transverse direction, which likely affects the size of the structures in the y direction. Therefore, the orientation of the streamlines is given more emphasis than the relative sizes of the LSE results in the discussion above.

The evolution of the roller and braid structures as they become flatter and more horizontal with increasing M_c is in agreement with the flow visualization, turbulence length scales, POD, and spatial correlations. They all give the same description of large-scale structures elongating and becoming aligned in the streamwise direction with increasing M_c — a result linked to the domination of the pulsing mode with increased compressibility, since the streamwise pulsing causes the round shapes to stretch out. As mentioned previously, this evolution is likely also linked to the reduced ability of highly compressible mixing layers to entrain freestream fluid and grow in the transverse direction. The next section attempts to quantitatively show the differences in entrainment mechanisms and the turbulence interfaces in general for the current mixing layers.

5. 3. Entrainment Analysis

Information about the size and shape of turbulent eddies is helpful for understanding the large-scale organization within the mixing layer; however, in order to better understand the interactions at the interface between the mixing layer and the freestreams, a local entrainment analysis is useful. As previously noted, the physical process by which the mixing layers are able to grow (in thickness) as they develop, is the entrainment of freestream fluid into the turbulent region; thus, an investigation of the local physics at the turbulent boundary should give further insight into the reduced growth rate of higher M_c shear layers.

In the literature, entrainment mechanisms have been categorized as either large-scale engulfment, an inviscid phenomenon by which packets of non-turbulent fluid are entrapped by the turbulent flow, or nibbling, for which small-scale eddies at the interface cause viscous diffusion of vorticity across it (causing freestream fluid to become rotational and thereby part of the mixing layer).⁸⁵ In previous works, nibbling was found to be dominant for incompressible jets and wakes, with large-scale engulfment contributing to less than 10% of the total mass flux for either flow.⁸⁶

⁸⁷ For compressible free shear layers, Jahanbakhshi and Madnia (2018) performed a DNS study and showed that for a range of $M_c = 0.2 - 1.8$, the engulfment mass flow rate was found to decrease with increasing M_c , and was never above 8% of the total mixing layer mass flow rate.⁸⁸ These results are somewhat surprising, considering that intuition would lead to the belief that large-scale structures with large-curvature interfaces would engulf large amounts of fluid from the freestreams. It should therefore be emphasized that, when reviewing these empirical analyses of entrainment, one needs to take into account the specific methodology followed in each analysis. Many of the studies, while agreeing on the heuristic definition of engulfment and nibbling, go about quantifying the contributions of each mechanism very differently. For example, Westerweel *et al.* (2009) use an engulfment definition based on light intensity from acetone PLIF images, while Jahanbakhshi and Madnia define engulfment as the mass of irrotational fluid pockets in the mixing layer.^{87, 88}

Entrainment studies on experimental data of planar shear layers have generally been limited to an integral analysis involving turbulent zone averages of velocity and the intermittency factor to determine the entrainment ratio of the two streams (*e.g.*, Brown, 1974).⁸⁹ Furthermore, in Brown's analysis, the limits of integration in the transverse direction required a level of arbitrariness due to experimental data being used from multiple different investigations. The previous lack of high-resolution instantaneous velocity fields also required past mixing layer entrainment analyses to be based strictly on mean quantities. Some researchers have even attempted to model entrainment for planar shear layers based on the existence of Brown-Roshko rollers and a constant spacing between them.⁹⁰ As emphasized throughout this writing, however, the roller structures, while coherent in the incompressible limit, become highly disorganized with increasing compressibility. Thus, using a constant spacing between them to determine the mass and/or volume flux into the mixing layer is less than ideal for higher convective Mach numbers.

Since dense, planar, instantaneous velocity fields are available in the present study, an analysis based on identifying instantaneous turbulent/non-turbulent interfaces (TNTIs) is performed here. First, the methodology of detecting the TNTI for each image is discussed (a non-trivial matter), and statistics of the interface itself, as well as conditional averages of turbulence quantities across the interface are presented. Then, analyses based on identifying length scales that are pertinent to the engulfment and nibbling mechanisms are given. While the two previous flow analysis methods (POD and LSE) are fairly straightforward in their application to SPIV fields, the methods of

extracting relevant information from TNTI entrainment analyses are less structured and agreed-upon in the literature. Techniques that have been attempted in previous works with similar experimental data are chosen here, with modifications where appropriate. As before, the most downstream FOVs, where self-similar conditions have been verified, are investigated for each case.

5. 3. 1. Detection of the Turbulent/Non-Turbulent Interface

The first step of the entrainment analysis described above is determining the TNTI for each image. Scalar concentration measurements from planar laser-induced fluorescence (PLIF) images have been shown to clearly demarcate the turbulent, rotational flow from the irrotational non-turbulent region in a jet (imaged simultaneously with PIV measurements).⁸⁷ Since concurrent flow visualization-SPIV images are not available here, a turbulence quantity based on velocity measurements must be used. Two-dimensional vorticity (*i.e.*, only the spanwise vorticity component) was considered for detecting the TNTI in this application and has been shown to work well for a turbulent jet, since the freestreams are irrotational, and the spanwise vorticity component generally dominates. However, when examining a few instantaneous vorticity fields for the current flow, images showed non-zero spanwise velocity fluctuations where the spanwise vorticity component was zero. This is to be expected, as the TNTI is highly three-dimensional and two-dimensional vorticity does not capture the spanwise velocity fluctuations. Therefore, a method of determining the TNTI involving the local turbulent kinetic energy, $k' = \frac{1}{2}(u'^2 + v'^2 + w'^2)$, is chosen, similar to Chauhan *et al.* (2014) who examined an incompressible boundary layer (the prime here denotes an instantaneous TKE definition, as opposed to $k = \frac{1}{2}(\overline{u'^2} + \overline{v'^2} + \overline{w'^2})$).⁸⁵ The best possible representation of the turbulent region is determined from using all three fluctuating velocity components. With this k' quantity defined, the interface that separates turbulent fluid ($k' > \text{threshold}$) from the non-turbulent fluid ($k' < \text{threshold}$) can be resolved on both the high-speed, primary and low-speed, secondary sides of the mixing layer.

Upon choosing k' as the quantity to identify the TNTI, an empirical procedure must be put in place to actually determine the interface transverse location at each streamwise location. Prior to determining a threshold to demarcate the turbulent fluid from the freestream, a sliding average technique is used to filter the small-scale noise present in the freestreams (*i.e.*, low-pass filter). This is important since the numerical algorithm for determining the interface location starts in the

freestreams (top of image for primary stream and bottom of image for secondary stream) and scans the image towards the shear layer until the turbulent threshold for k' is met. Without using a sliding average, a single pixel location in the freestream subject to measurement noise would cause an unphysical spike in the interface location. Since a sliding average, in effect, reduces the spatial resolution of the data, the size of the local sliding window was kept as small as possible. For each case, the smallest window size that filtered the freestream noise was $4 - 5\%$ of the mean shear layer thickness, which ended up being, in order of increasing M_c , $\pm 1.53, 1.50, 0.70, 0.64$, and 0.89 mm in each direction ($9 \times 9, 9 \times 9, 5 \times 5, 5 \times 5$, and 7×7 pixel windows, respectively). An example of the difference that using a sliding average makes is given in Figure 96, where the unphysical spikes can be seen clearly on the left. In addition to the sliding average, a slightly lower-pass filter (larger spatial scale) is used, by which, if the threshold is met for a certain location, a region $2 - 3$ mm below (if in the primary freestream) or above (if in the secondary freestream) is subsequently checked for non-turbulent fluid ($k' < \text{threshold}$). This is required in the case that a longitudinal noise pattern slightly larger than the sliding window is present in the freestream. This level of redundancy is necessary due to the importance of obtaining physically feasible interfaces with no sharp discontinuities.

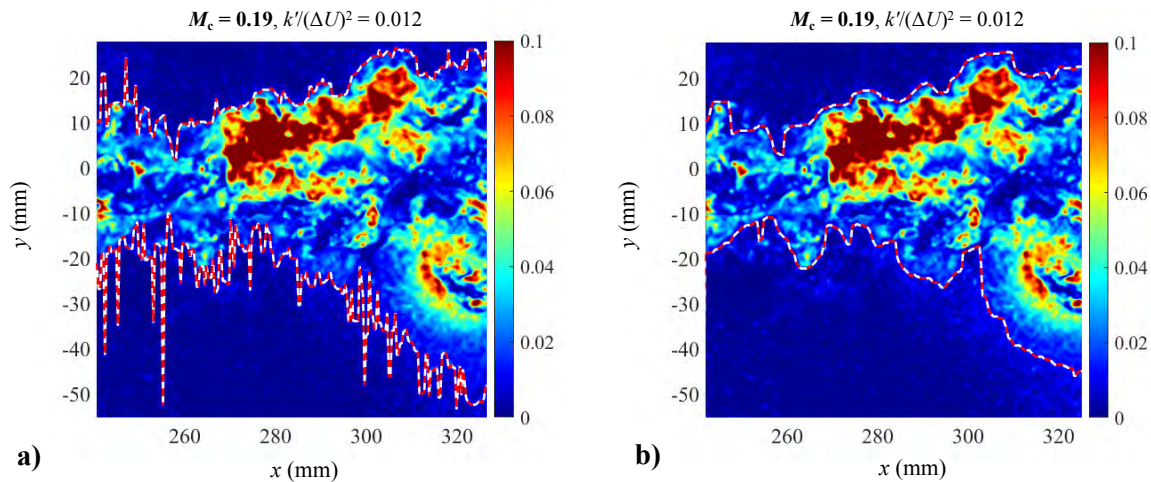


Figure 96. Finding TNTI (red-white line) for $M_c = 0.19$ with fixed threshold of $k' / (\Delta U)^2 = 0.024$ using a) no sliding average vs. b) sliding average of 4 pixels in each direction.

The process of determining the threshold for k' is also optimized in a way such that any non-physical spikes in the interface towards the mixing layer side are minimized. While in Figure 96,

noise in the freestreams is eliminated via the sliding average, it is difficult to know the exact optimal threshold to use. Further increasing the threshold eventually causes the TNTI to spike into the mixing layer in regions where k' is lower, as shown in Figure 97, which is also likely unphysical. It was found that simply setting a single threshold for k' was not as effective as checking a range of k' values and minimizing a parameter that best captures the unphysical spikes. The parameter is defined as the sum-square of the difference between interface transverse locations at each x -location, which has increased sensitivity to large spikes (*i.e.*, the quantity to minimize is: $SS_{TNTI} = \sum_{i=2:N_x} [y_{TNTI}(i) - y_{TNTI}(i - 1)]^2$). Since the definition of this parameter is fairly simple and only checks the TNTI geometry, much attention was given to defining the threshold range such that the resulting TNTIs at the low and high ends of each range were still very similar in most locations. Thus, the minimization of the sum-square parameter is simply an additional optimization technique performed on top of a manually well-defined threshold range. The ranges used for each mixing layer case (top and bottom sides) were $k'/(ΔU)^2 = [0.0088 – 0.0151], [0.0080 – 0.0096], [0.0057 – 0.0066], [0.0046 – 0.0052]$, and $[0.0037 – 0.0041]$, in order of increasing M_c .

As previously discussed, the method of determining the TNTI varies across the researchers who study entrainment instantaneously; thus, the many careful considerations that were laid out in this section are essential. The quantitative analyses in the subsequent subsections require TNTIs that are both physically feasible and accurate. As examples, the TNTI is shown for an instantaneous k' field for each M_c case in Figure 98. The qualitative differences that are apparent between the cases are explored with quantitative analyses in succeeding sections.

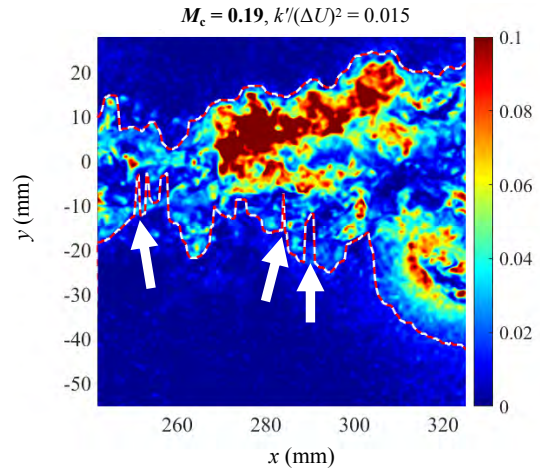


Figure 97. Threshold set too high for $M_c = 0.19$ (arrows showing unphysical spikes).

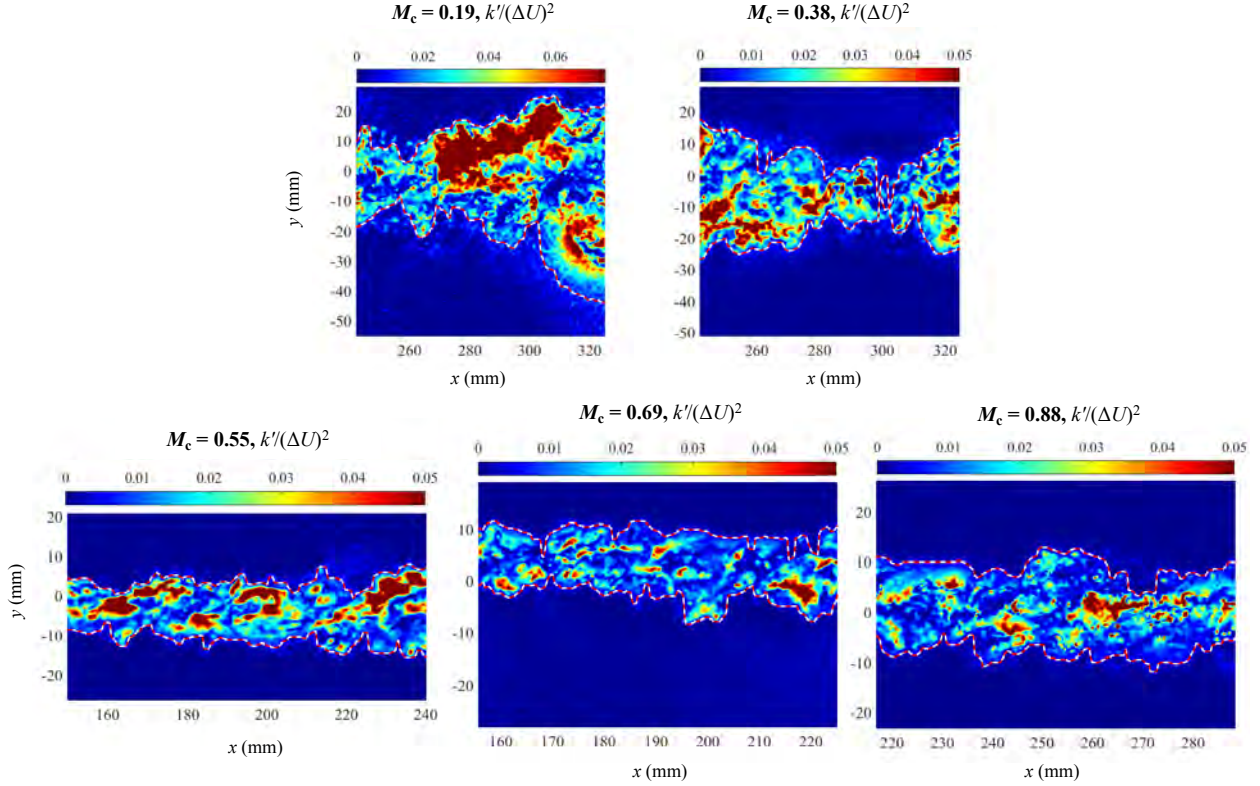


Figure 98. k' color contours with TNTIs shown at primary and secondary boundaries in red-white lines for $M_c = 0.19, 0.38, 0.55, 0.69$, and 0.88 mixing layers.

5.3.2. TNTI Statistics

An initial check as to whether the interface is accurately being captured from the procedure above is to compare its mean location to the transverse locations that define the mean shear layer thickness, y_1 and y_2 . It is expected that they should be close for both the primary and secondary sides of the mixing layer, since the $10\%\Delta U$ thickness definition should theoretically identify the mean boundaries between the freestream and turbulent region. The locations of the two different mean definitions are plotted together in Figure 99 for the five M_c cases. It can be seen that for all five cases, the mean TNTI location compared to y_1 and y_2 are very close for both sides and < 2 mm different everywhere. This result serves as a validation both ways, indicating that the $10\%\Delta U$ thickness is indeed well-founded as a mean definition that differentiates the freestream from the shear layer, and that the mean TNTI locations determined from the k' definition are in agreement with the mean velocity results. The agreement shown in Figure 99 also indicates that, on average,

the turbulent fluid can be defined as having streamwise velocity below $U_1 - 0.1\Delta U$ and above $U_2 + 0.1\Delta U$.

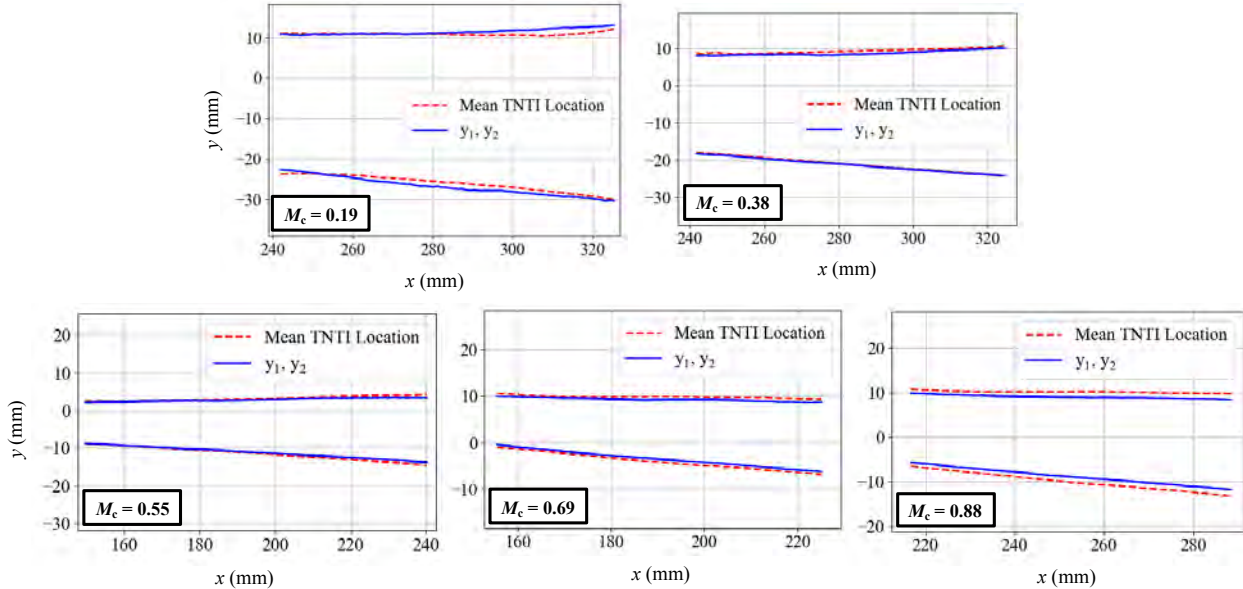


Figure 99. Mean TNTI location compared to y_1 and y_2 .

Also of interest, in terms of the TNTI statistics, is the probability density function (PDF) of the instantaneous interface locations. In incompressible, turbulent boundary layers and jets, the TNTI has been shown to have a near-normal distribution.^{85, 87} The PDFs of each TNTI are shown in Figure 100 for the fully-developed regions of the current mixing layers, and it is clear that the shapes of the distributions are affected by compressibility, especially on the primary side. The kurtosis and skewness of each TNTI are reported in Table 8. Kurtosis of the primary TNTI is most affected by compressibility, as it increases monotonically from a close-to-Gaussian value of 3.25 for $M_c = 0.19$, to as high as 6.11 for $M_c = 0.88$. This trend can be seen qualitatively in Figure 100, as the shapes of the red PDFs become sharper and more condensed near the mean value with increasing compressibility. Values outside of one standard deviation contribute most to the kurtosis; therefore, the probability mass being centered near the mean decreases the standard deviation and increases kurtosis contributions from the tails in the higher compressibility cases. The resulting trends of the red PDFs can physically be interpreted as the amplitudes of the TNTI oscillations decreasing with increasing M_c , as well as the TNTI, as a whole, remaining near the mean location from image to image. While skewness of the primary TNTI increases to 0.38 and 0.88 for the two highest M_c cases, the high concentration of probability mass so close to the mean

for those cases causes any slight asymmetry in the PDF to greatly affect the skewness value. However, in general, the skewness is slightly positive for the primary TNTI and slightly negative for the secondary TNTI (except for $M_c = 0.19$, which has negative skewness for both sides). For the secondary-side interface (blue PDFs), the distributions are less affected by compressibility, with similar skewness and kurtosis values that are fairly constant (~ -0.2 for skewness, $\sim 3 - 3.5$ for kurtosis) across all M_c .

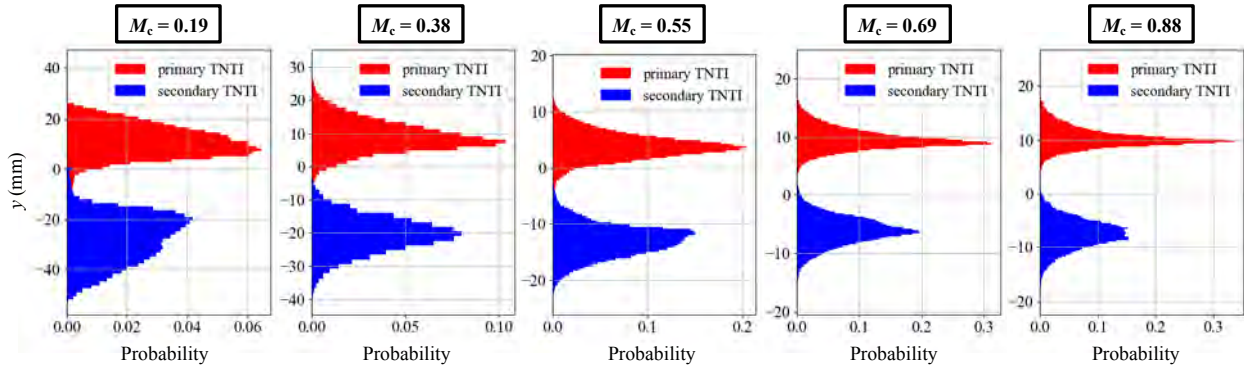


Figure 100. TNTI location histograms for primary-side (red) and secondary-side (blue).

Table 8. TNTI location skewness and kurtosis.

		$M_c = 0.19$	$M_c = 0.38$	$M_c = 0.55$	$M_c = 0.69$	$M_c = 0.88$
Skew	Primary	-0.144	0.230	0.153	0.378	0.877
	Secondary	-0.172	-0.176	0.021	-0.199	-0.190
Kurt	Primary	3.253	3.521	4.307	4.395	6.113
	Secondary	2.559	3.664	3.573	3.942	3.496

The average length of the TNTI is also a quantity of interest, since it is expected that the amount of freestream fluid entrained is related to the length of the interface itself, along which interactions between the turbulent and non-turbulent fluid take place. A proper normalization for the ensemble average of the TNTI length is the length of the mean TNTI location, as defined by $((\Delta x_{\text{mean TNTI location}})^2 + (\Delta y_{\text{mean TNTI location}})^2)^{1/2}$ from the dashed red lines in Figure 99 (*i.e.*, length of dashed red lines). The normalized length is therefore a measure of the interface tortuosity and is not affected by the FOV dimensions. The ensemble averages of the primary and secondary TNTI normalized lengths are plotted for each case in Figure 101. On the primary side (in red), the average TNTI

length decreases monotonically with increasing compressibility, while on the secondary side (in blue), the TNTI decreases from $M_c = 0.19$ to 0.55, then remains relatively constant around a normalized length of 1.55. Additionally, the average length of the secondary TNTI is always higher than the primary TNTI, agreeing with the PDF results from Figure 100 that the amplitudes of the interface oscillations are smaller on the primary side. The results in Figure 101 also indicate that, in a general sense, larger engulfment entrainment mechanisms are more prevalent in less compressible mixing layers and on the lower-speed, secondary side, since engulfment physically requires a longer interface length than nibbling. Furthermore, the consistently longer interface length on the lower-speed side of the mixing layer agrees with the faster growth of the mixing layer into the lower-speed side that is observed in experiments.

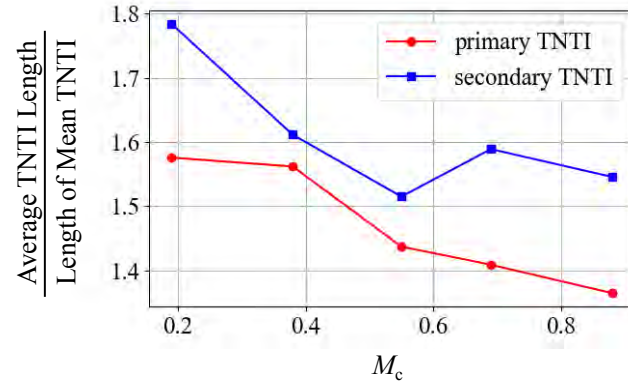


Figure 101. Normalized TNTI length vs. M_c .

5.3.3. Conditional Statistics Across the TNTI

In addition to the location of the interface itself, conditional statistics based on distance from the TNTI can be calculated and are useful for examining the transfer of flow properties across the TNTI. One clear use for this analysis is to confirm that the interface-identifying k' term shows a jump across the interface (for both primary and secondary sides), in part, to validate the algorithm used to identify the interface in each image. In addition to k' , quantities such as (2-D definition of) vorticity and the Reynolds stresses can be conditionally averaged as a function of distance from the interface both towards the freestream and turbulent regions. Interestingly, the conditionally averaged statistics from a TNTI analysis of an incompressible free jet show that there is a large vorticity jump across the interface, with a slight peak on the inner, turbulent side.⁸⁷ No such peak

is found in planar mixing layers for any level of compressibility.⁸⁸ For the latter study, the thickness of the vorticity jump is representative of the interface thickness and shows little variation for different M_c mixing layer cases. Conditional averaging of the Reynolds stresses also gives relevant information about the momentum transfer across the TNTI. A schematic that describes the concept of conditional averaging based on distance from the interface is shown in Figure 102 below, where the solid red line represents the instantaneous location of the primary TNTI, the white dashed line represents a Δy displacement above the TNTI (into the freestream), and the white-red dashed line represents a Δy displacement below the TNTI (into the turbulent region). The conditional average, which is denoted by an overbar in the succeeding figures, is then the ensemble average of the flow quantity under consideration at the same Δy displacement locations.

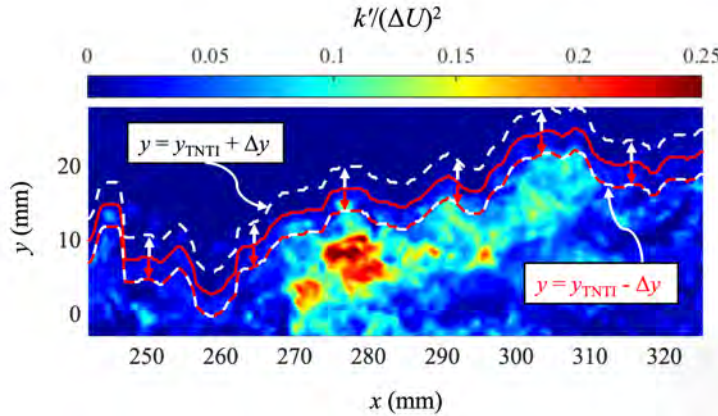


Figure 102. Schematic showing location of conditional statistics based on distance from interface for primary TNTI ($M_c = 0.19$).

The conditional averages of $k'/(ΔU)^2$ across the interfaces are shown in Figure 103 for both the primary and secondary sides of the mixing layer in the cases' fully-developed regions. As expected, there is a sharp jump across the interface from the non-turbulent region to the turbulent region for both sides, where the interface location is shown with a black dashed line. All cases have a similarly shaped \bar{k}' profile across the TNTIs, and are also similarly spaced apart as in the conventional $k/(ΔU)^2$ profiles plotted in Figure 43 (due to the same $(ΔU)^2$ normalization). Additionally, the increase of \bar{k}' in the shear layer as the profiles approach their peak is in agreement with the $k/(ΔU)^2$ profiles (the peak values themselves are also similar between k and \bar{k}'), confirming that the turbulent fluctuations are stronger near the center of the shear layer than at the edges. It also does not appear that there is much of a difference in \bar{k}' between the primary and secondary

sides, as both show a large jump at $(y - y_{\text{TNTI}})/b = 0$, show similar spacing between the M_c 's on the turbulent side, and show a gradual decrease of \bar{k}' into the freestreams. The decrease of \bar{k}' into the freestreams indicates that, while the TNTI-identification algorithm is able to locate the instantaneous interface where k' has the sharpest increase (as shown by the spike in \bar{k}' at the interface location), there is still slightly non-zero k' on the freestream side of the interface, on average. The very-small, non-zero values far from the interface towards the freestreams at $(y - y_{\text{TNTI}})/b = +0.6$ (left) and -0.6 (right) is likely due to actual freestream turbulence present in the flow, as well as measurement noise.

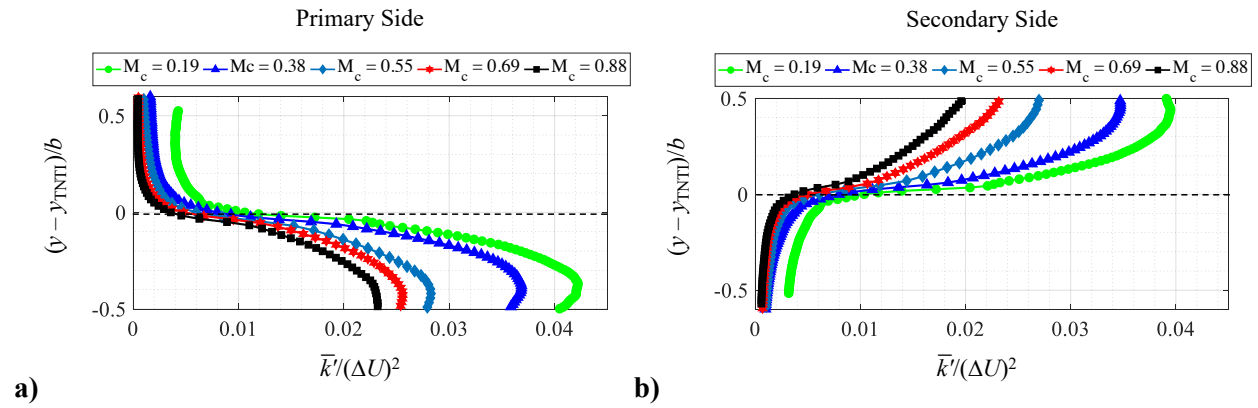


Figure 103. Conditional average of normalized k' ($= \frac{1}{2}(u'^2 + v'^2 + w'^2)$) across the a) primary-side TNTI and b) secondary-side TNTI.

The spanwise component of vorticity, while not chosen here as the quantity to determine the TNTIs (for reasons explained previously), is also a clear indicator of turbulence. The conditional average of the normalized spanwise vorticity magnitude is plotted in Figure 104, where it can be seen that the TNTIs, on average, capture the location where the spanwise vorticity jumps from near-zero in the freestreams to non-zero magnitude in the shear layer very well. Its jump across the interface is sharper than \bar{k}' , and unlike \bar{k}' , it seems to have a flatter profile across the mixing layer region, with a more uniform distribution. If not for the fact that the full 3-D vorticity vector is not available in the present study, the sharper jump across the TNTI of spanwise vorticity compared to \bar{k}' implies that the former quantity would be a better choice for identifying the TNTI. Nevertheless, the currently-defined TNTIs do well to differentiate irrotational, freestream fluid from rotational, turbulent fluid, as shown by the $(y - y_{\text{TNTI}})/b = 0$ location overlapping the vorticity magnitude jump. The shapes of the profiles in Figure 104 are also very similar to the conditionally averaged vorticity results from Jahanbakhshi and Madnia (DNS), with no local peak found on the

turbulent side (in contrast to the free jet), a constant uniform profile across the shear layer middle, and normalized vorticity magnitude approaching a constant value for M_c values greater than 0.8 (0.55 here).⁸⁸ A few key differences lie, however, between their entrainment study and the present one, which should be kept in mind when comparing the two works. Mainly, they identify the TNTI based on the full vorticity magnitude (using all three components), and they normalize their results based on the Taylor length and velocity scales, leading to vastly different normalized magnitudes. Even with these differences, the fact that the conditional vorticity results between their computational, and the present experimental entrainment studies show similar profile shapes and trends, reinforces the notion that there are multiple ‘correct’ ways to identify the TNTI in turbulent flows.

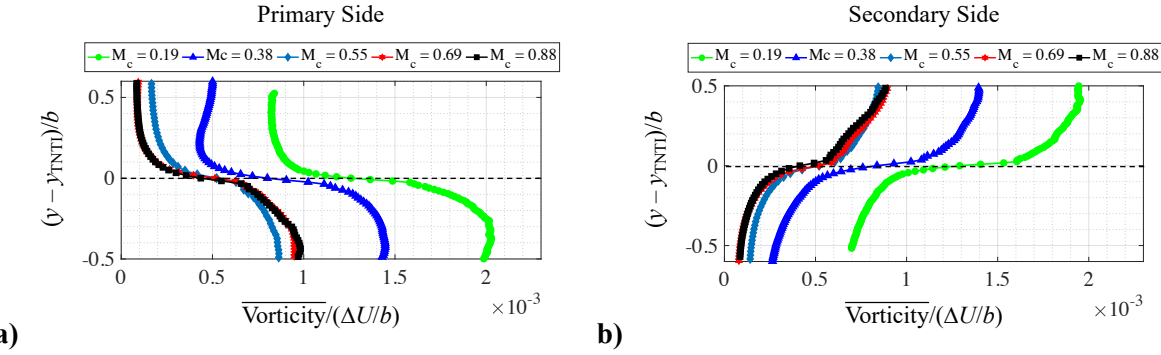


Figure 104. Conditional average of normalized spanwise vorticity magnitude across the a) primary-side TNTI and b) secondary-side TNTI.

In order to determine how each component of Reynolds stress contributes to the jump in \bar{k}' across the TNTI, conditional averages of the three normal stresses and the primary shear stress are plotted in Figure 105. Here, an interesting phenomenon can be seen, in which the spanwise normal stress shows the most discontinuous jump across the interface compared to the other stresses for all M_c cases. This result is certainly surprising, since no such characteristic can be intuited from the Reynolds stress or anisotropy plots that were shown in Section 4. 2. Careful consideration of the assumptions being made must be taken when attempting to explain this phenomenon. While the discontinuity implies that spanwise transport of spanwise velocity occurs only in the turbulent mixing region and abruptly stops at the interface between the freestream and turbulent fluid, this cannot be said with certainty, since only a planar slice of the interface is known. Jahanbakhshi and Madnia show that, in general, the TNTIs are highly three-dimensional and not constant across the span.⁸⁸ Thus, it is still possible that there is continuous spanwise transport of fluid across the

interface that cannot be resolved with a two-dimensional study. In fact, upon further consideration, the discontinuity for Re_{zz} should even be expected, since it is being assumed here that the TNTI has no curvature in the spanwise direction (true distance from the interface would require knowledge of the tangential plane at each location to resolve the normal direction to the interface), and therefore, spanwise velocity components would be parallel to the interface in that direction. The result is still a noteworthy one however, as the discontinuity occurring exactly at the interface location is further support that the identification algorithm works well. An additional interesting finding is that there seems to be a linear region for Re_{zz} from the jump-point at the interface to the peak location in the shear layer for the three highest M_c cases (on both sides). Again, this is not seen in the Re_{zz} profiles that are plotted against η in Section 4.2, and no such linear region is seen for the $M_c = 0.19$ and 0.38 cases.

For Re_{yy} , the higher M_c cases show a more uniform distribution (similar to vorticity) in the mixing layer than the lower M_c cases, indicating higher transverse fluctuations being concentrated near the center for lower compressibility. Re_{xx} in Figure 105 most closely resembles the unconditionally averaged stress profiles plotted against η . The profiles are much closer across compressibility levels on the primary side than on the secondary side, and the peaks occur on the primary side, as in Figure 57 in Section 4.2. Note that, since the conditional averages are determined independently from instantaneous TNTI locations (with each having slightly different ensembles, since interfaces that run into the top/bottom FOV borders are not used), the primary and secondary TNTI sides are not expected to match exactly at the mean centerline ($y - y_{\text{TNTI}})/b = \pm 0.5$.

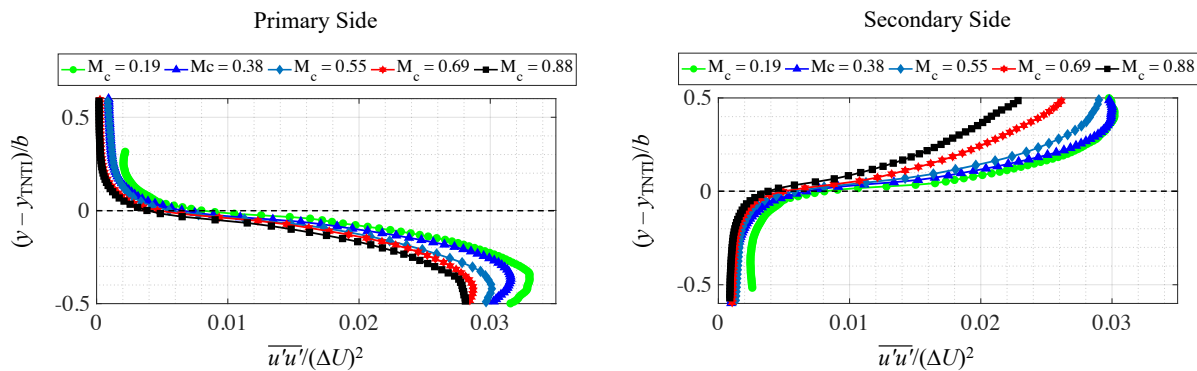


Figure 105. Conditional average of Re_{ij} across the primary-side TNTI (left) and secondary-side TNTI (right).

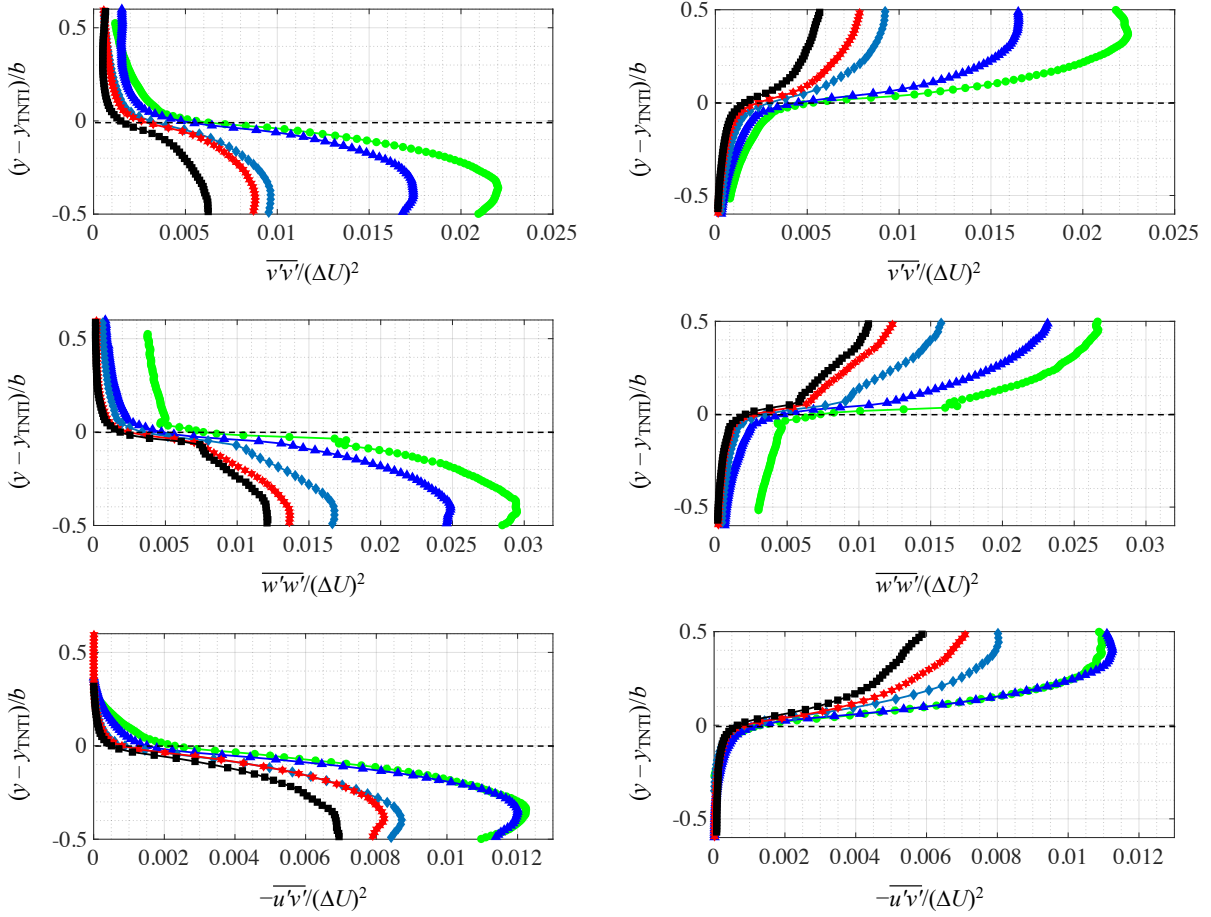


Figure 105. (cont.)

5.3.4. Entrainment Length Scales and Mechanisms

As discussed in the introduction to this entrainment section, the ultimate goal of the present entrainment analysis is to quantify the difference between mechanisms across the current M_c range as either being dominated by large-scale engulfment or small-scale nibbling. With information about the instantaneous interface location, as well as the flow velocity there, length scale analyses based on autocorrelations of various quantities are possible. The autocorrelations presented in this section are performed as in a typical time-series signal processing method, albeit in the spatial domain.

One effective way to identify the length scales of entrainment is to analyze the normal component of the flow velocity (u_n) at the interface. Since the interface location is now known with high spatial resolution, the local slope of the interface can be calculated at each streamwise location using a second-order central finite difference scheme. Furthermore, the TNTI-

identification algorithm is applied in such a way that the interface location is on the same spatial grid as the SPIV fields; thus, the flow velocity components are known at the exact x - y location of the interface. With these two quantities (TNTI slope and velocity vector) known at the same locations, u_n can be calculated with simple trigonometry. Two examples of u_n plotted (as black vectors) with the local TNTI locations (plotted as red lines) are shown for $M_c = 0.19$ and 0.88 in Figure 106. Due to the dominant streamwise velocity component, whether the normal component is toward the mixing layer (inward) or toward the freestream (outward) is largely dependent on the slope of the TNTI. On the primary edge of the mixing layer, if the TNTI is positively sloped, u_n is generally inward facing, and if the TNTI is negatively sloped, u_n is generally outward facing. The opposite is true on the secondary side of the mixing layer. It should be emphasized that the normal component of velocity is not necessarily equal to the flux of fluid across the interface, as that would require knowledge of the velocity of the TNTI itself. Rather, the normal velocity component can be analyzed as a spatial signal to examine the correlated length scales for each M_c . It is expected that engulfment mechanisms would manifest as large regions of correlated u_n along the interface, and nibbling would be represented by high spatial frequency fluctuations of u_n leading to smaller regions of correlated u_n . Qualitatively, in Figure 106a, the green highlighted regions can be seen as a large cluster of correlated inward-facing u_n for the least compressible case, likely indicating a region of engulfment. Similar large regions of engulfment are not seen in Figure 106b for the highest M_c case. A quantitative length scale analysis is laid out below to determine if, on average, the qualitative observations in Figure 106 are consistent.

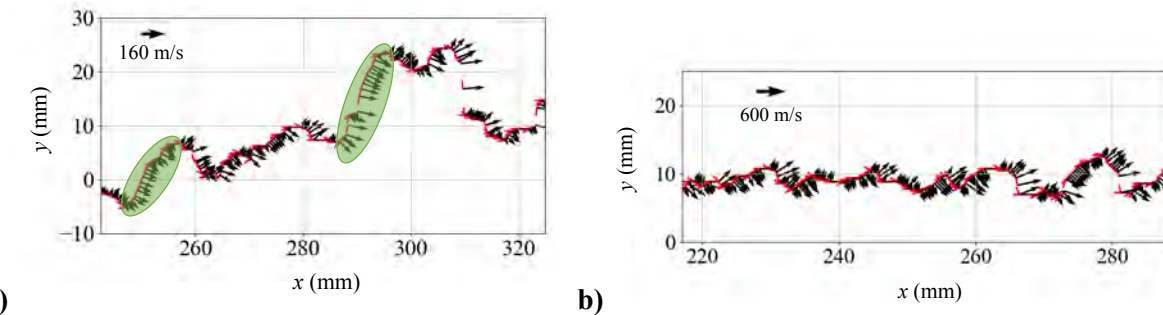


Figure 106. Normal component of flow (lab-frame) to the primary TNTI for a) $M_c = 0.19$ and b) $M_c = 0.88$ mixing layers.

From Figure 106, u_n can be plotted as a function of interface location, s , with outward-facing normal components defined as positive and inward-facing components defined as negative. By

constructing the spatial signal as a function of s instead of x , locations where the TNTI has a large slope angle (closer to vertical) will be better represented in terms of physical length. It follows from the definition of s that, for each image, the furthest downstream element of s is the total length of that image's TNTI, and the mean TNTI length plotted in Figure 101 is the ensemble average of the furthest downstream elements of s . Additionally, the mean normal velocity of the instantaneous signal (\bar{u}_n) can be subtracted from u_n to obtain an oscillating signal that is more appropriate to examine via autocorrelations. The mean normal velocity for a given signal is defined in Equation (24), where s_{end} is total length of the TNTI (as just explained) and N_s is the number of grid points. The oscillating signals, $u_n - \bar{u}_n$, are plotted in Figure 107 for the same instances as in Figure 106 with the same green regions of possible engulfment being highlighted for the $M_c = 0.19$ case.

$$\bar{u}_n = \sum_{s=0}^{s_{\text{end}}} u_n(s) / (N_s) \quad (24)$$

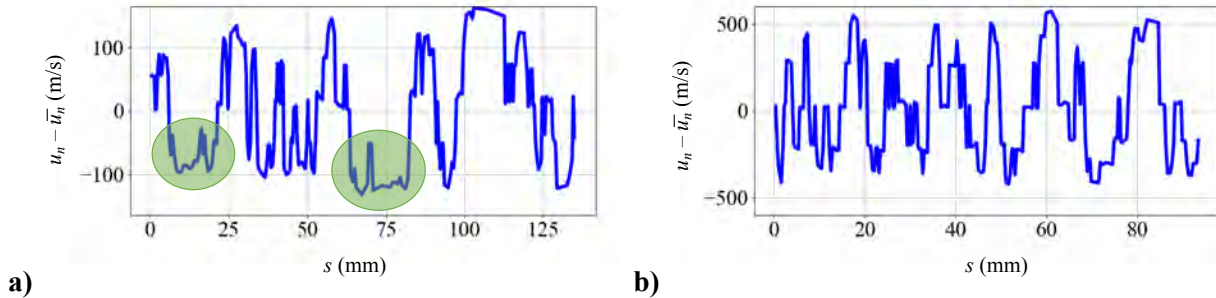


Figure 107. Spatial signal of flow velocity normal component along interface, defined by $(u_n(s) - \bar{u}_n)$, for a) $M_c = 0.19$ and b) $M_c = 0.88$ primary TNTIs.

In Figure 107, qualitative differences between the two levels of compressibility are again evident, where the less compressible $M_c = 0.19$ case shows longer regions of consecutively-positive or consecutively-negative u_n . A quantitative comparison is sought to identify entrainment length scale trends with compressibility. For this purpose, A_{u_n} , the autocorrelation of u_n , can be examined. It is defined in Equation (25) below and is a function of the displacement Δs along the interface. If a signal has large-scale correlations present (*i.e.*, lower spatial frequencies), the autocorrelation function should be large and positive for a large shift in Δs , while smaller length scales would result in a faster decay of A_{u_n} for small shifts in Δs . The autocorrelations are plotted for various displacements for the primary and secondary sides of the mixing layers in Figure 108

below. Since the autocorrelations are performed as a function of Δs (*i.e.*, a different grid from x where u_n are known), linearly interpolated values are used to find $u_n(s + \Delta s)$.

$$A_{u_n}(\Delta s) = \frac{\sum_{s=0}^{s_{\text{end}} - \Delta s} (u_n(s) - \bar{u}_n)(u_n(s + \Delta s) - \bar{u}_n)}{\sum_{s=0}^{s_{\text{end}} - \Delta s} (u_n(s) - \bar{u}_n)(u_n(s) - \bar{u}_n)} \quad (25)$$

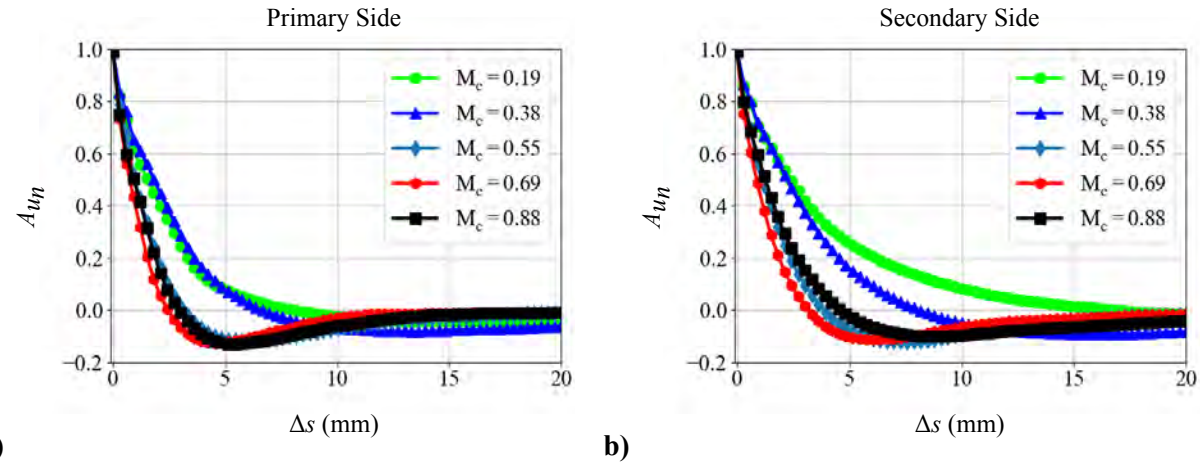


Figure 108. Autocorrelations of u_n along a) primary TNTI and b) secondary TNTI for $M_c = 0.19, 0.38, 0.55, 0.69$, and 0.88 mixing layers.

The autocorrelation functions in Figure 108 show faster decay for higher M_c on both sides of the mixing layers, a result that indicates larger entrainment length scales being present for the less compressible cases. In addition, for a given Δs , the lower-speed secondary TNTI consistently shows higher correlation values than the higher-speed primary TNTI for all levels of compressibility. Both trends are in agreement with the more general average interface length trends that are shown in Figure 101. Interestingly, on the primary side of the mixing layer, the two lowest M_c cases have very similar autocorrelations (green and blue curves), as do the three highest M_c cases (teal, red, and black curves). The two distinct results for $M_c \leq 0.38$ and $M_c \geq 0.55$ are likely due to the previously noted differences in large-scale structure organization within the mixing layer as roller structures become less organized and less dominant with increasing M_c (with a key transition point between $M_c = 0.38$ and 0.55). The large, round contours of the rollers lead to extended regions along the TNTIs where u_n is positively correlated, while as compressibility increases, the less organized TNTIs, with higher-frequency oscillations, decrease the u_n correlation. The secondary-side TNTI shows a larger difference between $M_c = 0.19$ and 0.38 ,

which indicates that compressibility effects start to become more prevalent for the secondary interface at lower levels of compressibility.

As in the previous length scale analyses presented in this dissertation, the autocorrelation functions in Figure 108 can be integrated to determine entrainment integral length scales. Since not all autocorrelation functions approach zero as Δs is increased (the $M_c = 0.19$ and 0.38 cases tend toward a negative value), the integral is taken for $A_{u_n} \geq 0$. A negative autocorrelation implies that, on average, Δs is larger than one half-wavelength of the u_n signal (*i.e.*, $(u_n(s) - \bar{u}_n)$ is generally the opposite sign as $(u_n(s+\Delta s) - \bar{u}_n)$), which would physically be grouping entrainment and detrainment mechanisms together. Thus, only the positively-correlated regions of A_{u_n} are considered. The integral length scales are normalized by the length of the mean TNTI location (same normalization factor as in Figure 101) and plotted in Figure 109 as a function of M_c . On the secondary side, the integral length scales decrease from $M_c = 0.19$ to 0.55 , then remain fairly constant to $M_c = 0.88$, as expected from the shapes of the autocorrelations. On the primary side, the two lowest M_c have very similar length scales, as do the three highest M_c (again, as expected from Figure 108a). From these results, it can be concluded that, in general, the difference between the entrainment length scales present on the primary and secondary sides decreases with M_c , as the red and blue curves in Figure 109 become closer together with increasing M_c . Larger engulfment mechanisms are expected to be most prevalent on the secondary-stream boundary of the least compressible case, while small-scale nibbling likely dominates the three most compressible cases. The decrease in entrainment length scales with increasing M_c is likely related to the reduction in growth rate with increasing M_c , as entrainment via engulfment would allow larger amounts of fluid to be part of the mixing layer faster as it develops. The same reasoning can be used to elucidate the faster growth into the secondary stream, especially for the two lower $M_c = 0.19$ and 0.38 cases, since larger length-scale mechanisms would allow more of the secondary freestream to be entrained into the mixing layer than for the primary.

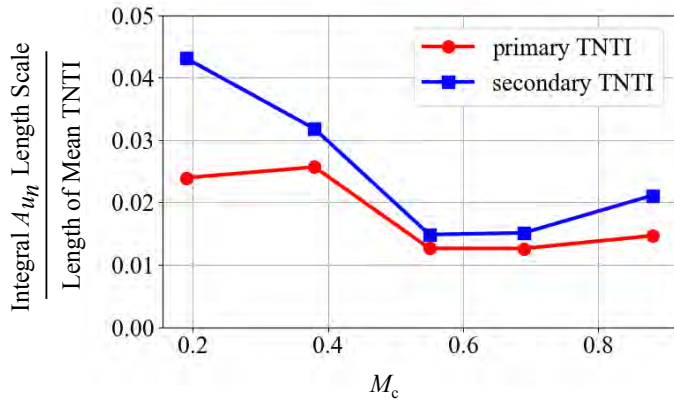


Figure 109. Integral normal velocity entrainment length scales for $M_c = 0.19, 0.38, 0.55, 0.69$, and 0.88 mixing layers.

In addition to the normal velocity component, a length scale analysis can be conducted on the interface geometry as a function of s . Following the same Equation (25), $y_{\text{TNTI}}(s)$, the local interface location can be autocorrelated as a function of displacement Δs . Note, since the mean location is subtracted for each signal, no differentiation between the primary and secondary interfaces is required. Example spatial signals are plotted in Figure 110 for $M_c = 0.19$ and 0.88 , where the least compressible case shows large-curvature, low spatial frequencies in its interface, while the most compressible case has high-frequency small-scale contortions present in its interface (note the different y -axis scales). The examples shown below are in good qualitative agreement with the PDFs shown in the previous section in Figure 100 (*i.e.*, difference in amplitude). The autocorrelation functions of y_{TNTI} for the five different mixing layer cases are presented in Figure 111, and their integral length scales are plotted in Figure 112.

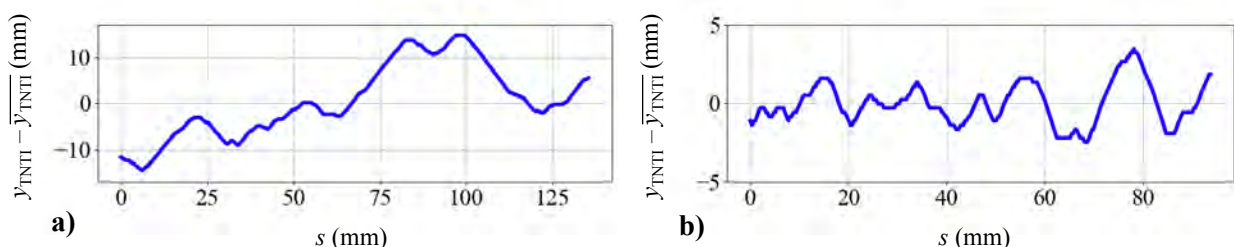


Figure 110. Spatial signal of interface location along interface, defined by $(y_{\text{TNTI}}(s) - \bar{y}_{\text{TNTI}})$, for a) $M_c = 0.19$ and b) $M_c = 0.88$ primary TNTIs.

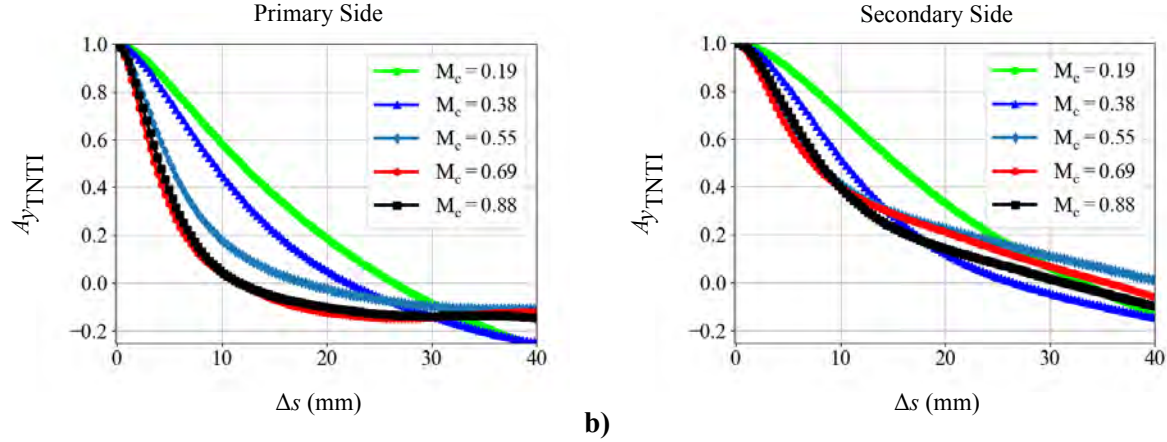


Figure 111. Autocorrelations of y_{TNTI} along a) primary and b) secondary sides for $M_c = 0.19, 0.38, 0.55, 0.69$, and 0.88 mixing layers.

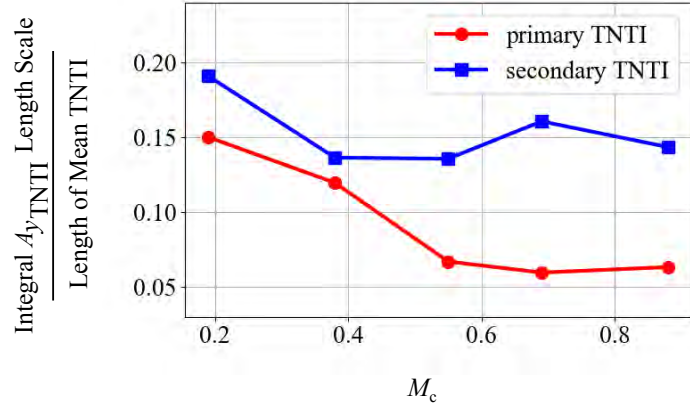


Figure 112. Integral interface length scales for $M_c = 0.19, 0.38, 0.55, 0.69$, and 0.88 mixing layers.

Since no velocity data are included for the autocorrelations and integral length scales of y_{TNTI} , only information about the geometry of the TNTIs is directly obtained. The results in Figure 112, once again, show the dual trend of decreasing length scales for increasing M_c (though the secondary TNTI levels off much quicker here than for u_n), and larger length scales being present on the lower-speed, secondary side. Unlike the integral length scales for u_n , however, the length scales for y_{TNTI} show a significant difference between the primary and secondary interfaces at high levels of compressibility, with the difference increasing for higher M_c . This result agrees with the PDFs shown for those cases ($M_c \geq 0.55$) in Figure 100, as the smaller-scale interface distortions on the primary side would lead to a more-condensed PDF near the mean, and the larger-scale distortions on the secondary side would lead to a wider distribution.

While the normal velocity component analysis gives more direct insight into the entrainment mechanisms that are present, the interface location length scale results are also relevant for comparing engulfment and nibbling. The higher correlations in the least compressible $M_c = 0.19$ case (green curves in Figure 111) indicate TNTIs with large-radius of curvature and large-scale oscillations, while the faster-decreasing correlations in the more compressible cases indicate interfaces with smaller-radius of curvature and higher spatial frequencies. These outcomes, in addition to the smaller-amplitude oscillations observed in Figure 110 (supported by the primary-side, red PDFs in Figure 100), indicate that the physical interface geometry required for engulfment is not present on the primary side of the higher M_c mixing layers. In order for engulfment to be a dominant mechanism, the interface must be able to enclose large packets of freestream fluid, requiring longer wavelengths and large-amplitude oscillations. For the $M_c = 0.19$ and 0.38 mixing layers, larger features of the interface geometry ($>12\%$ of the length of the mean TNTI in Figure 112) are present on both sides, while for the $M_c = 0.55$, 0.69, and 0.88 cases, the primary side interfaces have greatly reduced length scales. The difference between the u_n and y_{TNTI} length scale results for the three highest M_c cases are interesting, since they indicate that, while the secondary TNTIs have longer length scales than the primary TNTIs for high M_c , the normal velocity loses correlation along both interfaces for those cases. This is likely to reduce either side's ability to engulf fluid and lead to nibbling being the dominant entrainment mode at high levels of compressibility.

These conclusions regarding entrainment can also be linked to the flow dynamics that were observed via the spatial correlation, POD, and LSE analyses. As the pulsing mode becomes dominant for $M_c \geq 0.55$, the streamwise fluctuations dictate the instantaneous flow organization, and the elongated, horizontally-aligned large-scale structures lead to overall decreased entrainment length scales. Additionally, the wider range of turbulence length scales at high levels of compressibility lead to smaller-scale contortions along the TNTI, which reduces the ability to entrain fluid in large packets. The diffusion of smaller-scale eddies becomes more significant as the interface contorts at a higher spatial frequency, and since nibbling has a lower volume flux rate, the more compressible mixing layers grow less quickly.

The length scale analyses presented in this section are useful for a general examination of the large-scale vs. small-scale entrainment mechanisms for differing levels of compressibility, but they are not intended to be interpreted directly as engulfment vs. nibbling percentages relating to

mass/volume flux. While it is certainly reasonable to differentiate the entrainment mechanisms as engulfment and nibbling, as described in the literature (this notion is supported especially when observing the high frame-rate schlieren movies, which clearly indicate the two dynamic processes as they are nominally described), they are still subjective terms; as such, obtaining a direct mass flux percentage of each mode is difficult. The general length scale comparisons of the normal velocity component and interface location are thus useful methods of analysis.

Finally, a brief note is included here concerning the ability to obtain the entrainment ratio between the primary and secondary sides of the mixing layer, as this is generally a principal quantity in regard to mixing layer entrainment analyses. While much effort was given to finding an appropriate method to determine the instantaneous volume flux across the TNTI, it was deemed an ineffective analysis without knowledge of the instantaneous velocity of the interface itself (as briefly mentioned at the start of this section). This information is only available with time-resolved velocity fields, wherein the instantaneous rate-of-change of the TNTI position can be combined with the flow velocity in the laboratory frame-of-reference to obtain the instantaneous volume — or mass, with appropriate density approximations — flux across the interface. An analysis of the mean volume flux across the ensemble-average TNTI location is less effective due to the three-dimensionality of the interfaces, and since the mean shear layer angle becomes slightly bent wherever reflecting waves in the primary streams impinge on the shear layer.

6. UNCERTAINTY OF EXPERIMENTAL RESULTS

Having reviewed all mixing layer results in the form of presenting the acquired data and discussing various flow analyses, this final section reports the uncertainties of the obtained results and documents the methodology used to calculate them. A critical aspect of the current work being CFD validation-quality is providing a measure of the uncertainty of the data. All reported uncertainties of the operating conditions in Table 4 (Section 3.1) were determined using the analysis outlined below. For each quantitative diagnostic technique performed (*i.e.*, SPIV, pressure/temperature measurements), a 95% confidence interval (CI) of the measurement is given. Uncertainties of the measurements, their propagation into the derived operating conditions, and uncertainties of statistical turbulence quantities are discussed. The analysis is not conducted for the end-view SPIV measurements, since these data were examined mainly in a qualitative sense.

6.1. Operating Condition and Pressure Measurement Uncertainties

In general, the uncertainty of a calculated quantity (*e.g.*, a_1 , a_2 , M_1 , M_2 , M_c , etc.) can be estimated based on its functional relationship with its independent variables and their associated uncertainties. The uncertainty of each independent variable is propagated to the resulting, calculated quantity via its partial derivative, as shown in Equation (26).^{91, 92} Here, ω_f is the uncertainty of the example variable f , which is a function of independent variables y_1, y_2, \dots, y_N , each having its own uncertainty, $\omega_{y_1}, \omega_{y_2}, \dots, \omega_{y_N}$. Note that if any of the independent variables are themselves also a calculated quantity (as opposed to a directly measured quantity), the same process will have to be conducted for its uncertainty.

$$\omega_{f(y_1, y_2, \dots, y_N)} = \sqrt{\left(\frac{\partial f}{\partial y_1} \omega_{y_1}\right)^2 + \left(\frac{\partial f}{\partial y_2} \omega_{y_2}\right)^2 + \dots + \left(\frac{\partial f}{\partial y_N} \omega_{y_N}\right)^2} \quad (26)$$

For direct measurements (*i.e.*, pressure, temperature, velocity), their uncertainties are calculated on the basis of their random (precision) and systematic (bias) errors. Each measurement's systematic error is given by the accuracy of the data acquisition system (ω_{accuracy}). For pressure and temperature measurements, these are the pressure transducers and differential temperature meters/thermocouples, respectively. The accuracies of the temperature and pressure hardware used in these experiments are given in Table 10 (Appendix B). As for the accuracy of

the velocity measurements, a robust SPIV uncertainty analysis is performed as described in the next subsection (Section 6. 2). In order to determine a certain CI for the measurement mean, a statistical random error is also included. Both errors are combined in a root-sum-square manner, as shown in Equation (27).⁹¹ The random error (second term) includes a student *t*-test value ($t_{N,P}$) based on the number of samples (N) and probability desired (P), and the standard deviation of the means ($S_{\bar{p}}$, defined in Equation (28)). All uncertainties reported in Table 4 are for a 95% CI, for which $t_{N,P}$ is ~1.96 when $N > 1000$.

In addition, uncertainties of all sidewall static pressure measurements are documented in Table 11 (Appendix B). Since all *x-y* locations on the side-wall pressure tap insert are plumbed to the same transducers, and the pressure remains fairly constant throughout the test-section, the uncertainties are identical across the entire sidewall for each case.

$$\omega_p = \sqrt{(\omega_{\text{accuracy}, p})^2 + (t_{N,P} S_{\bar{p}})^2} \quad (27)$$

$$S_{\bar{p}} = \sqrt{\frac{1}{N(N - 1)} \sum_{n=1}^N (p_n - \bar{p})^2} \quad (28)$$

6. 2. SPIV Uncertainty

The SPIV uncertainty analysis presented here is an updated version from that of Lazar *et al.* (2010) who used an approach based on four error sources: equipment, particle lag, processing, and sampling size.⁹² An instantaneous uncertainty field is first calculated for each velocity component from the first three error sources, then mean velocity and Reynolds stress uncertainties are determined using the instantaneous uncertainties and a statistical sampling error term.

6. 2. 1. Instantaneous Uncertainty

An advantage of the current SPIV uncertainty analysis is the ability to determine an instantaneous uncertainty field for each velocity component, which allows for the robust calculation of total uncertainties in the mean and fluctuating components. While experimental uncertainties of the mean velocity are often determined using both systematic and random error, uncertainty of the Reynolds stresses are often reported using a simple statistical relationship based

on the standard deviation of the measured quantity (random error only).⁹³ In the current analysis, each instantaneous uncertainty is used to determine the uncertainty in the fluctuating components, and thus, the Reynolds stresses. As previously mentioned, the instantaneous uncertainty is calculated from three sources: equipment error, particle lag error, and processing error.

The equipment error (ω_{equip}) takes into account the accuracy of the image scaling calibration as well as the laser pulse timing. Since PIV, in general, uses double-frame particle-seeded images with a known Δt to calculate physical velocity values, these two error sources are the most prevalent in terms of the equipment uncertainty.⁹² The pixel-to-physical length scaling factor is determined via a two-level calibration plate with known dimensions and marker size/spacing, and the timing between the two frames is controlled by the laser and a delay generator (see Section 2.2.4 for details on SPIV equipment). Parameters relevant to the scaling factor include the calibration plate physical length (l), calibration plate length in pixels (L), image distortions due to aberrations (ω_{L_2}), and distance from illumination plane to camera lens (λ). The optical aberrations are assumed to be 0.5% of the calibration plate length (in pixels), which was shown to be a conservative estimate by Lazar *et al.*⁹² Parameters relevant to the timing include laser accuracy (*i.e.*, jitter) (t_1) and delay generator accuracy (t_2). Combining all these equipment error sources in a root-sum-square manner yields Equation (29), where \tilde{u}^i is the measured velocity component in the pixel frame-of-reference. Input parameters for all five M_c cases are either measured directly, or taken from hardware data specification sheets, and are listed in Table 12 (Appendix B).

$$\omega_{\text{equip}} = \sqrt{\tilde{u}^i \left[\left(\frac{1}{L} \omega_l \right)^2 + \left(\frac{-l}{L^2} \omega_L \right)^2 + \left(\frac{-l}{L^2} \omega_{L_2} \right)^2 + \left(\frac{l}{\lambda L} \omega_\lambda \right)^2 \right] + \tilde{u}^i \left(\frac{l}{\Delta t L} \right)^2 [\omega_{t_1}^2 + \omega_{t_2}^2]} \quad (29)$$

In addition to the equipment error, for any particle-based velocimetry method, a certain amount of particle lag error (ω_{lag}) is inevitable due to external forces. While there are numerous acting forces (*e.g.*, gravity, buoyancy, pressure gradient, Stokes' drag, etc.), the only non-negligible force in the current flow is the particle drag. This drag force will cause the particle to have a different velocity than that of the fluid itself, thus imparting a slip velocity ($u_{\text{slip}} = u_{\text{particle}} - u_{\text{fluid}}$). Using the conventional aerodynamic drag relation, $F_D = \frac{1}{2} \rho u_{\text{slip}}^2 S C_D$, where C_D is the drag coefficient, $\frac{1}{2} \rho u_{\text{slip}}^2$ is the dynamic pressure based on the slip velocity, and S is particle frontal area, a relation for u_{slip} can be obtained (Equation (30)). Newton's second law is also used here to relate the particle

mass (assuming a sphere), $m_p = \rho_p(4/3)\pi(d_p/2)^3$, and acceleration, $a_p^i = \partial u^i/\partial t + u(\partial u^i/\partial x) + v(\partial u^i/\partial y) + w(\partial u^i/\partial z)$, to the drag force (F_D). ρ_p and d_p are the particle density and diameter, respectively, which are known quantities for the current experiment (see Section 2.2.4). For the particle acceleration, the first and last terms are omitted in its calculation due to the nature of the SPIV diagnostic not being time-resolved, nor having spatial derivatives in the out-of-plane (z) direction. Also note that the acceleration of the particle here is calculated from finite difference operations on the SPIV fields. Sutherland's formula is used to determine the fluid viscosity, and the ideal gas law is used to calculate the fluid density (with side-wall pressure measurements and adiabatically determined temperature fields).

$$\omega_{\text{lag}} = u_{\text{slip}} = \frac{4\rho_p d_p^2 a_p}{3\mu_f C_D Re_p}, \quad Re_p = \frac{\rho_f d_p |u_{\text{slip}}|}{\mu_f} \quad (30)$$

In order to determine C_D , Stokes' assumption $C_D = 24/Re_p$ is used initially, which holds true for small Re_p ($<<1$). While this is mathematically convenient (removes Re_p from the equation) and serves as a reasonable initial guess (since d_p is small at ~ 0.2 micron), Hortensius⁴⁸ improved upon the drag prediction by iteratively converging upon u_{slip} using an updated particle drag model from Clift *et al.*,⁹⁴ given in Equation (31). This model holds true for $Re_p < 800$ and thus allows for greater accuracy in regions of the flow where Stokes' assumption may be invalid. Details about the iteration process and relative improvement from the Stokes' model can be found in Hortensius.⁴⁸

$$C_D = \frac{24}{Re_p} (1 + 0.15 Re_p^{0.687}) \quad (31)$$

The final instantaneous error source is the processing error (ω_{proc}), which is where another major difference lies between the current analysis and that from Lazar *et al.* In their work, a synthetic particle image processing method is used, whereby the processing error is determined from the differences between the originally processed velocity field (using the original particle images) and a synthetically processed velocity field (using randomly generated particle images) using the same processing steps.⁹² In the present uncertainty analysis, the processing error for each velocity component is taken directly from the LaVision DaVis 8.4 program, a feature added in their recent versions. Beyond the obvious benefit of simplicity, the program takes into account the

correlation strength for each velocity vector, among other factors. In addition, since no additional computing time is required (uncertainty is calculated in parallel with the vector processing), the entire vector ensemble can be used to estimate the confidence interval. Details on how the DaVis program calculates processing uncertainty can be found in the work of Weineke (2015).⁹⁵

Once all three instantaneous error sources are determined, the total instantaneous uncertainty (ω_{inst}) can be calculated as the root-sum-square of ω_{equip} , ω_{lag} , and ω_{proc} , as in Equation (32). An example of each error source and the calculated total instantaneous uncertainty is shown in Figure 113 for the w -component of velocity. Note that the processing error term dominates, as the equipment and particle lag errors are minimized due to careful experimental set-up considerations (e.g., well-focused cameras, high-accuracy calibration plate dimensions from LaVision, low laser jitter, optimized Δt , etc.) and the absence of any strong waves/local velocity gradients in the flow (which minimizes the particle lag), respectively.

$$\omega_{\text{inst}} = \sqrt{(\omega_{\text{equip}})^2 + (\omega_{\text{lag}})^2 + (\omega_{\text{proc}})^2} \quad (32)$$

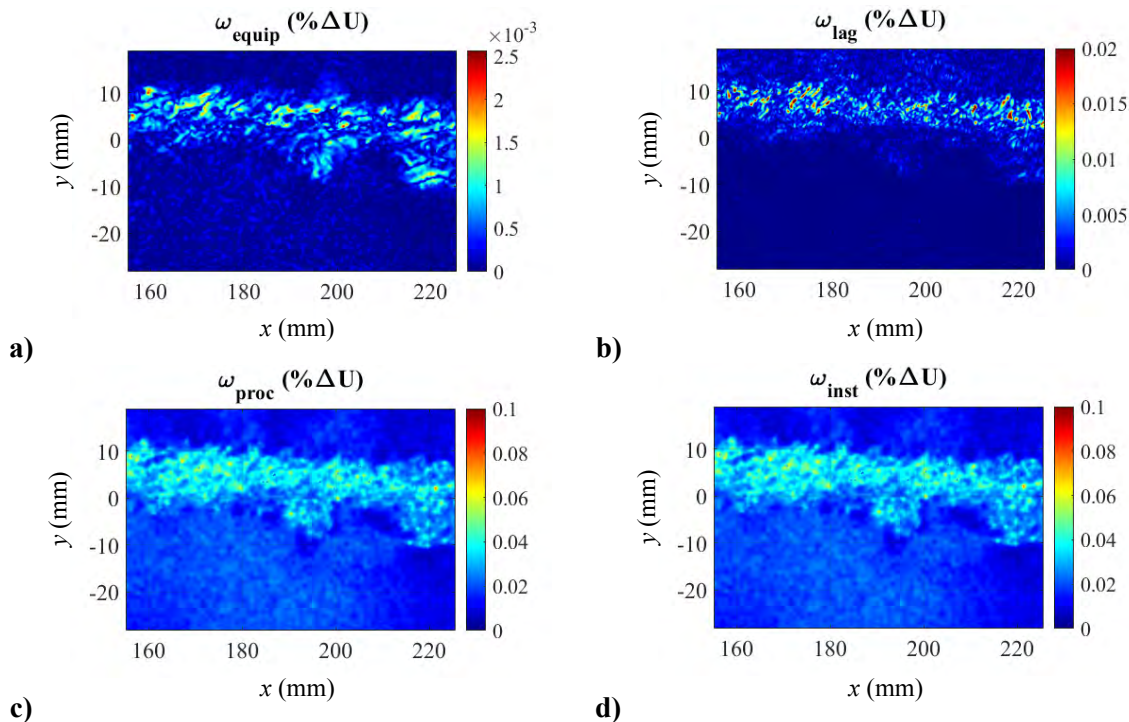


Figure 113. Instantaneous SPIV error sources (a – c) and total instantaneous uncertainty (d) for w -velocity of $M_c = 0.69$ mixing layer.

6. 2. 2. Uncertainty of Mean Velocities

Once the total instantaneous uncertainty of each realization is calculated, ω_{inst} can be combined in a root-mean-square manner to obtain the mean experimental uncertainty ($\omega_{u^i, \text{exp mean}}$). This is laid out in Equation (33), where N is the ensemble size and u^i is the velocity component under consideration. While this term represents the mean experimental error in the measured velocity fields, a statistical confidence interval term must also be included to account for the fact that the ensemble size is finite (as in Section 6. 1). Equation (34) shows the root-sum-square of these two terms, where $t_{N,P}$ is the student t -test value, and $S_{\bar{u}^i}$ is the standard deviation of the mean quantity \bar{u}^i (defined in Equation (28)).

$$\omega_{u^i, \text{exp mean}} = \sqrt{\frac{(\omega_{u^i, \text{inst}_1})^2 + (\omega_{u^i, \text{inst}_2})^2 + \dots + (\omega_{u^i, \text{inst}_N})^2}{N}} \quad (33)$$

$$\omega_{u^i, \text{total mean}} = \sqrt{(\omega_{u^i, \text{mean exp}})^2 + (t_{N,P} S_{\bar{u}^i})^2} \quad (34)$$

The total mean velocity uncertainty ($\omega_{u^i, \text{total mean}}$) is shown as color contours of each component in Figure 114 (for $M_c = 0.69$). It can be seen that the W -component of velocity has the highest uncertainty, a result that can be attributed to the nature of the SPIV diagnostic, which generally has the highest processing uncertainty for the out-of-plane direction. Figure 115 shows mean velocity profiles with uncertainty bars (corresponding to 95% CI) in the fully developed region for each mixing layer. Again, the uncertainty of the spanwise velocity component is shown to be the highest for all cases. In addition, since the uncertainties are normalized by ΔU , their normalized values generally decrease with increasing M_c (which corresponds to increasing ΔU). This result is a consequence of the dominating processing error term having a relatively constant absolute value for each velocity component across the five cases, as evidenced by freestream uncertainties in Table 4. The maximum uncertainties in the shear layer for the lowest $M_c = 0.19$ case (which has the highest normalized uncertainty) are 4%, 3% and 8% for $(\omega_U/\Delta U)$, $(\omega_V/\Delta U)$, and $(\omega_W/\Delta U)$, respectively.

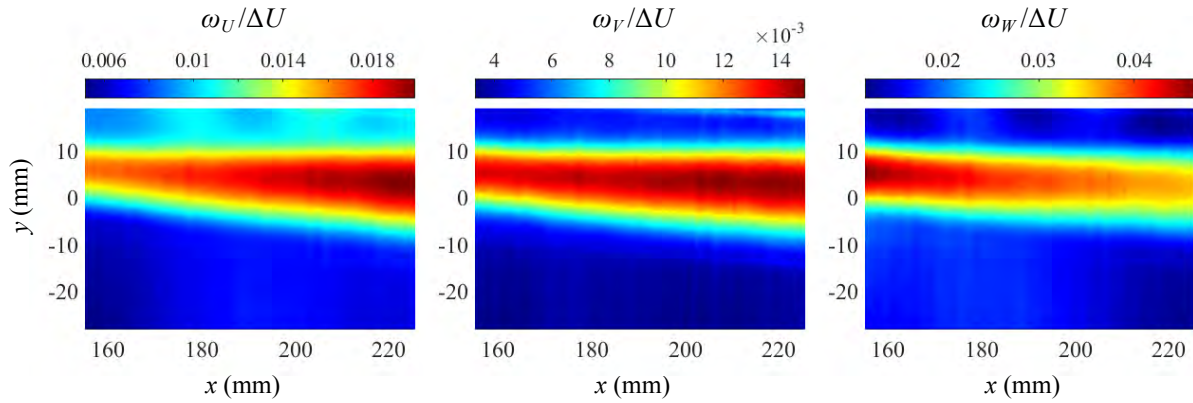


Figure 114. Color contours of mean velocity uncertainties for $M_c = 0.69$ mixing layer.

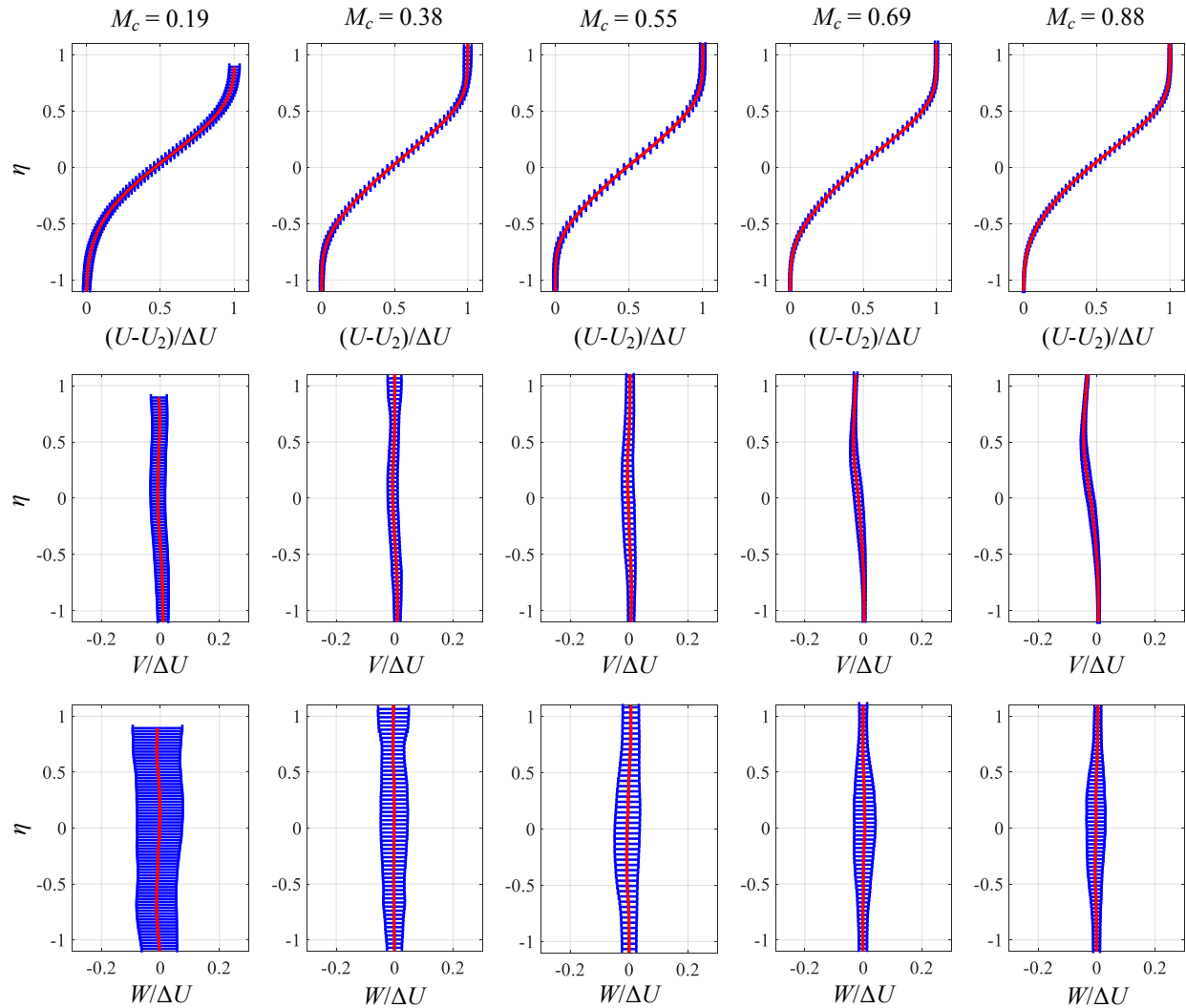


Figure 115. Fully-developed mean velocity profiles with uncertainty bars (95% CI) for $M_c = 0.19, 0.38, 0.55, 0.69$, and 0.88 mixing layer cases.

6. 2. 3. Uncertainty of Reynolds Stresses

The uncertainties of the Reynolds stresses are estimated in an analogous way to the mean velocity results. By definition of the Reynolds decomposition ($\mathbf{u}' = \mathbf{u} - \bar{\mathbf{U}}$, bold denoting three velocity components), the two error sources of an instantaneous fluctuation are from the error of the measured instantaneous velocity and the error of the calculated mean. Thus, Equation (35) can be used to estimate the uncertainty of an instantaneous velocity fluctuation via a root-sum-square. Note that this formula follows directly from the error propagation given in Equation (26). The experimental uncertainty of a Reynold stress component ($\omega_{Re_{ij}, \text{exp}}$) can then be calculated by root-mean-squaring the product of the two uncertainty components that make up that Reynolds stress (Equation (36)). Finally, the total uncertainty of Re_{ij} can be determined using the familiar *t*-test value for a 95% confidence interval and the standard deviation of the mean Reynold stresses (again, defined in Equation (28)).

$$\omega_{u_i', \text{inst}} = \sqrt{(\omega_{u_i, \text{total mean}})^2 + (\omega_{u_i, \text{inst}})^2} \quad (35)$$

$$\omega_{Re_{ij}, \text{exp}} = \sqrt{\frac{(\omega_{u_i', \text{inst}_1} \omega_{u_j', \text{inst}_1})^2 + \dots + (\omega_{u_i', \text{inst}_N} \omega_{u_j', \text{inst}_N})^2}{N}} \quad (36)$$

$$\omega_{Re_{ij}, \text{total}} = \sqrt{(\omega_{Re_{ij}, \text{exp}})^2 + (t_{N,P} S_{u_i'})^2} \quad (37)$$

To best illustrate the Reynolds stress uncertainties, color contours of their uncertainties are shown for the same $M_c = 0.69$ case in Figure 116, and fully-developed profiles with uncertainty bars are shown in Figure 117 for all cases. As expected, Re_{zz} shows the highest uncertainty across all mixing layers, and the lowest M_c case has higher normalized stress uncertainties. The Reynolds stress uncertainties are generally highest in the shear layer, also as expected. The maximum uncertainties in the shear layer for the lowest $M_c = 0.19$ case (which has the highest normalized Reynolds stress uncertainties) are 0.31%, 0.20%, 1.42%, and 0.24% of $(\Delta U)^2$ for $\omega_{Re_{xx}}$, $\omega_{Re_{yy}}$, $\omega_{Re_{zz}}$, and $\omega_{Re_{xy}}$, respectively.

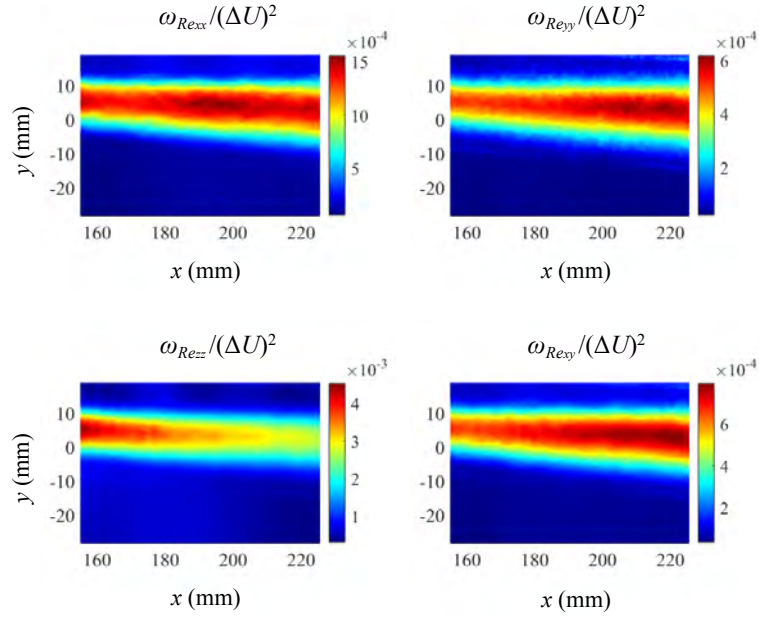


Figure 116. Color contours of Reynolds stress uncertainties for $M_c = 0.69$ mixing layer.

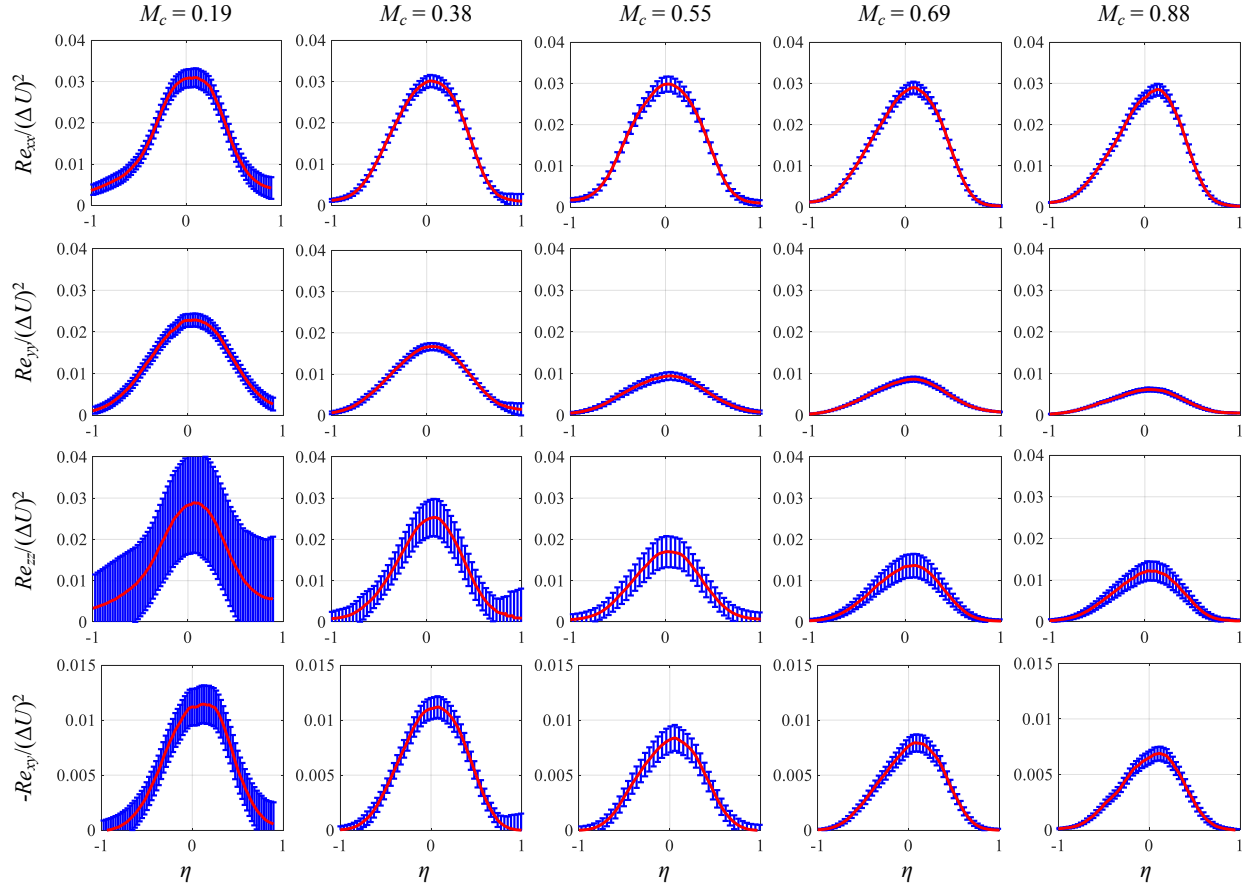


Figure 117. Fully developed Reynolds stress profiles with uncertainty bars (95% CI) for all five mixing layer cases.

7. CONCLUSIONS

7.1. Summary of Present Work

The two-stream planar free shear layer is a flow that has a wide range of applicability, and as such, it has been the subject of numerous experimental and computational investigations. In high-speed and/or supersonic applications, such as the mixing of fuel and oxidant in scramjet engine combustors, the effects of compressibility on mixing layer turbulence become increasingly important. Thus, many researchers examine this very subject with an aim to improve the current understanding of the complex physics that are involved in this seemingly simple, basic geometry flow. Due, in part, to the commonality of the two-stream mixing layer, a parameter that gives a nominal measure of the level of compressibility in this flow has been defined in the literature (and used universally) as the convective Mach number, M_c .^{8, 9} Physically, M_c is the Mach number of the convecting large-scale structures in the mixing layer relative to the freestreams, and in flows where the gases of the two streams have equal specific heat ratios, it is equal for both streams. Its derivation requires the assumption that a saddle point exists between two contiguous large structures where the stagnation pressures are equal for both streams in the convective frame of reference. While this assumption may be an over-simplified one, its definition is used regularly throughout the mixing layer literature; thus, it is used in the current study.

In the present work, five different M_c mixing layers with $M_c = 0.19, 0.38, 0.55, 0.69$, and 0.88 , are experimentally investigated primarily via stereo particle image velocimetry. A key area that is notably missing from the compressible mixing layer literature is a set of high-resolution, three-component experimental velocity measurements that can be used to calculate the full three-dimensional Reynolds stress tensor. A few areas of possible improvement and/or reinforcement exist in the current knowledge of compressibility effects on the Reynolds stresses. In previously available experiments, the trend of the peak streamwise normal stress with M_c is not unanimously agreed upon, with some researchers reporting a constant trend while some report a decrease with increasing M_c .^{17, 20} Moreover, only a few experiments measure the spanwise normal stress, and no experimentalists measure it for a range of compressibility in the same facility.^{23, 30} In the results reported here, the full Reynolds stress tensor is obtained for each M_c case, and furthermore, fully-developed, self-similar conditions are verified for each component with constant peak values in the fully-developed region. This verification is imperative, since it is shown here that the stresses

require long streamwise lengths to become fully developed and are very sensitive to any disturbances in the flow such as unavoidable waves in supersonic freestreams. The results from the present study indicate that the streamwise normal stress does in fact remain constant, while all other stresses become reduced with increasing compressibility. In addition, this study shows that the spanwise normal stress decreases monotonically, relative to the value in incompressible mixing layers, down to ~55% of the incompressible value for $M_c = 0.88$.

Knowledge of the full Reynolds stress tensor also allows for novel analyses of the Reynolds stress anisotropy tensor for the five different M_c cases. Previous experiments only report a two-dimensional definition due to the noted lack of spanwise velocity measurements. The constant streamwise normal stress trend causes the anisotropies of the transverse and spanwise normal stresses to decrease (since their peaks decrease with M_c) while the streamwise normal stress anisotropy increases (since its peak remains constant with M_c). The primary shear stress anisotropy remains constant, indicating that its magnitude remains constant relative to the total turbulence kinetic energy. Analyzing the entire anisotropy tensor in regard to the Lumley triangle constraints shows that the turbulence trends toward one-component that is streamwise-dominated with increasing compressibility, from near-isotropic in the incompressible case.⁵⁹ There is also a constant anisotropy region near the middle of each shear layer, which is in agreement with analytical work that arrives at this same conclusion by showing that the self-similar Reynolds stress profiles are simply scaled from one another for a given shear layer (near the transverse middle).⁵⁷

In addition to the Reynolds stresses, the current study conclusively shows that the turbulence production decreases with increasing M_c , while the turbulence and gradient Mach numbers increase with M_c . Calculation of the production terms are possible due to the obtained Reynolds stresses and the high resolution of the velocity fields, which allows for velocity gradients to be estimated numerically. While spanwise velocity gradients are unknown directly, end-view, cross-sectional velocity measurements show that the mean velocity is essentially constant across the span. Thus, all components of the production tensor can be calculated and/or estimated closely, and it is shown that the streamwise normal and primary shear production terms decrease with increasing M_c , while the transverse and spanwise normal terms are close to zero for all mixing layer cases. The velocity gradient terms also allow for the calculation of the gradient Mach number. Its peak value in the shear layer is shown to agree very well with the linear model of Sarkar and

DNS results of Freund *et al.*, as it increases linearly with M_c .^{67,33} The turbulence Mach number (M_t , using all three components) increases monotonically with M_c , while the transverse turbulence Mach number (M_{tr}) reaches a limiting value near the high end of the M_c cases examined here. These results also agree well with those of Freund *et al.*, who show that the two trends (M_t continually increasing and M_{tr} leveling off around $M_c \sim 0.7$) continue for M_c above the current range.³³

Flow analyses that take advantage of the high resolution of the planar data are also performed in the present work that include: turbulence length scale analyses, proper orthogonal decomposition (POD), two-point spatial correlations, linear stochastic estimation (LSE), and entrainment analyses. In previous experimental mixing layer studies, the large-scale structures in the mixing layer were shown to evolve from round, spanwise coherent rollers with thin interconnecting braid regions, to elongated, three-dimensional structures that were highly disorganized and polygonal in shape.²² The same observations are made via the flow visualization techniques (schlieren and Mie scattering images) here; however, the organization and shapes of the large structures are examined quantitatively as well with the velocity measurements. Turbulence length-scale analyses show that, for increased levels of compressibility, the streamwise velocity fluctuation length scales increase in both the streamwise and transverse directions, while the transverse velocity fluctuation length scales decrease in the transverse direction. These results, combined with the shapes of the two-dimensional spatial velocity correlations and the shapes of the dominant POD modes, lead to the conclusion that for higher M_c mixing layer cases, there is a strong axial (streamwise-aligned) pulsing dynamic that can be linked to the streamwise stretching and elongation of the structures. In turn, this dominant pulsing mode leads to the loss of the structures' round shapes and clear organization. The conditionally averaged roller and braid structures from the LSE technique also support this notion, as both structure types become flatter in the transverse direction and stretched in the streamwise direction relative to the local mixing layer thickness. These specific structure types are only resolved with the conditional averaging technique however, and in unconditional ensemble averaging, they are difficult to detect due by the strong pulsing motions for high M_c . Furthermore, spanwise velocity fluctuations are shown to be aligned closer to the horizontal for increased compressibility, and the spatial correlations of all velocity fluctuations, except for the streamwise component, decrease in size with increasing M_c .

These changes in the shapes, sizes, and orientations of the coherent structures and velocity correlations are shown to have an effect on the geometry of the instantaneous interfaces that demarcate irrotational, non-turbulent fluid from the turbulent mixing layer fluid. Local entrainment analyses, based on the normal velocity component along the interface and geometry of the interface itself, are performed to identify length scales associated with the entrainment mechanisms for the current M_c cases. The results indicate that larger length-scale mechanisms (*i.e.*, engulfment) are likely present in lower compressibility cases, while smaller length-scale mechanisms (*i.e.*, nibbling) are prevalent at higher levels of compressibility. Additionally, the lower-speed secondary side interface consistently shows longer length scales, which, in part, explains the faster growth of the shear layers into the secondary stream. The effectiveness of the interface identification method is shown via conditional averages of turbulence quantities based on distance from the interface, with all conditionally averaged quantities showing a sharp jump at the interface location.

The characterized elongation and flattening of the large-scale structures with increasing M_c is in agreement with the fundamental result of the streamwise normal Reynolds stress remaining on the same relative scale as the freestream velocity difference, in contrast to the other stresses all decreasing with increasing compressibility. The dominant streamwise fluctuations at high M_c are also consistent with the entrainment interface results, as the large-amplitude, longer-wavelength interface shapes in the incompressible case would become flattened-out by the dominant streamwise pulsing. The smaller-scale distortions at higher levels of compressibility, which are less capable of entraining freestream fluid into the mixing layer, cause the inhibited growth rates at higher M_c , and thus this analysis helps to physically explain the unanimously agreed-upon reduction of normalized growth rate for increased M_c . Indeed, this phenomenon was clearly observed in the present experiments as well, with the extent of reduction matching that of previous authors for a given level of compressibility.

Interestingly, results from all the analyses in this dissertation indicate a distinct critical point between the M_c values of 0.38 and 0.55. Schlieren images, turbulence length scales, POD modes, spatial velocity correlations, and the entrainment length scales all show a clear difference between the two least compressible cases ($M_c = 0.19$ and 0.38) and the three highest compressibility cases ($M_c = 0.55$, 0.69 , and 0.88). The schlieren images and movies show that roller structures are consistently present and dominate the flow for $M_c \leq 0.38$, while they are absent for $M_c \geq 0.55$. The spatial correlations and POD modes further elucidate this evolution, as the streamwise fluctuations

are found to be dominant, both in intensity and correlation, throughout the mixing layers for $M_c \geq 0.55$, leading to a streamwise pulsing dynamic being the dominant mode for those cases. The entrainment length scales also show a large change between $M_c = 0.38$ and 0.55 , with the overall length scale results remaining fairly constant from $0.55 - 0.88$. Clemens and Mungal also report the complete loss of spanwise-coherent braid-roller structure organization between their $M_c = 0.42$ and 0.50 cases,³¹ agreeing with the critical M_c value being between 0.38 and 0.55 here. Future experimental or computational investigations regarding the exact transition point and the associated physical causes would certainly be useful additions to the literature. Furthermore, computations would be able to determine if the pressure-strain rate correlation that is coupled to the reduced growth rate also shows a large difference between these M_c values.

Lastly, to conclude the scope of the current work, a full uncertainty analysis is performed for the pressure, temperature, and velocity measurements. For directly measured quantities such as pressure and temperature, random and systematic errors are combined to derive the total error of a measurement. For calculated quantities such as M_c , M_1 , M_2 , etc., the uncertainties of their dependent variables are propagated to the calculated quantities' uncertainties using their functional relationships. Velocity measurement uncertainty is calculated for each component independently from four different error sources: equipment, particle lag, processing, and statistical. Uncertainties of the mean velocity and Reynolds stresses are calculated in a root-mean-square manner from the instantaneous uncertainties of each image. In general, the spanwise velocity component has the highest uncertainty (since it is the out-of-plane measurement in this flow), and for the lowest $M_c = 0.19$ case, which has the highest relative uncertainty, it is $\leq 8\%(\Delta U)$. This uncertainty quantification, in addition to other various aspects of the current experiments (*i.e.*, incoming boundary layer, sidewall pressure, and cross-sectional velocity measurements; complete documentation of wind tunnel geometry; flow visualizations to minimize splitter-plate tip pressure difference; large ensemble sizes of velocity measurements; confirmation of self-similarity for all turbulence statistics; etc.) were all conducted in an effort to provide a comprehensive set of compressible mixing layer experimental data that could be used for CFD validation purposes. The data, as well as the wind tunnel geometries, are available on a project website that was specifically created to disseminate the present results (URL: <https://wiki.illinois.edu/wiki/display/NCSLF/>). In addition, other material pertinent to this project are also available there (*e.g.*, conference papers, presentations, journal papers).

7.2. Suggestions for Future Work

For such a canonical flow, there are many parameters worth investigating, in terms of their effects on the mixing layer turbulence. One such work that is currently taking place, with the same wind tunnel facility and nozzle set-up as the $M_c = 0.69$ case here, is the effect of increased temperature in the lower-speed stream. Clearly, the change in temperature will alter the density of the flow, but to examine how the heat affects the turbulence in regard to distinct thermodynamics-related compressibility effects will be interesting. In fact, the nominal convective Mach number for that work is close to that of the $M_c = 0.55$ case here, and differences in normalized growth rate, Reynolds stress, and anisotropy values, among others, will be interesting points of discussion.

Additionally, while much of the analyses in the present work used the same definitions of mixing layer characteristics from previous investigations (*e.g.*, shear layer thickness, compressibility parameter M_c , normalized growth rate relation) and compared results to the existing literature, it would be a useful venture to work on obtaining possible updated definitions using the present high-quality data. For example, the $10\%\Delta U$ thickness was defined only when velocity data became available and improves upon the visual thickness that was used when flow visualizations were the state-of-the-art diagnostic technique. A thickness definition based on the turbulent kinetic energy is a possible candidate, and while the resulting mean shear layer boundary locations might end up being very similar to the $10\%\Delta U$ definition, a characterization of the thickness based on a turbulence quantity might be better physically founded. Likewise, the convective Mach number (while a brief attempt was made at an empirical definition here) is a compressibility parameter that could use an update from its definition from isentropic relations. The normalized growth rate relation could also be updated using data acquired with advanced flow diagnostics, which are higher in resolution and likely lower in uncertainty (or at least with uncertainty being quantified). Slessor *et al.* (2000) attempt to address these last points about the growth rate and compressibility parameter (by using the growth rate to scale compressibility); however, at the time of their writing, the data available were still mainly point-by-point velocity measurements.⁹⁶

As for suggestions of additional flow analysis techniques, there are a few that were considered but not pursued in this dissertation that could prove to be interesting. A conditional averaging technique based on using the POD coefficients is an analysis that has been performed in the fluid dynamics literature. Since the coefficients give information about which instantaneous images

most resemble a certain mode, grouping instantaneous images that have large coefficient magnitudes for a given mode and ensemble averaging (or performing more complicated analyses on that subset of images) could give more information about the dynamics for a given mode. At the very least, the images should somewhat resemble the mode dynamic on average. Determining which conditions to use for the LSE analysis is also an area that could use further investigation. As mentioned in Section 5.2.3, structures with more detail, or different structures entirely, may be possible to identify with enhanced conditioning (such as using the full velocity deformation tensor). Since that would require the velocity gradients to be known at each point, and the ability to identify specific tensor components for a given desired structure, an iterative method involving a machine learning technique could be a possibility. A learning model (in the machine learning sense) could be utilized for which the inputs are the deformation tensor components and currently identified conditional structure, and the output is newly identified conditional structure, with parameters of the model being tuned appropriately with a specific machine learning algorithm.

There are many more possible analyses that could be performed with the data acquired from the present experiments, and many computational models may find the results that are reported here useful in improving their parameters. This is all to say that, while planar free shear layers have been the subject of many different researchers, and there have been many experimental investigations on the compressibility effects on mixing layer turbulence, this flowfield was due for an updated set of data that could be used for analyses that were previously not possible. And as flow diagnostic techniques are sure to continue to advance, there will be a time when this current dataset will require an update of its own. Until the likely next step of time-resolved and/or three-dimensional tomographic velocity measurements (or instantaneous coupled velocity-pressure or velocity-density measurements) of supersonic flows can be performed on the scale that was achieved here, the present work will serve as a tool for the advancement of scientific research, as previous works have done.

REFERENCES

- ¹Dutton, J. C., "Compressible Turbulent Free Shear Layers," NATO Advisory Group for Aerospace Research and Development, Report No. AGARD-R-819, 1997, pp. 2-1–2-42.
- ²Zhou, Q., He, F., and Shen, M. Y., "Direct numerical simulation of a spatially developing compressible plane mixing layer: Flow structures and mean flow properties," *Journal of Fluid Mechanics*, Vol. 711, 2012, pp. 437–468.
- ³Javed, A., Rajan, N., and Chakraborty, D., "Reynolds averaged Navier-Stokes simulations of compressible mixing layers of similar and dissimilar gases: Performance of k-e turbulence model," *Journal of Aerospace Engineering*, Vol. 229, No. 9, 2015, pp. 11.
- ⁴Mankbadi, M. R., Georgiadis, N. J., and DeBonis, J. R., "Comparison of High-Order and Low-Order Methods for Large-Eddy Simulation," AIAA Fluid Dynamics Conference, Dallas, TX, 2015.
- ⁵Shi, K., Morris, S., and Jemcov, A., "Entropy Generation and Transport Mechanism in Compressible Mixing Layer: A Direct Numerical Study," AIAA SciTech 2016, San Diego, CA, AIAA Paper 2016-0334, 2016.
- ⁶Schlichting, H., *Boundary-Layer Theory*, 7th ed., McGraw-Hill, New York, 1979, pp. 737-739.
- ⁷Brown, G. L. and Roshko, A., "On Density Effects and Large Structure in Turbulent Mixing Layers," *Journal of Fluid Mechanics*, Vol. 64, 1974, pp. 774–816.
- ⁸Bogdanoff, D.W., "Compressibility Effects in Turbulent Shear Layers," *AIAA Journal*, Vol. 21, No. 6, 1983, pp. 926–927.
- ⁹Papamoschou, D. and Roshko, A., "The compressible turbulent shear layer: an experimental study," *Journal of Fluid Mechanics*, Vol. 197, 1988, pp. 453–477.
- ¹⁰Liepmann, H. W. and Laufer, J., "Investigation of free turbulent mixing," *NACA Technical Note*, No. 1257, 1947.
- ¹¹Miles, J. B. and Shih, J., "Similarity parameter for two-stream turbulent jet-mixing region," *AIAA Journal*, Vol. 6, No. 1429, 1968.
- ¹²Mills, R. D., "Numerical and experimental investigations of the shear layer between two parallel streams," *Journal of Fluid Mechanics*, Vol. 33, No. 591, 1968.
- ¹³Spencer, B. W. and Jones, B. G., "Statistical investigation of pressure and velocity fields in the turbulent two-stream mixing layer," *AIAA Paper*, No. 71-613, 1971.
- ¹⁴Yule, A. J., "Two-dimensional self-preserving turbulent mixing layers at different free stream velocity ratios," *Aerospace Research Council R. & M.*, No. 3683, 1972.
- ¹⁵Abramovich, G. N., *The Theory of Turbulent Jets*, M.I.T. Press, 1963.
- ¹⁶Sabin, C. M., "An analytical and experimental study of the plane, incompressible, turbulent free-shear layer with arbitrary velocity ratio and pressure gradient," *Trans. A.S.M.E.*, D 87, No. 421, 1965.
- ¹⁷Goebel, S. G. and Dutton, J. C., "Experimental Study of Compressible Turbulent Mixing Layers," *AIAA Journal*, Vol. 29, No. 4, 1991, pp. 538–546.
- ¹⁸Ikawa, H. and Kubota, T., "Investigation of supersonic turbulent mixing layer with zero pressure gradient," *AIAA Journal*, Vol. 13, No. 5, 1975, pp. 566–572.
- ¹⁹Chinzei, N., Matsuya, G., Komura, T., Murakami, A., and Kudou, K., "Spreading of Two-Stream Supersonic Turbulent Mixing Layers," *Physics of Fluids*, Vol. 29, No. 5, 1986, pp. 1345–1347.
- ²⁰Elliott, G. S. and Samimy, M., "Effects of Compressibility on the Characteristics of Free Shear Layers," *AIAA Journal*, Vol. 28, No. 3, 1990, pp. 439–445.
- ²¹Fourquette, D. C., Mungal, M. G., and Dibble, R. W., "Time evolution of the shear layer of a supersonic axisymmetric jet," *AIAA Journal*, Vol. 29, No. 7, 1991, pp. 1123–1130.
- ²²Clemens, N.T. and Mungal, M. G., "Two- and Three-Dimensional Effects in the Supersonic Mixing Layer," *AIAA Journal*, Vol. 30, No. 4, 1992, pp. 973–981.
- ²³Gruber, M. R., Messersmith, N. L., and Dutton, J. C., "Three-dimensional velocity field in a compressible mixing layer," *AIAA Journal*, Vol. 31, No. 11, 1993, pp. 2061–2067.

- ²⁴Hall, J., Dimotakis, P., and Rosemann, H., "Experiments in Nonreacting Compressible Shear Layers," *AIAA Journal*, Vol. 31, No. 12, 1993, pp. 2247–2254.
- ²⁵Goebel, S. G., "An Experimental Investigation of Compressible, Turbulent Mixing Layers," Ph. D. Thesis, Dept. of Mechanical Engineering, Univ. of Illinois, Urbana, IL, 1990.
- ²⁶Bell, J. H. and Mehta, R. D., "Development of a Two-Stream Mixing Layer from Tripped and Untripped Boundary Layers," *AIAA Journal*, Vol. 28, No. 12, 1990, pp. 2034–2042.
- ²⁷Mehta, R. D. and Westphal, R. V., "Near-field turbulence properties of single and two-stream plane mixing layers," *Experiments in Fluids*, Vol. 4, 1986, pp. 257–266.
- ²⁸Debisschop, J. R., Chambres, O., and Bonnet, J. P., "Velocity Field Characteristics in Supersonic Mixing Layers," *Experimental Thermal and Fluid Science*, Vol. 94, No. 9, 1994, pp. 147–155.
- ²⁹Urban, W. D. and Mungal, M. G., "Planar Velocity Measurements in Compressible Mixing Layers," *Journal of Fluid Mechanics*, Vol. 431, 2001, pp. 189–222.
- ³⁰Barre, S. and Bonnet, J. P., "Detailed experimental study of a highly compressible supersonic turbulent plane mixing layer and comparison with most recent DNS results: "Towards an accurate description of compressibility effects in supersonic free shear flows," *International Journal of Heat and Fluid Flow*, Vol. 51, 2015, pp. 324–334.
- ³¹Clemens, N.T. and Mungal, M.G., "Large-scale structure and entrainment in the supersonic mixing layer," *Journal of Fluid Mechanics*, vol. 284, 1995, pp. 171–216.
- ³²Olsen, M. G. and Dutton, J. C., "Planar velocity measurements in a weakly compressible mixing layer," *Journal of Fluid Mechanics*, Vol. 486, 2003, pp. 51–77.
- ³³Freund, J. B., Lele, S. K., and Moin, P., "Compressibility effects in a turbulent annular mixing layer. Part 1. Turbulence and growth rate," *Journal of Fluid Mechanics*, Vol. 421, 2000, pp. 229–267.
- ³⁴Zeman, O., "Dilatation dissipation: The concept and application in modeling compressible mixing layers," *Physics of Fluids A*, Vol. 2, No. 2, 1990, pp. 178–188.
- ³⁵Zeman, O., "On the decay of compressible isotropic turbulence," *Physics of Fluids A*, Vol. 3, No. 5, 1991, pp. 951–955.
- ³⁶Sarkar, S., Erlebacher, G., Hussaini, M. Y., and Kreiss, H. O., "The analysis and modelling of dilatational terms in compressible turbulence," *Journal of Fluid Mechanics*, Vol. 227, 1991, pp. 473–493.
- ³⁷Vreman, A. W., Sandham, N. D., and Luo, K. H., "Compressible mixing layer growth rate and turbulence characteristics," *Journal of Fluid Mechanics*, Vol. 320, 1996, pp. 235–258.
- ³⁸Sandham, N. D. and Reynolds, W., "Three-dimensional simulations of large eddies in the compressible mixing layer," *Journal of Fluid Mechanics*, Vol. 224, 1991, pp. 133–158.
- ³⁹Pantano, C. and Sarkar, S., "A study of compressibility effects in the high-speed turbulent shear layer using direct simulation," *Journal of Fluid Mechanics*, Vol. 451, 2002, pp. 329–371.
- ⁴⁰Foysi, H. and Sarkar, S., "The compressible mixing layer: an LES study," *Theoretical and Computational Fluid Dynamics*, Vol. 24, 2010, pp. 565–588.
- ⁴¹Vreman A. W., "An Eddy-Viscosity Subgrid-Scale Model for Turbulent Shear Flow: Algebraic Theory and Applications," *Physics of Fluids*, Vol. 10, 2004, pp. 3670–3681.
- ⁴²Lee, G. S., "Design and Development of a Wind Tunnel for the Investigation of Turbulent Compressible Mixing Layers," M.S. Thesis, Dept. of Aerospace Engineering, University of Illinois, Urbana, IL, 2017.
- ⁴³Carroll, B. F., Dutton, J. C., and Addy, A. L., "NOZCS2: A Computer Program for the Design of Continuous Slope Supersonic Nozzles," UIUC Report No. UILU ENG 86-4007 ed., Urbana-Champaign: University of Illinois at Urbana-Champaign, 1986.
- ⁴⁴*FlowMaster Product-Manual*, DaVis Version 8.4, LaVision, Göttingen, Germany, Sept. 2017.
- ⁴⁵Prasad, A. K., "Stereoscopic particle image velocimetry," *Experiments in Fluids*, Vol. 29, 2000, pp. 103–116.
- ⁴⁶Samimy, M. and Lele, S. K., "Motion of particles with inertia in a compressible free shear layer," *Physics of Fluids A*, Vol. 3, No. 8, 1991, pp. 1915–1923.
- ⁴⁷Scarano, F., "Iterative image deformation methods in PIV," *Measurement Science and Technology*, Vol. 13, 2002.

⁴⁸Hortensius, R., "The Fluid-Structure Interaction of an Axisymmetric Underexpanded Jet Flowing Across an Adjacent Compliant Surface," Ph.D. Thesis, Dept. of Aerospace Engineering, University of Illinois, Urbana, IL, 2017.

⁴⁹Sun, C., and Childs, M. E., "A Modified Wall Wake Velocity Profile for Turbulent Compressible Boundary Layers," *Journal of Aircraft*, Vol. 10, No. 6, 1973, pp. 381–383.

⁵⁰Mathews, D. C., Childs, M. E., and Paynter, G. C., "Use of Coles' Universal Wake Function for Compressible Turbulent Boundary Layers," *Journal of Aircraft*, Vol. 7, No. 2, 1970, pp. 137–140.

⁵¹White, F. M., *Viscous Fluid Flow*, 3rd Ed., McGraw-Hill, New York, NY, 2006, Ch. 5–6.

⁵²Fernholz, H. H., and Finley, P. J., "A Critical Commentary on Mean Flow Data for Two-Dimensional Compressible Turbulent Boundary Layers," AGARDograph, No. 253, 1980.

⁵³Elliott, G. S., Samimy, M., and Arnette, S. A., "The characteristics and evolution of large-scale structures in compressible mixing layers," *Physics of Fluids*, Vol. 7, No. 4, 1995, pp. 864–876.

⁵⁴Messersmith, N. L. and Dutton, J. C., "Characteristic Features of Large Structures in Compressible Mixing Layers," *AIAA Journal*, Vol. 34, No. 9, 1996, pp. 1814–1821.

⁵⁵Rossmann, T., Mungal, M. G., and Hanson, R. K., "Evolution and growth of large-scale structures in high compressibility mixing layers," *Journal of Turbulence*, Vol. 3, No. 9, 2002, pp. 1–18.

⁵⁶Pope, S. B., *Turbulent Flows*, 10th Ed., Cambridge University Press, New York, NY, 2013.

⁵⁷Eisfeld, B., "Turbulence Modeling for Free Shear Flows," AIAA Aviation 2019 Forum, AIAA Paper 2019-2962, 2019.

⁵⁸Hinze, J. O., *Turbulence*, 2nd Ed., McGraw-Hill, New York, NY, 1975.

⁵⁹Lumley, J. L., "Computational Modeling of Turbulent Flows," *Advances in Applied Mechanics*, Vol. 18, No. 3, 1978, pp. 123–176.

⁶⁰Simonsen, A. J. and Krogstad, P. A., "Turbulent Stress Invariant Analysis: Clarification of Existing Terminology," 15th Australasian Fluid Mechanics Conference, Univ. of Sydney, Sydney, Australia, 2004, pp. 1–4.

⁶¹Gatski, T. and Bonnet, J. P., "Compressibility, Turbulence and High Speed Flow," Academic Press, New York, 2009, pp. 117–160.

⁶²Nagano, Y. and Tagawa, M., "A structural turbulence model for triple products of velocity and scalar," *Journal of Fluid Mechanics*, Vol. 215, 1990, pp. 639–657.

⁶³Olsen, M. E. and Lillard R. P., "Improvement of Reynolds-stress and triple-product Lag models," 23rd AIAA Computational Fluid Dynamics Conference, AIAA Paper 2017-3954, 2017.

⁶⁴Adrian, R. J., Christensen, K. T., and Liu, Z.-C., "Analysis and interpretation of instantaneous turbulent velocity fields," *Experiments in Fluids*, Vol. 29, 2000, pp. 275–290.

⁶⁵Papamoschou, D., "Structure of the Compressible Turbulent Shear Layer," 27th AIAA Aerospace Sciences Meeting, AIAA Paper 89-0126, 1989.

⁶⁶Poggie, J. and Smits, A. J., "Large-scale coherent turbulence structures in a compressible mixing layer flow," 34th AIAA Aerospace Sciences Meeting and Exhibit, AIAA Paper 96-0440, 1996.

⁶⁷Sarkar, S., "The stabilizing effect of compressibility in turbulent shear flow," *Journal of Fluid Mechanics*, Vol. 282, 1995, pp. 163–186.

⁶⁸Lumley, J. L., "The structure of inhomogeneous turbulent flows," *Atmospheric Turbulence and Radio Wave Propagation*, A. M. Yaglom, V. I. Tatarsky, eds., Publishing House Nauka, Moscow, 1967, pp. 166–178.

⁶⁹Fukunaga, K., *Introduction to Statistical Pattern Recognition*, 2nd ed., Academic Press, 1990.

⁷⁰Delville, J., Ukeiley, L., Cordier, L., Bonnet, J. P., and Glauser, M., "Examination of large-scale structures in a turbulent plane mixing layer. Part 1. Proper orthogonal decomposition," *Journal of Fluid Mechanics*, Vol. 391, 1999, pp. 99–122.

⁷¹Citriniti, J. H. and George, W. K., "Reconstruction of the global velocity field in the axisymmetric mixing layer utilizing the proper orthogonal decomposition," *Journal of Fluid Mechanics*, Vol. 418, 2000, pp. 137–166.

⁷²Sirovich, L., "Turbulence and the Dynamics of Coherent Structures. Part I: Coherent Structures," *Quarterly of Applied Mathematics*, Vol. XLV, No. 3, 1987, pp. 561–571.

- ⁷³Meyer, K. E., Pedersen, J. M., and Özcan, O., “A turbulent jet in crossflow analysed with proper orthogonal decomposition,” *Journal of Fluid Mechanics*, Vol. 583, 2007, pp. 199–227.
- ⁷⁴Towne, A., Schmidt, O. T., Colonius, T., “Spectral proper orthogonal decomposition and its relationship to dynamic mode decomposition and resolvent analysis,” *Journal of Fluid Mechanics*, Vol. 847, 2018, pp. 821–867.
- ⁷⁵Nygard, K. J. and Glezer, A., “Evolution of streamwise vortices and generation of small-scale motion in a plane mixing layer,” *Journal of Fluid Mechanics*, Vol. 231, 1991, pp. 257–301.
- ⁷⁶Humble, R. A., Scarano, F., and van Oudheusden, B. W., “Unsteady flow organization of compressible planar base flows,” *Physics of Fluids*, Vol. 19, 2007.
- ⁷⁷Favale, J. V., Hortensius, R., Elliott, G. S., and Dutton, J. C., “Stereoscopic PIV Measurements of a Supersonic Axisymmetric Base Flow,” 55th AIAA Aerospace Sciences Meeting, AIAA Paper 2017-0522, 2017.
- ⁷⁸VerHulst, C. and Meneveau, C., “Large eddy simulation study of the kinetic energy entrainment by energetic turbulent flow structures in large wind farms,” *Physics of Fluids*, Vol. 29, 2014.
- ⁷⁹Yang, J., Liu, M., Wu, G., Gu, H., and Yao, M., “On the unsteady wake dynamics behind a circular disk using fully 3D proper orthogonal decomposition,” *Fluid Dynamics Research*, Vol. 49, No. 1, 2017, pp. 18–35.
- ⁸⁰Antonia, R. A., “Conditional Sampling in Turbulence Measurement,” *Annual Review of Fluid Mechanics*, Vol. 13, 1981, pp. 131–156.
- ⁸¹Adrian, R. J. and Moin, P., “Stochastic estimation of organized turbulent structure: homogeneous shear flow,” *Journal of Fluid Mechanics*, Vol. 190, 1988, pp. 531–559.
- ⁸²Christensen, K. T. and Adrian, R. J., “Statistical evidence of hairpin vortex packets in wall turbulence,” *Journal of Fluid Mechanics*, Vol. 431, 2001, pp. 433–443.
- ⁸³Olsen, M. G. and Dutton, J. C., “Stochastic Estimation of Large Structures in an Incompressible Mixing Layer,” *AIAA Journal*, Vol. 40, No. 12, 2002, pp. 2431–2438.
- ⁸⁴Kirchner, B. M., Tetef, T. J., Elliott, G. S., and Dutton, J. C., “Three-Dimensional Structure of the Compressible Mixing Layer of an Axisymmetric, Supersonic, Separated Flow,” AIAA AVIATION Forum 2018 Fluid Dynamics Conference, AIAA Paper 2018-3084, 2018.
- ⁸⁵Chauhan, K., Philip, J., de Silva, C. M., Hutchins, N., and Marusic, I., “The turbulent/non-turbulent interface and entrainment in a boundary layer,” *Journal of Fluid Mechanics*, Vol. 742, 2014, pp. 119–151.
- ⁸⁶Mathew, J. and Basu, A. J., “Some characteristics of entrainment at a cylindrical turbulence boundary,” *Physics of Fluids*, vol. 14, no. 7, 2002, pp. 2065–2072.
- ⁸⁷Westerweel, J., Fukushima, C., Pederson, J. M., and Hunt, J. C. R., “Momentum and scalar transport at the turbulent/non-turbulent interface of a jet,” *Journal of Fluid Mechanics*, Vol. 631, 2009, pp. 199–230.
- ⁸⁸Jahanbakhshi, R. and Madnia, C. K., “Entrainment in a compressible turbulent shear layer,” *Journal of Fluid Mechanics*, Vol. 797, 2016, pp. 564–603.
- ⁸⁹Brown, G. L., “The Entrainment and Large Structure in Turbulent Mixing Layers,” *Proceedings of the 5th Australian Conference on Hydraulics and Fluid Mechanics*, 1974, pp. 352–359.
- ⁹⁰Dimotakis, P. E., “Two-Dimensional Shear-Layer Entrainment,” *AIAA Journal*, vol. 24, no. 11, 1986, pp. 1791–1796.
- ⁹¹Abernethy, R. B., Benedict, R. P., and Dowdell, R. B., “ASME Measurement Uncertainty,” *Journal of Fluids Engineering*, Vol. 107, 1985, pp. 161–164.
- ⁹²Lazar, E., DeBlauw, B., Glumac, N., Dutton, J. C., and Elliott, G. S., “A Practical Approach to PIV Uncertainty Analysis,” 27th AIAA Aerodynamic Measurement Technology and Ground Testing Conference, AIAA Paper 2010-4355, 2010.
- ⁹³Benedict, L. H. and Gould, R. D., “Towards better uncertainty estimates for turbulence statistics,” *Experiments in Fluids*, Vol. 22, 1996, pp. 129–136.
- ⁹⁴Clift, R., Grace, J. R., and Weber, M. E., “Bubbles, Drops, and Particles,” Academic Press, Inc., New York, NY, 1978, pp. 111–112.

⁹⁵Weineke, B., "PIV uncertainty quantification from correlation statistics," *Measurement Science and Technology*, Vol. 26, No. 7, 2015, pp. 1–10.

⁹⁶Slessor, M. D., Zhuang, M., and Dimotakis, P. E., "Turbulent shear-layer mixing: growth-rate compressibility scaling," *Journal of Fluid Mechanics*, Vol. 414, 2000, pp. 35–45.

APPENDIX A: Website Documentation

This Appendix details the experimental data and wind tunnel facility files that are uploaded to the project website (in Table 9 below), which can be found at the following URL: <https://wiki.illinois.edu/wiki/display/NCSLF/>. Each mixing layer convective Mach number case has the same structure for the data uploaded, with most of the actual data files being hosted on a Box folder for this project. Some smaller data files are attached directly on the website itself. The descriptions given below are also included on the website where relevant (*i.e.*, descriptions of each dataset are given on the page containing that data).

Table 9. Project website documentation of experimental results.

<u>Wind Tunnel Facility</u>	<u>Description</u>
Engineering Drawings	Engineering drawing PDFs for all wind tunnel facility parts. Prints used for part fabrication.
Inventor CAD Part and Assembly Files	CAD design files for each facility part as well as entire tunnel assembly. All files in Autodesk Inventor format.
Iges Files for CFD	Iges files that contain fluid domain. One file per nozzle configuration (four configurations for the five cases). Domain starts at stagnation temp/pressure measurement location and ends at diffuser exit. Compatible with CFD meshing tools.
<u>Experimental Data (for each case)</u>	<u>Description</u>
Flow Conditions	Operating conditions with uncertainties, values taken directly from Table 4. Results given in table on website.
Fully Developed Mixing Layer Similarity Profiles	Ensemble-averaged similarity profiles from the fully developed region of each mixing layer. Results include mean velocities, Reynolds stresses, triple products, fourth moments, skewness, kurtosis, and triple product correlation coefficients in Tecplot .dat format. Files are given as external Box (cloud storage) links where data are stored.
Incoming Boundary Layer Characteristics	Incompressible BL integral parameters given in a table on website, with mean velocity profiles given in Tecplot .dat format as attachments on website.
Instantaneous (3-Component) Velocity Data	Instantaneous velocity fields (.dat) for all three components given as external Box links that contain compressed .zip folders for each FOV.

Table 9. (cont.)

Mean/Statistical Velocity Results	Mean velocities, Reynolds stresses, triple products, and fourth moments for full FOVs given as links to .dat files on Box cloud storage. Both side views and end views uploaded.
Schlieren	Schlieren images (.tiff) for full test section FOV stills and time-correlated high-speed movies given as external Box links.
SPIV Uncertainty	Uncertainty fields for mean velocities and Reynolds stresses for most downstream FOV of each case given as external Box links to .dat files.
Test Section Static Pressure	Test section static pressures given at the three transverse locations specified in Section 2.2.1 as Excel spreadsheets attached directly to website.

APPENDIX B: Uncertainty Parameters

Various parameters that pertain to calculating the uncertainties presented in Section 6 are given in this Appendix. Table 10 contains the accuracies and dynamic ranges for the pressure and temperature transducers used in the current experiments. For the pressure transducers, different ports on the same PSI Netscanner 9116 module were used depending on the different operating pressures for each measurement. Accuracies of the Netscanners are given as percent of full-scale dynamic range, while the temperature transducer (Omega DP26-TC-A) accuracy is given as an absolute temperature. Both are taken from their respective user manuals. Table 11 lists the total uncertainty for each sidewall pressure measurement, with the methodology being the same as for the other pressure measurements (explained in Section 6. 1). Lastly, Table 12 gives the uncertainty parameters used to calculate the SPIV equipment error for each case. The differences in parameters between each case have mainly to do with the calibration used for each case, which affects the pixel-to-mm ratio and the uncertainty of the calibration board in pixels.

Table 10. Accuracy of pressure and temperature transducers.

<u>Transducer</u>	<u>Full-scale (FS) dynamic range</u>	<u>% Accuracy FS</u>	<u>Accuracy</u>
PSI Netscanner 9116	103.4214 kPa, 689.476 kPa, 2585.535 kPa	0.05%	0.0517 kPa, 0.3447 kPa, 1.293 kPa
PSI Netscanner 9816	206.843 kPa	0.05%	0.1034 kPa
Omega DP26-TC-A	-	-	0.5 K

Table 11. Sidewall pressure measurement uncertainty (same value for all locations).

<u>Case 1: P (kPa)</u>	<u>Case 2: P (kPa)</u>	<u>Case 3: P (kPa)</u>	<u>Case 4: P (kPa)</u>	<u>Case 5: P (kPa)</u>
± 0.104	± 0.106	± 0.104	± 0.104	± 0.104 to 0.131

Table 12. SPIV equipment uncertainty parameters.

Parameter		Case 1	Case 2	Case 3	Case 4	Case 5
l	(calibration board length, mm)	106.0	106.0	106.0	106.0	106.0
ω_l	(uncertainty of l , mm)	0.02	0.02	0.02	0.02	0.02
L	(calibration board length, pixels)	2386.4	2389.6	2275.3	3163.7	3145.8
ω_L	(uncertainty of L , pixels)	0.6023	0.6021	0.3086	0.7938	1.0710
ω_{L_2}	(image distortion from aberrations $= 0.005L$, pixels)	11.93	11.95	11.38	15.82	15.73
λ	(lens to illumination plane distance, mm)	474.3	477.5	460.4	381.3	358.4
ω_λ	(uncertainty of λ , mm)	1.5	1.5	1.5	1.5	1.5
Δt	(laser delay time, μs)	1.0	1.0	1.0	1.0	1.0
ω_{t_1}	(laser timing uncertainty/jitter, μs)	0.001	0.001	0.001	0.001	0.001
ω_{t_2}	(delayer generator uncertainty, μs)	0.001	0.001	0.001	0.001	0.001

APPENDIX C: Velocity Comparison Between Diagnostics

Since these experiments serve as a validation tool for computations, a useful (yet simple) analysis is to compare the mean freestream velocities as measured by the SPIV and as calculated by isentropic relations using the stagnation/static pressure measurements. The stagnation pressure in the plenums and mean static pressure on the sidewall are measured for each stream; thus, the mean velocity of each freestream can be calculated at the transverse locations available from the pressure-tap sidewall insert (at the middle of each freestream). The $y = 0$ location is omitted in this analysis since the stagnation pressure is not directly measured there. Velocity magnitude comparisons between the two diagnostic techniques are plotted in Figure 118 for the primary and secondary freestreams. It can be seen that the results from both techniques are in good agreement, and the isentropic relations closely predict the velocity for streamwise locations that are fairly far downstream (up to and including the fully-developed regions). This agreement gives further confidence to the accuracy of the SPIV measurements, as they are confirmed with a redundant, non-particle-based diagnostic technique here.

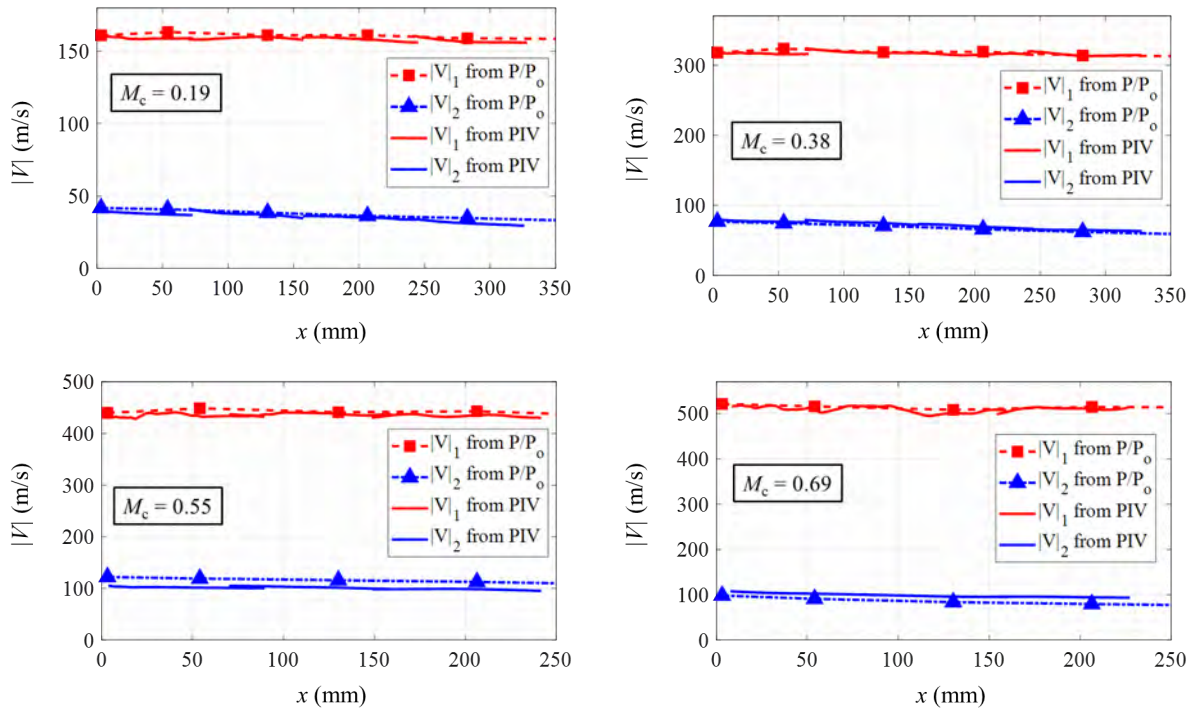


Figure 118. Mean freestream velocity comparisons for $M_c = 0.19, 0.38, 0.55, 0.69$, and 0.88 mixing layers.

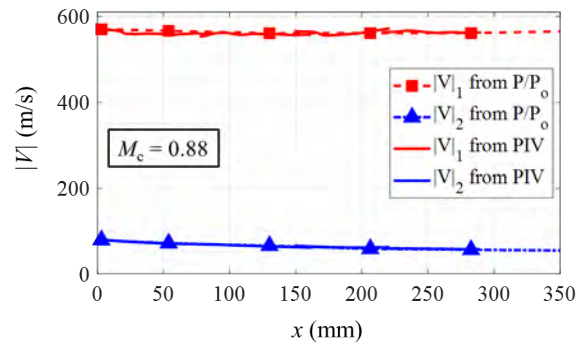


Figure 118. (cont.)

APPENDIX D: Expansion of Turbulence Production Terms

The full turbulence production tensor is given in Equation (38). As explained in Section 4.4, various terms that include Re_{xz} and Re_{yz} , and spanwise velocity gradients can be neglected due to the planar geometry of the current problem. To see where these terms appear, each component of P_{ij} is expanded in Equations (39) – (42). Terms that are neglected in Section 4.4 are crossed out below.

$$P_{ij} = -\overline{u_i' u_k'} \frac{\partial \bar{u}_j}{\partial x_k} - \overline{u_j' u_k'} \frac{\partial \bar{u}_i}{\partial x_k} \quad (38)$$

$$P_{xx} = -2 \left[\overline{u'u'} \frac{\partial \bar{u}}{\partial x} + \overline{u'v'} \frac{\partial \bar{u}}{\partial y} + \cancel{\overline{u'w'} \frac{\partial \bar{u}}{\partial z}} \right] \quad (39)$$

$$P_{yy} = -2 \left[\overline{u'v'} \frac{\partial \bar{v}}{\partial x} + \cancel{\overline{v'v'} \frac{\partial \bar{v}}{\partial y}} + \cancel{\overline{v'w'} \frac{\partial \bar{v}}{\partial z}} \right] \quad (40)$$

$$P_{zz} = -2 \left[\cancel{\overline{u'w'} \frac{\partial \bar{w}}{\partial x}} + \cancel{\overline{v'w'} \frac{\partial \bar{w}}{\partial y}} + \cancel{\overline{w'w'} \frac{\partial \bar{w}}{\partial z}} \right] \quad (41)$$

$$P_{xy} = - \left[\overline{u'u'} \frac{\partial \bar{v}}{\partial x} + \overline{u'v'} \frac{\partial \bar{v}}{\partial y} + \cancel{\overline{u'w'} \frac{\partial \bar{v}}{\partial z}} \right] - \left[\cancel{\overline{u'v'} \frac{\partial \bar{u}}{\partial x}} + \overline{v'v'} \frac{\partial \bar{u}}{\partial y} + \cancel{\overline{v'w'} \frac{\partial \bar{u}}{\partial z}} \right] \quad (42)$$

PART II

HEATED MIXING LAYER STUDIES

(Based on the M.S. Thesis of Nicholas Tymkiw)

ABSTRACT

Experiments on a compressible planar shear layer with a sharp thermal gradient between the mixing streams were conducted with the goal of adding to a set of benchmark computational fluid dynamics validation datasets for unheated mixing layers as well as obtaining the first temperature measurements within this kind of shear layer. The shear layer itself was a dual-stream air mixing layer with a convective Mach number of 0.541 and a stagnation temperature difference of about 200 K between the streams. A preexisting mixing layer facility was modified to provide for the addition of the heated stream while maintaining the original operational capacities of the facility. Three-component velocity fields along the central streamwise-transverse plane of the shear layer were obtained through the use of stereo-particle image velocimetry. Even with the novel stagnation temperature gradient, it was found that there were minor to negligible effects on the turbulence or mean velocity fields compared to previous similar investigations into the compressible shear layer, albeit with a higher shear layer growth rate. Temperature probe traverses throughout the shear layer were obtained at different streamwise points, as well as static pressure measurements along the entire test section side-wall. Schlieren visualizations in the form of high-speed videos as well as instantaneous images were also obtained, giving additional qualitative insight. Temperature field measurements were made via Filtered Rayleigh Scattering along the central streamwise-transverse plane, and the mean transverse profiles of those temperature fields calculated. It was found that the temperature field of the thermal mixing layer becomes fully self-similar much closer to the splitter plate in the streamwise direction than that of the velocity field. This work provides a basis for future studies to build upon and to further investigate compressible shear layers with gradients in stagnation temperature between the streams.

ACKNOWLEDGEMENTS

This project was supported by the D.3 Transformation Tools and Technologies Project (TTT1) issued by NASA Headquarters: Award No. NNX15AU94A. I wish to thank the project technical managers at NASA Glenn Research Center for their assistance, especially Jim DeBonis.

TABLE OF CONTENTS

CHAPTER 1: INTRODUCTION	1
1.1 Background.....	1
1.1.1 Previous Experimental Planar Shear Layer Studies.....	1
1.1.2 Mixing Enhancement in the Shear Layer.....	3
1.1.3 Recent Work at UIUC on the Compressible Mixing Layer.....	4
1.2 The Filtered Rayleigh Scattering Technique	6
1.2.1 Filtered Rayleigh Scattering Theory	6
1.2.2 Application of Filtered Rayleigh Scattering	10
1.3 Current Work	11
CHAPTER 2: EXPERIMENTAL METHODOLOGIES	13
2.1 Wind Tunnel Facility	13
2.1.1 Facility Modifications	17
2.1.2 Modification Analyses	20
2.2 Experimental Operation.....	23
2.2.1 Experimental Operating Procedure.....	23
2.2.2 Experimental Operating Condition	26
2.3 Flow Diagnostic Techniques	27
2.3.1 Schlieren Measurements	27
2.3.2 Sidewall Static Pressure Measurements.....	29
2.3.3 Temperature Probe Measurements.....	30
2.3.3.1 Initial Thermocouple Measurements	31
2.3.3.2 TAT Probe Measurements	32
2.3.4 Boundary Layer PIV	33
2.3.5 Stereo-PIV.....	35
2.3.6 Filtered Rayleigh Scattering	39
CHAPTER 3: SCHLIEREN, PRESSURE, AND TEMPERATURE PROBE MEASUREMENTS IN A COMPRESSIBLE MIXING LAYER WITH A THERMAL GRADIENT	44
3.1 Schlieren Visualizations	44
3.1.1 High-speed Schlieren Videos.....	44
3.1.2 Full-resolution Schlieren Visualization	45
3.2 Static Pressure Tap Measurements	46
3.3 Temperature Probe Measurements	48

3.3.1 Total Temperature Traverses	48
3.3.2 Static Temperature Traverses	50
CHAPTER 4: VELOCITY FIELD MEASUREMENTS IN A COMPRESSIBLE MIXING LAYER WITH A THERMAL GRADIENT	53
4.1 Challenges.....	53
4.1.1 Seeding Injection and Density	53
4.1.2 Secondary Seed Persistence	54
4.1.3 SPIV Camera Alignment and Calibration.....	58
4.2 Boundary Layer PIV Results	59
4.3 SPIV Results	63
4.3.1 Velocity Vector Results	63
4.3.2 Statistical Results: Reynolds Stresses and Higher Moments	71
4.3.3 SPIV Uncertainty	77
CHAPTER 5: TEMPERATURE FIELD MEASUREMENTS IN A COMPRESSIBLE MIXING LAYER WITH A THERMAL GRADIENT	81
5.1 Filtered Rayleigh Scattering Implementation	81
5.1.1 Initial Parameters	81
5.1.2 Iodine Cell Calibration.....	82
5.1.3 Imaging System and Laser Sheet Parameters	84
5.1.4 Image Processing and Temperature Calculation.....	85
5.1.5 Challenges with FRS.....	88
5.2 FRS Temperature Results	89
5.2.1 Mean Temperature Trace Results	89
5.2.2 FRS Temperature Fields	90
CHAPTER 6: CONCLUSION	93
6.1 Summary of Work and Concluding Remarks.....	93
6.2 Future Work and Recommendations	94
REFERENCES	96
APPENDIX A: AIR HEATER SPECIFICATIONS AND SAFETY SUPPLEMENT	100
APPENDIX B: BILL OF MATERIALS FOR FACILITY ADDITION OF HEATER..	103
APPENDIX C: ENGINEERING DRAWING OF TAT PROBE.....	104

CHAPTER 1: INTRODUCTION

1.1 Background

1.1.1 Previous Experimental Planar Shear Layer Studies

The work of Brown and Roshko (1974)¹ is the fundamental study in the planar mixing world, setting the foundation for all future work. Their experiment compared a series of incompressible mixing layer flows with varying density differentials between the two flows; originally their intent was to study the effects of the density difference on turbulent mixing, but the study revealed much more about the flow structure itself. Of particular note was their discovery that compressibility effects were separate from the effects of the density ratio at low Mach numbers. However, they do note that compressible flows have the capacity to introduce new effects that may tie into the effects of the density ratio.

Continued work on the mixing layer led to the compressibility parameter definition by Bogdanoff (1983)² and Papamouschou and Roshko (1988)³ of the convective Mach number, M_c , by arguing that the two streams have a shared stagnation point in the mixing layer. In cases where the static pressures are equivalent between the streams and the gases are identical in composition, M_c can be defined as shown in Equation (1), where U_1 and U_2 are the two freestream velocities in the streamwise direction and a_1 and a_2 their respective speeds of sound. This definition is quite easy to determine in all studies, both computational and experimental, and therefore has been widely adopted in the literature, including this one.

$$M_c = \frac{U_1 - U_2}{a_1 + a_2} \quad (1)$$

The shear layer thickness itself, b , has been variously defined depending on the experimentalist, study, and measurement method in use (as well as the mood of the researchers). For this study, the 10% ΔU thickness is utilized, defined as the transverse distance between two

points in the flow y_1 and y_2 , where ΔU is the difference in the freestream velocities U_1 and U_2 , y_1 is the location at which the mean velocity is $U_1 - 0.1\Delta U$ and y_2 is the location at which the velocity is $U_2 + 0.1\Delta U$. Other approaches have included the vorticity thickness and the visual thickness; the 10% ΔU definition is most typically used in velocimetry studies of the mixing layer such as this one.

The growth rate of the shear layer, db/dx , has been of great interest in many of the studies, including the oldest experiments. Early on researchers used a similarity variable, dependent on the velocity ratio r (U_2/U_1), to collapse the growth rate to a linear function, as borne out in Sabin (1965)⁴; Brown and Roshko¹, for instance, use this parameter for their work. However, all of the works using this similarity variable assumed uniform density; for the experiment of interest here, as well as others in the past, a more robust function was required. Papamoschou and Roshko (1988) argued for a proportional growth rate for incompressible mixing layers related to the differential velocity ΔU divided by the convective velocity U_c that accounted for the difference in density. Their equation, for a variable-density shear layer, is given below in Equation (2).³

$$\frac{db}{dx} \Big|_0 = c \frac{(1-r)(1-\sqrt{s})}{1+r\sqrt{s}} \quad (2)$$

The constant of proportionality in Equation (2), c , was determined to be $0.165/2$ by Goebel and Dutton (1991)⁵; this relation has borne out well for experimental studies of incompressible shear layers. As many studies of shear layers are incompressible, the easiest method of comparing compressible growth rates of all studies is to normalize by this term, as was performed by Barre and Bonnet (2015)⁶ or Kim et al. (2019)⁷. The work of Kim is of particular interest to this study, as it was the previous work performed in the same facility, and it is discussed in greater detail in Section 1.1.3.

1.1.2 Mixing Enhancement in the Shear Layer

The mixing within the shear layer is of particular interest from an application-based perspective. Enhancement of the mixing process is highly desired in combustion applications, especially for those of novel or limited geometries. Supersonic combustors may find particular relevance in studies such as this, where the effects of injector and flameholder geometry have major impact on the viability of designs. Scramjets in particular suffer from short residence times of the oxidizer/fuel mixture within the combustion chamber itself as well as poor entrainment of the fuel/flame mixture into the freestream. Vorticity and recirculation, then, are central to such applications: given that these effects are dominant in the mixing layer, its enhancement, therefore, is of paramount importance.^{8,9}

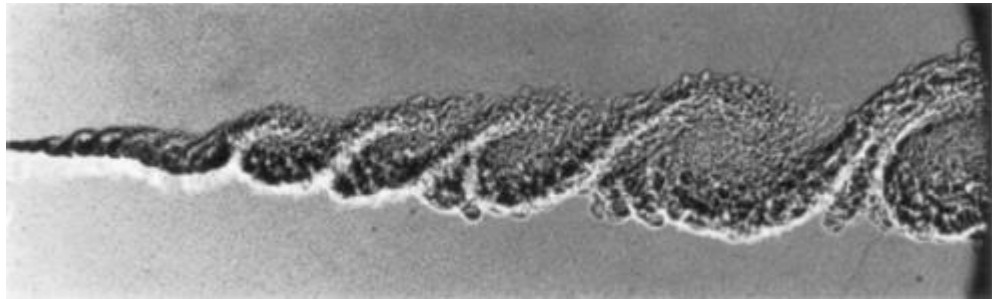


Figure 1. Shadowgraph from Brown and Roshko (1974) showing large-scale structures in a gaseous mixing layer¹

Large-scale structures within the mixing layer, at lower convective Mach numbers, are the most easily understood features relating to the enhancement. However, as multiple studies have shown in schlieren visualizations^{2,3,5,7}, the large-scale structures as seen by Brown & Roshko¹ above in Figure 1 reduce in size and organization as the compressibility increases to become more like those as visualized by Rossman et al. (2002) in Figure 2 on the following page.¹⁰ Smaller and less coherent structures, then, must be investigated for increasing the efficacy of the mixing layer at higher compressibility. Abraham and Magi (1997) performed DNS simulations of an incompressible mixing layer with differing density ratios. As the density ratio s increased in their

study, the spatial mixing layer growth rate slowed. This effect on the growth rate was inferred to be due to a faster effective mean velocity in the mixing layer; however, they posited its effects also may be highly influenced by instabilities at the interface between the mixing layer and freestreams¹¹. For mixing enhancement into the freestreams, Zhang et al. (2015) studied the effects of oblique shocks on the mixing layer and moreover its Reynolds stresses. The oblique shocks for their LES of a weakly compressible ($M_c = 0.3$) planar shear layer were found to modulate the growth rate of the shear layer as well as locally incline the layer as it progressed downstream. They additionally found that there was local enhancement in the vorticity of the flowfield around the shocks, and intensification of the turbulent kinetic energy and transverse Reynolds normal stress.¹²

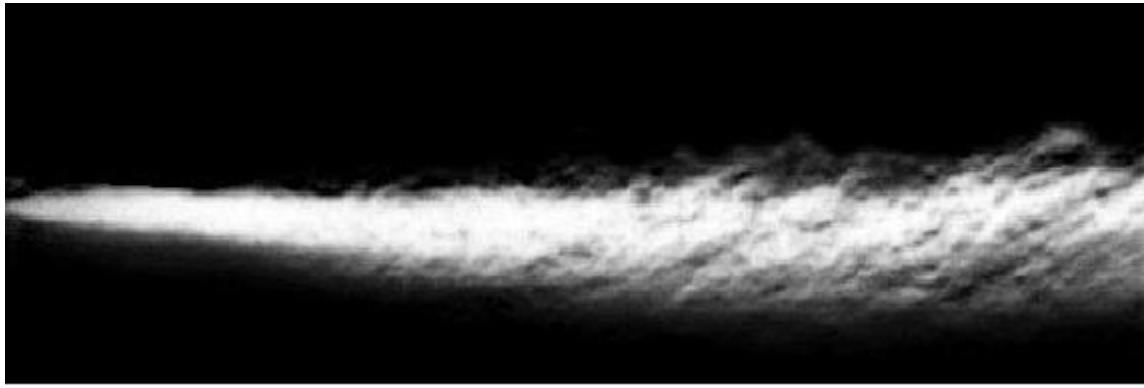


Figure 2. Schlieren of Rossman et al. (2002) for an $M_c = 0.86$ condition¹⁰

1.1.3 Recent Work at UIUC on the Compressible Mixing Layer

As noted in Section 1.1.1, the wind tunnel facility of the current investigation has already been used for previous planar mixing experiments. Kim et al. have performed a multitude of experiments and analyses on mixing layers with M_c ranging from 0.19 to 0.88, with all cases save one involving a supersonic primary stream. Large ensembles of stereo-PIV measurements were gathered, with an emphasis on confirmation of fully-developed, self-similar mean velocity and Reynolds stress conditions. Furthermore, this dataset was of high enough quality (and low enough uncertainty) that higher-order moment results (including third- and fourth-order moments) were

obtainable for all cases studied. The evolution of the large-scale structures was also of interest in the studies, particularly with respect to the growth of the mixing layer and trends in turbulence development.^{7,13-15}

In short, this dataset was used to determine trends of the entire (three-dimensional) Reynolds stress tensor, production trend and length scales of the turbulence, and entrainment mechanisms. Fundamentally, one of the most important trends to come from Kim's work was the confirmation that the streamwise-normal Reynolds stress remains constant as M_c increases. This discovery, stemming from the study's ability to consistently and clearly obtain fully-developed, self-similar conditions in the fully-developed region, is crucial, laying to rest a debate spanning the better part of three decades on the behavior of the streamwise-normal Reynolds stress with compressibility. Furthermore, by taking high-quality data of the entire stress tensor, it was discovered that the spanwise-normal Reynolds stress decreases monotonically with M_c , relative to the incompressible mixing layer value. From overall consideration of the Reynolds stress trends, it was also found that the turbulence production definitively decreases with increasing M_c ; confirming the earlier results of CFD studies by Freund et al. (2000) and Pantano and Sarkar (2002).^{16,17} It was further shown that as the compressibility increases in the mixing layer, the streamwise and transverse fluctuations both increase in length scale, while the length scale of the transverse fluctuations decreases, giving a more "flattened" planar shear layer. The entrainment into the shear layer, investigated through analyses including proper orthogonal decomposition to determine the modes of the entire mixing layer, as well as local analyses of the normal velocity component along the interface, indicate that larger length-scale mechanisms such as engulfment are more common in lower compressibility cases, while smaller-scale mechanisms begin to dominate as the compressibility rises. Furthermore, the boundary along the lower-velocity

secondary freestream was shown to consistently have larger- and longer-scale mechanisms compared to the higher-speed primary stream boundary. These findings are in self-agreement with each other, especially with respect to the streamwise-normal Reynolds stress trend: by damping out the higher-amplitude larger structures as the compressibility rises, the fluctuations are only able to grow at the same relative rate as the difference in freestream velocities. This understanding also provides a compelling reason for the previously found inhibition of the mixing layer growth rate at higher M_c .¹⁴

It is from discussions related to the work of Kim et al. that this study was born, as a corollary to a specific case he studied with $M_c = 0.69$. For further discussion, much deeper than it is of benefit to delve into for the current work, the reader is directed to Kim's doctoral dissertation, which is the best current summary of his work studying the supersonic compressible mixing layer.¹⁴ It should be noted that while all cases that Kim studied were of practically equivalent stagnation temperatures between the flows, the case of interest here rather calls for a major difference in the stagnation temperatures of the two streams.

1.2 The Filtered Rayleigh Scattering Technique

1.2.1 Filtered Rayleigh Scattering Theory

For the temperature measurements within the test section, an optical diagnostic technique known as filtered Rayleigh Scattering (FRS) was utilized. This technique, best described in the work of Forkey et al. (1996)¹⁸ (coincidentally, published in the same year this author was born), utilizes the elastic Rayleigh scattering effect from molecules in the flow to determine the velocity, temperature, and pressure of the area of interest. Undesirable background and Mie scattering are filtered from the signal by an absorption cell that acts as a molecular notch filter, given a laser tuned to a specific frequency. The Rayleigh scattered light is broadened from the laser profile and

is able to transmit through the filter; it is then imaged on the camera. FRS, then, is a technique most commonly applied when in use in a particle-laden or otherwise dirty flow; the filter greatly reduces the noise that any particulates would otherwise cause.

$$S = C \left[\int_{-\infty}^{\infty} R_{gas} t(f) df + \int_{-\infty}^{\infty} R_{bg} t(f) df \right] \quad (3)$$

The signal S as imaged onto the sensor of the camera is the raw data of interest in an FRS experiment. Equation (3) above shows the formulation in full, where R_{gas} is the Rayleigh signal of the medium, R_{bg} is the background Rayleigh signal from stray scattering, $t(f)$ is the transmission function of the absorption filter at an arbitrary frequency, and C is a constant value for the imaging environment, including the camera sensor and lens system.

When a laser pulse with uniform spatial profile and frequency f_L interacts with the air, it scatters in the form of a Rayleigh signal that is a function of the composition of the gas. This Rayleigh signal is an integral sum of the signals individually scattered from each molecule present into the solid angle $d\Omega$, scaled by their mole fraction χ_i and Rayleigh cross-section σ_i^{19} , as shown in Equation (4).

$$R_{gas} = E_l \frac{PV}{kT} \frac{d\sigma}{d\Omega} d\Omega \times \int_{-\infty}^{\infty} [l(f - [f_L + f_D] - f') \times g(Y, f')] df' \quad (4)$$

Each Rayleigh signal is the integral of the convolution of the laser lineshape l with an input amplitude E_l and the entire Rayleigh-Brillouin scattering profile $g(Y, f)$, and is well characterized by the Y parameter defined by Tenti et al.²⁰ and shown in Equation (5)

$$Y = \frac{nkT}{\sqrt{2}Kv_0\mu} \quad (5)$$

where n is the gas number density, μ the viscosity, v_0 the molecular thermal velocity, and K the magnitude of the scattering wave vector given in Equation (6).

$$K = \frac{4\pi}{\lambda} \sin\left(\frac{\theta}{2}\right) \quad (6)$$

The Tenti Y parameter is the measure of the ratio of the scattering wavelength to the molecular mean free path.²⁰ It is also important to note that the scattering profile is frequency shifted relative to the incoming laser profile due to the Doppler shift, given by Equation (7)

$$v_D = \frac{2v}{\lambda} \sin\left(\frac{\theta}{2}\right) \quad (7)$$

where v is the flow velocity along the line bisecting the laser propagation vector and the pointing vector of the camera, λ is the incoming vacuum wavelength of the laser sheet, and θ the scattering angle.²¹ This in turn gives the shifted central frequency f' of the Rayleigh signal; by virtue of the Doppler shift the Rayleigh signal typically is less affected by the absorption filter and is therefore stronger with increasing velocity. Figure 3 shows computed Filtered Rayleigh signals for a simplified air ($N_2 - O_2$) model with different velocities and temperatures; note that the center of the Rayleigh signal changes with increased velocity, and that the width of the profile increases. This increased width, known as thermal Doppler broadening, comes from its higher energy state (that is, a higher temperature) having an increased-width Maxwell distribution of its velocity, causing the Doppler effect on the motion of the individual molecules to correspondingly broaden.

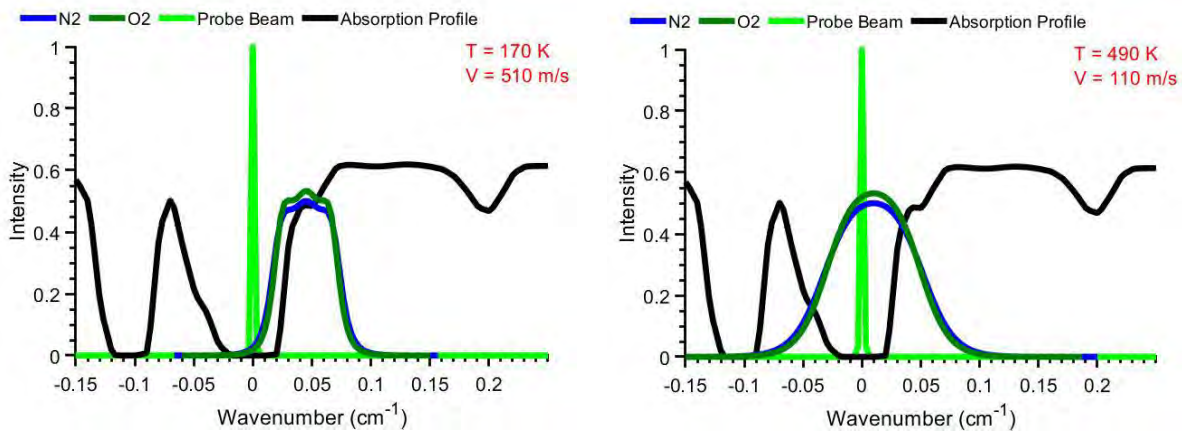


Figure 3. Computed FRS signal profiles for given temperature and velocity

The additional Rayleigh scattering from stationary objects in the imaged field of view from windows, walls, and other objects in the background may be calculated in the same way. Their

signals are of the same frequency as the laser, however, and as stated above, are almost entirely absorbed by the filter. Their contribution is therefore entirely dependent on the laser frequency and as a result the filter transmission function; for a consistent laser frequency, the background signal may be assumed to be the same between shots. For many approaches, including the current one, the filter is one of molecular iodine, which has multiple usable absorption lines around the central frequency of a frequency-doubled Nd:YAG laser. Given the transmission of the laser lineshape through a second reference filter, the location in frequency space may be found for each laser shot.

For this work, the technique is further simplified in that the velocity may be assumed to be known from another technique—that is, the particle image velocimetry (PIV) data. Furthermore, the pressure of the flow is assumed to be relatively constant and known from measurements made while monitoring the tunnel. The system of equations that affects the received signal may then be thought of as a system in which two values are known and constant throughout (f_L, P), one is known and varies based on location (V), and one is unknown and therefore may be solved for based on the received signal S : the temperature T . By normalizing by the reference signal value of the flatfield, taken at ambient conditions of temperature, pressure, and velocity, a simple relation may be obtained that yields directly the temperature based on the grayscale value of each pixel on the image sensor. This can be summarized in Equation (8)

$$\frac{S(f)}{S_{ref}(f)} = \frac{T_{ref}}{T} \frac{P}{P_{ref}} C_1 + C_2 \quad (8)$$

where Equations (3 & 4) have been combined and simplified given the reference values. From this relation, it is trivial to determine the temperature at each pixel given its normalized signal, the reference temperature and pressure, and the flow-on pressure and velocity, especially in the current application, where calibration constants C_1 and C_2 are applied to fit the signal response of the camera to the known temperature values in the freestreams.

1.2.2 Application of Filtered Rayleigh Scattering

Filtered Rayleigh scattering work has been achieved previously for a wide variety of flows, including the compressible shear layer. Forkey et al. made planar velocity, pressure, and temperature measurement in a Mach 2 free jet for their work.¹⁸ Other early works focused primarily on velocity measurements using the technique, such as in Elliott et al. (1992) where velocities in compressible mixing layers were measured with the technique²², and Miles et al. (1992) which first demonstrated FRS with iodine filters with an Nd:YAG laser while investigating the boundary layer structure in Mach 3 and Mach 5 flows²³. The latter work was later extended by Forkey et al. (1994) where supersonic boundary layers were further imaged.²⁴

The work of Forkey et al. (1996) is best known, then, for being the initial paper describing the multiple-property measurement capability of the FRS technique. This work, it should be stated, was in a fairly ideal environment—with a well-defined, clean flow and a simple setup to apply calibrations to the background.¹⁸ The use of the technique in its most effectual environment, a sooted combustion case, came with the work of Elliott et al. (1997), as temperature field measurements were obtained in two different premixed flames from multiple burners.²⁵

Extension of the FRS technique has come in multiple forms. Work by Boguszko, Elliott, and Huffman in the first decade of the 2000s at UIUC obtained multiple property measurements through the use of angularly resolved FRS, which they called FARRS; this was intended to reduce the uncertainty of the measurement by curve-fitting the effect of off-angle imaging on the relative intensity.²⁶⁻²⁹ At around the same time, Most and Leipertz (2001) used the molecular filter to great effect, allowing simultaneous PIV measurements while using FRS to determine the thermodynamic state of their premixed flame.³⁰ This approach has been utilized in multiple recent studies by McManus and Sutton, where they have used joint FRS and stereo-PIV measurements to

obtain single-shot temperature and velocity measurements in non-premixed flames.³¹⁻³³ Such an approach indicates a possible future of FRS, where it is used in conjunction with particle-based methods in order to take advantage of the latter's lessened uncertainty for velocity, while being able to determine the thermodynamic state of the molecules in environments unsuitable for other techniques.

1.3 Current Work

Given past and recent work on supersonic compressible mixing layers, especially that of Kim et al., it was necessary to investigate an area that had, until the beginning of this study, been neglected: a thermal difference in non-reacting mixing layers. It is not unreasonable that until this work it had not been studied: after all, it fits in a regime between supersonic mixing studies closest to reality (either two flows mixing and reacting, or a reacting flow mixing with a nonreacting flow), or simplest to model and study (no reaction, but at high speed). On the other hand, work has been done in studying thermally buoyant flows: ones whose speeds were very slow, albeit with strong thermal differentials, but where the dominant forces are not at all the same. Therefore, it is prudent to investigate such a case where the supersonic mixing layer is influenced by such a thermal difference.

From such an impetus, studies of velocity, density, and temperatures were taken with multiple different measurement methods in a compressible mixing layer with a primary stream of supersonic Mach number and ambient stagnation temperature and a secondary stream of subsonic yet weakly compressible Mach number and significantly elevated stagnation temperature. This case was studied using multiple different methods, including stereoscopic-particle image velocimetry (SPIV), stagnation temperature probe traversals, and Filtered Rayleigh Scattering (FRS), the first work of its kind for a heated mixing layer with a stagnation temperature differential.

While neither the methods used nor the experiment itself are groundbreaking or wholly encompassing by themselves, this work on the whole serves to provide a foundation for future research in identifying the challenges and initial effects of interest, giving the studies to come an initial point from which to build more holistic studies.

The remainder of this thesis is laid out in the following manner. Chapter 2 describes the facility used for the supersonic thermal mixing layer studies and outlines the utilized experimental measurement techniques. Chapter 3 discusses the results stemming from the classical measurement methods: schlieren visualizations, static-pressure measurements, and total air temperature probe traverses. Chapter 4 entails the stereo particle image velocimetry results, including the incoming boundary layers and mean velocity and turbulence analysis. Chapter 5 summarizes the Filtered Rayleigh Scattering thermometry work, to include the mean transverse temperature profiles as well as the temperature fields. The work is then summarized in Chapter 6, the conclusion.

CHAPTER 2: EXPERIMENTAL METHODOLOGIES

This chapter details the facility, experimental approaches and setups, and difficulties encountered therein while obtaining data to fully document (to the state-of-the-art) the flow phenomena of interest in the heated, compressible mixing layer. Project CAD files are available at the project website (<https://wiki.illinois.edu/wiki/display/NCSLF>) in PTC Creo format, including previous drawings of the wind tunnel facility; renderings are included for clarity.

2.1 Wind Tunnel Facility

The wind tunnel facility, located in the Gas Dynamics Lab within the Aerodynamics Research Laboratory at the University of Illinois at Urbana-Champaign, was designed to allow the investigation of different convective Mach number cases in compressible mixing layers. The facility is a blowdown wind tunnel, fed by a low-pressure line nominally charged to 150 psi, held in a tank farm of volume 4660 ft³. The design, construction, and testing of the wind tunnel were performed by Gyu-Sub Lee as his Master's thesis; five convective Mach number cases were implemented in the facility during this time by utilizing a replaceable nozzle design. Details of the tunnel that exceed what is discussed in this section may be found in his thesis, to include the initial structural and safety analyses of the facility.³⁴ The discussion here will rather entail the *modifications* that were made to the preexisting facility in order to enable the heated mixing layer experiment.

Two air streams, both taken from the low-pressure-line, are mixed after traveling lengthwise along a “splitter plate” through respective nozzles. The first, “primary” stream, is of a higher inlet Mach number, meets with a “secondary” stream, which is at a lower Mach number and in this application a higher stagnation temperature. In this instance, the nozzles used are nominally Mach 2.0 and Mach 0.3 for the primary and secondary streams, respectively. The air

flow to the streams themselves is modulated by a main gate valve as seen in Figure 4 below. The flow then splits off of a tee and flows to the primary and secondary inlets of the tunnel separately. The primary stream has a pneumatic valve to act as a safety backup to the tunnel, but otherwise flows directly to the wind tunnel; when the tunnel is in operation, the pneumatic valve is set fully open. The secondary stream is modulated by a second gate valve that limits the flow through to the electric heater. The heater brings the stagnation temperature of the secondary air to the target stagnation temperature of 495 K as it flows through; it then enters the tunnel after this process. Successful operation of the mixing layer tunnel is predicated upon reliably matching the static pressures of the two streams downstream in the test section; this is achieved by measuring a differential static pressure between the two streams just prior to the splitter tip.

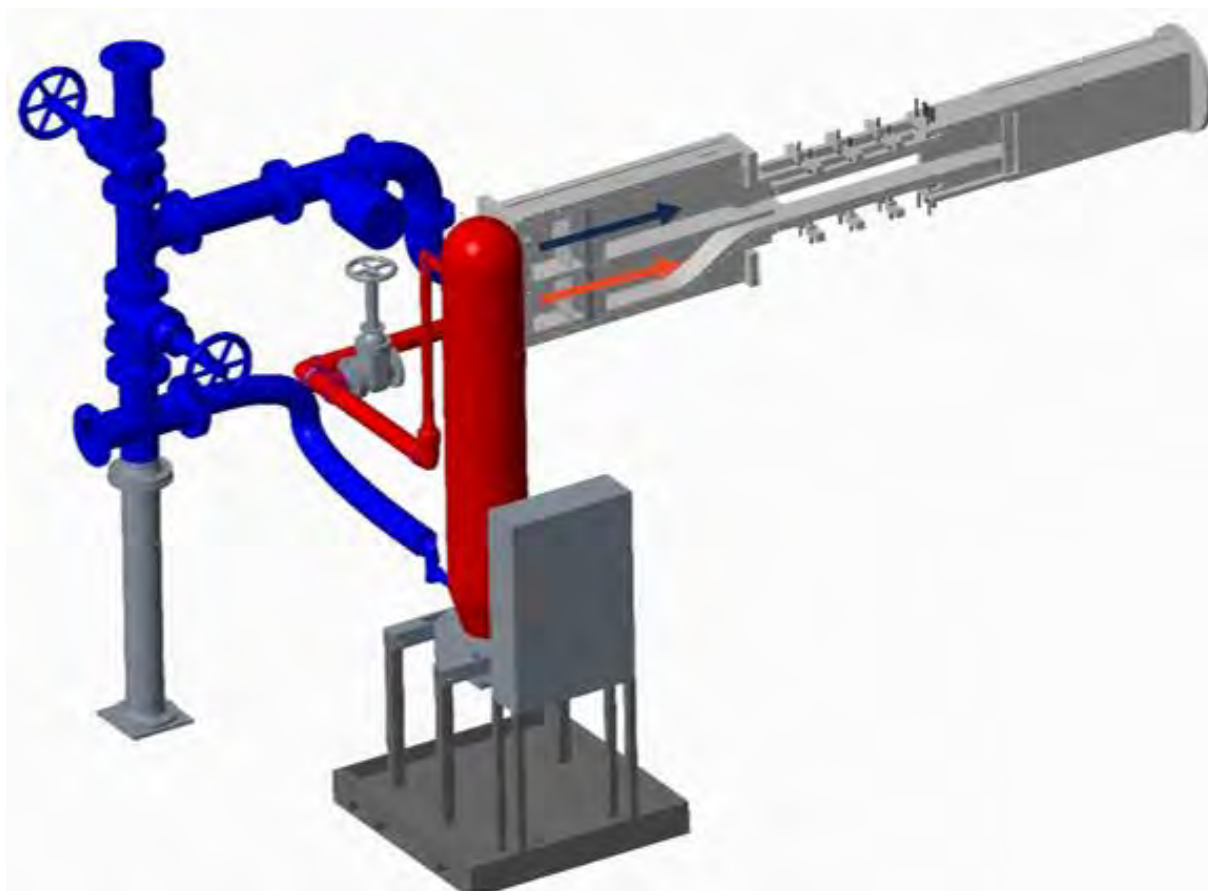


Figure 4. CAD rendering of wind tunnel facility (with ambient temperature stream in blue and heated stream in red)

Monitoring and overall operation of the tunnel are performed through a LabVIEW virtual instrument (VI) that pulls in pressure and temperature data pertinent to the facility. Further details on the pressure- and temperature-monitoring capability displayed on the front panel (which is seen in Figure 5) are given in Section 2.2.1. The VI controls the startup and shutdown of the tunnel through the pneumatic valve by virtue of a 20 mA signal via a National Instruments 9265 current output module. The VI also monitors the status of the laser system when it is in use.

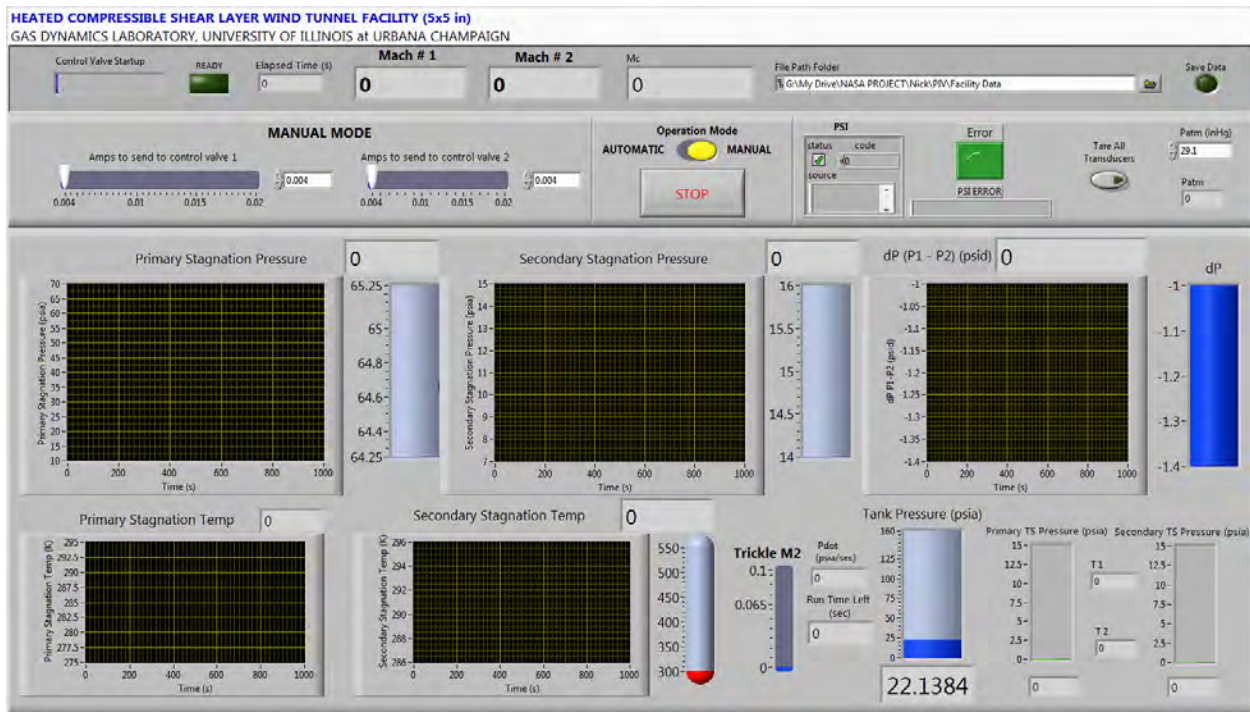


Figure 5. LabVIEW VI front panel

The facility was designed to support many methods of flow analysis, primarily that of optical, nonintrusive techniques: stereo particle image velocimetry (SPIV) and schlieren visualization were of particular interest at its conception, with later extension to filtered Rayleigh scattering (FRS). At the same time, it allows for traditional measurements as well: static pressure measurements along both freestreams and down the test section centerline, and pitot-static probe analysis at various streamwise station. Probe traces may also be made with the replacement of

either the top or bottom wall of the wind tunnel test section; this includes pitot-static and hot-wire anemometry, as well as total air temperature thermocouple measurements.

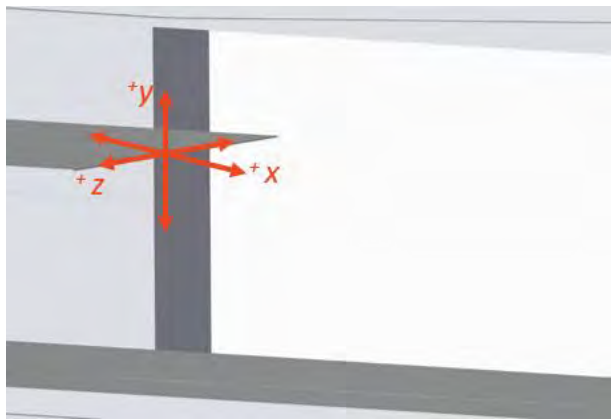


Figure 6. Laboratory reference frame

All measurements made within the test section are made with respect to the laboratory frame of reference. The origin of the coordinate system is at the center of the splitter plate tip and is shown in Figure 6. The x -axis goes with the overall flow direction, with the y -axis as transverse to the mixing layer and the z -axis spanwise to the flow. The

test section itself has a range of 762 mm in the x -direction, from +50.8 mm to -76.2 mm in the y -direction and is 63.5 mm wide in the z -direction on either side (providing 127 mm in total width). Each side-view window is able to view the flow entirely in the y -direction and has a range of 254 mm streamwise, with the windows moveable—allowing for full optical access along the test section for side-views. The top and bottom walls of the tunnel, when configured for optical measurements, have a 25.4 mm-wide window at the spanwise center to provide optical access for the laser sheet along the entire test section length.

For measurements made with the moveable probe, the bottom wall of the tunnel with the window is replaced with an alternative bottom wall. This bottom wall has a narrow slot running streamwise along the center measuring 3.175 mm in width. Moveable blanking plates allow the probe to be placed at multiple streamwise positions, at $x = 34.7, 85.5, 186.6, 287.7$, and 338.5 mm. Probe traces (in the y -direction) can be made at all of these positions, allowing for measurements to be made along nearly the full length of the test section. More to the point, measurement traces

are possible near to the splitter plate, in the developing mixing layer, and in the fully developed region, allowing for verification of the non-intrusive results throughout.

2.1.1 Facility Modifications

Major modifications, however, were required in order to perform the experiment of interest, with a heated incoming secondary flow. The facility was not originally designed with such a thermal requirement in mind; therefore, it did not support heating the incoming air to the stagnation temperature required of the current experiments. In order to support these needs, a preexisting heater used in former heated work was taken out of long-term storage and rehabilitated. The heater, a HEAT model CHP-0824S-60-74Y-483, can be seen in Figure 7; its specifications are listed in Appendix A. Piping to and from the heater in order to mate it with the preexisting facility also required a great deal of early design work in order to guarantee safe operation of the modified wind tunnel.

Installation of the heater was without major issue; it was taken out of storage and placed in the Gas Dynamics Lab in short order. Final adjustments to its location and orientation were made shortly thereafter in order to align it with the wind tunnel inlet. Once the power supply had been replaced by new cabling able to be safely routed to the lab's 480VAC circuit breaker, electrical checkouts were performed and the heater was turned on for the first time. The internal PID control



Figure 7. Electric air heater in GDL

system tuning was then examined to verify that its settings were as documented—that is, at the factory-set points. The heater’s internal thermoprosbes were removed and checked for measurement accuracy, as well as the sealing of their mountings. No issues were found, nor deviations with the prior documentation; the heater has since been operated without event or issue, to the relief of all involved.

In tandem with the addition of the heater itself was the supporting piping running to and from the heater, supplying the heated air to the wind tunnel. All design work was performed in PTC Creo Parametric 3.0, with an emphasis on using a minimum (if any) of custom parts and not requiring the work of an external party in order to reduce costs. Standard parts were sourced from McMaster-Carr, and a bill of materials (seen in Appendix B) was created. All new parts that were under pressure or thermal load were threaded; in doing so, the second goal was attained. The CAD rendering is shown alongside a photo of the actual implementation in Figure 8 and Figure 9 on the next page. The most notable part of the new plumbing was the decision to utilize a steel-reinforced flexible hose for the incoming air to the heater, coming off the facility air supply. This allowed for the only system constraint to be mating the exit of the heater with the wind tunnel inlet; as this was the heated air flow, it was of course the priority during design. Along this heated air flow, a tee was placed before the bend in the piping, intended to allow for seeding of the flow during the PIV measurements. More discussion on the seeding may be found in Sections 2.3.5, 4.1.1, and 4.1.2.

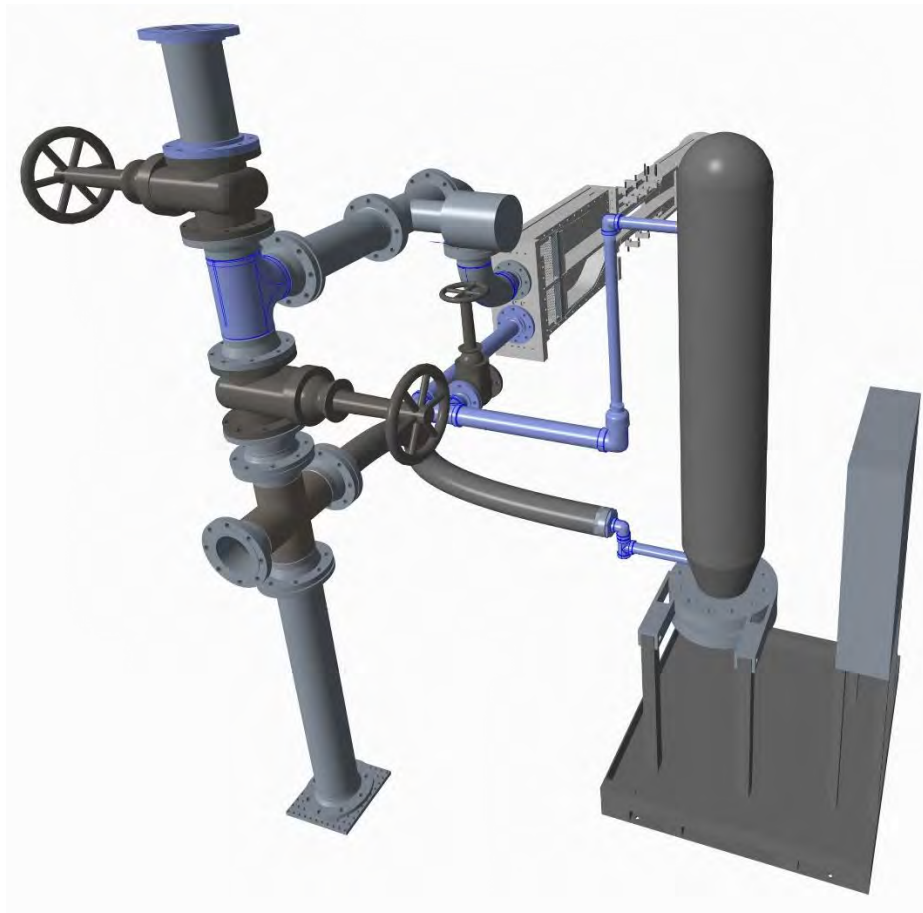


Figure 8. CAD rendering of wind tunnel with heater addition



Figure 9. Facility with installed heater in Gas Dynamics Lab

2.1.2 Modification Analyses

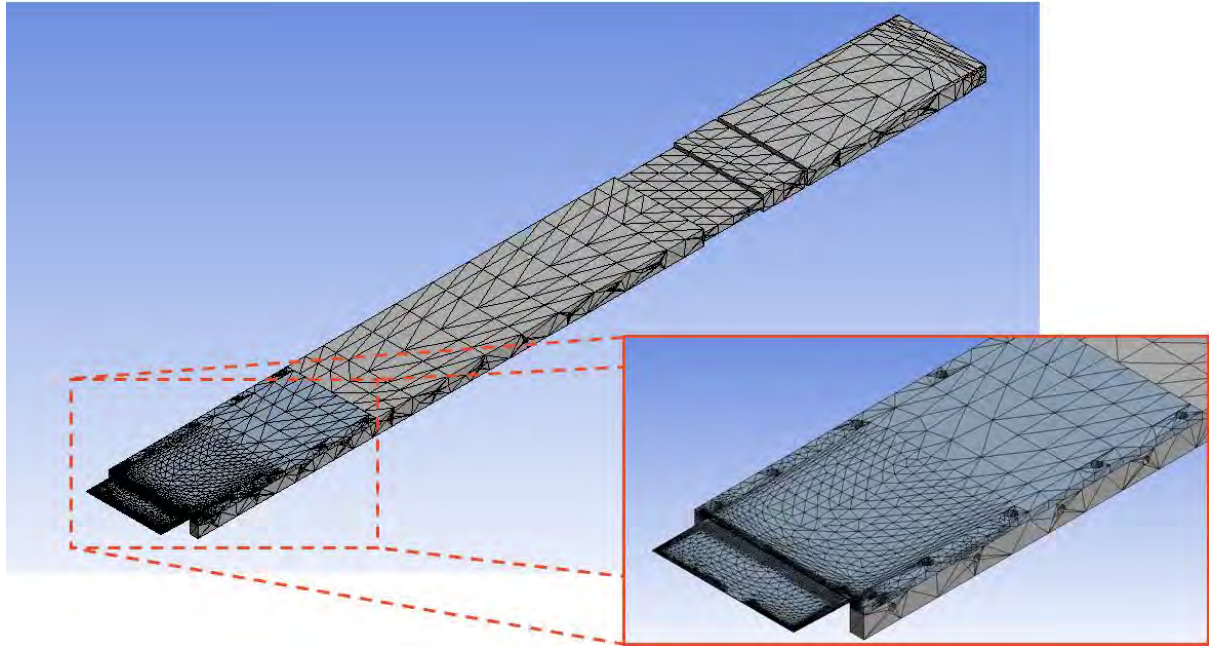


Figure 10. FEA mesh of splitter plate with tip feature

The goal of this work was to compare the behavior of the splitter plate during simulation and in actual operation, with the intention to glean insight into whether fatigue (especially cracking) near the root and/or tip may occur over time. Comparisons to the work done by Lee³⁴ in his static-state analysis of the original tunnel operation were also made, although they are not presented here for brevity. The only major differentiation between the two static analyses was the increased quality of the mesh capable via ANSYS, reducing the von Mises stress value at the splitter plate root corners by an order of magnitude.

Table 1. Typical Transient Simulation Operating Conditions

	P1 [kPa]	P2 [kPa]	T01 [K]	T02 [K]	M1	M2	h ₁ [W/m ² K]	h ₂ [W/m ² K]
Warm-up	98.4	98.5	288	400	0.076	0.065	3400	2900
Full Flow	53.046	60.515	285	495	2.06	0.328	74200	6300

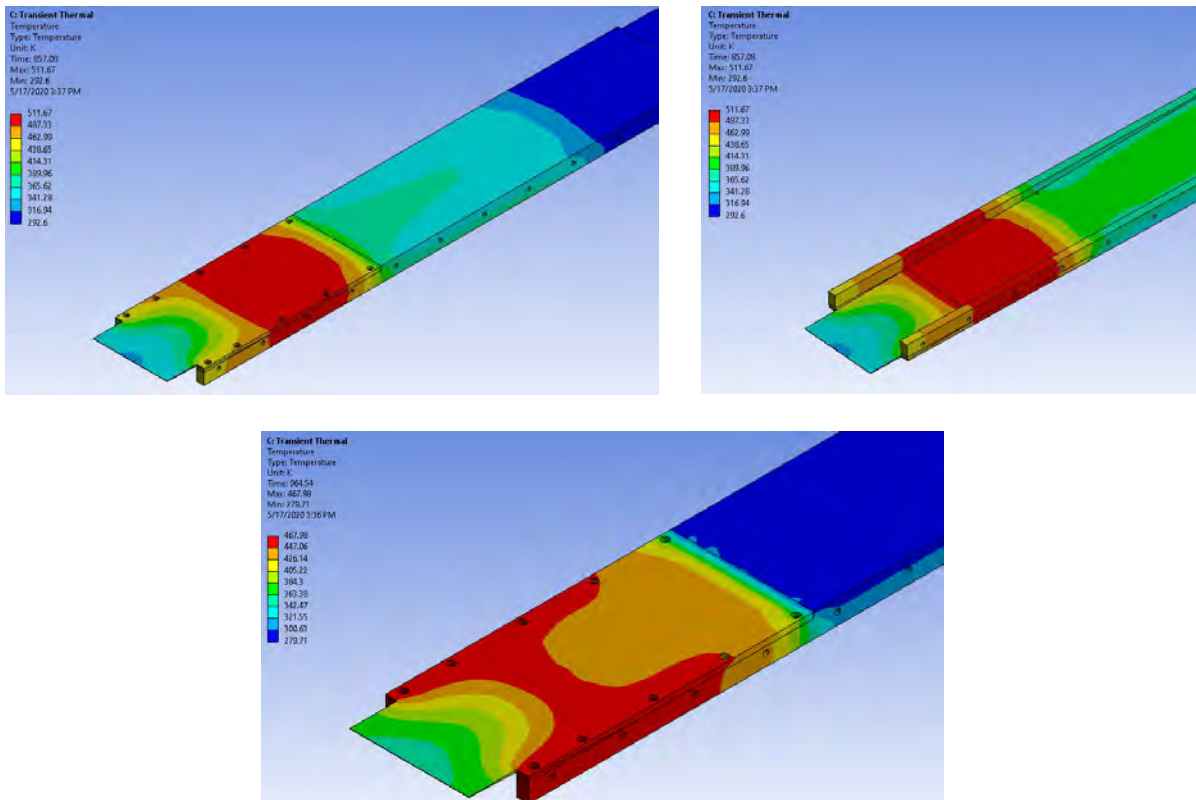


Figure 11. Temperature distribution on splitter plate at end of warmup (top L and R) and end of run (bottom)

For the FEM analysis itself, early facility run conditions, taken from the data recorded in LabVIEW, were provided as inputs to the transient thermal and then the transient structural simulation blocks in ANSYS. These conditions of interest gave both static and stagnation temperatures and pressures for both streams, which were then used to calculate all required inputs including the enthalpies of the respective streams. Both operating conditions are summarized in Table 1 above. The temperature distribution at the top and bottom of the splitter plate at its peak during operation is all shown in Figure 11. This calculated temperature distribution then was applied as an additional load to the transient structural analysis. This notably produced a deformation that changed in direction from the “warm-up” phase of the run where the secondary stream heats to its desired stagnation temperature, to the “full-flow” phase, where the experiment of interest takes place. While the deformation appeared to be reasonable, the stress calculation

seemed to be off by at least an order of magnitude; it was predicted by ANSYS to be on the order of 3 GPa.

Mesh refinement along the splitter plate titanium insert, especially along the sides and filleted edge were the main point of further improvement to the analysis. Figure 10 highlights the density of the mesh, especially at and around the splitter plate's stress concentrations. Using these improvements, as well as minor adjustments to the application of the operating conditions, new transient simulations were run on the system; Figure 12 shows these results. It is evident from the stress contours that the refinements and minor improvements in the applied boundary conditions (BCs) alleviated the issues in overpredicting the stress concentration at the corners of the splitter root. The newly computed safety factor, at minimal points 1.05 and largely above 3, was acceptable for the wind tunnel's operation, especially as the current thermal experiment is now concluded.

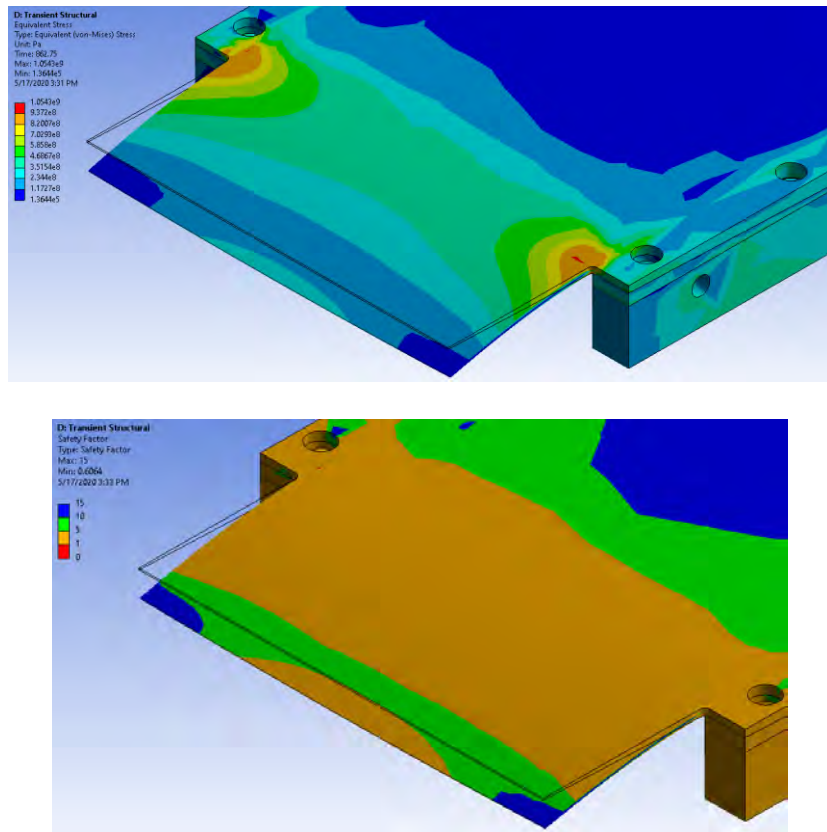


Figure 12. Maximum von Mises stress (top) and safety factor (bottom) on deformed model

2.2 Experimental Operation

Operation of the tunnel itself is performed manually to maintain the necessary operating condition. This operating condition is defined by matched static pressures at the splitter plate tip. Pressure taps are located near to the splitter plate tip in both streams, after the nozzle; however, physical constraints dictated that these taps are approximately 4" upstream of the splitter tip. As such, an alternative method of pressure matching based on a differential pressure between the two pressure taps is utilized. This operating condition is determined through the use of schlieren visualizations to view the behavior of the shear layer and subsequent sidewall pressure tap measurements to verify the differential pressure.

2.2.1 Experimental Operating Procedure

Manual operation of the tunnel is primarily performed by controlling a gate valve that is positioned before the piping split into the primary and secondary streams. Normal operation of the tunnel may be thought of in three phases: warm-up, primary operation, and cool-down. Warm-up and cool-down are lengthy, necessary portions due to the slow heating time of the heating coil and latent thermal mass of the facility, respectively. Initial preparation of the tunnel requires purging of the tunnel (discussed briefly in Section 4.1.1) and manual cleaning of oil buildup (from PIV seed particles) in the tunnel. The tunnel walls are scrubbed to remove as much of the accumulated oil as possible, particularly in the nozzle sections. The windows are then cleaned, especially the bottom windows, which occasionally accrue oil tracks across them, preventing the laser sheet from properly illuminating the test section. Once the windows have been fully secured back onto the tunnel, the pressure transducers are zeroed to ambient pressure prior to the warm-up phase.

The warm-up phase typically takes on the order of fifteen minutes to complete. To begin, the primary pneumatic valve is cracked open a small amount. The main gate valve is then opened

to a position allowing a “trickle flow”, about $M = 0.065$, to run in the secondary stream. This was found over time to be the most effective approach for heating up the combined thermal mass of the heater, tunnel, and flow most quickly. During the warm-up phase, the data acquisition systems are checked out, especially when camera systems are in use. Previous lab experience has shown that some camera systems, especially PCO cameras, suffer from data transfer issues and even crashes while recording data. It has been found that recording checks just prior to actually taking data are the most consistent way to prevent any configuration issues. No matter the method being used for data collection, by using the low flow conditions of the warm-up phase as a “dry run” to verify that the acquisition method is in order and all components are working in sync has prevented “dead runs” where no data are able to be acquired.

Once the secondary stagnation temperature has reached the desired point, about 495 K, the primary operation phase may begin. A check is made to verify that no oil or condensate has accumulated on the windows during warm-up as can be seen in Figure 13; in the case that there is oil on the windows, the heater and flow are temporarily stopped, and the windows removed carefully to be cleaned. It should be noted that prior to running the tunnel at the intended run conditions, the walls and windows only warm up a small, tolerable amount to the touch. Once the windows are verified to be clean, the primary pneumatic valve is opened to its full open position and the primary seeder (if in use) is started early to allow it to come up to full pressure prior to full-flow. After a set time elapses after the primary seeder is turned on,



Figure 13. Minor oil accumulation on window from warm-up

the manual gate valve is opened until the desired operating conditions are reached. The gate valve position must be manually varied throughout the duration of the run to maintain the operating conditions while the data acquisition takes place. At the end of the data acquisition, the primary seeder is turned off, and the tunnel is continued to run at full until the gate valve to the secondary seeder (see Section 4.1.1 for more detail on the seeding configuration) is closed.

For cool-down, the heater is turned off, the pneumatic valve is closed to once again only allow a small amount of flow through, and the main gate valve closed back to the “trickle flow” point. This is maintained while the heater and tunnel cool down to safer temperatures, a process that typically takes about twenty to thirty minutes. Typically, near the end of the cool-down process, a purge run is made, further cooling the wind tunnel. During the lengthy cool-down period, all data are saved and backed up, and data acquisition equipment is turned off. At the end of the cool-down period, the tunnel is still warm, typically between 315-320 K; all flow is shut off through the tunnel and it is left to cool down naturally until it returns to near-ambient temperatures. In total, the entire process of running the tunnel to acquire data requires about 40 minutes, and the cool-down period afterward takes about three hours depending on how many purge runs take place. As a result of these limitations, runs of the facility were intermittent, and a premium was placed on acquiring as much high-quality data as possible in each run. It was paramount that for maximum efficiency in taking this large amount of data that as few “dead runs” without data as possible would occur, especially when considering the large time investment that each run requires. Of additional consideration was the stress loading from both the thermal condition as well as the action of running the tunnel itself; as Section 2.1.2 and Lee³⁴ discuss, the possible fatigue of the splitter plate was a constant consideration during tunnel operation. Minimization of the number of runs would therefore behoove both the safety and expediency of the experiment.

2.2.2 Experimental Operating Condition

Schlieren still images and high-speed video provide a real-time, qualitative analysis of the mixing layer while determining the proper operating conditions. In doing so, the operating condition is found where (1) there is a weakly switching compression / expansion wave in the primary stream off the splitter tip along with (2) a straight mixing layer, not bending into either stream. These operating conditions are then utilized as sidewall pressure tap measurements are obtained, verifying that in the fully developed region, static pressures become stable and constant, and no vortices or other dynamic processes are present. Table 2 below shows the nominal operating conditions for this experiment.

Table 2. Experiment Operating Conditions

P ₁ (kPa)	P ₂ (kPa)	P ₀₁ (kPa)	P ₀₂ (kPa)	T ₁ (K)	T ₂ (K)	T ₀₁ (K)	T ₀₂ (K)	U ₁ (m/s)	U ₂ (m/s)	M ₁	M ₂
58.58 ± 0.11	61.97 ± 0.11	443.89 ± 2.83	64.573 ± 0.67	177.98 ± 3.06	467.80 ± 12.5	297.01 ± 0.08	473.71 ± 0.31	488.87 ± 8.40	108.95 ± 2.92	1.83 ± 0.05	0.251 ± 0.01
s			θ			r			M_c		
ρ_2 / ρ_1			T_{02} / T_{01}			U_2 / U_1			0.541		
0.402 ± 0.01			1.59 ± 0.01			0.2229 ± 0.007			± 0.02		

It must be noted that while the tunnel is running, however, the operating conditions are more of a targeted optimum rather than a true steady-state value. The most varying condition is the temperature; unfortunately, it is not feasible for the heater to perfectly maintain a constant temperature at the flowrates required. Therefore, the secondary stagnation temperature is brought above the desired point and allowed to fall below as data are obtained. Both the schlieren and sidewall pressure analysis showed no major difference in flow structures as long as the temperature stayed reasonably close to its target point of 495 K. The maximum range was between 515 and 455 K, with more typical range between 505 and 470 K. Furthermore, as outside weather conditions changed, the incoming air temperature would respond in kind, leading to a variance in

stagnation temperature throughout the experiments in the *primary* stream as well. However, this variance in stagnation temperatures is largely negligible to the data obtained, which was taken at seasonally similar times (winter-spring for velocity data, summer-fall for temperature data).

2.3 Flow Diagnostic Techniques

A multitude of flow diagnostic techniques were utilized over the course of the project, including both intrusive and non-intrusive methods. Classical methods of observation (in order of measurement taken) were: Z-type schlieren imaging and video recording, sidewall static pressure tap measurements, and thermocouple probe measurements. Constant-voltage hot wire anemometry was attempted, but ultimately proved too costly in time and expense to complete. Modern methods of observation were stereo and planar particle image velocimetry (PIV) and filtered Rayleigh scattering (FRS).

2.3.1 Schlieren Measurements

Table 3. Schlieren Equipment Summary

Component	Description	Parameters Used
Photron SA-5 Camera	CMOS camera with max resolution of 1024x1024 pixels and max framerate of 1,000,000 fps	Full-resolution: 7000 fps High-speed: 120,000 fps at 900x320 resolution
Nikon AF Nikkor telephoto zoom lens	70-210 mm focal length with f/4.0~5.6 maximum aperture	Zoomed to fill image upon camera sensor
2 Parabolic Mirrors	12-inch diameter 96-inch focal length	Placed to fully collimate incoming light beam
LED (Thorlabs MWWHLPI)	LED light source: warm white color (3000 K, 400-700 nm range)	Full brightness 700 mA current applied
Knife-edge	Blade tip blocks bent rays of light	Placed at focal point, horizontally mounted

Schlieren visualizations were the first obtained in this configuration: this method was initially used to simultaneously determine the operating condition for the case while also monitoring the safety of initial test runs. A classical Z-type setup was utilized, with mirrors large enough to illuminate the entire test section during measurement. Table 3 above shows the

equipment used for the schlieren images and videos, while Figure 14 shows the conceptual setup schematic. The schlieren technique is line-of-sight averaged, where a collimated beam of light passes through the test section. These collimated rays are bent slightly due to density changes within the test section (notably, due to shocks and expansions). At the knife-edge, light rays bent towards the knife-edge are cut off while those bent away are passed through, allowing for the density gradients to become visible. Physical flow features, especially in a mixing layer, therefore become much more apparent as a result.

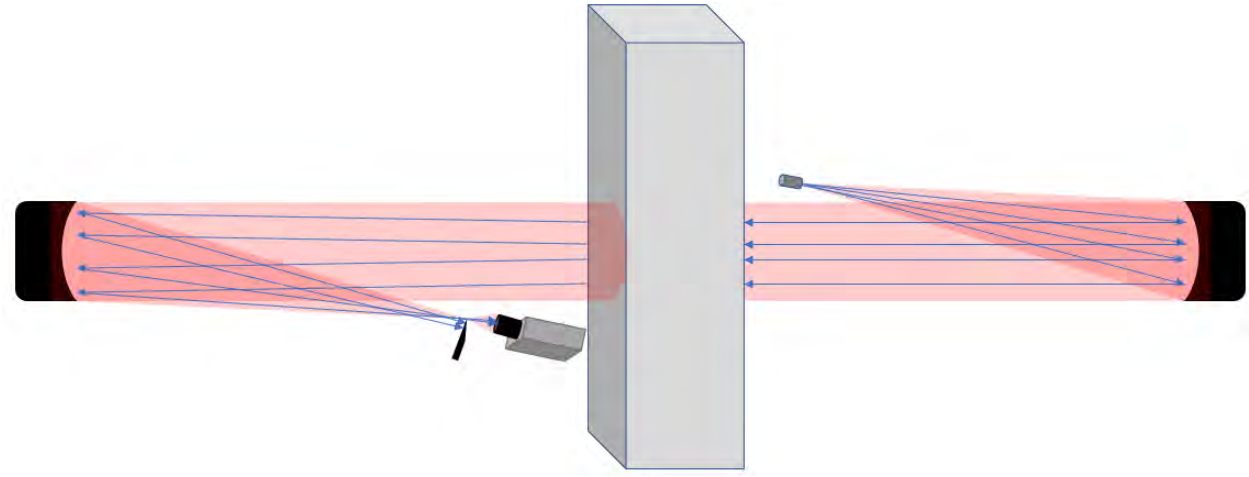


Figure 14. Z-Type schlieren schematic

After initial setup and determination of the run conditions, full-field high-speed videos were obtained using the Photron camera capturing at a framerate of 120,000 frames/second. It should be noted, however, that the higher framerate comes at a cost of resolution as the SA-5 camera is only capable of 900x320 pixel resolution at this recording speed. These high-speed images allowed for an early qualitative analysis of the entire flowfield, from splitter tip to its fully-developed region. Furthermore, at such a high framerate, features that were not possible to be noticed at lower framerates (and would have been smeared out) are visible during playback. A selection of frames from the high-speed video may be seen later, in Section 3.1.1.

Full-resolution (1024x1024 pixel) images were also obtained at the maximum framerate possible, 7000 frames/sec, for instantaneous schlieren images of the whole flowfield. From the full-resolution images, the shock structure comes into full relief, showing the multitude of smaller shocks that result from minor imperfections in the primary stream nozzle. Discussion of the schlieren results, both high-speed movies and full-resolution images, is undertaken in Section 3.1.

2.3.2 Sidewall Static Pressure Measurements

Further verification of the tunnel operating condition was performed by interchanging the typical tunnel sidewall, with its windows for optical access, with an alternate sidewall replete with pressure taps. Three rows of taps are installed on this sidewall, which can be seen schematically in Figure 15. Taps are placed in the middle of the primary and secondary freestreams, at y -locations of +25.4 and -38.1 mm, respectively, and along the centerline at $y = 0$ mm. The taps are spaced out along the x -axis; each line has a tap at $x = 3.175$ and 739.775 mm, with the secondary and primary lines having a tap every 101.6 mm in between, and the centerline every 25.4 mm in between. Pressures were monitored using a custom LabVIEW program capable of capturing all the pressure tap data, as well as the facility temperatures and pressures necessary for operation.

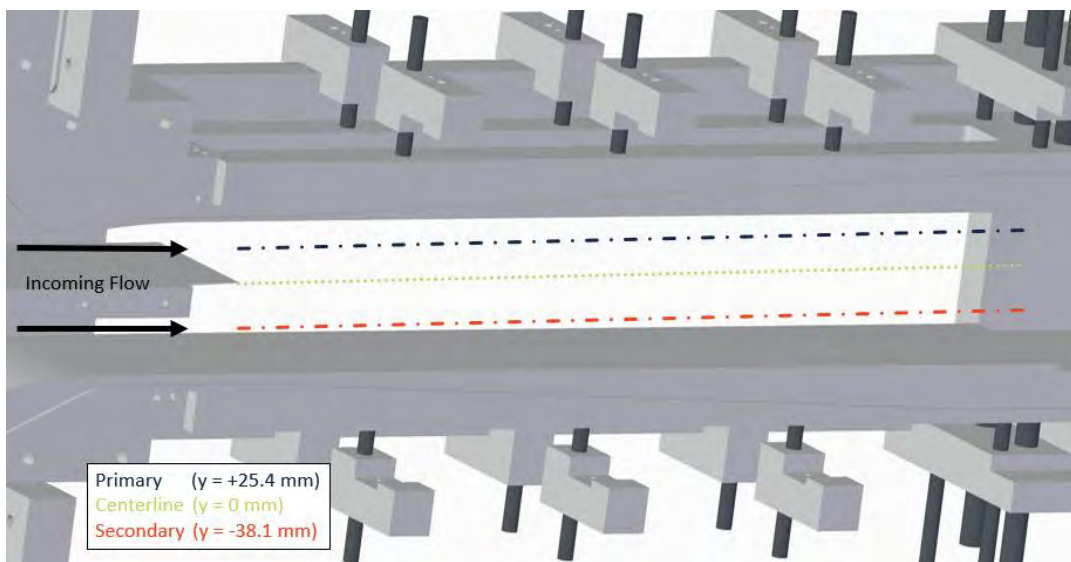


Figure 15. Schematic of static tap layout

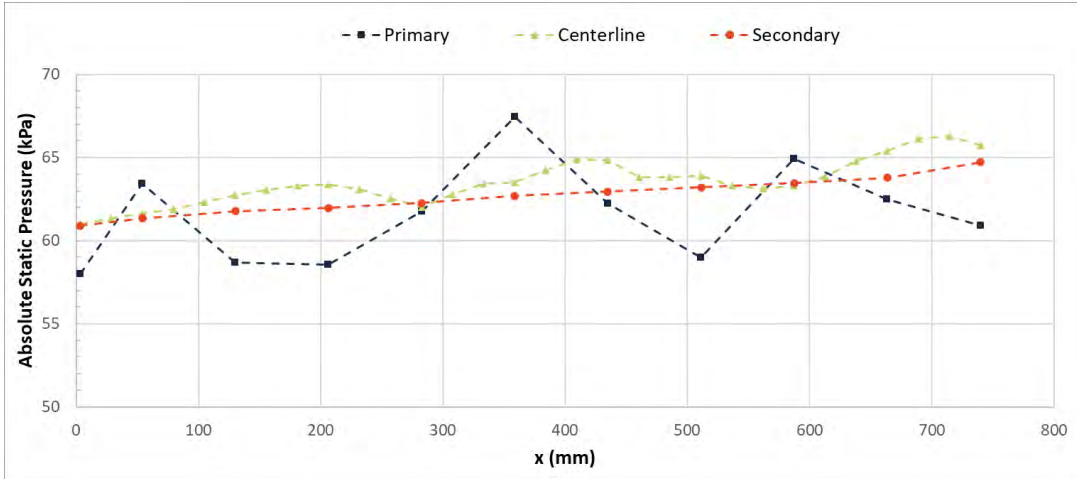


Figure 16. Static pressure tap results at tunnel operating condition

The primary aim of the static pressure tap measurements is to verify the assumed operating condition found with the schlieren measurements. This is done by checking that the operating condition is achieved by having no strong adverse or favorable pressure gradients along the length of the mixing layer. Looking at the typical results in Figure 16 above, a slight adverse pressure gradient is noted along the length of the test section, but it is less than 5 kPa over the course of the 750 mm-long mixing layer. Larger fluctuations are noted in the primary stream and are due to the inevitable weak compression/expansion waves present there; these are discussed in detail in the schlieren analysis (Section 3.1) and the stereo-PIV analysis (Chapter 4). In all, these are minor effects that demonstrate that the desired operating condition is achieved, confirming that it is usable for the later analyses and not requiring further tuning.

2.3.3 Temperature Probe Measurements

Early temperature measurements were performed using a pitot probe in the wind tunnel with a thermocouple affixed to the probe, as can be seen in Figure 17. This probe,

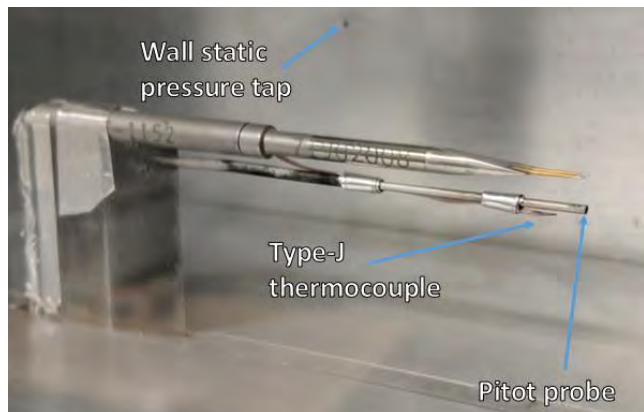


Figure 17. Pitot probe in tunnel with Type-J thermocouple mounted. Static pressure tap wall installed in background

based on the same design as a set on loan from NASA Glenn Research Center, only measures the total pressure—there is not a static pressure ring or tap on the probe. It is operated as part of a linear traverse system able to take traces through the y -direction at specific points along the x -axis: at 34.7, 85.5, 186.6, 287.7, and 338.5 mm from the splitter tip. This system is actuated by a Zaber stage, and is controlled by a combined LabVIEW VI capable of controlling the probe traverses in addition to the typical task of operating and monitoring the wind tunnel; the traverse system is shown in Figure 18. The Zaber stage, chosen for its high resolution, had a positional uncertainty of less than 100 μm . The probe traverses are best operated by a second user that defines the probe trace requirements (y -limits and step size), and then both begins the traverse once the operating condition is achieved as well as monitors the probe during the traverse itself.



Figure 18. Zaber stage traverse system

2.3.3.1 Initial Thermocouple Measurements

Initial temperature traverses were primarily intended to provide an early study of the temperatures in the mixing layer. The field measurements provided by the filtered Rayleigh Scattering (discussed later in Section 2.3.6) were scheduled to be performed late in the project. The traverses also had the secondary role of verifying the accuracy of the FRS measurements, albeit with some increased uncertainty as a result of the probe intruding into the flow.

Initially, attempts were made to measure the total temperature of the flow by simply adhering a bare-wire thermocouple to the pitot probe. However, the increased temperature in the secondary stream caused a multitude of issues. The adhesive on the aluminum mounting tape failed; alternative mounting tapes were explored that utilized a silicone-based adhesive instead.

Double-sided tape intended for electrical mounting was attempted, but the adhesive was not strong enough to hold up to the combination of the secondary's thermal condition and the drag forces in the supersonic primary stream. Eventually, a solution using high-temperature heat-shrink plastic was utilized; this had the disadvantage, however, of requiring a heat source imposed on the thermocouple itself during installation on the probe. Burn-through of several thermocouples occurred as a result, primarily due to the high temperature required to shrink the wrap and the tight confines of the test section (the thermocouple had to be mounted *in-situ*). Further issues came during operation, as the heat-shrink would intermittently move or bunch up on the probe, leading to the thermocouple moving in the flow and sometimes even breaking off as can be seen in Figure 19. While



these issues were able to be largely overcome, the overall lack of trust in the data necessitated a second stagnation temperature method.

Figure 19. Broken thermocouple on pitot probe

2.3.3.2 TAT Probe Measurements



Figure 20. TAT probe mounted in tunnel

To alleviate the issues with using the bare-wire thermocouple above, as well as to remove the worry of inaccuracy with the measurements, a total air temperature probe was sourced from United Sensor Corp. This probe, a TD-10-J-36-C-1-F, a 1/8" diameter, 10" long probe with a type-J thermocouple, is typically used in flows with a temperature below 550 K and a velocity below 615 m/s. As such, the

probe can be seen in Figure 20, mounted in its adapter such that it can be used with the same

traverse hardware as the other probes. Appendix C has an engineering drawing of the TAT probe, furnished by the manufacturer.

The total air temperature probe is designed to allow pass-through of flows through cut-outs on the back of its housing seen in Figure 21. In doing so, it has a greatly decreased response time between temperature readings. This response time was found to be less than 4 seconds for a flow with a stagnation temperature rise of 200 K at near-zero velocity; when in the tunnel at its operating condition, this response time was even shorter—typically on the order of a second to overcome the maximum thermal difference. Such performance allowed for quick traverses through the thermal mixing layer at high recording rates.

All temperature profiles took a minimum of 30 samples per measurement point, with multiple temperature profiles at each x -location, no less than four and typically six. These temperature profiles had a typical measurement uncertainty of 0.1 K in the freestreams and 0.25 K in the mixing layer, based on the Student t-distribution using a 95% confidence interval.



Figure 21. TAT probe front and back showing holes for airflow (with inch ruler for reference)

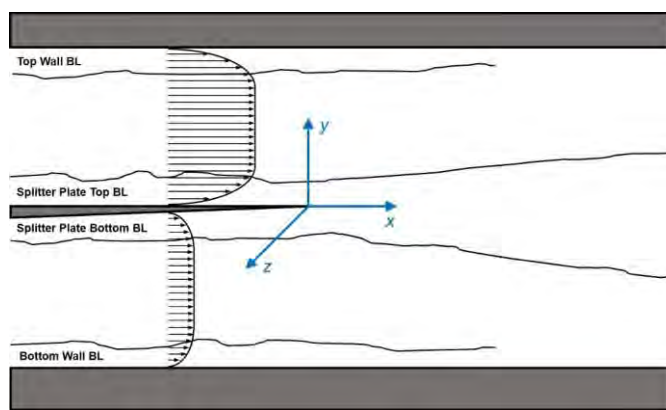


Figure 22. Incoming boundary layers

2.3.4 Boundary Layer PIV

As the primary purpose of this study is to provide benchmark-level measurements for CFD validation, especially with respect to turbulence in compressible mixing layers, the incoming boundary layers were

measured to provide a holistic definition of the incoming flow boundary conditions. Figure 22

shows the four boundary layers of interest, along the wind tunnel top wall, both the top and bottom walls of the splitter plate, and the bottom wall of the wind tunnel. Three of the boundary layers, the bottom wind tunnel wall and splitter plate top and bottom walls, were studied herein. It was assumed that the characteristics of the top wall boundary layer were the same as for the $M_c = 0.690$ case of Kim^{13,14}, as the heating of the secondary stream would presumably not affect the incoming primary freestream nor the top wall itself to any measurable degree.

Table 4. Boundary Layer PIV Configuration

Component	Description	Parameters Used
PCO 2000 Camera	CCD camera, 2048x2048 resolution	Double-frame mode
Nikon Micro-Nikkor Camera Lenses	60 mm focal length f/2.8D min aperture	Empirically focused with aperture set to f/2.8D
LaVision DaVis 8.4	Computer program for and computation of PIV vectors	See Table 7 for computation settings
LaVision Type 058-5 Calibration Plate	Double-sided, dual-level marker plate	--
Quantum Composers 9518 Pulse Generator	Delay and pulse generator to sync cameras and laser	Laser $\Delta t = 1 \mu\text{s}$
New Wave Gemini Laser	Double-Pulsed Nd:YAG laser Frequency doubled to 532 nm	Laser power empirically tuned based on timing
Laser Sheet Optics	Plano-concave cylindrical lens ($f = -50 \text{ mm}$), plano-convex spherical lens ($f = 1000 \text{ mm}$), dichroic turning mirrors (coated for 532 nm)	Empirically located for desired sheet thickness ($>1 \text{ mm}$) and streamwise length (30-40 mm)

Boundary-layer PIV was performed to characterize these boundary layers in a planar configuration using the settings as listed above in Table 4. Data were obtained into the freestream and as close to the wall as possible: velocity vectors in the x - y planes were recorded, along with normal and shear Reynolds stresses in this plane. These measurements proved, as has been typical for this lab in other experiments, to be difficult to obtain due to the large amount of laser light reflections near the surface. These reflections were exacerbated by the slight (but at this scale non negligible) movement of the splitter tip during tunnel operation. These challenges were eventually

overcome by careful adjustment of the laser sheet's incoming angle as well as by cutting off the laser sheet edges by an aperture, to minimize laser light impinging on the splitter plate.

2.3.5 Stereo-PIV

Table 5. Overview of SPIV Components

Component	Description	Parameters Used
2x LaVision Imager sCMOS Cameras	CMOS camera with 2560x2160 pixel resolution	Double-frame mode
Nikon Micro-Nikkor Camera Lenses	60 mm focal length f/2.8D max aperture	Empirically focused with aperture set to f/2.8D
2x LaVision Scheimpflug Adapters	Adjusts lateral focal range of cameras by tilting lens away from image sensor	Empirically tilted, between 30-45°
LaVision DaVis 8.4	Computer program for both capture of particle images and computation of SPIV vectors	See Table 7 for computation settings
LaVision Type 11 Calibration Plate	Double-sided, dual level marker plate	--
LaVision PTU	Timing pulse generator to sync cameras and laser from computer settings	Laser $\Delta t = 1 \mu\text{s}$ Camera delay = -0.3 μs
New Wave Gemini Laser	Double-pulsed Nd:YAG laser Frequency doubled to 532 nm	Laser power empirically tuned based on timing
Laser Sheet Optics	Plano-concave cylindrical lens ($f = -50 \text{ mm}$), plano-convex spherical lens ($f = 1000 \text{ mm}$), dichroic turning mirrors (coated for 532 nm)	Empirically located for desired sheet thickness (1-2 mm) and streamwise length (70-80 mm)

The data obtained via stereo-PIV are one of the two primary advances of this work. SPIV data were obtained along the spanwise center of the test section, in the streamwise direction, until the flow is fully turbulently developed. At a minimum, data were obtained from y -values between $\pm 20 \text{ mm}$, well into the freestream on both sides of the mixing layer. The maximum spacing between points was 0.263 mm, with over 100,000 points per measurement field of view. Each point in the data field had a three-component velocity vector calculated for over 3000 instantaneous images, which allowed for a multitude of statistical measurements to be performed upon the dataset. Table

5 lists the hardware used for the stereo-PIV; Figure 23 and Figure 24, showing the notional setup and a photo of the physical setup, respectively, are presented below.

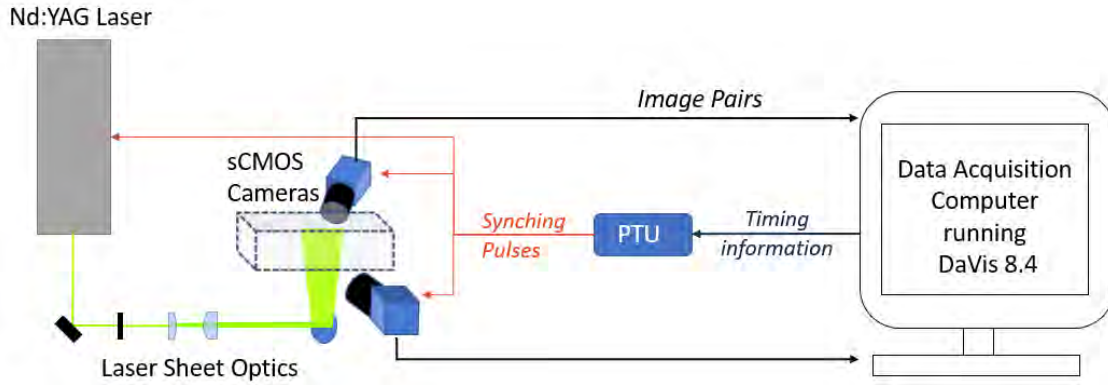


Figure 23. SPIV notional equipment schematic

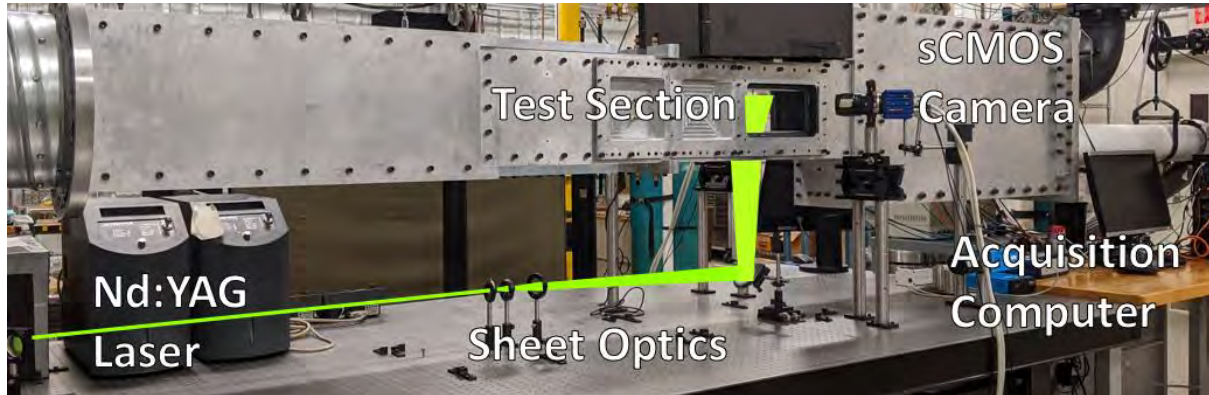


Figure 24. Photo of wind tunnel & SPIV physical lab setup

As with any PIV study, determining the optimal seeding density was paramount in recording the most accurate data possible. Numerous runs were made, starting with seeding settings used in previous work performed in the same lab group with similar flow conditions. From there, seed pressure was adjusted over time empirically until a window of operating conditions was established. With respect to the secondary flow, this was adjusted numerous times as its method of seeding changed until a viable final method was determined (discussed in much greater detail in the following section). Given time, the seeding settings for both the ViCount and the

Laskin nozzle were determined, and are listed in Table 6 below. Further discussion of the seeding is given in Section 4.1.2.

Table 6. Summary of Seeding Settings

Seeder	Seeding Oil	Flow Seeded	Seeding Method	Input Pressure	Seed Size
ViCount 1300	White Mineral Oil	Primary	Combustion- Condensation	68 psig	0.2-0.3 micron
TSI Model 9307	Avocado Oil	Secondary	Droplet Bursting	15 psig	0.5-1.0 micron

The entire SPIV process, from data acquisition to processing, was performed using the DaVis 8.4 software package developed by LaVision. DaVis controls the data acquisition phase through a physical timing unit (PTU) that interprets the desired execution of the physical system as prescribed in the software. This PTU connects to the laser system as well as the cameras; it modulates the power of the lasers by varying the Q-switch time delay of each pulse. On the data acquisition side, the cameras are connected via a proprietary bus to the computer, allowing data transfer during live capture. Furthermore, this capability means that not only is the camera's RAM supplemented by the RAM of the acquisition computer, but also that data may be saved to the hard drive during recording. Through the combination of these advantages, a larger ensemble of images may be captured during each run compared to previous work without binning or other methods of cutting down on image size. When this is considered in tandem with the much higher downtime required for the heating and cooling of the facility (see Section 2.2.1), it becomes clear that the capabilities made possible by the LaVision software and cameras were central to the success of this study.

A camera-dependent calibration is applied to each frame captured, based upon the use of a double-sided, dual-height calibration marker plate seen in Figure 25. Using the calibration plate, the DaVis software is able to make a mapping for each camera in three dimensions; this mapping drives the calibration that converts the raw images into the lab reference frame. A further calibration is necessary for stereo PIV, where the initially calibrated images are used to create a second disparity map and calibration in the software's self-calibration procedure. A further discussion of the stereo-self calibration is found in Section 4.1.3.



Figure 25. Type 11 calibration plate in wind tunnel

Table 7. SPIV Processing Parameters

Operation	Description	Parameters Used
Add default attribute	Apply calibration and physical recording parameters	See Table 5
Subtract Sliding Average (Gaussian Profile)	Apply Gaussian intensity distribution to illuminated particles to reduce noise and oil blur	Filter length: 9-11 pixels
Subtract Constant	Reduce noise floor	60 counts
Min-Max filter for Intensity Normalization	Local normalization to increase SNR of particles	5-7 pixels
PIV particle image processing	Calculate u , v , & w velocity components along with uncertainty for each image pair	Multi-pass Stereo cross-correlation: 64x64 with 50% overlap @ 2 passes 32x32 with 75% overlap @ 4 passes Adaptive PIV weighting function High Accuracy mode for final pass

Operation	Description	Parameters Used
Vector Postprocessing	Reduce errant vectors calculated from PIV step based on expected velocity range and Q peak ratio	$U: 305 \pm 300$ m/s $V: 0 \pm 200$ m/s $W: 0 \pm 250$ m/s Delete vector if Q peak ratio < 3 Median filter: strongly remove & iteratively replace with removal if diff to avg. $> 3x$ stdev reinsert if diff to avg. $< 4x$ stdev Remove groups with < 10 vectors Reapply allowable vector range
Append Data Set	Reorganize computed vector fields	Append to all other runs for same field of view
Vector Statistics: Vector Field Result	Compute statistics for all runs of each field of view	Compute means, standard deviation, processing uncertainty

Once calibrated, the double-frame image groups are processed using the settings given above in Table 7. These settings are optimized to minimize noise in the images as well as boost gain in the mixing layer. The settings are based upon a common base that this lab uses for similar Mach number flows. It should be noted that in the vector-calculation step, for SPIV at least two cameras are required in order to have differing views of the same particles; these differing views are used to compute the out-of-plane (w -axis) component of the vector. Furthermore, these cameras have viewing angles offset from the normal in order to better capture the intensity change. In doing so, only a fractional portion of the image would necessarily be in focus; to alleviate this, a Scheimpflug adapter is used, offsetting the angle of the lens from that of the image sensor. A tilt angle may be found for moderate ($30\text{--}45^\circ$) offset that puts the entire image plane in focus albeit at non-uniform magnification, known as the Scheimpflug condition. Post-processing of the vector images was performed to filter poorly correlated vectors, as presented in Table 7.

2.3.6 Filtered Rayleigh Scattering

The data obtained through Filtered Rayleigh Scattering (FRS) is the second of the two primary advances of this work. FRS temperatures results were obtained along the spanwise center

of the test section, streamwise through where the flow is thermally fully developed. Data were obtained from y -values between ± 20 mm, just as for the SPIV, allowing for analysis well into the thermal freestreams of both the primary and secondary flows. Figure 26 below shows the notional FRS equipment schematic with arrows indicating the flow of information for each image taken.

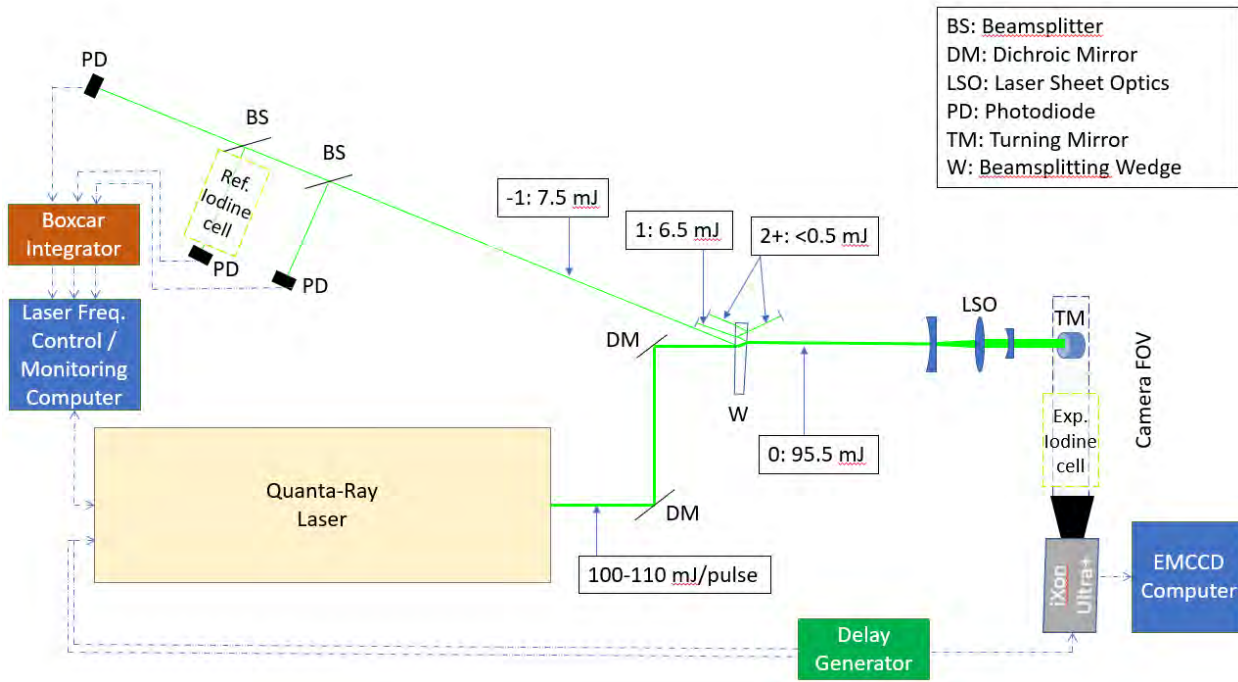


Figure 26. Notional FRS equipment schematic

Table 8. Overview of FRS Components

Component	Description	Parameters Used
Andor iXon Ultra+ Camera	EMCCD camera with 512x512 pixel resolution	Pre-amplifier gain of 5.0x E-M gain of 12x
Nikon Nikkor 85mm f/1.4 AI-s camera lens	85 mm focal length f/1.4D max aperture	Empirically focused with aperture set at f/1.4
LaVision Type 11 Calibration Plate	Double-sided, dual level marker plate	--
Quantum Composers 9514 Delay Generator	Timing pulse generator to sync camera and laser	Q-switch delay = 164 ns
Spectra-Physics Quanta-Ray GCR 230 Laser	Nd:YAG laser Frequency doubled to 532 nm Nominal power of 110 mJ/pulse	Full oscillator power with no amplifier Fine frequency control via LabVIEW computer

Component	Description	Parameters Used
2x Iodine Cells	Provides molecular absorption filter to provide measurement basis	Ref: Sidearm temp = 25 C Exp: Sidearm temp = 100 C
3x Thorlabs DET10A photodiodes	Si-based photodetector 1 ns rise time	--
Laser Sheet Optics	Plano-concave cylindrical lenses ($f = -50$ mm and $f = -20$ mm), plano-convex spherical lens ($f = 200$ mm), dichroic turning mirrors (coated for 532 nm)	Empirically located for desired sheet thickness (>1 mm) and streamwise length (20-25 mm)

Table 8, on the previous page and above, gives an overview of the components used for the FRS measurements. Two computers running LabVIEW are also utilized, one for frequency control of the laser and recording of the photodiode outputs, and one for the normal tunnel operation. Initial frequency scans of the laser, including the linear fit of the input voltage to output frequency, were accomplished. These initial frequency scans had the dual purpose of detailing the absorption profiles of the reference and experimental iodine absorption cells. The absorption lines of the experimental cell are shown with comparison to the predictive code written by Forkey et al. in Figure 27, with good overlap throughout the operating range of the laser.³⁵ In particular, the strong absorption line at 18789.27 cm^{-1} and the twin absorption lines around 18788.37 cm^{-1} are

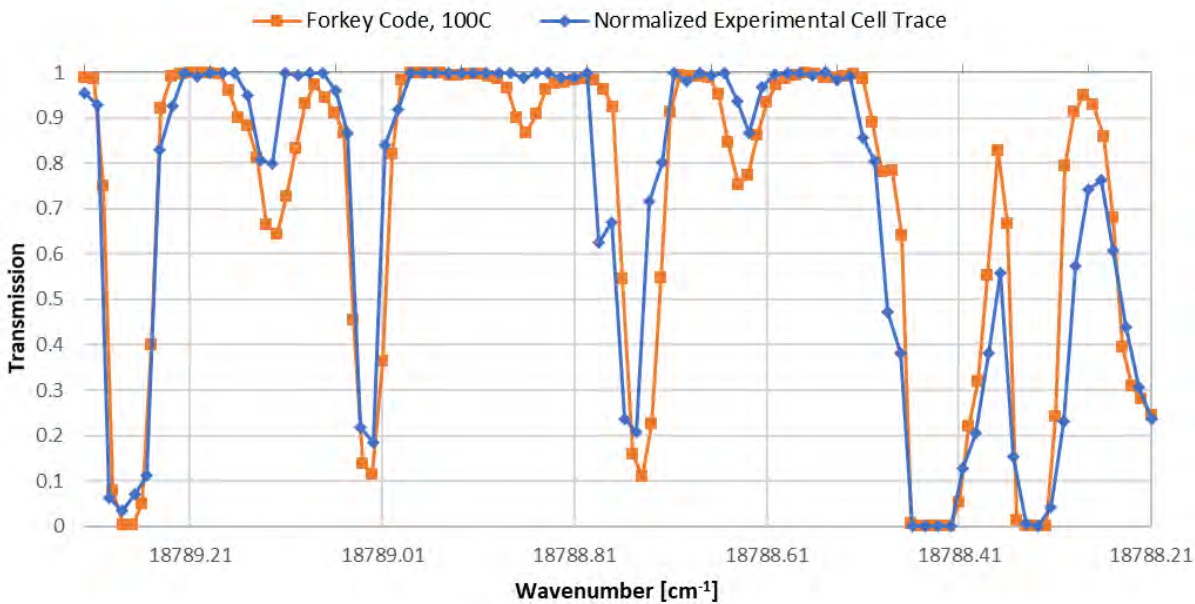


Figure 27. Absorption line comparison of Forkey code and experimental cell

rendered well by the cell. The former line was chosen as the nominal operating point of the experiment, with the input frequency at the center of the absorption line.

Given this absorption line setting, initial background and reference flatfield images were obtained for intensity normalization of the flow-on FRS images. A major benefit of the iodine cell is its ability to inhibit the transmission of strong reflections due to Mie scattering in the field of view. Therefore, stray oil particles or other laser reflections from the tunnel walls are negligible; this is crucial as Rayleigh scattering, being an elastic effect, gives off a fairly weak signal. Figure 28 on the next page shows the utility of the absorption cell, with the laser frequency set to the center of the absorption line in one image and outside of the line in the other. Without such filtering, the particles would at best wash out the information from the Rayleigh scattering if not damage the sensor due to the high gain setting needed to resolve the signal in the first place.

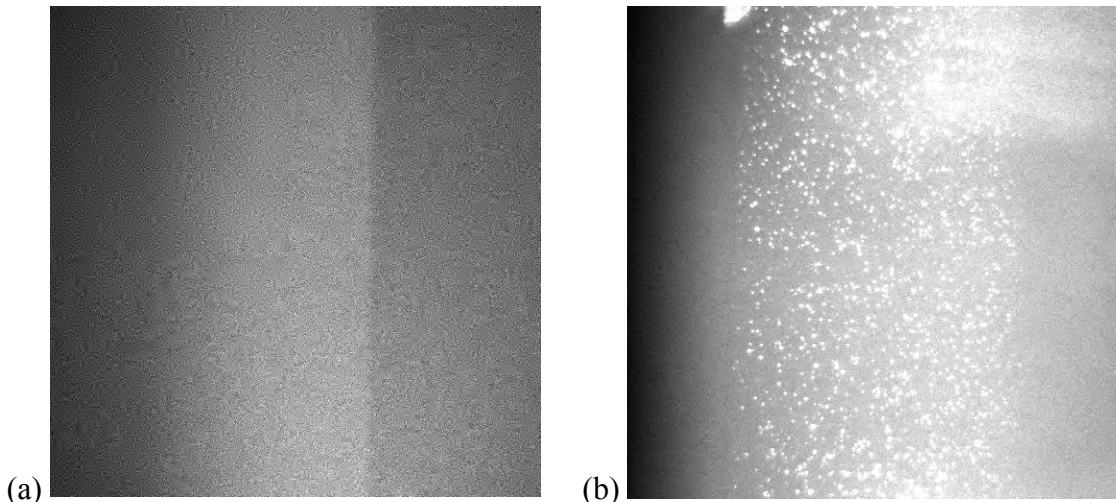


Figure 28. Comparison of Filtered Rayleigh Scattering signal (a) with filter and (b) without

During the FRS data collection, the outputs from the photodiodes were captured as well as the recorded laser frequency and its build-up reduction time (BURT) value. The BURT, a measure of the main laser pulse build-up, is a crucial component in monitoring the spectral output of the laser, of paramount interest during FRS. When the BURT exceeds a set limit, this indicates that

the seed laser has “unlocked” from the desired frequency. This in turn means that the output laser beam from the laser head will be spectrally broadened—in turn meaning that the iodine cell will not absorb the reflected light as it is not all at the correct frequency. Each shot with a BURT above the cutoff, or with particle intensities above a given threshold, was discarded prior to image processing. The processed temperature field results, as well as a greater discussion of the processing method, are detailed in Chapter 5.

Uncertainty of the Filtered Rayleigh Scattering technique was evaluated using a procedure developed by Forkey et al (1998).³⁶ While time limitations in the project have precluded such an analysis at the time of the publication of this work, it will be completed prior to the conclusion of the project. This uncertainty analysis may be found at the project website; a discussion will be included with the results.

CHAPTER 3: SCHLIEREN, PRESSURE, AND TEMPERATURE PROBE MEASUREMENTS IN A COMPRESSIBLE MIXING LAYER WITH A THERMAL GRADIENT

3.1 Schlieren Visualizations

3.1.1 High-speed Schlieren Videos

On the right in Figure 29 is a sequence of stills from the high-speed (120,000 frame/second) schlieren movies. This sequence in particular highlights the utility of the movies, in that the formation and movement of structures within the mixing layer may be visualized individually and used for later analysis and correlation with the other measurements. From this sequence, taken over five frames spanning slightly less than 200 milliseconds in time, two main features stand out. The first feature, valuable more for its validation of the operating condition, is the changing shock/expansion wave coming off the splitter tip. This switching between the two features is highly indicative that the static pressures in the two freestreams match closely at the splitter plate and therefore is a useful mixing layer condition. The second feature, however, is one lending insight into the shear layer itself: the growth of a braid structure in the shear layer. This structure, which begins in the first frame as a small

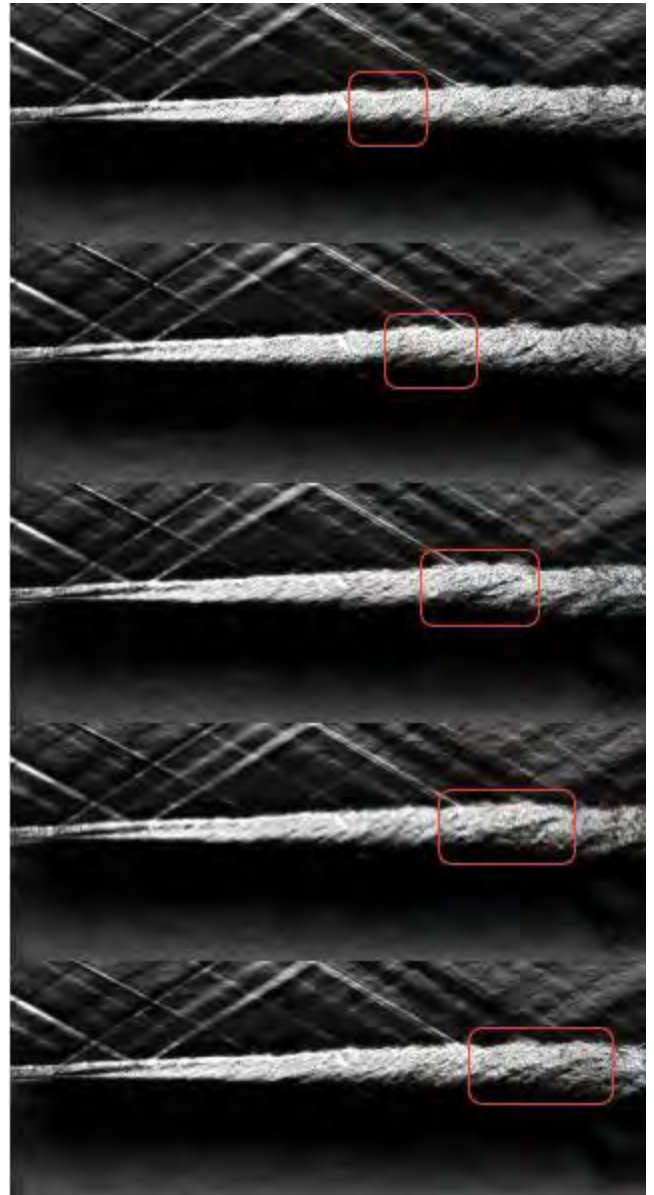


Figure 29. Sequence of high-speed schlieren frames showing growth of a braid structure

rippling band in the mixing layer, grows over the next two frames into a clearly visible feature in the flow. As it continues to pass down the test section, the braid elongates; the upper portion of the braid stretches out as the velocity differential across the shear layer takes effect. Furthermore, this sequence of images serves to illustrate the insight of Kim with respect to the relative size of the structures on the two sides of the mixing layer¹⁴: as the high-speed side of the braid moves in time, it stretches out and remains small in amplitude, whereas the low-speed edge of the braid is able to remain larger and extend further downward as it moves along the shear layer.

3.1.2 Full-resolution Schlieren Visualization

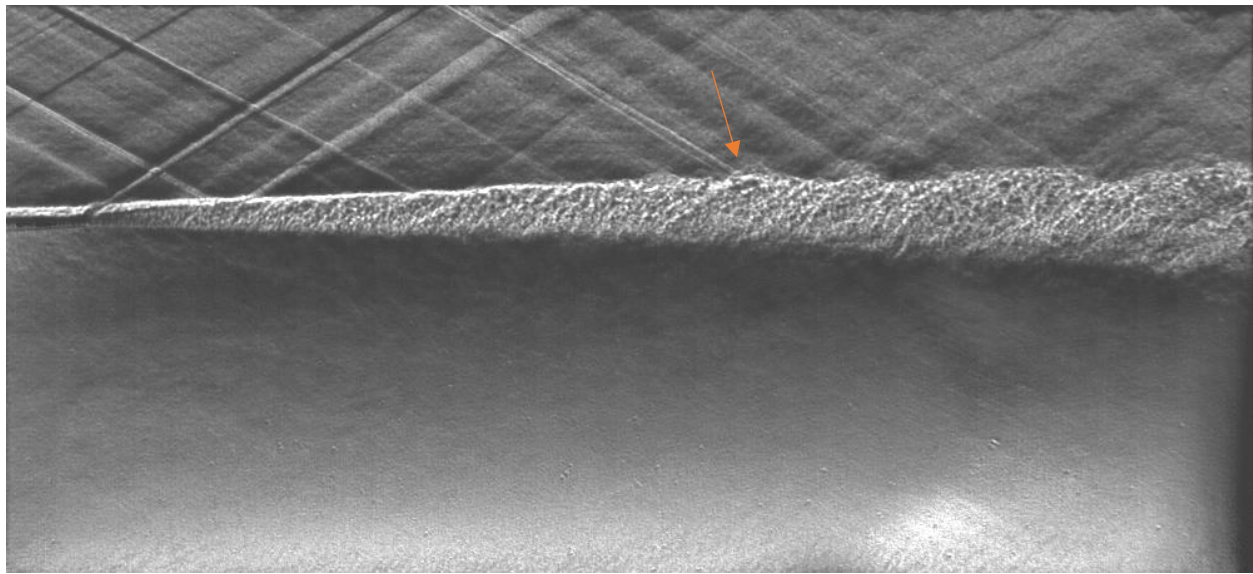


Figure 30. Instantaneous full-resolution schlieren visualization with arrow marking impingement of reflected wave

The full-resolution, slower frame-rate schlieren images, an example of which is shown above in Figure 30, show much more of the shock structure and better visualize the braids along the mixing layer. The interaction of the mixing layer with the waves becomes much more evident at higher resolution; note the increase of the braid height at the point where the reflection of the splitter tip wave impinges back on the shear layer. This, in addition to the shear layer's post-shock increases in the number of fluctuating structures (braids and rollers), aligns with the findings of Zhang that would expect such behavior after the impingement of the wave into the shear layer.¹²

Minor waves are noted to come off of the braids in the mixing layer and into the primary stream, reminiscent of the canonical wavy wall supersonic flowfield, as discussed by Rossman et al.¹⁰

The mixing layer qualitatively appears to be possibly fully developed about 4/5^{ths} of the way across the field of view: the two final braid structures are nearly identical to one another, and the visual growth rate of the shear layer is nearly linear. This will be investigated and verified by the PIV measurements in Section 4.3. The flattened structure is expected for such a convective Mach number; the trend Kim noted of larger structures on the secondary side of the mixing layer appears to be corroborated here, as the instabilities clearly begin from the bottom half of the shear layer and stretch to the top.

As a minor remark, there is of course the matter of the reflected shock/expansion wave off of the top wall of the test section and possibly interacting with the shear layer itself before reflecting back up again. Given that this would certainly affect the velocity measurements, and likely all the other measurements as well, it must be given some discussion. There are two main ways to check whether the impinging wave affects the shear layer: whether it bends either away from or nearer to the shock, which can be easily seen in the schlieren, or by examining whether the pressures along the shear layer remain relatively constant throughout. The first requirement for a stable testing condition is met by checking the schlieren visualizations and may also be used in the PIV field results in the streamwise U velocity trends. The second requirement is investigated through analyzing the static pressure along the length of the shear layer—this confirmation of a stable operating condition being the primary goal of the static pressure measurements.

3.2 Static Pressure Tap Measurements

While meeting the primary goal of the static tap measurements is clearly key to the work, the secondary goal is no less important: checking the strength of the shocks in the primary stream.

Figure 31 below shows a comparison between the present case of interest, and the work of Kim et al. on the same tunnel, for the most similar case, Case 4 ($M_c = 0.690$).¹³

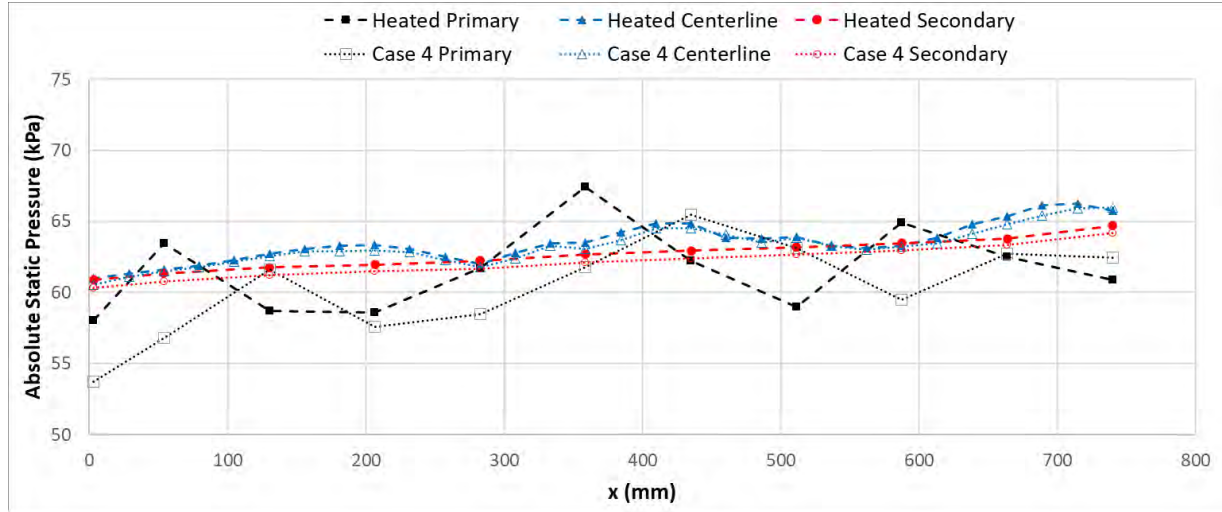


Figure 31. Comparison of sidewall static pressures for current work (Heated) and $M_c = 0.690$ (Case 4) of Kim et al.

Two remarks are immediately clear from the comparison: first, that the static pressure along the centerlines, as well as the secondary flows, is almost exactly the same between the cases. This, while it may be surprising at first glance, makes sense with thought: the static pressure in the secondary is what is being adjusted in order to match to the pressure of the supersonic primary stream. The second remark is much more interesting: that the primary stream has marginally stronger shocks, therefore at higher angle and occurring earlier, in the heated case when compared to Case 4 of Kim. These shocks are represented in the visualizations by the static pressure peaks in the primary stream; for the heated work, the shock peaks (and expansion troughs) occur a tap before that of the non-heated case. The slightly stronger shock that the heated case experiences is inferred to be due to the increased density difference between the primary and secondary streams: while the primary stream has largely the same incoming characteristics as what Kim et al. found, the secondary, with its nearly doubled static temperature, has a correspondingly nearly halved density. Therefore, in order to match the post-shock characteristics, the shock must be stronger

than in the case of Kim et al. Furthermore, this stronger shock (and its corresponding reflected second shock) also has implications for the operating condition. Due to the increased strength of the shock, it is likely that the window for the operating condition would be much tighter than what would be seen for a non-heated case. The stronger reflected shock has the ability to “bend” the mixing layer downwards, affecting the accuracy of the data; this would be most visibly seen in the schlieren visualizations and velocity measurements, although all data would of course be affected. Also of interest when the velocity and turbulence statistics are measured is whether the region where turbulence would be fully developed will come sooner than in the work of Kim et al.¹³ If so, some consideration may be due as to whether the reflected shock off of the top wall has any effect on the turbulence statistics.

3.3 Temperature Probe Measurements

3.3.1 Total Temperature Traverses

Total temperature traverses were obtained using the TAT probe with the approach outlined in Section 2.3.3.2. These traverses were made at four streamwise positions, at $x = 24.7, 125.8, 204.9$, and 284 mm, and encompassed the entirety of the thermal mixing layer, extending well into the thermal freestreams on both sides of the mixing layer. A minimum of four traverses per position were performed, with the values at each position within the traverse averaged and then normalized between the stagnation temperatures of each freestream. It should be noted that this normalization was performed given

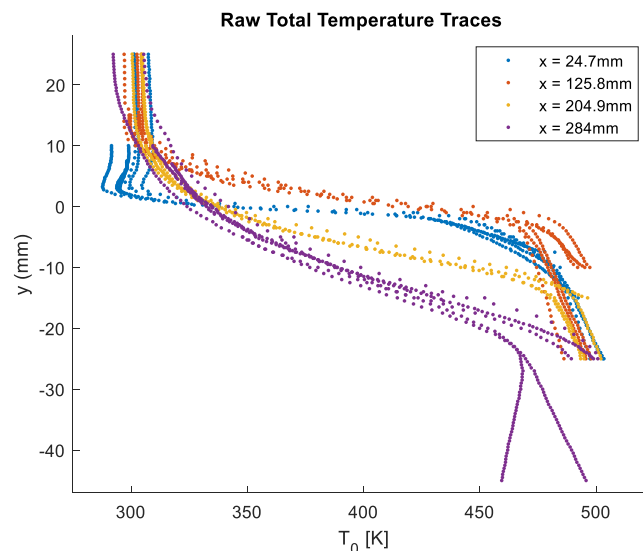


Figure 32. All raw total temperature traces

the simultaneous values *in time*, as the freestream stagnation temperatures varied somewhat as the tunnel was run and therefore must be synchronized with the correct probe temperature value. This behavior may be seen in Figure 32 with the non-normalized total temperature values (particularly in the secondary freestream where the value does come to a constant value); it should also be noted that an additional comparison run was made at $x = 284$ mm to verify that there was no difference traversing the probe from the secondary to the primary or vice versa. Once verified, all later traverses were made from the secondary to the primary stream; this was done to protect the probe from experiencing the shocks produced during tunnel startup.

The normalized total temperature traverses were then used to determine the thicknesses of the thermal freestreams using a 10% ΔT_0 definition in the same vein as the 10% ΔU definition for velocity thickness. Equation (13) gives the normalized y-parameter η , where y_0 is defined as the average position between the edges of the thermal layer y_1 and y_2 , and b as the distance between the two—the thickness of the thermal mixing layer at that point.

$$\eta = \frac{y - y_0}{b} \quad (13)$$

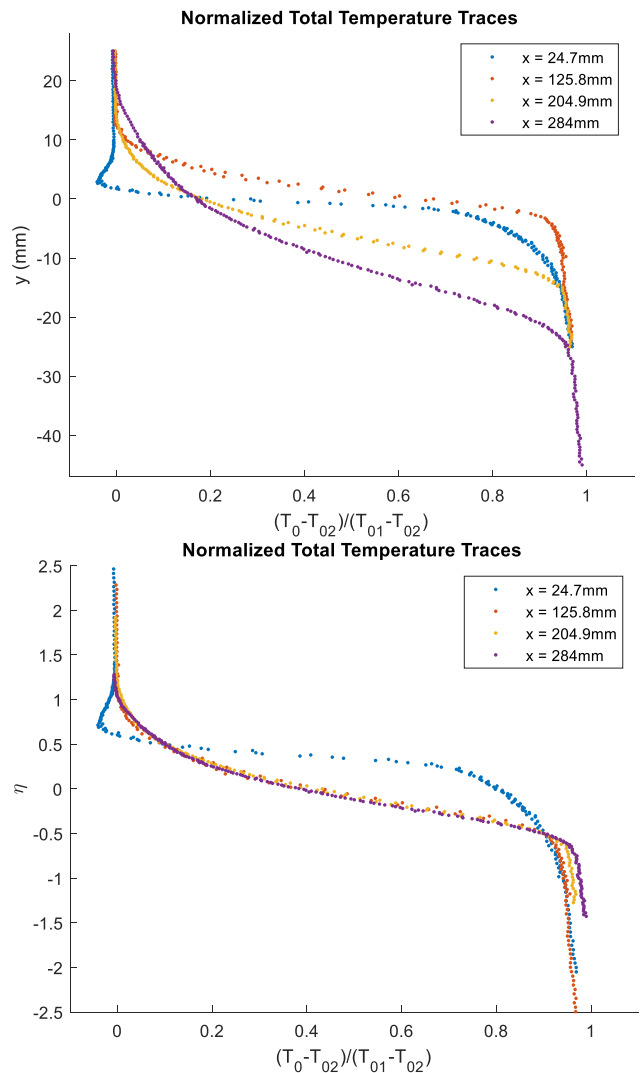


Figure 33. Normalized total temperature traverses plotted on raw and normalized transverse position

The η parameter was then used to create traces normalized by the thickness of the thermal layer, along the transverse direction to the flow. These normalized traces may be seen in Figure 33 on the previous page. It is immediately clear from the normalized traces that the thermal mixing layer is fully developed at or before $x = 125.8$ mm; this is because the normalized traces essentially collapse completely upon each other after this location. The normalization procedure also increases the resolution of certain effects that are difficult to discern from the raw traverse data, best highlighted from the $x = 24.7$ mm traverse. There appears to be a deficit occurring in the total temperature, to values much less than that of the primary freestream value, an effect not anticipated prior to data collection. This indicates a thermodynamic effect taking place within the near field of the splitter plate, possibly due to residual cooling effects of the plate itself. This deficit is an effect that bears greater investigation, indicating a possible effect on the mixing that had not been highlighted by the schlieren or velocity results. From the normalized traces there is also a slight effect that is most noticeable in the normalized temperature- η plot in the secondary thermal freestream but is seen in both plots. This effect, where the stagnation temperature as measured by the TAT probe does not quite reach the level found in the secondary stream stagnation temperature, is attributed to both slight time difference in the measurements (keeping in mind that the tunnel temperature is constantly falling as it is run) as well as entropy effects that are more pronounced further downstream and nearer to the shear layer. However, this is a minor issue that does not affect the quality of the normalized data, particularly once the static temperatures are considered.

3.3.2 Static Temperature Traverses

Static temperatures were calculated from the total temperature traverses using PIV velocity data to inform the adiabatic relation for each point of the traverse; see Figure 34. This determination was not able to be performed for the $x = 284$ mm traverse, because there did not

exist any PIV data for that streamwise location. These static temperatures show the same general spatial trend as the total temperatures; they normalize similarly, using the same method utilized for the total temperature traverses, and the profiles have approximately the same shape across the mixing layer. What is notable is their highly linear change in static temperature across the thermal mixing layer, especially in comparison to the stagnation temperatures, at the fully developed positions. While the first position appears to indicate something near to this linear behavior, it is less pronounced than at the other two positions. This linearity in the static traces may be partially attributable to the thermocouple's response time, but this is *extremely* unlikely due to the high responsivity of the probe as well as the extremely low variation across the ensemble for each position; it will be fully investigated with the Filtered Rayleigh Scattering temperature results in Chapter 5.

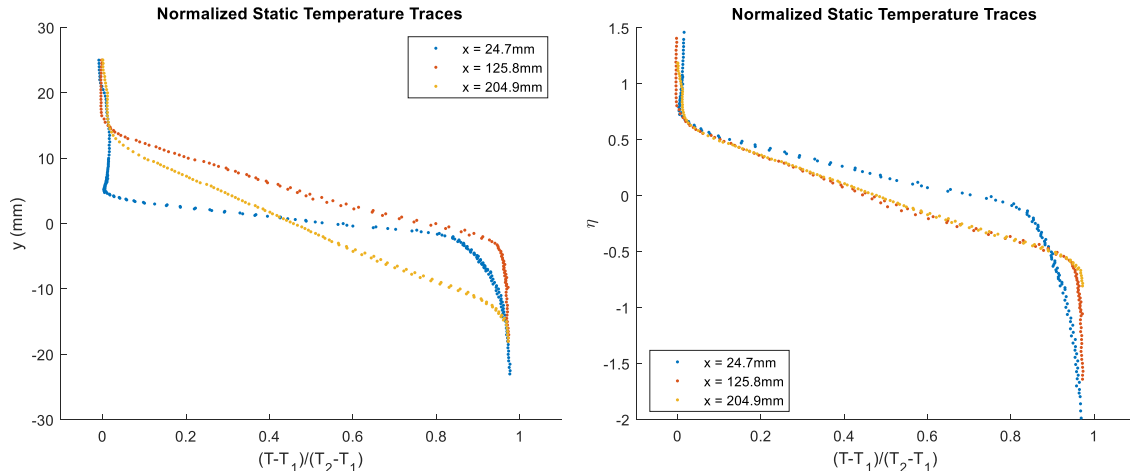


Figure 34. Normalized static temperature traverses plotted on raw and normalized transverse position

The two downstream temperature profiles, once normalized and plotted against η , collapse to nearly the same profile, indicating that the static temperature distribution remains self similar. This lends further evidence that the thermal mixing layer is fully developed, even as the static temperature calculation has a dependence on velocity with the total temperature profiles. Given this behavior, the thermal layer growth rate was calculated from b thickness data at these two

locations. The db/dx value from this analysis was found to be 0.0946. Additionally, when the conversion to the static temperature occurs, the temperature deficit effect noted in the total temperature traverses is substantially reduced; indeed, in the normalized- T vs η plot, it would be easy to miss the slight deficit if it was not noticed from the earlier stagnation temperature plots. However, even with the less pronounced deficit, the static temperature does have a sharply defined interface between the freestream and mixing layer at this early position. Again, this is an effect that bears further investigation with the Filtered Rayleigh Scattering results, as well as in future works.

CHAPTER 4: VELOCITY FIELD MEASUREMENTS IN A COMPRESSIBLE MIXING LAYER WITH A THERMAL GRADIENT

4.1 Challenges

A variety of issues slowed and delayed the PIV data collection process for this heated, compressible mixing layer; these were due to initial inexperience with the technique on behalf of the author, as well as due to the unique thermal environment that the experiment required. Ultimately, high-quality data were recorded that achieved the project's requirements. These challenges and their solutions are detailed in the following section primarily to assist future experimental work of a similar type.

4.1.1 Seeding Injection and Density

For high-quality particle image velocimetry measurements, the particulate seed must be evenly distributed throughout the field of view that is to be measured, allowing the processing algorithm to track the seed particles across image pairs. The required particle density is primarily dependent on the speed of the flows and seeding method, but is also affected by features in the flow, especially shocks and vortices. In the complex heated mixing layer that is of interest here, an additional difficulty is that both streams must be seeded evenly. Each stream will have its own seeding requirements, particularly with their different flow rates, pressures, and temperatures. Two methods of seeding were eventually used in this experiment, one for each stream: a commercial smoke generator for the high-speed primary and a Laskin-type nozzle seeder for the low-speed secondary, both of whose capabilities are briefly described in Table 6 of Section 2.3.6.

Seeding the streams evenly can be described to be as much of an art as a skill, where minor adjustments to the seeder or even the flow itself can have outsized effects on the quality of the images obtained. Furthermore, for the liquid seeders that were used in this study, oil droplets

accumulate along the top, bottom, and sidewalls of the tunnel over the course of the tunnel runs. This in turn leads to buildup of oil streaks across the viewing windows, blurring or even outright obscuring the views of the imaging cameras. As should be then clear, overseeding the flow can



Figure 35. Examples of seeding quality (left-right): Overseeded primary stream, Acceptable, Good
be just as detrimental as underseeding, particularly in that it may cause the aforementioned negative effects over the course of a run. It should be noted that while purging runs (runs that do not have any seeding and are rather used to clear accumulated oil from the tunnel) do take place, they cannot fully clean the inside of the tunnel. Rather, over time, a pseudo-steady-state is reached with respect to the amount of accumulated oil in both streams of the tunnel, but it must again be emphasized that individual runs are improved by meeting an optimum seeding condition. Above, Figure 35 shows different levels of seeding quality.

4.1.2 Secondary Seed Persistence

The largest challenge in the experiment to be overcome was the lack of seed persistence in the secondary stream due to its high temperature. During initial PIV setup, a two-component planar configuration was used to obtain early flow images, with the goal to understand the setup process and workflow with fewer variables. It was during this setup period that an intermittent phenomenon was noticed in the images that may be seen on the next page in Figure 36: a clouding effect taking place in the secondary stream and extending into the mixing layer.

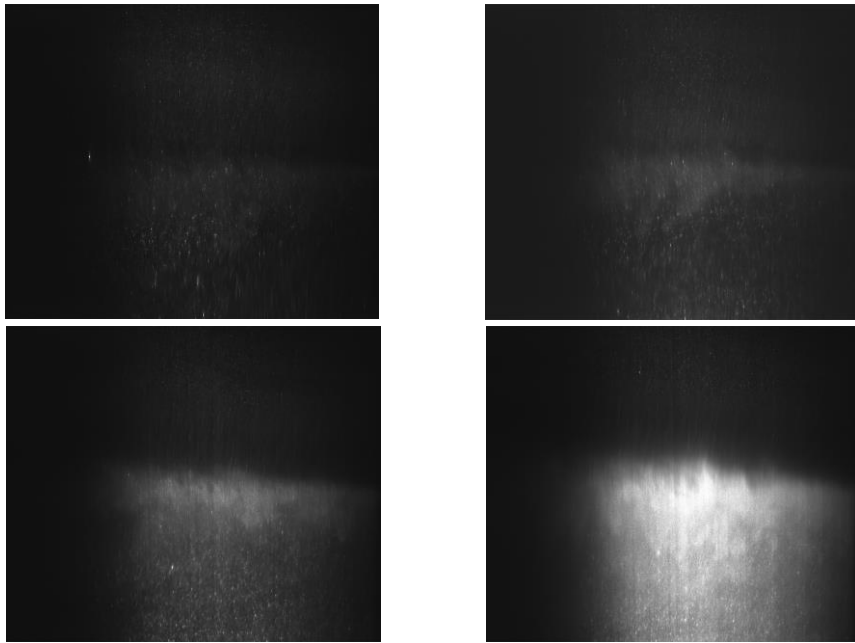


Figure 36. Development of oil clouding in test section (Time progression: left-right, top-bottom)

Initially, it was thought that this clouding effect was due to water vapor in the secondary flow that was condensing upon meeting the much colder primary flow. Condensation had been seen previously in the same lab and even in the same wind tunnel when ambient humidity was high, especially if the facility dryer desiccant material was nearing end-of-life. With the initial seeding method being an ambient air entrainment method where a commercial seeder would exhaust into an open pipe, the entrainment valve was adjusted along with other checks. The phenomenon was initially judged to not occur if the temperature of the secondary stream was reduced slightly, generally below 470 K. While this was not ideal, particularly as the thermal differential between the streams was the crux of the experiment, it was close enough to the original proposed operating conditions to be within reason.

However, after the changeover to the eventual stereo-PIV setup had been completed and data runs recommenced, the clouding returned even at the lower temperatures. Two items were added to concerns at this point: the facility dewpoints had been verified to be below even that of the primary stream's static temperature, and the clouding intensified over time. While still

operating under the assumption that the clouding was water vapor condensation, efforts shifted to remove all sources of water vapor. A series of changes occurred to the secondary seeding setup as a result, with the eventual configuration using a blanking plate over the main entrainment valve, with an NPT fitting tapped into the plate. A Swagelok adapter was threaded onto the fitting, with $\frac{1}{4}$ " tubing connected into a 3D-printed part to fully capture the smoke particles with minimal ambient air. When further testing of this configuration continued to show the clouding effect, consideration was given to whether the smoke oil itself had agglomerated water molecules from the air. Saturation of the oil with water could, in the higher-temperature environment of the secondary stream, possibly cause water vapor to form in high enough quantities to create condensation in the mixing layer when coming into contact with the cold primary stream. However, after a full replacement of the smoke oil with new, previously sealed oil, the clouding still occurred. It was at this point that attention turned to the smoke oil and generator itself.

Contact was made with the manufacturer of the smoke machine and smoke oil, requesting information on properties of the oil itself, as well as the method used within the generator to create the smoke particulates. According to the manufacturer, the ViCount machines burn the oil in the heat exchanger of the device, where the pressurized stream of nitrogen moves the combustion products out of the nozzle. The gaseous vapors from the combustion process then condense in the cooler outer air that the particles are exhausted into and create the smoke cloud. However, the smoke generation process is interrupted if exhausted into flows at temperatures higher than 450-470 K, when the heated flow is at or higher than the temperature in the ViCount machine. The high temperature sustains the occurring reactions; the products of these reactions then rapidly condense in the cold air of the primary stream and cause the clouding effect. Further discussions

were made with the manufacturer as to whether a higher-temperature product existed; a retrofit was offered, but at too steep a cost both in terms of time and money to be viable for this project.

Table 9. Comparison of Different Liquid Seed Properties

	180 Smoke Oil	DEHS	Avocado Oil	Olive Oil
Flash Point	112-160+ C	200+ C	330+ C	320 C
Smoke Point	140 C	190 C	250-270 C	160-205 C
Boiling Point	218-330 C	232-249 C	300+ C	570 C
Surface tension @ 23 C (180 C)	N/A	32 mN/m	--	31.9 mN/m (23.1 mN/m)
Refractive index @ 20 C, 589 nm	1.472	1.449	1.46-1.47	1.44-1.47

An investigation into finding an alternative method for seeding the hot secondary stream then began. Solid particulate methods, such as using titanium dioxide, were not strongly considered due to safety concerns; the facility was not designed to be seeded in such a way, and was without a method for safely collecting the material without exhausting the material either into the lab or outside. Therefore, liquid seed was still the primary focus of the investigation for an alternative. After a suggestion from a NASA collaborator who had tangential experience with a high-temperature experiment, avocado oil was cross-compared with other high-temperature organic oils as a possible seed material, as well as other nonorganic compounds that had been previously used by the lab in the past. Table 9 above summarizes the comparisons made.

After further investigation, avocado oil used in a TSI Model 9307 Laskin nozzle was chosen as the new seeding method; it has the highest smoke point of the oils investigated while still having fairly similar properties to these better known oils. As a side benefit of previous modifications to the seeding setup, the Laskin nozzle



Figure 37. Secondary seeding configuration with Laskin Nozzle seeder

exhaust could directly connect to the NPT port on the previously described blanking plate with minimal extra requirements. This approach is shown on the previous page in Figure 37; note the ball valve, used to prevent backflow of hot air to the seeder during tunnel warmup and cooldown. This ball valve is only opened while the tunnel is operated at full flow: the secondary flow pressure is sub-atmospheric and therefore will only entrain the seeding flow.

4.1.3 SPIV Camera Alignment and Calibration

The third challenge faced in obtaining the SPIV data came as a part of the physical setup, as haste to obtain data quickly after the avocado oil solution was found, combined with inexperience in setting up stereo-PIV, led to slight misalignments in the cameras along the streamwise-, or x -axis, for some of the data collected. As a result of the misalignment, the spanwise w -component of the velocity vector was biased depending on the angle of the cameras (positively for the first two fields of view in the streamwise direction, negatively for the third).

Typically, for slight misalignment of the cameras, especially in cases where the angles of the two cameras are not exactly equal with respect to the laser sheet, the stereo self-calibration routine in DaVis can correct the image mapping. This routine uses a common reference point in images from each camera to create an initial disparity mapping before using a set of images to create a correction mapping to match the images to each other. For cases in which the self-calibration is unable to correct the image mapping, continued realignment of the cameras must take place. However, because this self-calibration is a built-in feature of the PIV processing, it was not immediately evident to the author to verify the image alignment using the self-calibration until processing had begun and all images obtained. As a result, images obtained in the first and third fields of view both had to be discarded; the third field of view was retaken to verify the Reynolds stresses throughout the fully developed region. In order to prevent this issue from occurring again

when data were retaken, a 3D printed plate was created to assist with the alignment process. This plate, measuring 140x115x3 mm, has equidistant holes that go through its entire depth to serve as dual-sided markers, as can be seen in Figure 38.

By aligning these holes, the translation as well as rotation of the cameras may be easily matched. Furthermore, because the plate was designed to be approximately as wide as the laser sheet, the illuminated field of view during operation requires minimal final adjustment in the camera's focus using the laser-sheet illuminated particles themselves after being focused on the alignment plate. The second field of view, given the increased experience with how to conduct the stereo self-calibration in DaVis, was able to be retained for use without re-recording. While initially there was miscalculation of the w -component of the velocity vectors, after correction with the self-calibration, the results became accurate, with a high degree of confidence.

4.2 Boundary Layer PIV Results

Boundary layer PIV results were obtained for three of the four incoming boundary layers; the reasoning for this decision as well as the method of acquisition is discussed in Section 2.3.4. For the three boundary layers of interest, a mean two-component velocity profile as well as the Reynolds stresses were determined for a slice of the velocity field very near to $x = 0$ mm (i.e., the splitter tip). While optical access limitations precluded measurements at exactly $x = 0$, the boundary layer is shown to be fully developed prior to this point, such that all profiles are assumed to be applicable. For the boundary layers along the splitter plate, while the plate does technically move slightly under full-flow conditions, these effects were assumed to be negligible on the

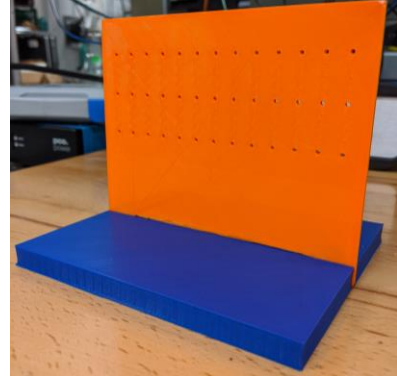


Figure 38. 3D-Printed alignment plate

boundary layer. Ensemble sizes for each boundary layer dataset ranged between 900 and 1200. These profiles were obtained in the boundary layer at locations as near to the wall as possible.

In order to determine the parameters used to define each boundary layer, the procedure outlined by Sun & Childs (1973) was utilized. Their procedure prioritizes elimination of the artificial non-zero velocity gradient at the edge of the wall-wake profile used in the Matthews' formulation. A departure in the Sun & Childs method that should be noted is their choice of U/U_∞ to be 0.995 at the boundary layer edge, as opposed to the conventional 99% definition.^{37,38} A method of least-squares fits a curve to the experimental data, which then is used in the modified wall-wake formulation with initial guesses as to the boundary layer thickness, δ , and skin friction coefficient, C_f . Plots showing the velocity profiles in both outer- and inner-wall normal coordinates of the three boundary layers of interest may be seen on the next page in Figure 39; the Reynolds stresses are plotted on the following page in Figure 40.

The best-fit mean velocity profile as calculated from the Sun & Childs procedure is then utilized to determine the incompressible displacement thickness, δ^* , incompressible momentum thickness, Θ , shape factor, $H = \delta^*/\Theta$, and the wake strength parameter, Π , through numerical integration. These integral parameters are listed for all four boundary layers of the experiment in Table 10 with comparison to Case 4 of Kim^{13,14}. From the comparison of boundary layer results, it becomes clear that the thermal boundary layers are much thicker than the corresponding ones of Kim, with correspondingly higher coefficients of friction except for the splitter plate bottom wall, which has nearly the same C_f between the cases. Of major note is the splitter plate top boundary layers: the 99.5% thickness extends further into the freestream by a factor of about 4/3—a major departure considering that the flow itself is the same. Given the hot splitter plate causing a thermal gradient into the cold primary stream, the boundary layer thickness correspondingly increases.

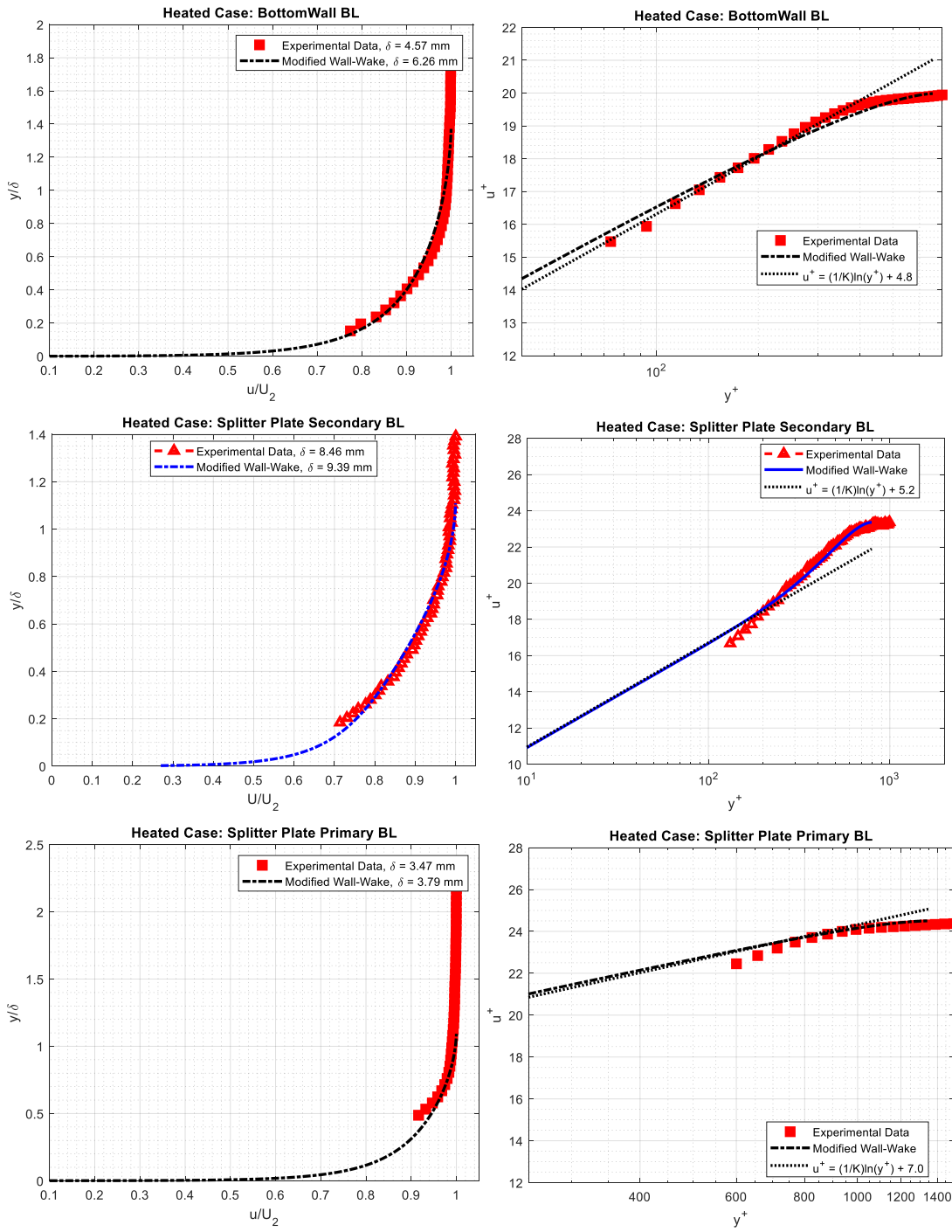


Figure 39. Boundary layers in outer-and inner-wall normal coordinates

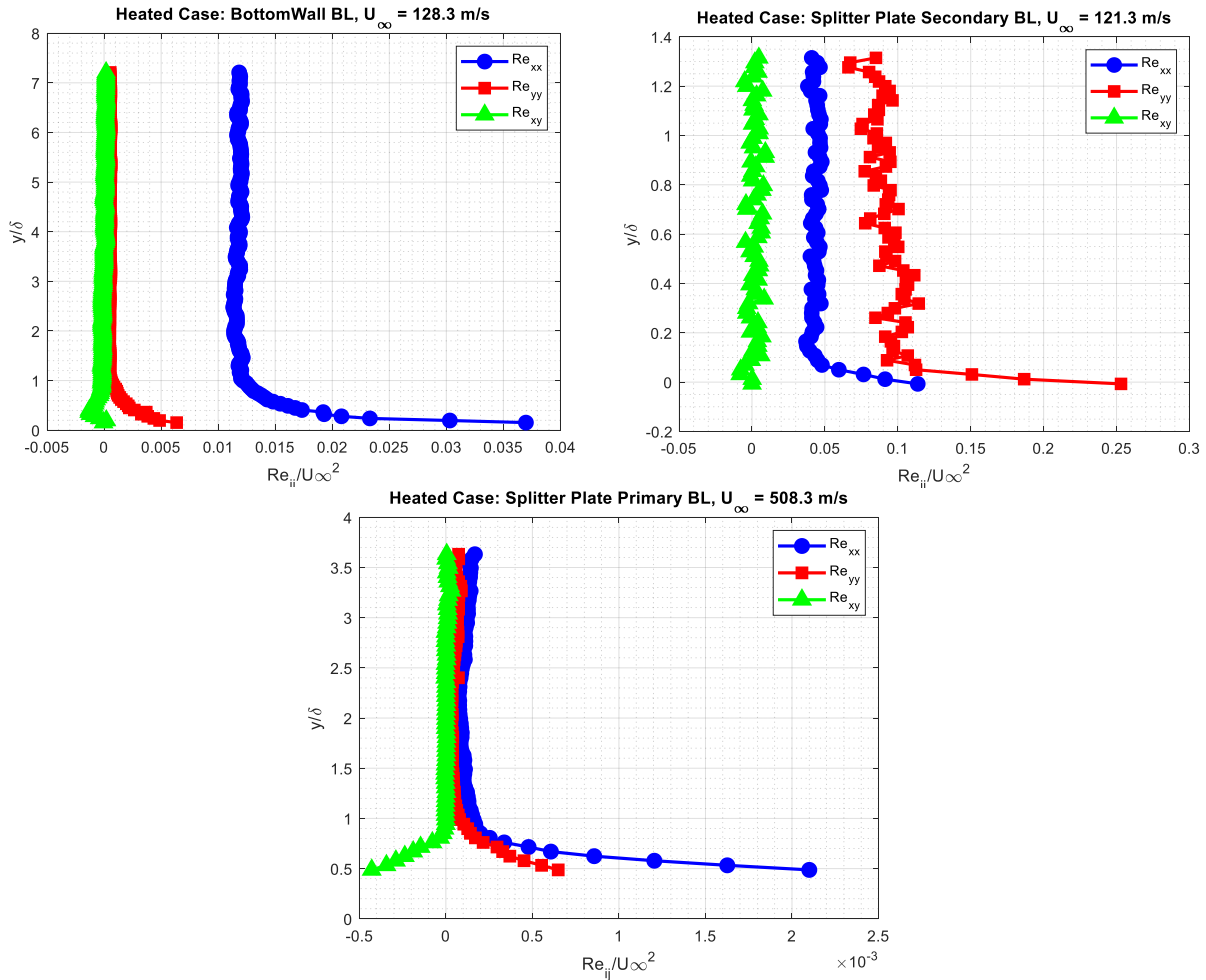


Figure 40. Reynolds stresses in boundary layers

Table 10. Comparison of Incoming Boundary Layers

Case	Location	δ_{99} (mm)	δ^* (mm)	Θ (mm)	H	C_f	Π
Heated ($M_c = 0.541$)	Top Wall*	3.599	0.574	0.429	1.338	0.001561	1.162
	Splitter Top	3.79	0.309	0.246	1.254	0.003332	0.108
	Splitter Bottom	9.38	1.271	0.940	1.353	0.003665	0.597
	Bottom Wall	6.26	0.537	0.417	1.289	0.005007	0.188
Kim Case 4 ($M_c = 0.690$) ^{13,14}	Top Wall	3.599	0.574	0.429	1.338	0.001561	1.1620
	Splitter Top	2.847	0.514	0.372	1.381	0.001526	1.3996
	Splitter Bottom	4.271	0.617	0.464	1.330	0.003711	0.4884
	Bottom Wall	4.212	0.646	0.474	1.364	0.003547	0.6700

4.3 SPIV Results

Stereo-PIV results were obtained with a minimum ensemble size of $N \geq 3000$ for each field of view. Moments of the instantaneous variations from the mean were obtained up to and including the fourth moment, and Reynolds stresses for the entire stress tensor were computed using the second moment. Uncertainty was calculated for all results, as a compilation of particle, processing, equipment, and sample size effects to the total uncertainty.

4.3.1 Velocity Vector Results

Mean velocity components were computed for all three coordinate directions from the instantaneous measurement ensembles. These results range from 8 to 217 mm in the streamwise (x) direction; they are centered in the transverse y -direction of the test section. As the end-view results from Kim^{13,14} showed, there is little variation along the spanwise (z) direction in the mixing layer, as expected. Therefore, these results can be considered to be valid throughout the spanwise width of the mixing layer.

Mean velocity fields may be found plotted in Figure 41. From these mean velocity fields, the most notable feature is the expected slow growth of the mixing layer in the streamwise direction. The effect of the splitter tip shock on the V component of the velocity is also noticeable, although it should be noted that the magnitude of this component is almost entirely less than ± 25 m/s . This shock, which reflects off the top wall of the test section, impinges on the mixing layer at about $x = 120$ mm and then reflects back upwards. The modestly positive V component preceding the impinging wave, and negative component after the impingement highlights the feature well. Looking at the U component around the same point, there is a slight upward tilt to the shear layer that then tilts slightly downward after the shock. Eventually, the shear layer straightens off to a flat layer, as seen in the region of $x = 150$ mm and beyond. The W component, meanwhile, stays

consistently near zero in the freestreams throughout the test section, which is effectively within the uncertainty of the measurements. There appears to be a slight positive bias, about 10 m/s, in the secondary stream, with greater effect near to the shear layer. From the schlieren visualizations, the braid structures indicated a small degree of transverse velocity in the shear layer, which is also seen in the PIV results. Non-physical effects are seen at the interfaces between the fields of view for all components, where the mean fields were stitched together; these, however, are expected in the fields and have little to no negative effect on the results. More worrisome were the laser light reflections, seen most strongly in the W -component after about $x = 200$ mm. These reflections have effects on the mean velocities as well as all other statistical results; as such, they preclude the use of measurements after this point. Fortunately, the Reynolds stress analyses in the following section indicate that the fully developed region occurs well prior to the region of laser reflections, and thus are of no major consequence.

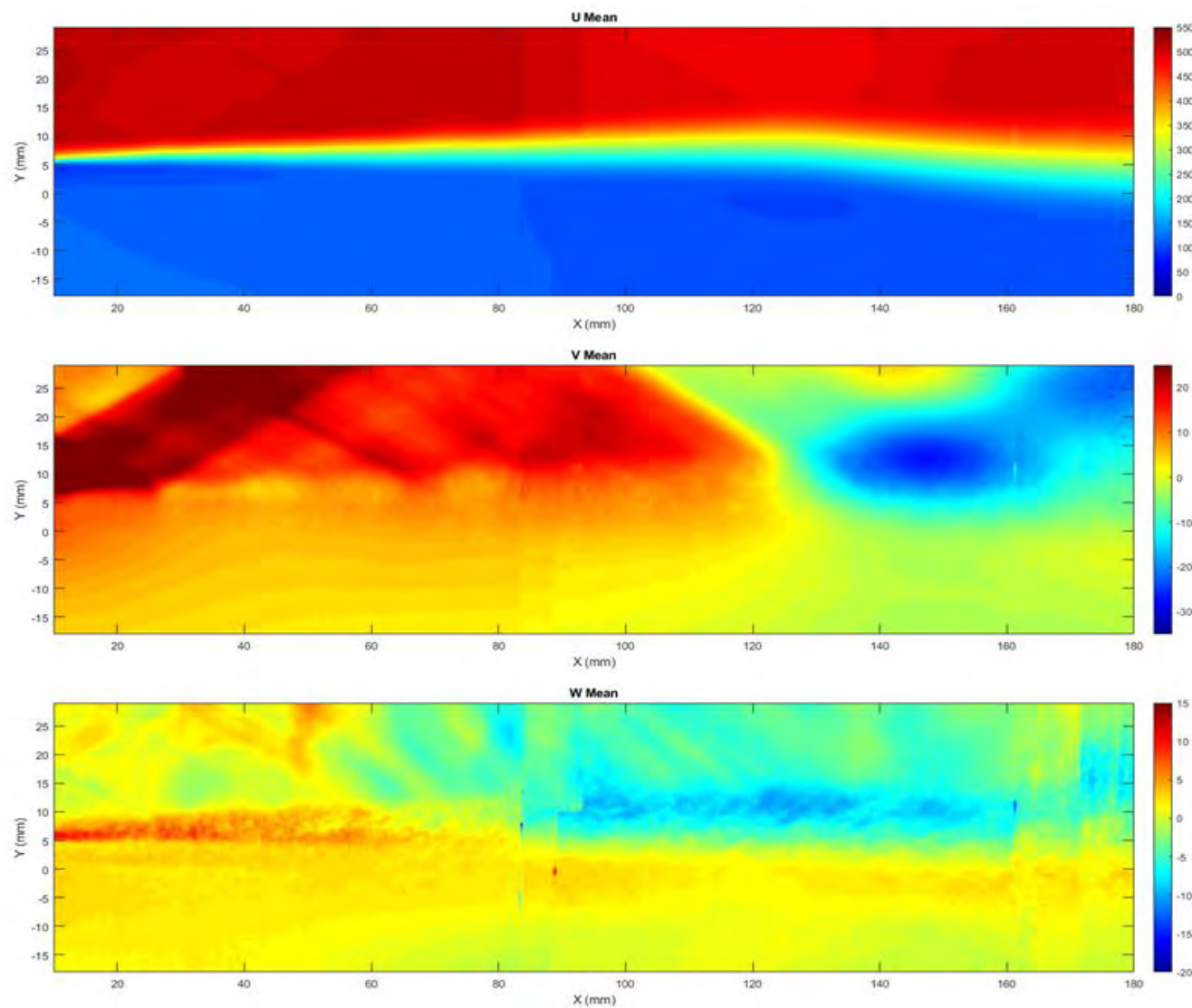


Figure 41. Mean velocity fields for U, V, and W

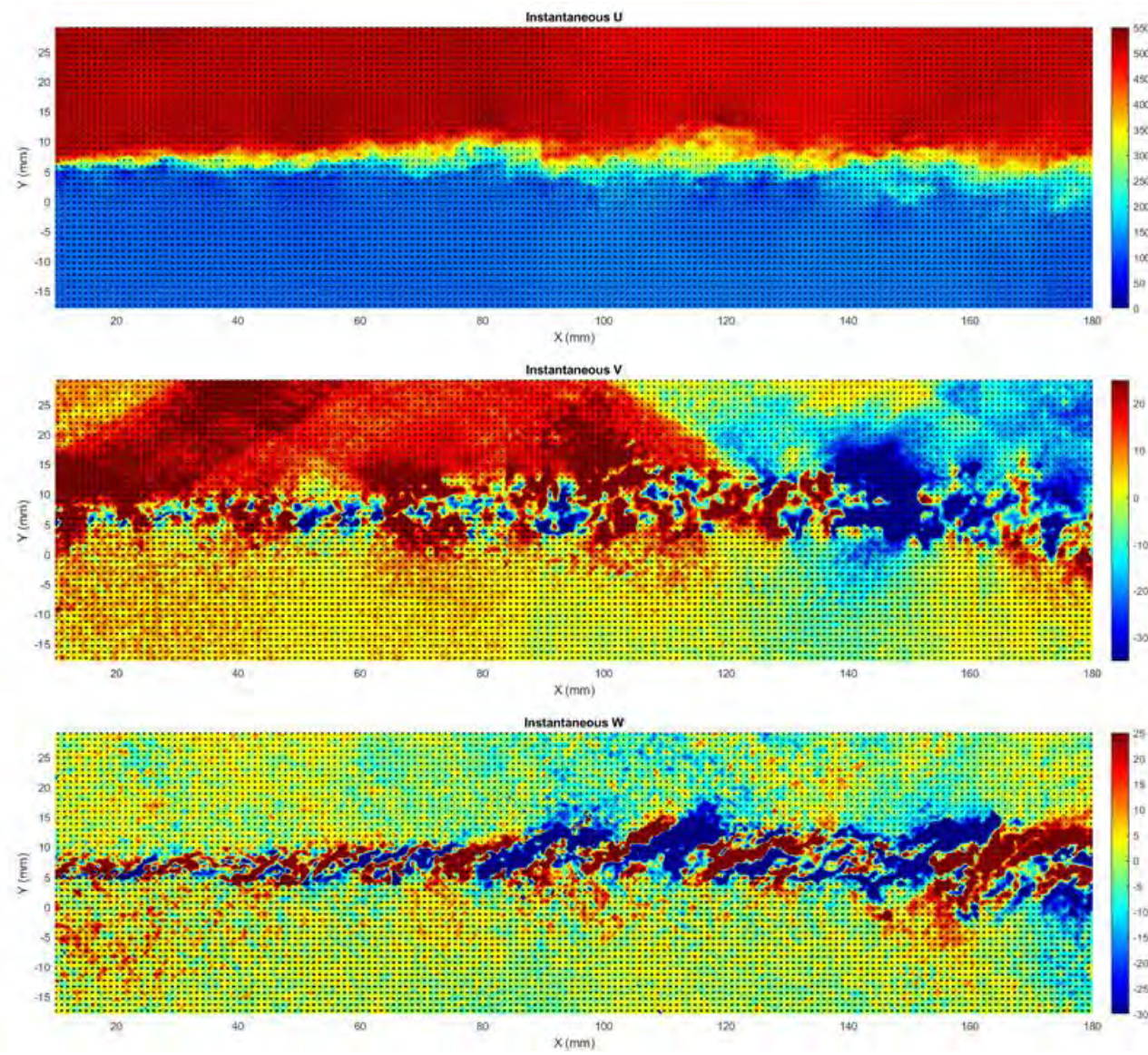


Figure 42. Selected instantaneous vector fields with overlaid instantaneous velocity component contours

Further and arguably deeper insights can be gleaned from the instantaneous results, shown in Figure 42 on the previous page. Here, the resemblance in the instantaneous u -component to the schlieren results can be seen. Flow features along the upper edge of the mixing layer show a slight change due to the impinging shock, although more clear is the slight downward bend in the mixing layer, resulting from the shock reflecting from the top wall of the test section and impinging on the shear layer. Additionally, the instantaneous v -component clearly shows the shock structure, but more interesting is the flipping in the mixing layer of the instantaneous v -component magnitude. A consistent up/down movement of the flow, switching from -30 to +30 m/s occurs as the small-scale mixing structures noted in Kim¹⁴ occur. When considered together with the spanwise switching in the instantaneous w -component, it appears that these structures largely line up together, and possibly indicate the existence of roller structures oriented along the streamwise direction.

Additional details may be noticed when the schlieren measurements are considered in tandem with the velocity measurements, as seen in on the next page in Figure 43. With this new lens, it can clearly be seen that the braid structures line up with the velocity fluctuations. Furthermore, the shocks stand out even more strongly in the primary freestream shifts in the instantaneous v -component. All fluctuations, in fact, overlay neatly onto the mixing layer as visualized by the schlieren results. When the instantaneous u -component is considered with the schlieren, the edges of the mixing layer become even more distinct. In all, the combined schlieren/PIV results stand to show that the instantaneous density gradients line up exceedingly well with the instantaneous gradients in velocity as measured by stereo-PIV.

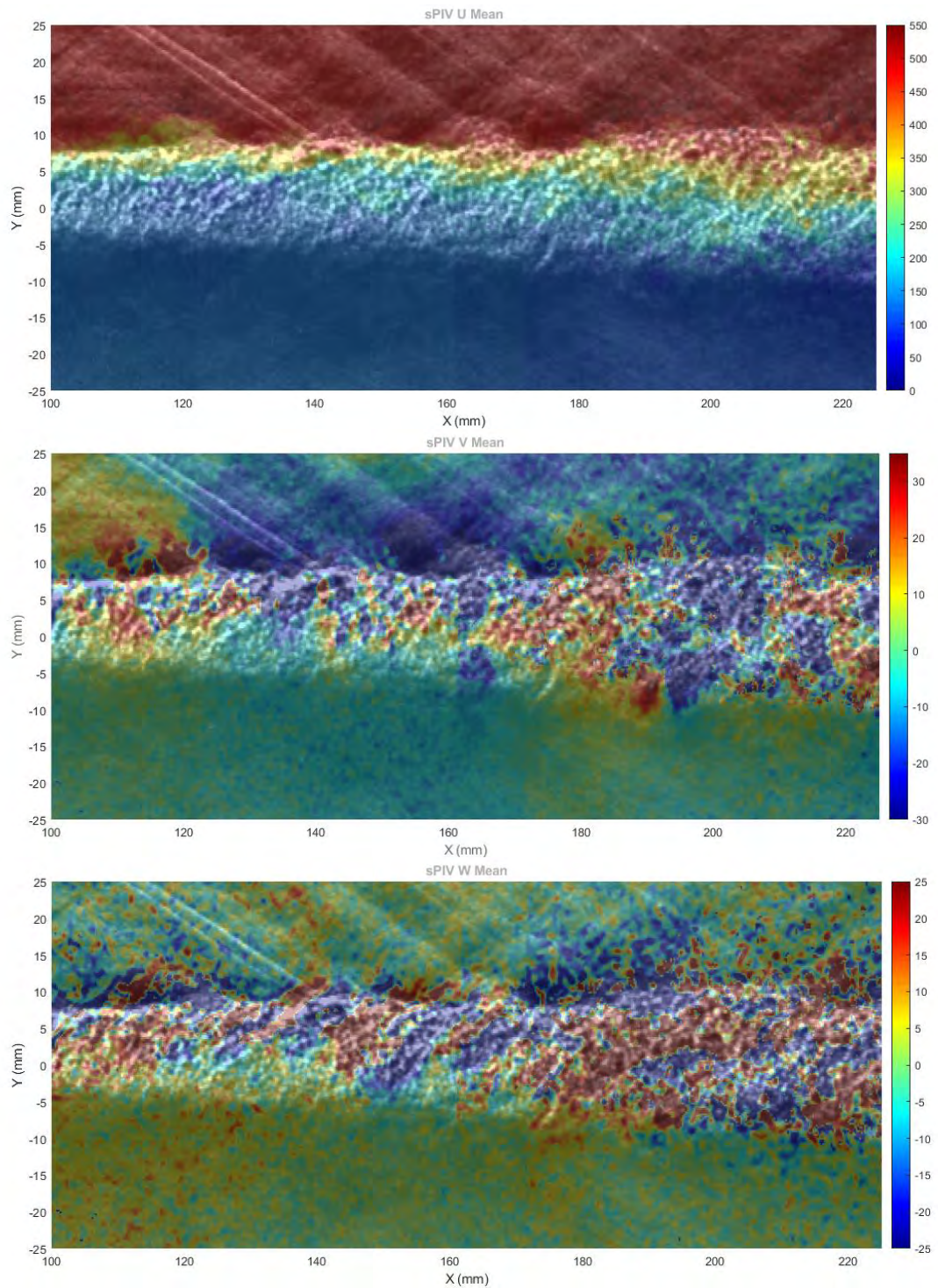


Figure 43. Instantaneous u -, v -, and w -component vector fields overlaid on schlieren stills in the Fully Developed Region

The mixing layer growth itself was examined and its characteristics measured from the mean velocity results. The ΔU shear layer thickness b and its centerline location y_0 , were

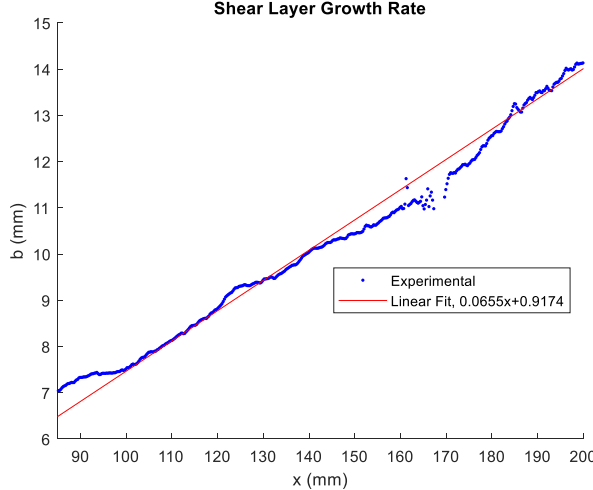


Figure 44. Shear layer growth rate

determined at each streamwise location along the shear layer, and from the thickness data, the shear layer growth rate db/dx was calculated. The growth rate itself was determined using a least-squares fit curve and is plotted in Figure 44. From these results the normalized growth rate db/dx^* was found by normalizing by the incompressible growth rate

at the same velocity and density ratios of Papamoschou and Roshko described in Equation 2.³ This normalized value is plotted against the convective Mach number in Figure 45; its value fits well within the values found by previously published work. With this said, however, the normalized growth rate is seen to be noticeably higher (about 22%) than the value found by Kim for the nearest similar M_c while using the same wind tunnel facility.

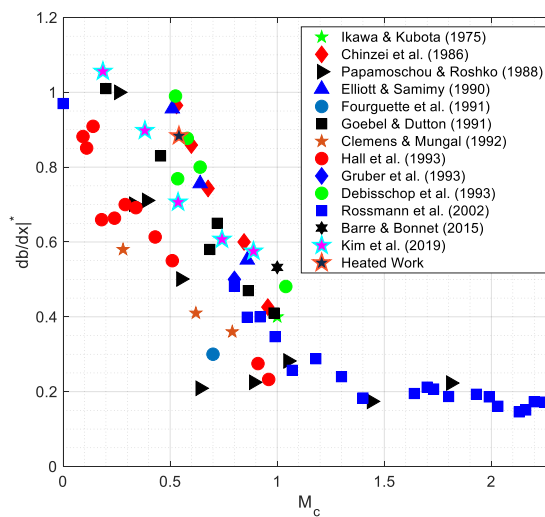


Figure 45. Normalized mixing layer growth rate versus M_c ^{39,40,3,41-46,10,6,13}

Analysis of self-similarity of the mean velocity profiles was also performed through the normalized velocity difference, $(U-U_2)/\Delta U$. Profiles of this quantity were made by plotting it against the normalized transverse coordinate η , which uses the local shear layer thickness and transverse centerline location y_0 in

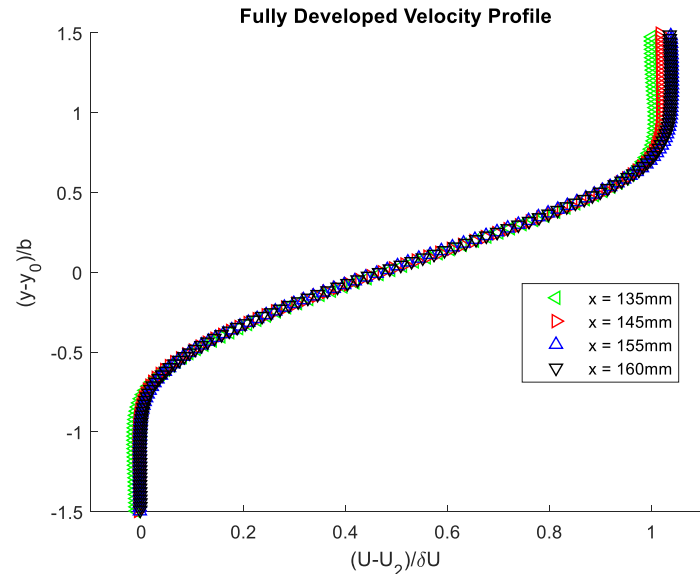


Figure 46. Fully Developed normalized mean velocity profiles

relation to the local mixing layer thickness b , and $\eta = (y-y_0)/b$. Plots showing these velocity profiles in the fully developed region of the flow are shown in Figure 46. A further plot showing the normalized velocity contours of $(U-U_2)/\Delta U$ is shown in Figure 47 plotted upon normalized η coordinates. Note that for the entire fully developed region, it remains flat and consistent throughout.

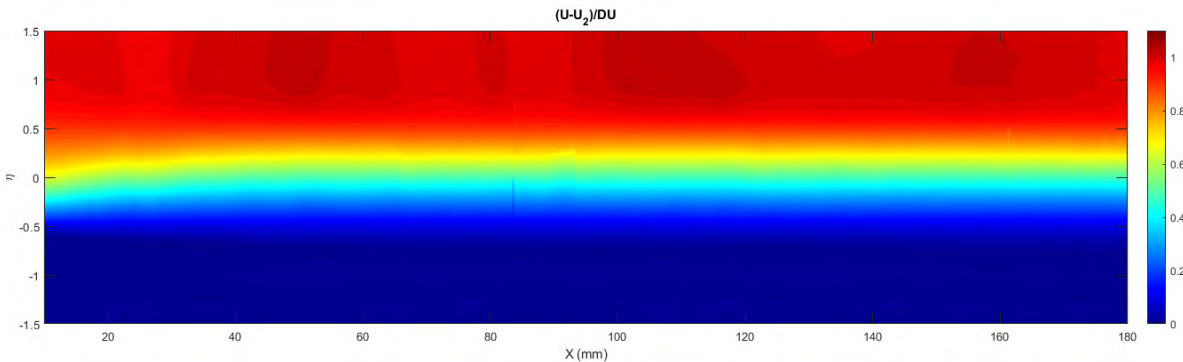


Figure 47. Normalized U contours in normalized transverse coordinates

Figure 46 in particular highlights how the mean velocity profiles collapse to the self-similar shape shown in the fully developed region; this is consistent with the findings of others for the shape of the self-similar mean velocity profile in the fully developed region of unheated mixing

layers, indicating that the stagnation temperature differential between the two streams does not have any major effect on the mean velocity profiles, normalized or non-normalized.

Fully developed turbulence within the mixing layer is critical; all statistical analyses will be drawn from this region. The self-similarity and linear growth of the mixing layer are two of the three criteria needed for the flow to be conventionally considered fully developed as per Mehta and Westphal's definition;⁴⁷ the third is self-similar Reynolds stress profiles, as will be discussed in the next section.

4.3.2 Statistical Results: Reynolds Stresses and Higher Moments

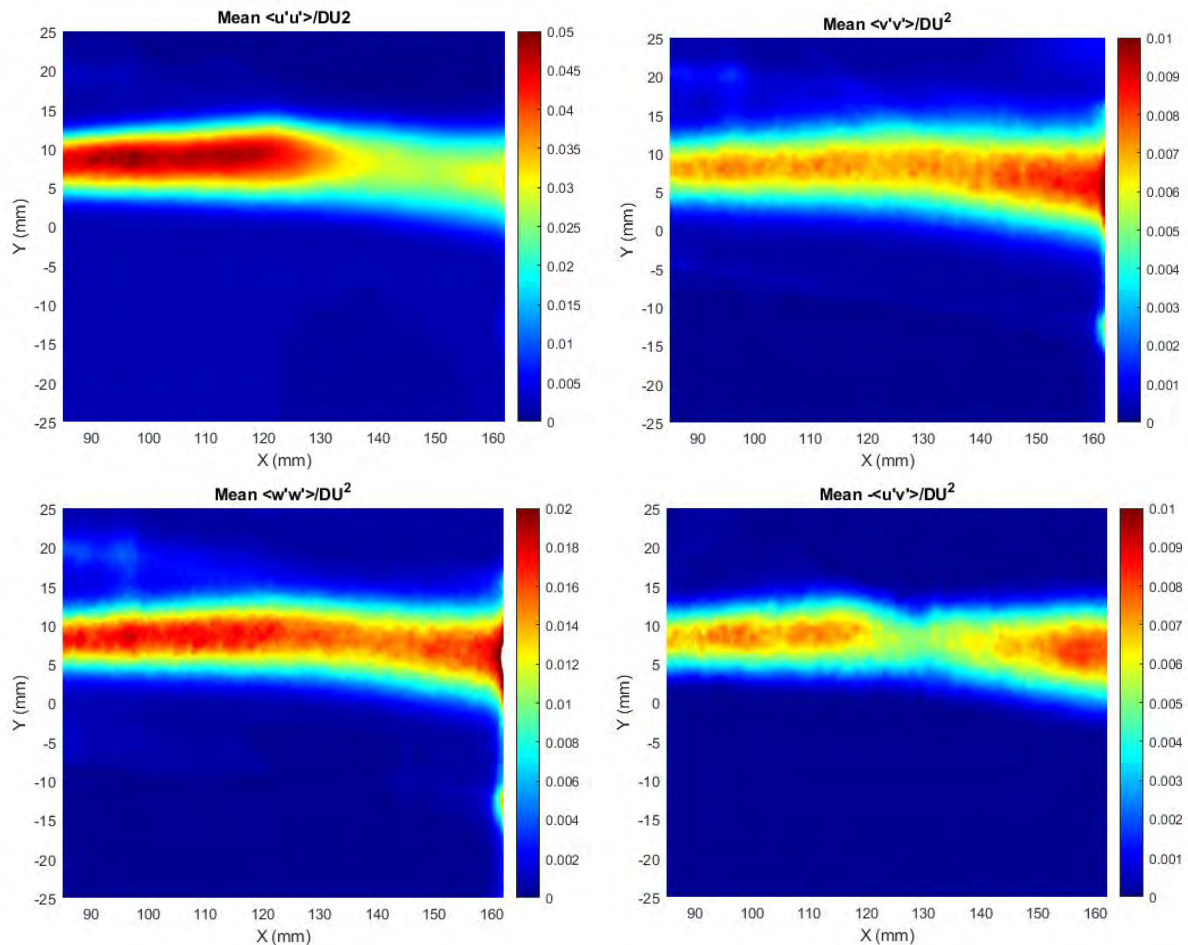


Figure 48. Contours of Reynolds stresses from the Fully Developed Region

Higher-order moments were also calculated using the complete ensembles of instantaneous velocity for each field of view. From these values, contours were plotted showing the Reynolds

stresses (i.e., second-order moments) for the region of interest; this is shown in Figure 48. From the contours, it appears that the stresses become self-similar around $x = 145$ mm. To confirm this, profiles were plotted at this point, and at nearby points prior to and after as well in order to show their convergence to self-similarity. These profiles, shown in Figure 49, confirm this finding.

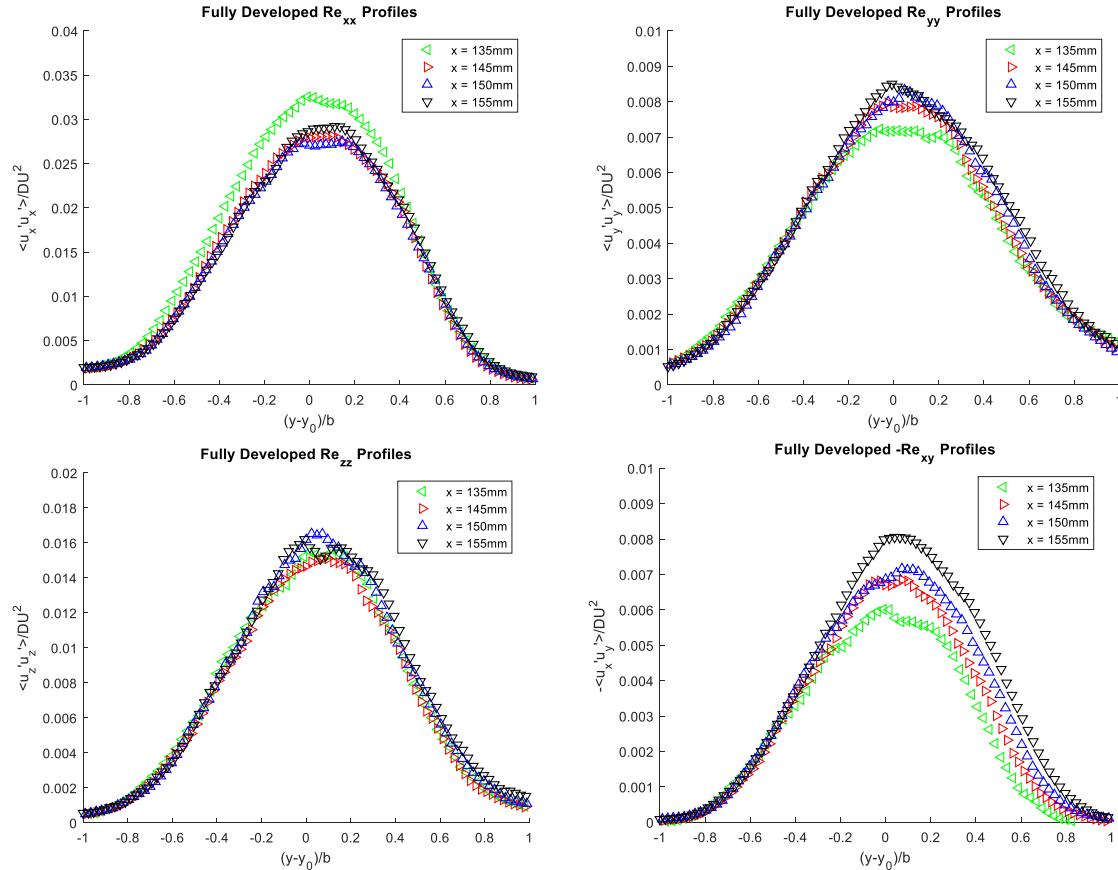


Figure 49. Reynolds stress profiles prior to and within the Fully Developed Region

Comparative profiles were also plotted showing the fully developed Reynolds stresses against those found by Kim for his similar operating conditions of Cases 3 and 4.^{13,14} These profiles, shown in Figure 50, indicate a clear similarity between the three experiments in terms of the Reynolds stresses. The largest deviation found is in the Re_{yy} profiles, where the peak for the current heated mixing layer drops off below either of the peaks Kim found. The other deviation of note is in the Re_{zz} profile; the current work sees its peak level off in between the two Kim cases.

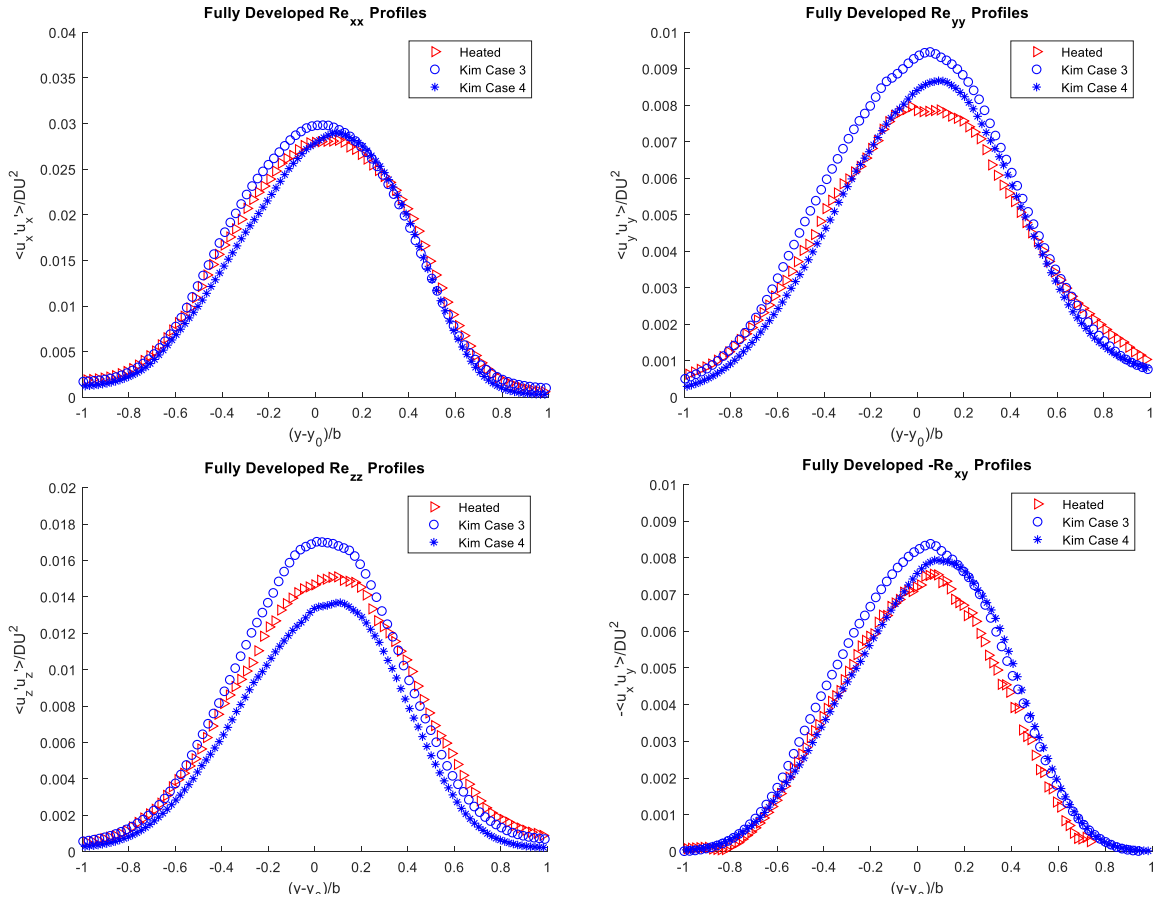


Figure 50. Comparison of Reynolds stresses in FDR with that of Cases 3 and 4 of Kim^{13,14}

These findings indicate that there may be weak effects from the thermal gradient on the turbulent mixing characteristics, which is not unexpected. When considering the schlieren results, the strong braid structures indicative of three-dimensional mixing (and therefore instantaneous deviations from the mean) were more strongly present in this case than Kim's Case 4 but less so than visually observed in Kim's Case 3.¹⁴ Likewise, the flatter mixing layer of the current case would indicate that variations would not have the same transverse distribution as the lower- M_c cases.

Further comparison of the peak Reynolds stresses in the fully developed region with respect to M_c is shown with data from the majority of previous, unheated, compressible mixing layer studies in Figure 51 on the next page. The peak values consistently match with previous trends

noted in the plots and are in particularly close agreement with the peak values from the previous unheated Case 3 mixing layer work of Kim at a very similar convective Mach number.

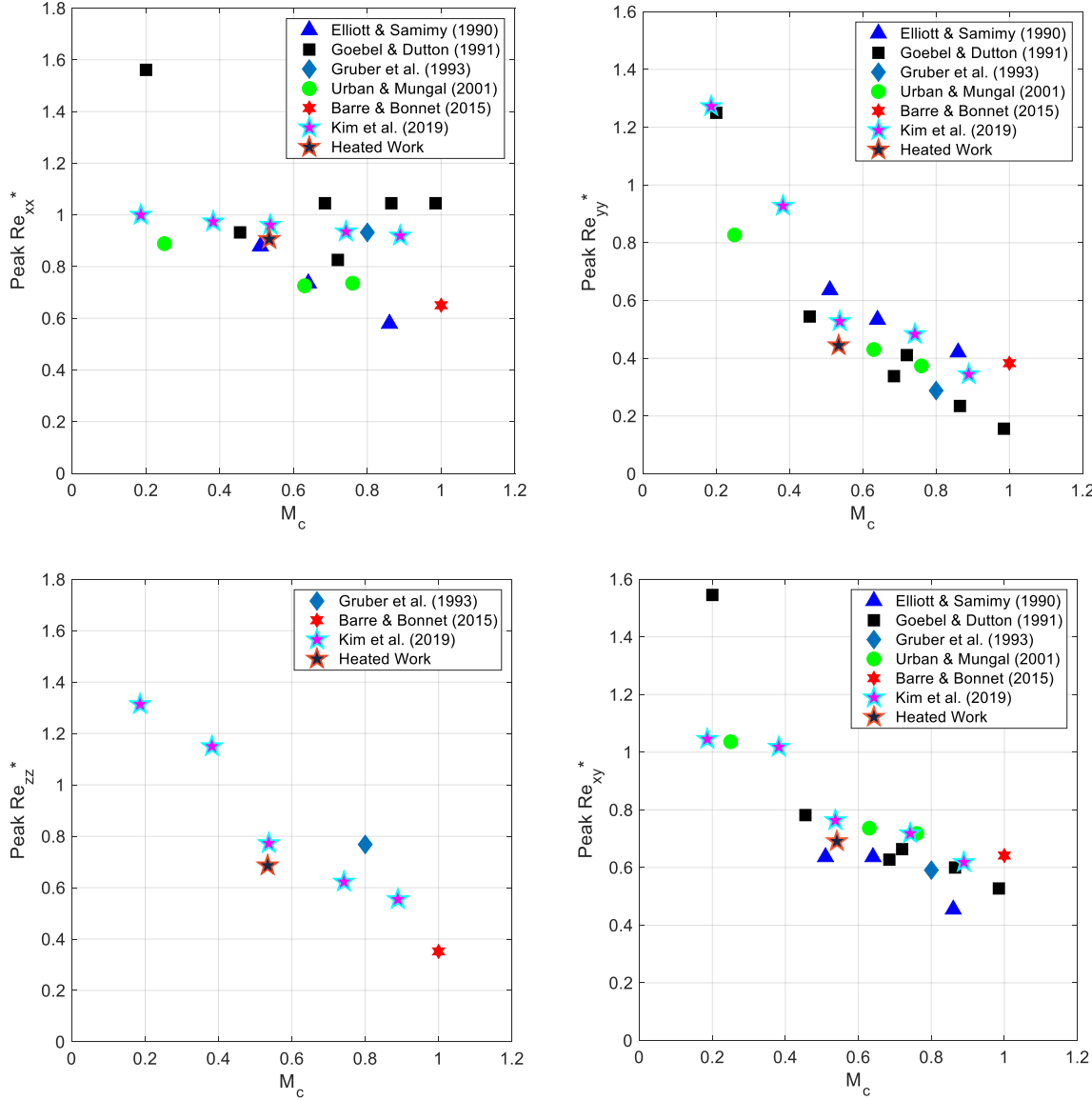


Figure 51. Peak Reynolds stress trends^{41,5,45,48,6,13}

In addition to the Reynolds stresses, it is typical in the computational studies that this experiment is intended to support to report the anisotropy tensor and turbulent kinetic energy (TKE). The anisotropy tensor gives indications as to how much the fluctuations of each velocity component contribute to the turbulence energy budget; it is used in certain studies to close the

averaged turbulence equations. Below, Equation (5) gives the equation for the Reynolds stress anisotropy tensor

$$c_{ij} = \frac{\bar{u}_i \bar{u}_j' - \delta_{ij}}{2k} \quad (5)$$

where c_{ij} is the anisotropy tensor, k is the turbulent kinetic energy, and δ_{ij} the Kronecker delta. Profiles of both anisotropy and the TKE within the fully developed region are plotted in Figure 52. The anisotropy tensor, plotted in normalized coordinates in the center of the mixing layer, $-0.5 < \eta < 0.5$, shows fairly constant values for each component through the fully developed region of the shear layer. In the same vein, the TKE profiles show self-similarity in the fully developed region as well as smooth Gaussian-like intensity distributions across the mixing layer. Both results are additional and sensitive indications that the flow has become fully developed at this point.

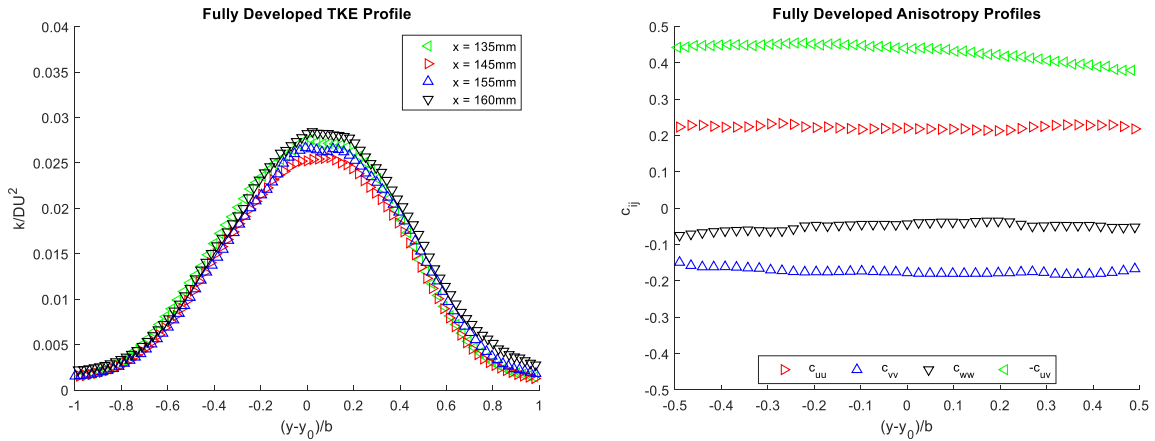


Figure 52. Fully Developed Region TKE and anisotropy profiles

With the large ensemble sizes available, it was also possible to compute triple products and fourth-order moments from the datasets. These higher-order statistical analyses give supporting insight into the fully developed region of the flow. Triple products are useful especially in computational studies that aim to study and model the Reynolds stress transport within the mixing layer. Normalized triple product similarity profiles in the fully developed region are plotted for the

u' , v' , and w' components in Figure 53 and Figure 54 on the following page. These all are essentially identical to those found by Kim in his comparable cases.¹⁴

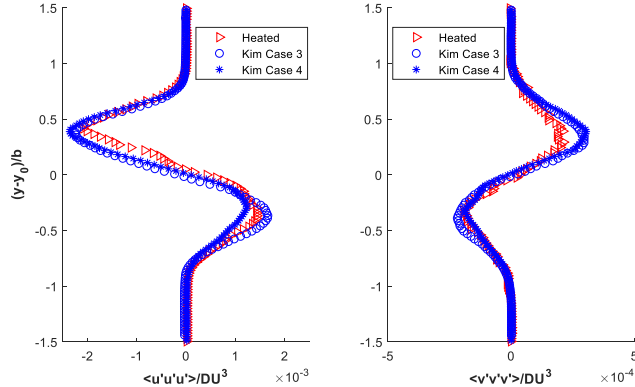


Figure 53. Normalized triple products compared with those of Kim^{13,14}

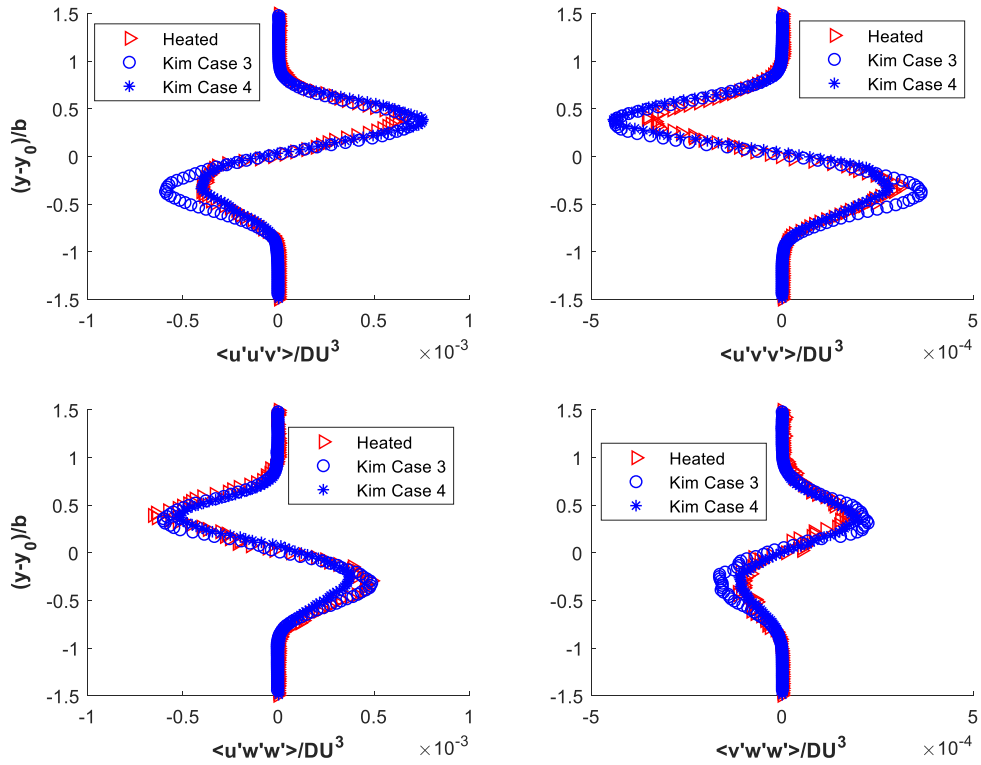


Figure 54. Comparison of normalized triple cross-products with Those of Kim^{13,14}

When the trends of the Reynolds stress tensor, particularly the dominance of the Re_{xx} component and its anisotropy are considered in tandem with the distribution of the triple products

against those found by Kim, the conclusion can be drawn that the thermal gradient of the present case has only minor effects on the turbulence within the mixing layer. This, however, stands in contrast with the moderately increased normalized growth rate; this could be attributed to the heating of the mixing layer but requires further research to make such a determination.

4.3.3 SPIV Uncertainty

The uncertainty in the stereo-PIV measurements was determined for the entire ensemble of all instantaneous images at each location. This uncertainty represents the linchpin in the dataset. For it to be used in its intended purpose as a CFD validation-quality dataset, the uncertainty must be quantified. A 95% confidence interval of the measurements is given for all data. Each instantaneous uncertainty field was first calculated for all three velocity components from what have been previously identified as the primary uncertainty sources: equipment, particle lag, and processing. Mean velocity and Reynolds stress uncertainties are then determined from the instantaneous uncertainties with respect to the statistical sampling error. The approach used here is based upon a standard procedure used in the UIUC Gas Dynamics Lab group, which itself is based upon the work by Lazar et al. and later extended by Hortensius.^{49,50}

The equipment error is primarily associated with the quality of the image scaling calibration in addition to the timing of the laser pulses. A pixel to real-space calibration, as discussed in Section 2.3.5, is determined using a dual-level calibration plate placed at a known location within the test section. This calibration plate, whose dimensions as well as marker size and spacing are known to the calibration routine in DaVis, has small uncertainty in its geometry. More important in the calibration is the image distortion due to this calibration, especially due to imperfect focusing of the camera lenses; minor effects are assumed due to aberrations of the calibration images themselves. Laser pulse timing error is due to the hardware limitations of the

delay pulse generator as well as accuracy of the laser system itself. Equipment error sources are all combined in a root-sum-square manner. Inputs to the equipment error terms are measured directly where possible, and all others are taken from the manufacturers' specifications.

The particle lag error, the difference in the measured particle velocity from the true fluid velocity, is inherent to any particle-based measurement method due to the myriad of forces acting on the individual particles (e.g. shocks, drag, gravity, buoyancy effects, etc.). For this case, all effects may be neglected with the exception of the Stokesian drag on the particles. A slip velocity due to the drag force that differs from the fluid velocity occurs, and may be calculated using a standard aerodynamic drag relation. Further assumptions are applied for the calculation of the drag force, as the lack of time-resolved data means that the particle acceleration is only able to be calculated from the spatial velocity field. To determine the drag coefficient C_d , Stokes' assumption $C_d = 24/Re_p$ is used as the initial value in an iterative scheme to find a value that is more accurate for Re_p that are not small. Details about this process can be found in Hortensius.⁴⁶

The third, and final, instantaneous error source considered is the processing error. This processing error is directly calculated in the DaVis software as it processes the instantaneous velocity fields. The method that DaVis uses to determine each field's processing uncertainty is a correlation-statistics approach described in Weineke (2015)⁵¹; it is the major difference in the present UIUC GDL approach from that of Lazar et al.⁴⁹

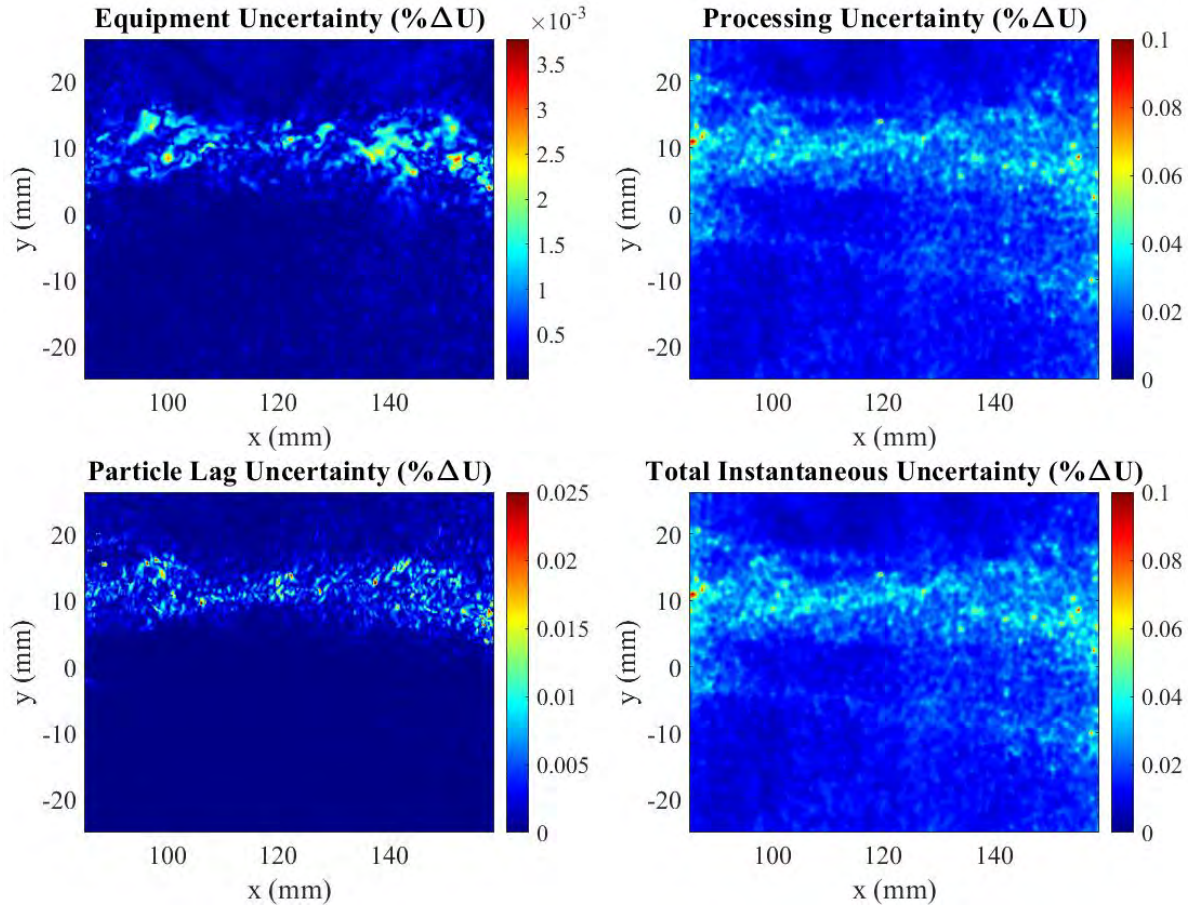


Figure 55. Instantaneous uncertainty for the *w*-component

Combination of the three instantaneous error sources is done in a root-sum-square sense to obtain the total instantaneous uncertainty for each velocity component at each measurement location. Examples of the instantaneous error for each source, as well as the combined error, are shown in Figure 55 for a typical *w*-component field. For this example, as well as for all the instantaneous fields, the processing error is the major contributor to the uncertainty and is found to be maximal in the mixing layer and at the edges of the field of view (due to laser sheet edge effects as well as camera lens distortion). This relative dominance is attributed to high-quality equipment and meticulous setup of the cameras, particles selected to have minimal slip with respect to the fluid, and oil/laser sheet effects on the image quality that are quantified in the processing error term.

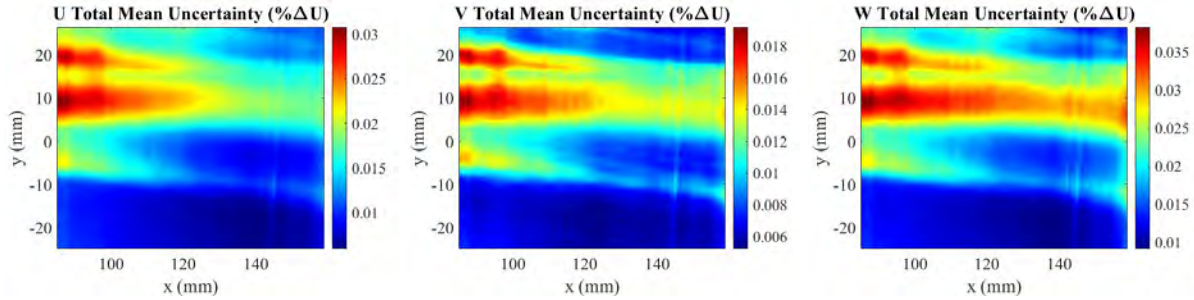


Figure 56. Mean uncertainty contours in FDR

Mean velocity uncertainty is calculated in a root-mean-square sense for the entire ensemble of each field of view. A statistical confidence term is added to this mean value, taken from the Student's t-test at 95% confidence where the finite ensemble size is used. These total mean velocity uncertainty fields normalized by ΔU are shown for each velocity component from the fully developed region in Figure 56.

From these, the W -component is seen to have the highest uncertainty value, although all three components have low uncertainty values for the measured fields of view, as they do not exceed more than 4% ΔU anywhere in the field of view. Here, it remains clear that the mixing layer is the locale of highest uncertainty in the measurements, although it stays well within acceptable bounds of uncertainty for the data's intended use for CFD validation.

CHAPTER 5: TEMPERATURE FIELD MEASUREMENTS IN A COMPRESSIBLE MIXING LAYER WITH A THERMAL GRADIENT

5.1 Filtered Rayleigh Scattering Implementation

5.1.1 Initial Parameters

This study utilizes Filtered Rayleigh Scattering (FRS) in order to measure the mean static temperature profiles in the heated shear layer. FRS was chosen as the primary thermometry method out of other possible approaches largely due to its ability to resolve temperature fields even in a dirty, particulate-laden environment. As a result of the PIV studies previously performed in the tunnel, as well as in this work, it was necessary to utilize a method that would not require a clean environment for measurement. The power of FRS, particularly its particle-filtering ability, is best illustrated in Figure 28 of Section 2.3.6. In this work, FRS was used to determine the static temperature, using previous mean measurements of pressure and velocity to assist processing.

These measurements of static temperature, as Section 1.2.1 discusses, are based on Rayleigh scattering from air molecules in the flow; to determine these quantitative measurements from the FRS signal, several parameters were separately experimentally determined. These preliminary parameters are intrinsic to the equation that determines the thermodynamic state of the molecule from the signal on each pixel in the camera sensor. The equations relating the behavior of the normalized filtered signal to the pressure and temperature of the air are defined in Section 1.2.1; they are summarized by Equations (3) and (8), which are restated below for clarity.

$$S = C \left[\int_{-\infty}^{\infty} R_{gas} t(f) df + \int_{-\infty}^{\infty} R_{bg} t(f) df \right] \quad (3)$$

$$\frac{S(f)}{S_{ref}(f)} = \frac{T_{ref}}{T} \frac{P}{P_{ref}} \quad (8)$$

From these equations, there are four major values of interest: the combined scattered signal from the background R_{bg} which is assumed an individual constant for each field of view, the

transmission function of the iodine cell $t(f)$, the filtered reference flatfield signal $S_{ref}(f)$, and the flow's filtered signal $S(f')$. Respectively, these correspond to the background scattering picked up by the camera system, the iodine cell absorption for a given frequency, the scattering for an ambient reference state, and the scattering from the flow and thermodynamic state of the case of interest.

Given the four parameters of interest, three of the four (the background signal, reference signal, and flow signal) are obtained *in situ*; the reference flatfield signal is obtained prior to each run of the experiment and normalizes the corresponding flow-on signal. The background signal, since it may be assumed to be constant for each field of view, is considered a dark count value on the sensor as a subtracted per-pixel value from the flatfield and flow-on images. The flow signal is simply acquired by recording the images for the flow-on condition. The fourth parameter, the transmission of the iodine cell, is not obtained *in situ* and rather requires an external calibration across the operating frequency range of the laser.

5.1.2 Iodine Cell Calibration

Figure 57 on the next page gives the schematic of the optical set-up that measures the transmission profile $t(f)$ of the iodine absorption filter. This schematic differs from the conceptual schematic for experimental data collection shown in Figure 22 of Section 2.3.6 by moving the iodine cell in front of the third photodiode (PD 3 in the schematic). In doing so, the transmission of the iodine cells may be determined by normalizing the response of the experimental cell photodiode by the signal received by the first photodiode (PD 1). It is also noted that absorptive neutral density filters were used to equilibrate the amount of laser power incoming on the three photodiodes prior to the inclusion of the iodine cells. This frequency trace had two purposes:

primarily, to fully define the transmission profile of the experimental and reference iodine cell; secondarily, to determine the operating frequency range of the laser.

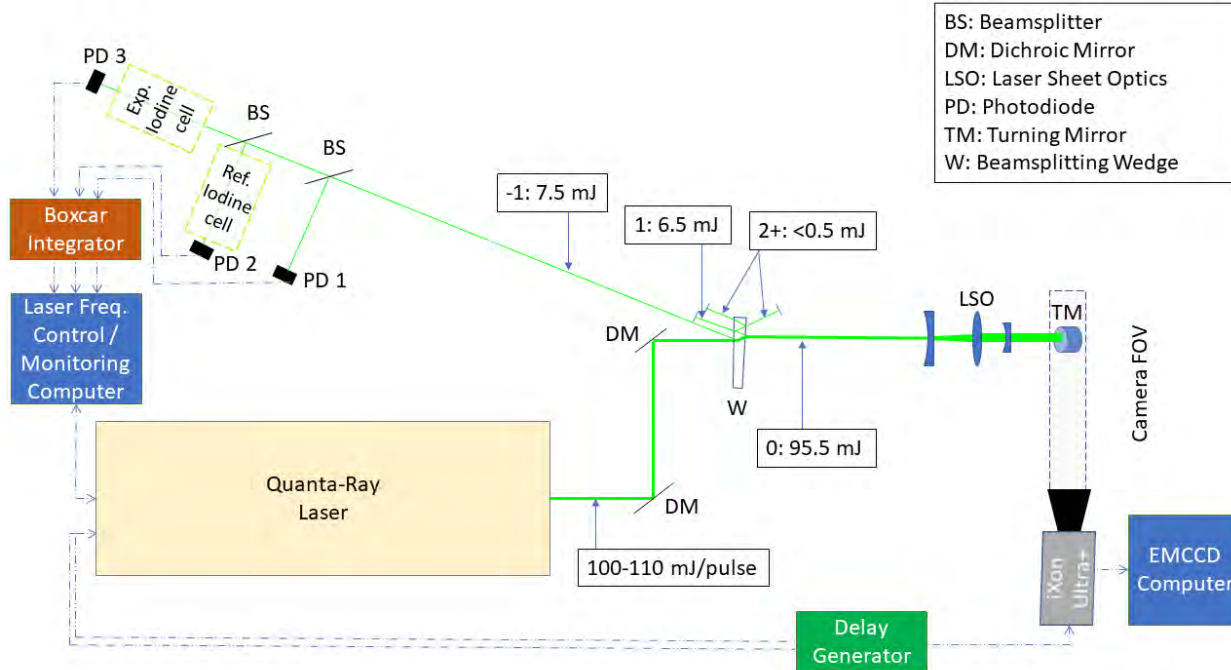


Figure 57. FRS conceptual schematic for iodine cell calibration

Once the profiles had been determined for both cells, they were compared to a computed profile using the model of Forkey et al. (1997), as shown in Figure 27 of Section 2.3.6.³⁵ The experimental iodine cell profile shows a good match to that of the computed model, especially along the absorption line at 18788.435 cm^{-1} . This absorption line has good absorption characteristics as well; it has a minimum transmission of less than 0.02% through the experimental cell. For the reference cell, there is a small amount transmitted, approximately 3.5%, since the number density, and therefore partial pressure of iodine, is less. While it may seem to be a downside, this actually turns out to be a benefit—it increases its sensitivity to how well the laser frequency matches to the desired value.

From the iodine cell transmission curve, it was determined that the operating range of the laser was from a wavenumber of 18789.318 to 18788.002 cm^{-1} , which included the fine absorption

line centered at 18788.435 cm^{-1} . This absorption line was chosen for two primary reasons: first, it resolved well in the reference cell as well, giving the ability to perform multiple-frequency observations if so desired; and second, it is wider and absorbs more than the other absorption line at 18788.74 cm^{-1} . Since the absorption profile is wider here, it is less susceptible to scattering from particles that experienced a Doppler shift relative to the laser frequency. This effect is illustrated in Figure 28 of Section 2.3.6, showing a comparison of a reference image taken at the two frequencies with otherwise similar settings. There are many more particles visible through the filter at the higher wavenumber; these decrease the quality of the instantaneous images and also present a risk in damaging the image sensor over time.

5.1.3 Imaging System and Laser Sheet Parameters

The imaging system and laser sheet were setup with the primary goal of measuring the temperature profile across the heated compressible shear layer and to obtain information about the development of the temperature profiles as the thermal shear layer grows downstream. An Andor iXon+ EMCCD camera was utilized with a seeded Spectra-Physics Quanta-Ray GCR-230 laser, due to the high quantum efficiency of the camera at the frequency doubled wavelength of the laser. This camera, with its quantum efficiency of over 95% at 532 nm, was a far superior option to less efficient cameras, even given its lower resolution (512x512 pixels).

The Quanta-Ray laser was tuned to maximize the power output under full oscillator, with no amplifier applied. Timing between the laser and camera was controlled by an external delay generator. The laser sheet itself was collimated to remain as thin as possible and to keep the intensity of the laser sheet constant across the shear layer and freestreams. This gave a usable width across the laser sheet of approximately 14 mm with the lower intensity edges of the width discarded; the burn



Figure 58.
Laser sheet
burn for
FRS

paper image of Figure 58 on the previous page illustrates this energy distribution across the laser sheet. Because of space limitations, all measurements made beyond 85 mm in the x - direction required an additional “periscoping” assembly of two mirrors, moving the laser sheet further down the test section. This proved to be a stable and highly flexible method of adjusting the position of the laser sheet for the downstream temperature measurements.

The camera itself was side-mounted to a Newport Optics linear stage, allowing it to be moved along the length of the test section at a constant distance, greatly reducing the time spent focusing the lens and also keeping the range of the field of view relatively constant between positions. The iodine filter was also mounted to a linear stage, allowing for minor adjustments to be made, reducing the effects of imperfections and inconsistencies through the filter. The camera sensor was cooled to -20°C to reduce noise; the camera sensor voltage was overclocked in order to reduce a vertical blind effect that occurred at the high framerate required of the system due to the high gain levels required to resolve the Rayleigh scattering signal.

5.1.4 Image Processing and Temperature Calculation

Below is a summary of the image collection process:

- For each field of view, a calibration image was taken using a LaVision calibration plate and physical calibration obtained using the DaVis software.
- Three sets of images were captured: a laser-off background (dark count) image, a laser-on flatfield (reference) image, and a flowfield image using the Andor SOLIS software.
 - The background and flatfield images were taken at ambient temperature and pressure and with no flow in the test section; the flowfield image was taken with the tunnel at its full operating condition.

- These images were all taken at the same camera gain, exposure time, and aperture settings; one hundred image frames were averaged to form the background and flatfield, and twelve hundred frames were recorded for the flowfield images.
- The flowfield images were taken in two sets of six hundred images each, in order to maximize the amount of time spent near the goal stagnation temperature condition of 495 K, as well as to stay within the RAM limitations of the imaging computer.
- For all images, the conditions in the wind tunnel test section, primarily the stagnation temperatures of the two streams, were saved, as well as the laser BURT voltage for the shot (for more on BURT, refer to Section 2.3.6).
- The two flowfield image sets were saved as 16-bit Tagged Image File Format (TIFF) images as well as in the Princeton Instruments SPE image file format.

Once the image data had been saved, it was transferred from the imaging computer to a secure cloud server. The images were then accessed by a custom MATLAB code that loaded in the SPE file, applied a physical calibration to the images, and sorted out images that were outside of the intensity range, indicating the laser frequency had unlocked. The images were then processed using the method below:

- The averaged background (dark count) image was subtracted from the averaged flatfield and each instantaneous flowfield image.
- The mean of the instantaneous flowfield images was calculated. The portion of the image that was not illuminated by the laser sheet was used to determine an average intensity value. This was then compared against the average value of the same non-illuminated area in the flatfield image outside of the laser sheet range. This difference was applied to the flatfield image to

correct for disparities between the shots (particularly variations in camera gain or laser power over the course of the run).

- A Rayleigh signal library is calculated for the run. This library is calculated based on the target locked frequency of the laser, known velocity range from the stereo-PIV results, and static pressure measurements. It also utilizes the stagnation temperatures of the facility to determine the upper and lower bounds of the temperature range: fifty degrees K above/below the maximum/minimum static temperature in the freestreams. This library is ultimately a two-dimensional table giving the signal as a function of temperature and velocity, as discussed in Section 1.2.1. A sample signal library is shown in Figure 3.

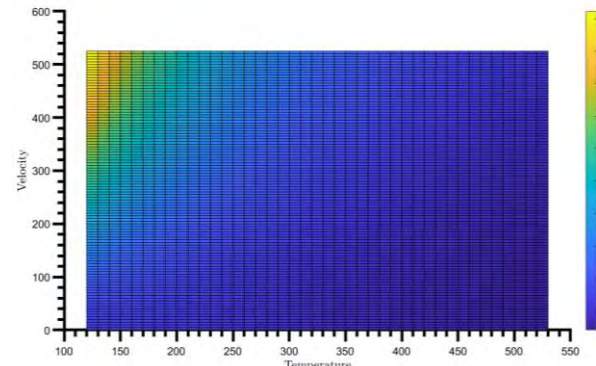


Figure 59. Example FRS signal intensity library

- Using the average stagnation temperature in the primary and secondary streams, as well as the average velocity from the PIV data, the average FRS signal for the freestreams was determined from the signal library using the Tenti formulation²⁰ and assuming an air composition of 79% nitrogen and 21% oxygen. This signal was then compared to the library signal and normalized image signal; this comparison formed a linear fit to adjust the signal library to fit the range of values found in the image.
- The temperature at each pixel in the normalized flowfield image is then calculated:
 - The velocity for the pixel is determined using the physical calibration of the image and the velocity data from the stereo-PIV.

- The temperature is then determined by using the MATLAB find function, to find the index within the signal library row of that pixel's velocity that is the nearest match between the adjusted signal library value and the intensity of the pixel in the image.
- The entire temperature field is plotted, as well as a temperature trace for the mean value at each transverse location. The thickness and height of the thermal mixing layer is then computed from the location of the two thermal freestreams using the 90% ΔT definition (similar to the method used for calculating the velocity shear layer thickness discussed in Section 3.3.2).

5.1.5 Challenges with FRS

The primary challenges implementing the Filtered Rayleigh Scattering measurements stemmed from the lack of a true background correction. The background correction, which came in two parts in this work (changing the flatfield non-signal area to have the same value as the flowfield, and scaling the signal values in the freestreams), were alternatives from the methods typically seen in the literature^{18,22-33,48} where the background is calculated from a vacuum or very low-density environment with the laser sheet present in the image. However, physical limitations related to the mixing layer facility itself meant that the Rayleigh signal background could not be determined in this manner or in a similar one. The background images in this work are correcting for the background signal from the room lights and associated with the camera not the effects of the entire imaging system and laser sheet. Compounding this difficulty, the vibrational environment encountered by the laser while running the wind tunnel led to unlock from the desired frequency far more often than in normal operation. While these vibrations did not affect the laser sheet itself, it did of course reduce the number of useable images in a run and therefore decreased the ensemble size by an appreciable amount. Furthermore, this behavior precluded the multiple-

frequency approach to taking the data, because the frequency variations are random and would have greatly limited the number of usable images per frequency.

5.2 FRS Temperature Results

5.2.1 Mean Temperature Trace Results

Mean temperature profiles were calculated for four streamwise positions, at $x = 33, 89, 128$, and 182 mm, approximately evenly spaced through the test section. In particular, the final two positions were intended to verify the FRS temperature results and provide a temperature trace within

the portion of the mixing layer that is fully developed in turbulence. These raw temperature profiles are shown in Figure 60; they can be seen to exhibit a nearly linear gradient in temperature across the shear layer, with the exception of the noisier trace taken at $x = 89$ mm. As with the temperature probe traverses, the temperature profiles are best visualized in a normalized form between the freestream static temperatures, and plotted on an η -coordinate calculated using the previously discussed 10% ΔT formulation. These normalized profiles may be viewed in Figure 61. From the normalized profiles it is quite clear that after a streamwise distance of 89 mm the profiles collapse upon one another. This corresponds with the behavior

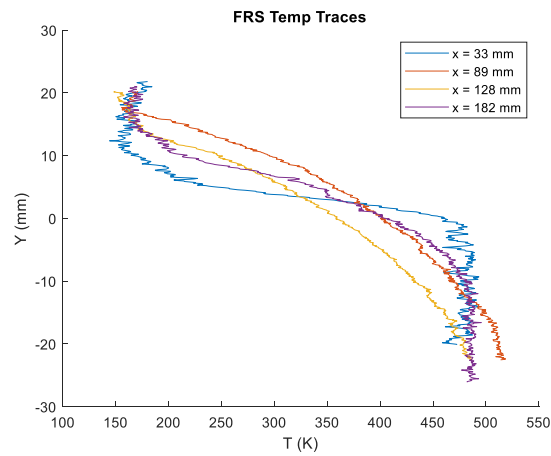


Figure 60. FRS mean static temperature profiles

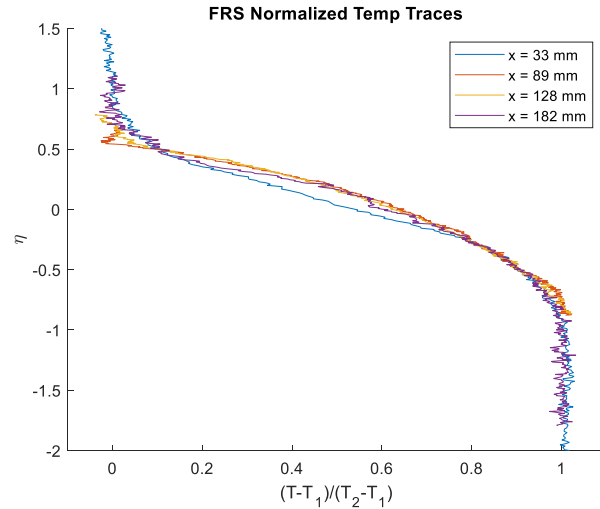


Figure 61. FRS normalized static temperature profiles

of the normalized traces from the temperature probe traverses. Furthermore, it should be noted that the thermally fully developed region begins even sooner than indicated from the temperature probe data. While there is noise in the data, self-similarity is extremely strong evidence to show that the flow is thermally developed by a streamwise position of at least 89 mm.

However, the overall quality of the temperature profiles appears to be poorer than what is possible when compared to the literature. Although the temperature profiles are found to be consistent with the probe measurements, due to the heavy assumptions required and difficulties associated with the experimental setup, the results are more qualitative than quantitative. The large amount of noise in the thermal freestreams is indicative that further work is necessary to improve the results, particularly to resolve the instantaneous profiles not shown here, due to their high level of noise which is smoothed out by the averaging process.

5.2.2 FRS Temperature Fields

Additional information may be gleaned from the two-dimensional temperature fields measured using FRS. The noise inherent to the measurement can have a major effect, and is most noticeable in the initial temperature field obtained between $x = 29$ to 35 mm, shown in Figure 62.

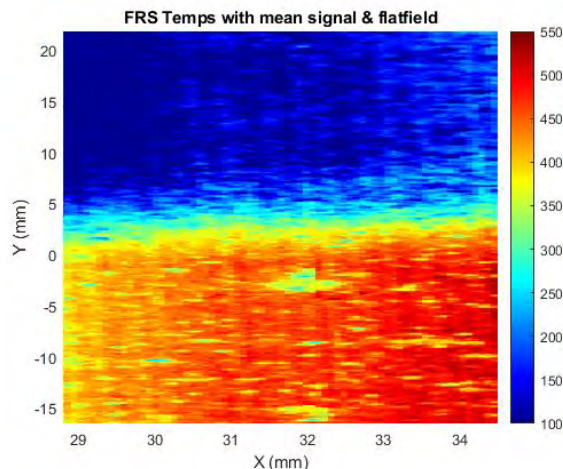


Figure 62. Early FRS temperature field result
show the effects of other noise sources in a few of the images. Even though the more aggressively

The cold spots as calculated from the processing are caused by particles that were not fully filtered by the iodine cell. From this regard it is clear that more preprocessing is necessary in order to better filter out such “hot spots” in the flowfield image stack. The temperature fields with a more stringent filter may be seen in Figure 63; they still

preprocessed temperature fields do not suffer from particle noise in the freestreams, their overall quality may still be improved from a more sophisticated method, such as the one proposed by

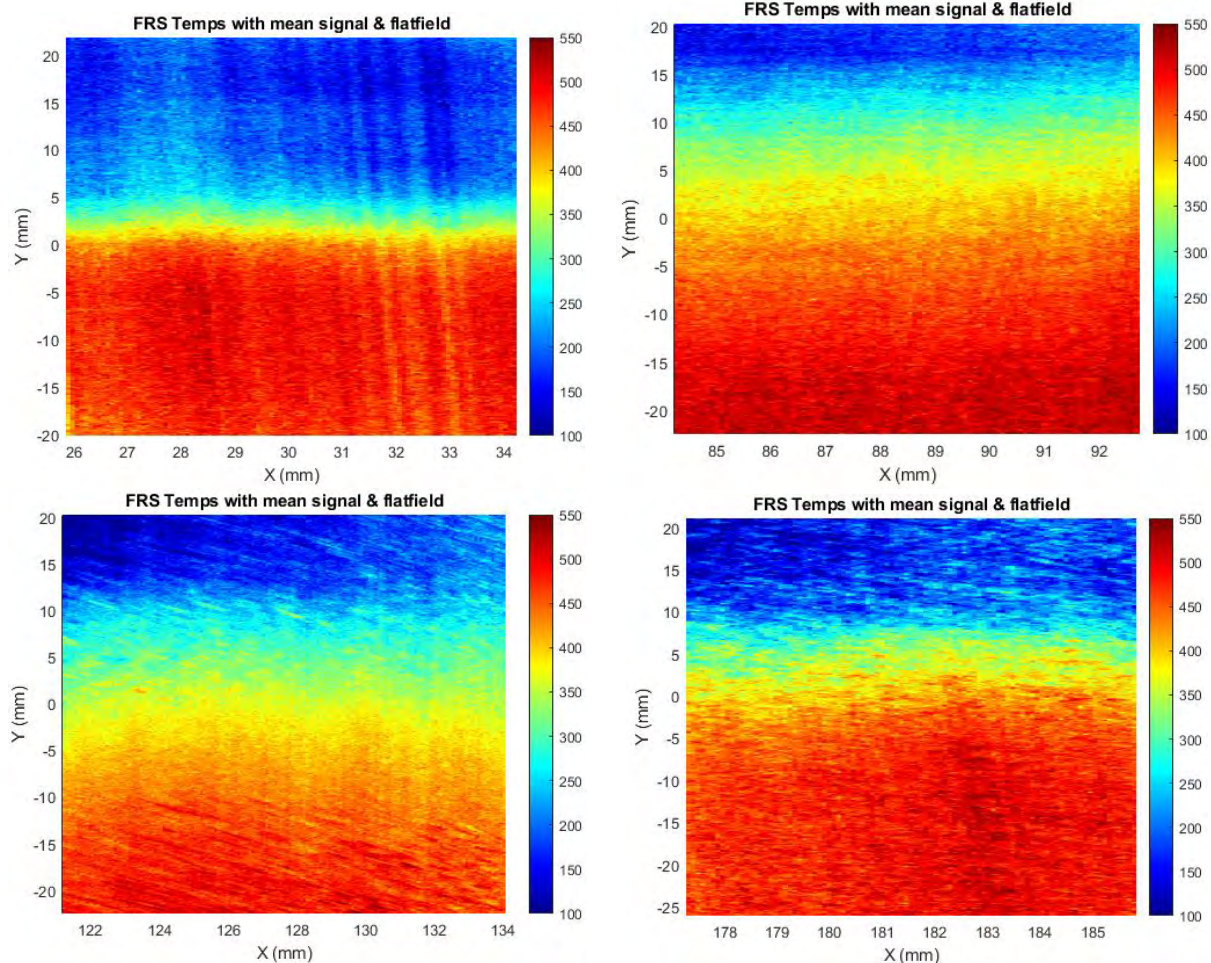


Figure 63. Filtered Rayleigh Scattering temperature field results

McManus and Sutton using a standard deviation rule to find particle-laden images.³³

Even as the temperature fields have the aforementioned shortcomings, they still show the general behavior of the thermal shear layer at the different streamwise measurement areas along the test section. The fields represent a temperature distribution that logically makes sense across the shear layer and into the freestreams; however, there is not the expected consistency in the mean locations of the shear layer boundaries with the freestreams. This shortcoming is further illustrated by plotting the shear layer growth rate as computed from the traces and mean fields in Figure 64

on the next page. From the temperature fields, a general widening trend across the mixing layer seems to occur from field-to-field; however, it is fairly difficult to discern individually in each field as a result of the noise in resolving the shear layer itself and general uncertainty with respect to the data. This lack of a distinct growth rate trend across each temperature field, and general lack of a consistently linear growth rate from field to field, indicates that the noise across the shear layer is a major area for improvement. However, the mean trend from each field shows that the growth rate can be generally trusted, especially once a line of best fit is plotted. In addition to this weakness, the unevenness of the thermal shear layer as determined through the FRS fields is far more likely to be a negative effect of the experimental setup, rather than a physical one. The diagonal hot/cold lines in the fields are further evidence to this end; they are attributed to inconsistencies in the laser shots, and possibly even minor laser sheet blockages on the bottom incoming window, due to accumulation of oil or other detritus during a test run. Overall, these limitations are not considered to be so much as to wash out the new information given by the mean FRS results, but it is still recommended to utilize the mean TAT probe-trace results prior to the FRS fields.

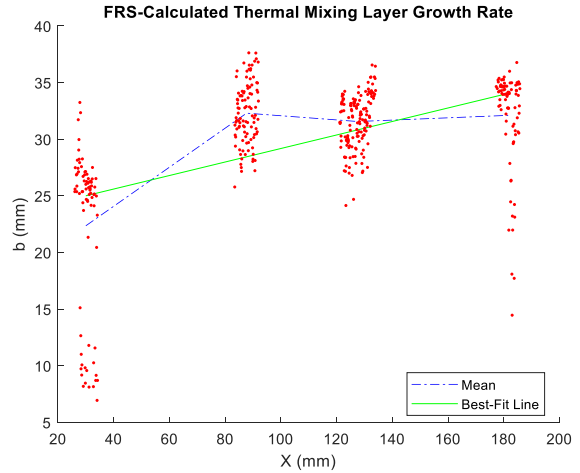


Figure 64. Thermal mixing layer growth rate trend

CHAPTER 6: CONCLUSION

6.1 Summary of Work and Concluding Remarks

This thesis serves to investigate a compressible shear layer with a thermal gradient between the two streams with the goal of obtaining CFD-validation quality temperature and velocity data. The dual-stream wind tunnel facility was modified from its original design in order to incorporate the addition of a heater capable of providing the requisite stagnation temperature in one of the two streams. Supporting measurements in order to qualitatively analyze the flow, including high-speed schlieren videos and static pressure measurements along the sidewall of the tunnel; these provided insights into the shear layer's development. Stereo-PIV results found that the statistical measurements in the compressible mixing layer, including that of the mean velocity profiles, entire Reynolds stress tensor including its anisotropy trends, and triple products, proved consistent with the literature, even though previous works were acquired using ambient stagnation temperature environments for both streams. At the same time, the stereo-PIV indicated a higher shear layer growth rate than for recent experiments at similar convective Mach numbers in the same facility. Stagnation temperature probe profiles were obtained at certain streamwise locations, including in the fully turbulently developed region, indicating the thermal mixing layer may become fully developed well before the turbulent mixing layer. Finally, Filtered Rayleigh Scattering was utilized to successfully capture the temperature fields at specific locations in the mixing layer as well as the freestreams, a first for non-reacting compressible shear layers with a stagnation temperature difference between the two streams. While the FRS temperature field results indicate that there may remain areas for improvement in the temperature determination, it is data of high enough quality to provide a starting point for future research in the field.

6.2 Future Work and Recommendations

This work, while certainly a strong starting point for the direct investigation of temperature mixing in shear layers, remains just that: a starting point. The velocity measurements from the stereo-PIV experiments represent a high-resolution, low-uncertainty dataset that certainly can be of immediate use in CFD validation. Furthermore, the schlieren visualizations, especially the high-speed movies, are quite useful for qualitatively examining the shear layer and provide an underpinning for deeper investigation of the current work. However, both the temperature data from both the Filtered Rayleigh Scattering as well as the total temperature probe traverses appear to need further refinement and examination.

While the mean accuracy of the FRS profiles appears to be correct, the fields show that continued work on their processing could provide better results—and quite possibly deeper insights than just the qualitative trend of the mean transverse temperature profile. On the other hand, the uncertainty of the total temperature probe traverses is quite low—however, they were only conducted for a few streamwise positions, and therefore are unable to offer the kind of spatial resolution needed to determine where the flow becomes fully thermally developed. While the Filtered Rayleigh Scattering data has the capability of a much larger field of view and therefore a much larger field of temperature results, it is still fairly limited by both the laser power density in the sheet as well as the camera resolution limitations. An improved experimental setup, especially FRS results performed at a higher laser power spread over a longer (in streamwise length) laser sheet (therefore corresponding to a similar power density in the sheet as the current experiments), would greatly improve the *utility* of the FRS approach. In doing so, analyses similar to those employed on the mean PIV data would be within reach. The other current limitation of both the FRS and temperature probe data is the lack of instantaneous temperature fields or even profiles.

While sustained analysis of the FRS data may put instantaneous results within reach, the temperature probe traverses by their nature are unable to take such instantaneous data. This limitation of the temperature probe indicates that moving forward, Filtered Rayleigh Scattering should be further developed with a focus on reducing uncertainty and experimental difficulties so that it can be reliably utilized for temperature measurements.

For future measurements of the shear layer, the most compelling result is computing the density from the FRS measurements to then determine the mass entrainment of the shear layer itself. While density is possible to be computed from merely the temperature and then using the static pressures in the flow (which have been shown to be essentially equal to one another and constant throughout) with the ideal gas law, an analysis of that type should likely utilize the multiple-property approach of FRS, be it FARRS or otherwise. Even if the processing is simplified by using an alternate method of computing the velocity, such as from PIV, it still would provide a marked improvement over using the single-property measurement approach. These density measurements could then be combined with an entrainment analysis similar to that employed by Kim¹⁴; his work specifically lacked such information and would have been greatly assisted in that respect. Of course, in order to use a multiple-property approach, refinements to the laser frequency control scheme are necessary, such that the laser frequency for each shot is well-known and not as affected by the highly vibrational environment induced by running the shear layer facility. The solution of these issues, then, is the clear next step in improving the understanding of a heated compressible shear layer.

REFERENCES

- ¹Brown, G.L. and Roshko, A., “On Density Effects and Large Structures in Turbulent Mixing Layers,” *Journal of Fluid Mechanics*, Vol. 64, 1974, pp. 774-816.
- ²Bogdonoff, D.W., “Compressibility Effects in Turbulent Shear Layers,” *AIAA Journal*, Vol. 21, No. 6, 1983, pp. 926–927.
- ³Papamoschou, D. and Roshko, A., “The compressible turbulent shear layer: an experimental study,” *Journal of Fluid Mechanics*, Vol. 197, 1988, pp. 453–477.
- ⁴Sabin, C. M., “An analytical and experimental study of the plane, incompressible, turbulent free-shear layer with arbitrary velocity ratio and pressure gradient,” *Trans. A.S.M.E.*, D 87, No. 421, 1965.
- ⁵Goebel, S. G. and Dutton, J. C., “Experimental Study of Compressible Turbulent Mixing Layers,” *AIAA Journal*, Vol. 29, No. 4, 1991, pp. 538–546.
- ⁶Barre, S. and Bonnet, J. P., “Detailed experimental study of a highly compressible supersonic turbulent plane mixing layer and comparison with most recent DNS results: “Towards an accurate description of compressibility effects in supersonic free shear flows,” *International Journal of Heat and Fluid Flow*, Vol. 51, 2015, pp. 324–334.
- ⁷Kim, K. U., Elliott, G. S., and Dutton, J.C., “A Three-Dimensional Experimental Study of Compressibility Effects on Turbulent Free Shear Layers,” *2018 Fluid Dynamics Conference*, AIAA Paper 2018-3864, 25-29 June 2018.
- ⁸Ghodke, C., Choi, J., Srinivasan, S., Menon, S., “Large Eddy Simulation of Supersonic Combustion in a Cavity-Strut Flameholder”, *49th AIAA Aerospace Sciences Meeting*, AIAA Paper 2011-0323, 4–7 Jan. 2011.
- ⁹Grady, N. R., Pitz, R. W., Carter, C. D., Hsu, K., Ghodke, C., Menon, S., “Supersonic Flow over a Ramped-Wall Cavity Flame Holder with an Upstream Strut,” *Journal of Propulsion and Power*, Vol. 28, 2012, pp. 982-990.
- ¹⁰Rossmann, T., Mungal, M. G., and Hanson, R. K., “Evolution and growth of large-scale structures in high compressibility mixing layers,” *Journal of Turbulence*, Vol. 3, No. 9, 2002, pp. 1–18.
- ¹¹Abraham, J., Magi, V., “Exploring Velocity and Density Ratio Effects in a Mixing Layer Using DNS,” *International Journal of Computational Fluid Dynamics*, Vol. 8, No. 2, 1999, pp. 147-151.
- ¹²Zhang, Y., Wang, B., Zhang, H., Xue, S., “Mixing enhancement of compressible planar mixing layer impinged by oblique shock waves,” *Journal of Propulsion and Power*, Vol. 31, No. 1, 2015, pp. 156-169.
- ¹³Kim, K. U., Elliott, G. S., and Dutton, J.C., “Three Dimensional Experimental Study of Compressibility Effects on Turbulent Free Shear Layers,” *AIAA Journal*, Vol. 58, No. 1, 2020, pp. 133-147.
- ¹⁴Kim, K., “Compressibility Effects on Large-Scale Structures and Entrainment in Turbulent Planar Mixing Layers,” Ph.D. Thesis, Dept. of Aerospace Engineering, University of Illinois, Urbana, IL, 2020.
- ¹⁵Kim, K. U., Elliott, G. S., and Dutton, J.C., “Compressibility Effects on Large Structures and Entrainment Length Scales in Mixing Layers,” *AIAA Journal*, Vol. 58, No. 12, 2020, pp. 5168-5182.

- ¹⁶Freund, J. B., Lele, S. K., and Moin, P., "Compressibility effects in a turbulent annular mixing layer. Part 1. Turbulence and growth rate," *Journal of Fluid Mechanics*, Vol. 421, 2000, pp. 229–267.
- ¹⁷Pantano, C. and Sarkar, S., "A study of compressibility effects in the high-speed turbulent shear layer using direct simulation," *Journal of Fluid Mechanics*, Vol. 451, 2002, pp. 329–371.
- ¹⁸Forkey, J. N., Finkelstein, N.D., Lempert, W.R., Miles, R.B., "Demonstration and Characterization of Filtered Rayleigh Scattering for Planar Velocity Measurements," *AIAA Journal*, Vol. 34, No. 3, 1996, pp. 442-448.
- ¹⁹Shardanand and Rao, A.D.P., "Absolute Rayleigh Scattering cross sections of gases and freons of stratospheric interest in the visible and ultraviolet regions," NASA TN-D-8442, March 1977.
- ²⁰Tenti, G., Boley, C. D., and Desai, R. C., "On the Kinetic Model Description of Rayleigh-Brillouin Scattering from Molecular Gasses," *Canadian Journal of Physics*, Vol. 52, No. 4, 1974, pp. 285-290.
- ²¹Yen, Y., and Cummins, H. Z., "Localized Fluid Flow Measurements with an He-Ne Laser Spectrometer," *Applied Physics Letters*, Vol. 4, No. 10, 1964, pp. 176-178.
- ²²Elliott, G. S., Samimy, M., and Arnette, S. A., "A Study of Compressible Mixing Layers Using Filtered Rayleigh Scattering," *30th Aerospace Sciences Meeting and Exhibit*, AIAA Paper 92-0175, Jan. 1992.
- ²³Miles, R. B., Forkey, J. N., and Lempert, W. R., "Filtered Rayleigh Scattering Measurements in Supersonic/Hypersonic Facilities," *28th Joint Propulsion Conference and Exhibit*, AIAA Paper 92-3894, July 1992.
- ²⁴Forkey, J. N., Lempert, W. R., Bogdonoff, S. M., Russell, G., and Miles, R. B., "Volumetric Imaging of Supersonic Boundary Layers Using Filtered Rayleigh Scattering Background Suppression," *32nd Aerospace Sciences Meeting and Exhibit*, AIAA Paper 94-0491, Jan. 1994.
- ²⁵Elliott, G.S., Glumac, N., Carter, C.D., Nejad, A.S., "Two-dimensional temperature field measurements using a molecular filter based technique," *Combustion Science and Technology*, Vol. 125, 1997, pp. 351-369.
- ²⁶Elliott, G.S., Boguszko, M., Carter, C., "Filtered Rayleigh Scattering: Toward Multiple Property Measurements," *39th AIAA Aerospace Sciences Meeting and Exhibit*, AIAA Paper 2001-0301, Jan. 2001.
- ²⁷Boguszko, M., Elliott, G.S., "On the use of filtered Rayleigh scattering for measurements in compressible flows and thermal fields," *Experiments in Fluids*, Vol. 38, 2005, pp. 33-49.
- ²⁸Boguszko, M., Huffman, R., Elliott, G.S., "Property and velocity measurements in a supersonic flow," *44th AIAA Aerospace Sciences Meeting and Exhibit*, AIAA Paper 2006-1390, Jan. 2006.
- ²⁹Huffman, R.E., Boguszko, M., Elliott, G.S., "Mean and Fluctuating Property Measurements with Filtered Angularly Resolved Rayleigh Scattering," *AIAA Journal*, Vol. 49, No. 10, 2011, pp. 2081-2089.
- ³⁰Most, D., Leipertz, A., "Simultaneous two-dimensional flow velocity and gas temperature measurements by use of a combined particle image velocimetry and filtered Rayleigh scattering technique," *Applied Optics*, Vol. 40, No. 30, 2001, pp. 5379-5387.
- ³¹McManus, T.A., Papageorge, M.J., Fuest, F., Sutton, J.A., "Spatio-temporal characteristics of temperature fluctuations in turbulent non-premixed jet flames," *Proceedings of the Combustion Institute*, Vol. 35, 2015, pp. 1191-1198.

- ³²Papageorge, M.J., McManus, T.A., Fuest, F., Sutton, J.A., "Recent advances in high-speed planar Rayleigh scattering in turbulent jets and flames: increased record lengths, acquisition rates, and image quality," *Applied Physics B*, Vol. 115, 2014, pp. 197-213.
- ³³McManus, T.A., Sutton, J.A., "Simultaneous 2D filtered Rayleigh scattering thermometry and stereoscopic particle image velocimetry measurements in turbulent non-premixed flames," *Experiments in Fluids*, Vol. 61, No. 134, 2020.
- ³⁴Lee, G. S., "Design and Development of a Wind Tunnel for the Investigation of Turbulent Compressible Mixing Layers," M.S. Thesis, Dept. of Aerospace Engineering, University of Illinois, Urbana, IL, 2017.
- ³⁵Forkey, J.N., Lempert, W.R., Miles, R.B., "Corrected and calibrated I₂ absorption model at frequency doubled Nd:YAG laser wavelengths," *Applied Optics*, Vol. 36, 1997, pp. 6729.
- ³⁶Forkey, J.N., Lempert, W.R., Miles, R.B., "Accuracy limits for planar measurements of flow field velocity, temperature, and pressure using Filtered Rayleigh Scattering," *Experiments in Fluids*, Vol. 24, 1998, pp. 151-162.
- ³⁷Sun, C., and Childs, M. E., "A Modified Wall Wake Velocity Profile for Turbulent Compressible Boundary Layers," *Journal of Aircraft*, Vol. 10, No. 6, 1973, pp. 381–383.
- ³⁸Mathews, D. C., Childs, M. E., and Paynter, G. C., "Use of Coles' Universal Wake Function for Compressible Turbulent Boundary Layers," *Journal of Aircraft*, Vol. 7, No. 2, March-April 1970, pp. 137-140.
- ³⁹Ikawa, H. and Kubota, T., "Investigation of supersonic turbulent mixing layer with zero pressure gradient," *AIAA Journal*, Vol. 13, No. 5, 1975, pp. 566–572.
- ⁴⁰Chinzei, N., Matsuya, G., Komura, T., Murakami, A., and Kudou, K., "Spreading of Two-Stream Supersonic Turbulent Mixing Layers," *Physics of Fluids*, Vol. 29, No. 5, 1986, pp. 1345–1347.
- ⁴¹Elliott, G. S. and Samimy, M., "Effects of Compressibility on the Characteristics of Free Shear Layers," *AIAA Journal*, Vol. 28, No. 3, 1990, pp. 439–445.
- ⁴²Fourguette, D. C., Mungal, M. G., and Dibble, R. W., "Time evolution of the shear layer of a supersonic axisymmetric jet," *AIAA Journal*, Vol. 29, No. 7, 1991, pp. 1123–1130.
- ⁴³Clemens, N.T. and Mungal, M.G., "Large-scale structure and entrainment in the supersonic mixing layer," *Journal of Fluid Mechanics*, vol. 284, 1995, pp. 171–216.
- ⁴⁴Hall, J., Dimotakis, P., and Rosemann, H., "Experiments in Nonreacting Compressible Shear Layers," *AIAA Journal*, Vol. 31, No. 12, 1993, pp. 2247–2254.
- ⁴⁵Gruber, M. R., Messersmith, N. L., and Dutton, J. C., "Three-dimensional velocity field in a compressible mixing layer," *AIAA Journal*, Vol. 31, No. 11, 1993, pp. 2061–2067.
- ⁴⁶Debisschop, J. R., Chambres, O., and Bonnet, J. P., "Velocity Field Characteristics in Supersonic Mixing Layers," *Experimental Thermal and Fluid Science*, Vol. 94, No. 9, 1994, pp. 147–155.
- ⁴⁷Mehta, R. D. and Westphal, R. V., "Near-field turbulence properties of single and two-stream plane mixing layers," *Experiments in Fluids*, Vol. 4, 1986, pp. 257–266.
- ⁴⁸Urban, W. D. and Mungal, M. G., "Planar Velocity Measurements in Compressible Mixing Layers," *Journal of Fluid Mechanics*, Vol. 431, 2001, pp. 189–222.
- ⁴⁹Lazar, E., DeBlauw, B., Glumac, N., Dutton, J. C., and Elliott, G. S., "A Practical Approach to PIV Uncertainty Analysis," *27th AIAA Aerodynamic Measurement Technology and Ground Testing Conference*, AIAA Paper 2010-4355, 2010.

⁵⁰Hortensius, R., “The Fluid-Structure Interaction of an Axisymmetric Underexpanded Jet Flowing Across an Adjacent Compliant Surface,” Ph.D. Thesis, Dept. of Aerospace Engineering, University of Illinois, Urbana, IL, 2017.

⁵¹Weineke, B., “PIV uncertainty quantification from correlation statistics,” *Measurement Science and Technology*, Vol. 26, No. 7, 2015, pp. 1–10.

Appendix A: Air Heater Specifications and Safety Supplement

**MODEL: CHP0824S-60-74Y-483
SERIAL: 02-2676-1A**

DESIGN DATA:

Temperature Limits: -20° F Min., 1175° F Max.

Pressure Limits: -15 PSIG Min., 525 PSIG Max.

Empty Weight of Unit: 800 Pounds

Terminal House Classification: NEMA 12

OPERATIONAL DATA:

Fluid: Air

Fluid Temperature Range: 70°F to 1100°F

Heater Rating: 60 KW on 480 VAC, 3-Phase, 60-Hz, 72 Amp

Heater Watt density: 13.4 Watts/sq. in.

Remarks:

High Temperature Stainless Steel Construction

Type "K" thermocouples used for over-temperature protection

Calcium Silicate Insulation with Stainless Steel Jacket

UTILITIES:

Power: 480 VAC, 3ø, 60 Hz, 100 FLA

Heated Compressible Mixing Layer Facility Standard Operating Procedure Supplement

PPE & Safety Considerations/Checks:

1. At least two people should be present in the lab when running the heated compressible mixing layer facility.
2. All those present must utilize ear and eye protection.
3. Be sure that all PPE is also rated for use with any diagnostic techniques in use (e.g., laser goggles if using lasers).
4. This is a high pressure and temperature facility. As such, care needs to be taken when operating the wind tunnel, especially with the windows. Avoid passing the windows while running, particularly during tunnel startup and shutdown (as shock waves pass the windows at these times). Be cognizant of the potential window blast zone.

Start-up:

1. Verify that all instrumentation is powered on and properly connected. Turn on computer.
2. Verify that the laboratory manifold valve is open and that the wind tunnel manual globe valve is shut.
3. Utilize appropriate PPE (safety glasses and hearing protection are minimums).
4. Ensure that wind tunnel is ready to run. Check the following:
 - a. All bolts are installed and tight
 - b. All windows are in place and properly secured
 - c. All pressure lines and taps are properly plumbed and secured
 - d. All data acquisition equipment (i.e., pressure systems) used by the LabVIEW program is turned on, has been allowed to warm up, and is operational. Pressure systems typically require approximately 30 min. to warm up.
 - e. Ensure no objects are near the secondary stream inlet when facility is configured to entrain air from the room for the secondary stream.
 - f. Heater is plugged in, and both the circuit breakers are turned to allow power through the system. Heater itself is turned on.
 - g. All additional experimental equipment is properly secured and readied for operation.
5. Turn on the pressure and temperature measurement box.
6. Note the tank farm pressure, then turn on the compressors (ARL mechanical room) according to their operating procedure.
7. Lock the entrance to GDL and place caution sign on both entrances.
8. Turn on laser light if laser is being operated.
9. Start the LabVIEW control program. Check that there are no errors and that data does record. Do not apply current to the pneumatic valve.
10. Open the valve supplying house air to the wind tunnel control pneumatic valve. Set the regulator to supply air at 80 psi to the control valve. When adjusting pressure, air may vent from the regulator.
11. Open the manual globe valve, and open pneumatic valve slightly to allow a “trickle” flow.
12. Verify that the setpoint for the heater is at the desired temperature. If necessary, change the setpoint.

13. Turn on the heater. While maintaining the “trickle” flow, monitor system status through the LabVIEW program.
14. **Tunnel is now ready to run.** Keep far away from the wind tunnel windows, especially during startup and shutdown (due to passing shock waves). Keep in mind the possible blast zone.
15. Verify LabVIEW mode is set to “Manual” and apply 4 mA of current to the pneumatic valve to open it fully. Then manually open the globe valve to achieve desired stagnation pressures.
16. Conduct your experiment – monitor the tank farm pressure and remember to avoid the windows during operation.
17. At end of experiment, close both manual globe valve and pneumatic valve to “trickle” flow conditions and turn off heater. Monitor system status until system has cooled for at least 15 min. and is at a temperature where flow can be turned off.
18. **Press red “stop” button in LabVIEW to turn off tunnel when desired (standard shutoff or emergency).**
19. Close the manual globe valve fully.
20. Close the house air valve.
21. Depower heater and close circuit breakers.
22. Save both experimental data and LabVIEW run profile data.

Shut-down:

1. STOP the LabVIEW program.
2. Close manual globe valve and pneumatic valve to “trickle” flow settings.
3. Turn off heater.
4. Wait until system temperature has cooled to reasonable level under the trickle flow.
5. Close the manual globe valve fully.
6. Close the house air supply valve.
7. Depower heater.
8. Turn off circuit breakers to heater and unplug.
9. Check condition of the wind tunnel model, windows, seals, etc. **once system has cooled sufficiently.**
10. Turn off other experimental equipment. Shut down computer.
11. Remove caution signs from GDL entrance/exit doors and shut off caution lights.
12. Turn off compressors in the ARL mechanical room according to their operating procedure.

In an emergency:

1. Push the STOP button in the LabVIEW program.
2. Close the manual globe valve. If possible, close to “trickle” flow setting.
3. Turn off heater (throw breaker if necessary).
4. Activate any other emergency kill-switches (or otherwise turn off) any other instrumentation.
5. Call Professor Elliott and, if necessary, emergency responders.

Appendix B: Bill of Materials for Facility Addition of Heater

Part Name	Size	Length	Material	Notes	McMaster Part #	Amnt	Cost	
TANK FARM SUPPLY								
Flange	6	SS 304/304L		Threaded, Forged, Raised	44685K21	1	\$ 244.00	
Flange Gasket	6	1/8"	Buna-N		85167143	1	\$ 3.64	
Reducing Flange	6 to 4	SS 304/304L		Threaded, Forged, Raised	44685K134	1	\$ 277.88	
Reinforced Hose	4	36"	316 SS (int), 304 SS (braid)	Threaded, 290# rated	5793K3	1	\$ 467.31	
Reducing Fitting	4 to 2	1.84"	SS 304/304L	Threaded, 150# rated	4464K187	1	\$ 120.18	
HEATER								
Expanding Fitting	1.5 to 4	1.84"	SS 304/304L	Threaded, 150# rated	4464K615	1	\$ 120.16	
Reinforced Hose	4	48"	316 SS (int), 304 SS (braid)	Threaded, 290# rated	5793K3	1	\$ 542.91	
Flange	4	SS 304/304L		Threaded, Forged, Raised	44685K119	1	\$ 145.25	
Flange Gasket	4	1/8"	Vermiculite	Ultra-Hi-Temp	1009N19	1	\$ 78.35	
Flange	4	SS 304/304L		Threaded, Forged, Raised	44685K119	1	\$ 145.25	
Pipe	4"	SS 304/304L		Threaded	4830K376	1	\$ 38.67	
Tee	4	SS 304/304L		Threaded	4464K143	1	\$ 212.88	
Pipe	4	4"	SS 304/304L	Single-Threaded	91571503	1	\$ 39.23	
Flange	4	SS 304/304L		Unthreaded, Forged	44685K228	1	\$ 168.87	
Flange Gasket	4	1/8"	Buna-N		85167141	1	\$ 2.23	
Gate Valve	4	7.66"	Cast Iron / Steel	Flanged, Cl: \$ 679.16	49505K54 / 49265K14	1	\$ 927.33	
Pipe	4	4"	SS 304/304L	Single-Threaded	91571503	1	\$ 39.23	
Mixer Layer Facility	4	SS 304/304L		Unthreaded, Forged	44685K228	1	\$ 168.87	
Flange Gasket	4	1/16"	Vermiculite	Ultra-Hi-Temp	1009N31	1	\$ 153.95	
MIXING LAYER FACILITY								
MS	Bolts	3/4"-10	6"	Steel	ASTM A193, Grade 87	907504317	16	\$ 41.28
MS	Bolts	5/8"-16	6"	Steel	ASTM A193, Grade 87	907504491	16	\$ 79.84
						Total (before shipping):	\$ 3,696.21	

Appendix C: Engineering Drawing of TAT Probe

